

MAGNETIC FLUX LEAKAGE (MFL) METHOD FOR DAMAGE DETECTION IN INTERNAL POST-TENSIONING TENDONS

FINAL REPORT
FDOT Contract No. BDV29-977-45

Submitted To:
FDOT Research Center
605 Suwannee Street
Tallahassee, FL 32399

Project Manager:
Chase C. Knight, Ph.D., P.E.
Florida Department of Transportation

Submitted By:
Atorod Azizinamini, Ph.D., P.E.
Florida International University
10555 W. Flagler Street,
Miami, FL 33174

Authors:
Ali Javed
Amir Sadeghnejad
Sheharyar Rehmat
Aaron Yakel
and Atorod Azizinamini

June 2021

DISCLAIMER

The opinions, findings, and conclusions expressed in this publication are those of the author(s) and not necessarily those of the Florida Department of Transportation or the U.S. Department of Transportation.

For clarity and completion of some discussion on available non-destructive testing and previous work on magnetic flux leakage method, portion of the earlier published work has been included.

- Azizinamini, Atorod, and Jawad Gull. "Improved inspection techniques for steel prestressing/post-tensioning strand: Volume I." (2012).

CONVERSION TABLES

Approximate conversion to SI Units

Symbol	When you know	Multiply by	To find	Symbol
Length				
in	inches	25.4	millimeters	mm
ft	feet	0.305	meters	m
yd	yards	0.914	meters	m
mi	miles	1.61	kilometers	km
Area				
in ²	square inches	645.2	square millimeters	mm ²
ft ²	square feet	0.093	square meters	m ²
yd ²	square yard	0.836	square meters	m ²
ac	acres	0.405	hectares	ha
mi ²	square miles	2.59	square kilometers	km ²
Volume				
fl oz	fluid ounces	29.57	milliliters	mL
gal	gallons	3.785	liters	L
ft ³	cubic feet	0.028	cubic meters	m ³
yd ³	cubic yards	0.765	cubic meters	m ³
Mass				
oz	ounces	28.35	grams	g
lb	pounds	0.454	kilograms	kg
T	short tons (2000 lb)	0.907	megagrams (or "metric ton")	Mg (or "t")
Temperature				
°F	Fahrenheit	5 (F-32)/9 or (F-32)/1.8	Celsius	°C
Illumination				
fc	foot-candles	10.76	lux	lx
fl	foot-Lamberts	3.426	candela/m ²	cd/m ²
Force and Pressure or Stress				
lbf	pound force	4.45	newtons	N
lbf/in ²	pound force per square inch	6.89	kilopascals	kPa

Approximate conversion to U.S. Customary Units

Symbol	When you know	Multiply by	To find	Symbol
Length				
mm	millimeters	0.039	inches	in
m	meters	3.28	feet	ft
m	meters	1.09	yards	yd
km	kilometers	0.621	miles	mi
Area				
mm ²	square millimeters	0.0016	square inches	in ²
m ²	square meters	10.764	square feet	ft ²
m ²	square meters	1.195	square yards	yd ²
ha	hectares	2.47	acres	ac
km ²	square kilometers	0.386	square miles	mi ²
Volume				
mL	milliliters	0.034	fluid ounces	fl oz
L	liters	0.264	gallons	gal
m ³	cubic meters	35.314	cubic feet	ft ³
m ³	cubic meters	1.307	cubic yards	yd ³
Mass				
g	grams	0.035	ounces	oz
kg	kilograms	2.202	pounds	lb
Mg (or "t")	megagrams (or "metric ton")	1.103	short tons (2000 lb)	T
Temperature				
°C	Celsius	1.8C+32	Fahrenheit	°F
Illumination				
lx	lux	0.0929	foot-candles	fc
cd/m ²	candela/m ²	0.2919	foot-Lamberts	fl
Force and Pressure or Stress				
N	newtons	0.225	pound force	lbf
kPa	kilopascals	0.145	pound force per square inch	lbf/in ²

TECHNICAL REPORT DOCUMENTATION

1. Report No.	2. Government Accession No.	3. Recipient's Catalog No.	
4. Title and Subtitle Magnetic Flux Leakage Method for Damage Detection in Internal Post-Tensioning Tendons		5. Report Date	
		6. Performing Organization Code	
7. Author(s) Ali Javed, Amir Sadeghnejad, Sheharyar Rehmat, Aaron Yakel, Atorod Azizinamini		8. Performing Organization Report No.	
9. Performing Organization Name and Address Florida International University, Miami http://breslint@servax.fiu.edu University Park, Room P.C. 539 Miami, FL 33199-0000		10. Work Unit No. (TRAIS)	
		11. Contract or Grant No. BDV29-977-45	
12. Sponsoring Agency Name and Address Florida Department of Transportation 605 Suwannee Street Tallahassee, FL 32399-0450 U.S.		13. Type of Report and Period Covered Final report Apr 2018-June 2021	
		14. Sponsoring Agency Code	
15. Supplementary Notes			
16. Abstract <p>The magnetic flux leakage (MFL) method has been identified as a promising non-destructive testing technique for detecting metal loss in external post-tensioned tendons and stay-cables. However, for internal tendons, the interfering signals from secondary ferromagnetic materials, such as mild reinforcement, can generate complicated signals and may lead to inaccurate prediction of damage location and severity. The objective of the study was to identify the improvements to be made on existing MFL technology, both in terms of hardware and testing protocols, which can be implemented for internal tendons in field conditions. A systematic study was conducted to improve the existing MFL system, and a fully functional measurement and magnetizing unit was developed. The developed system demonstrated that effective magnetization of steel strands, located at a depth of 8 inches, can be carried out. Also, a suite of user interfaces was developed in a programming language to improve data processing and visualization.</p> <p>As a proof of concept, the modified MFL system was used to conduct testing on laboratory mockup specimens and segments of a decommissioned bridge located at Florida International University. The results showed that the presence of transverse reinforcement and depth of magnetization have a significant effect on magnetic flux signals. The effect of transverse reinforcement was reduced using a novel testing protocol developed in this study. In this protocol, near-surface magnetization is initially carried out, followed by far-surface measurement, which allows identification of defects in embedded tendons. Additional laboratory testing was carried out on specimens which replicated conditions of an in-service bridge, and the developed system and testing protocol showed promising results in identifying the locations of the defects. To verify the merits of the equipment, a series of tests was conducted on an in-service bridge. The inspection methods showed that the MFL method is highly repeatable, and magnetization on the post-tensioned rods is retained over time. Area scans on the bridge spans showed anomalous patches which may be representative of a defect, coupler bar, or a construction deficiency.</p>			
17. Key Words Non-destructive testing, Magnetic flux leakage, Steel Tendons, Prestressed Concrete Bridges, Internal Tendons, MFL		18. Distribution Statement	
19. Security Classif. (of this report) Unclassified	20. Security Classif. (of this page) Unclassified	21. No. of Pages 166	22. Price

ACKNOWLEDGMENTS

The authors would like to thank the Florida Department of Transportation (FDOT) and project managers Chase Knight, Ivan Lasa, and Matthew Duncan.

The assistance provided by graduate research assistants as well as FDOT Office during field testing is acknowledged and greatly appreciated.

EXECUTIVE SUMMARY

Prestressed concrete bridge (PSC) structures have been designed and constructed for over 40 years in the U.S. with generally good structural and durability performance. Even though the prestressing steel is ideally protected from corrosion when either placed inside a grouted plastic or steel duct for post-tensioned (PT) applications or directly bonded with the concrete in pre-tensioning applications, corrosion remains a challenge. To ensure public safety and structural integrity, development of sound methodologies to assess the health of steel strands is crucial. Many non-destructive tests (NDT) are available for PSC, most of which are useful for predicting material properties of concrete. However, the limited capabilities of available NDT present challenges for practical field condition assessment of steel strand. Furthermore, few of these techniques can assess internal PT tendons.

Magnetic methods make use of the interaction between magnetic (and associated electric) fields with matter. Magnetic flux leakage (MFL) is the principal magnetism-based NDT method that has been applied to inspect distress in ferrous materials. Recent developments with static magnetic methods have shown improved capabilities to detect strand damage. The application of MFL to concrete structures is possible because the concrete medium does not affect the measurements unless ferromagnetic impurities are present in the concrete. Identification of damage of steel strands in actual PSC members may be masked by the presence of interfering ferromagnetic sources such as mild reinforcing steel. The main goal of this project was to develop magnetic NDT equipment for field inspection of internal tendons. The objective of the project is to develop a concept that could facilitate field applications of the MFL system. This outcome of the project is to develop a fully functional prototype equipment that can detect damage in internal tendons.

In this report, an overview of the main parts of the earlier version of the MFL system, the capabilities of this system, and the required improvements to adapt the system to the field conditions are presented. Efforts are devoted to identification of deficiencies of this early version of the MFL system. With the advancements of new sensors, microelectronics, and digital devices, the capabilities of an earlier measurement system were improved. Different modifications to an earlier version of the magnetizing system were also carried out, and modified permanent magnets were developed. The goal of modifications in the existing MFL system was to develop a fully functional prototype unit. To this end, a unit was fabricated which housed all main components of the MFL system. The unit can perform scans on horizontal surfaces, allowing measurements on deck slabs, cantilever, and continuity tendons of box girders, etc.

The objective of this research was to conceptualize a modified MFL system which is effective for internal tendons. Therefore, the effectiveness of these modifications to sensing and magnetizing systems needs to be demonstrated for field conditions. Based on consultation with the Florida Department of Transportation (FDOT), a bridge with a known defect was selected. Using the schematic drawings of the actual bridge, laboratory mock-up specimens were constructed. Different tests were carried out on mock-up laboratory specimens. These tests were focused on the far-side magnetization scheme and the effect of transverse reinforcement. Based on the results, it was found that the far-side magnetization and near-surface measurement resulted in a clear indication of defect

signal even in the presence of transverse reinforcement. This result demonstrated the feasibility the developed method for field use.

In the next phase of testing, the measurement unit and permanent magnet were used for testing the bridge segment with different section loss scenarios. A series of tests was carried out on a decommissioned bridge segment located at Florida International University. Different magnetization schemes were used to magnetize a group of strands placed in an empty duct. The test variables also considered the effect of magnetization depth, section loss, and location of transverse reinforcement. The test results were similar to laboratory mockup specimens where the far-side magnetization scheme was able to identify the defect in the presence of transverse reinforcement.

As an extra task, the developed MFL system and testing protocol were used to test an in-service bridge. The selected bridge was located in Florida and has been in service for more than 50 years. The tests were carried out on PT rods on all five spans of the bridge in three phases. An extensive number of tests were carried out in three phases. In the first phase, measurements were performed mainly on unmagnetized PT rods to establish a baseline signal. Due to limitations on site, the top magnetization was carried out on only select rods in span 1. In phase II, support railings were installed on the underside of the bridge to allow far-side magnetization. The results from this phase showed that the modified magnet was able to magnetize the embedded PT rods. Anomalous signals were obtained for rods in span 3 and span 4 which may be indicative of a defect, construction deficiency, or a bar coupler. In phase III, measurements were performed without any additional magnetization. The results showed that the magnetization is retained over time and the results are repeatable.

Due to the complex nature of magnetic fields, the application of the MFL system to internal tendons required an in-depth study of physical principles. Therefore, before proceeding with testing, a decision was made to carry out numerical simulations to study the parameters that may affect magnetic flux in ferromagnetic materials. The results showed that the depth of magnetization affects the development of the magnetic field in the rod. The damage in the rod was evident in results when no transverse reinforcement was present. However, when a transverse reinforcement was located in the vicinity of the rod, the behavior became complicated. Finite element analysis was also carried out on the subject bridge. To limit the computation time only a segment of the bridge was modeled with PT rod, transverse reinforcement, and ties. Different simulations were considered but results show that there is a complex interaction of various elements, and valid conclusions from numerical studies could not be drawn.

TABLE OF CONTENTS

Disclaimer	ii
Conversion Tables	iii
Technical Report Documentation	v
Acknowledgments	vi
Executive Summary	vii
List of Figures.....	xiii
List of Tables.....	xviii
List of Abbreviations and Acronyms	xix
1 Introduction	1
1.1 Prestressed Concrete	1
1.1.1 Corrosion Problems in PSC Bridges.....	2
1.1.2 Practices to Assure Durable PT Systems.....	2
1.1.3 Field Inspection Challenges.....	3
1.2 Non-Destructive Testing Methods.....	3
1.3 Magnetic Flux Leakage	4
1.3.1 MFL for External PT Systems.....	6
1.3.2 Application of MFL to Internal Tendons	6
1.4 Project Objectives	7
1.5 Research Approach	8
2 System Development and Testing	10
2.1 Introduction	10
2.2 Earlier MFL System	10
2.2.1 The Permanent Magnet on the Earlier MFL System.....	12
2.2.2 The Magnetic Sensors of the Earlier MFL Equipment	13
2.2.3 Linear Encoder and DAQ of the Earlier MFL Equipment	15
2.3 Development of New MFL system	15
2.3.1 Modification to Measurement System.....	15
2.3.1.1 MV2 Hall Sensor	15
2.3.1.2 HAL2425 Sensor	16
2.3.1.3 Flux Concentrators	16
2.3.2 Modification to Magnetizing System	16
3 Final MFL System.....	20
3.1 Magnetization Units	20
3.1.1 Magnet 1.....	20
3.1.2 Magnet 2.....	20

3.1.3	Magnet 3.....	21
3.2	Measurement Units.....	21
3.2.1	Experimental Measurement Units.....	22
3.2.2	Final Measurement Units.....	23
3.3	Capabilities of Developed System	24
3.3.1	Maximum Depth of Tendons.....	24
3.3.2	Mild Reinforcement Density.....	24
3.3.3	Access – Lane Closure Requirement	25
3.3.4	Coverage Area	25
3.3.5	Weather Conditions	25
3.3.6	End User Expertise.....	25
4	Laboratory and Segment Testing.....	26
4.1	Laboratory Testing	26
4.1.1	Testing on the Unmagnetized System.....	27
4.1.2	Bottom Magnetization on Laboratory Mockup Specimen	30
4.1.3	Summary of Laboratory Tests	34
4.2	Testing on Bridge Segments.....	35
4.2.1	Bridge Segments at FIU	35
4.2.2	Preliminary Tests on Bridge Segment	36
4.2.3	Top Magnetization Scheme	37
4.2.4	Bottom Magnetization Scheme.....	39
4.2.5	Segment Testing Summary	45
4.3	Bridge A Mockup Specimen.....	46
4.3.1	Comparison of MFL Signal with No Magnetization	49
4.3.2	Comparison of MFL Signal with Magnetization from Bottom Side.....	49
4.3.3	Effect of Gap Width on MFL Signal (Non-metallic duct).....	50
4.3.4	Metal Duct without Magnetization.....	50
4.3.5	Metal Duct with Magnetization.....	51
4.3.6	Effect of Gap Width on MFL Signal (Metallic duct)	51
4.3.7	Effect of Flux Concentrator on Signal of PT Rod	52
4.3.8	Effect of Flux Concentrator on Signal of Strands.....	52
4.3.9	Effect of Percentage of Defect on MFL Signal of Strands.....	53
4.3.10	Effect of Defect with Clear Gap & Connected with Rebars.....	53
4.3.11	Effect of Percentage of Defect on MFL Signal of PT Rod.....	54
4.3.12	“Bridge A” Mockup Testing Summary.....	54
5	Field Testing	55
5.1	Bridge A.....	55
5.1.1	Phase I Testing.....	55

5.1.2	Phase II Testing.....	56
5.1.3	Phase III Testing.....	57
5.1.4	Discussion on Test Results	57
5.1.4.1	Span 1 – Tendon 1	57
5.1.4.2	Span 1 – Tendon 2.....	60
5.1.4.3	Span 2 – Tendon 1.....	60
5.1.4.4	Span 3 – Tendon 2.....	61
5.1.4.5	Span 4 – Tendon 2.....	62
5.1.4.6	Area Scans.....	64
5.2	Summary of Field Testing for Bridge A	70
6	Summary of Important Findings and Conclusions	71
6.1	Future Research	73
	References.....	74
	Appendix A Details of Field Bridges.....	76
A.1	Bridge A Details	76
A.2	Bridge B Details	76
A.3	Bridge Segment Details	78
	Appendix B Field Testing Results	80
B.1	Bridge A Phase I Testing	80
B.2	Bridge A Phase II Testing	86
B.3	Comparison of Phase I and II on Bridge A.....	90
B.4	Bridge B Testing	94
B.4.1	Test Methodology	94
B.4.2	Test Results.....	96
	Appendix C Finite Element Analysis of MFL System	97
C.1	Parametric Study on Magnetization and Residual Magnetic Field	97
C.1.1	Material Properties	97
C.1.1.1	Strand Material	98
C.1.1.2	Magnet Grade 35 NdFe.....	99
C.1.1.3	Back Iron	100
C.1.2	Depth Study – Bar Only.....	101
C.1.2.1	Short Rod	101
C.1.2.2	Longer Rod.....	112
C.1.2.3	Depth Effect.....	115
C.1.3	Damage Study.....	121
C.1.3.1	Depth – 3 inches.....	122
C.1.3.2	Depth – 4 inches.....	125

C.1.4	Observation and Conclusions.....	128
C.1.4.1	Modeling.....	128
C.1.4.2	Depth Study.....	128
C.1.4.3	Damage Study.....	129
C.2	Field Simulation	129
C.2.1	Modeling.....	129
C.2.2	Results	132
C.2.3	Magnet Applied to End of Rod.....	136
C.2.4	Uniform Field	137
C.2.5	Observations and Conclusions	138
Appendix D	Operation Manual.....	139
D.1	Setup for DAQ System for Experimental Measurement Units.....	139
D.2	Setup for Hal Sensors.....	140
D.3	Final Measurement Unit Manual	141
D.4	Operation Manual	142
Appendix E	Testing with Magnet 3.....	144

LIST OF FIGURES

Figure 1-1: Typical cantilever segments with tendons (Corven and Moreton, 2013).....	1
Figure 1-2: Principle of magnetic flux leakage method.	5
Figure 1-3: MFL of an external PT tendon (Lau and Azizinamini, 2018) and cable stays (Alpin Technik Leipzig accessed online 2020).....	6
Figure 1-4: Balanced cantilever section showing location of internal tendons (Corven Engineering Inc., 2002).....	7
Figure 2-1: Components of the earlier MFL system.....	11
Figure 2-2: Instrumentation: (a) sensors, (b) magnet, (c) potentiometer and, (d) cart.	12
Figure 2-3: (a) Earlier magnet version, (b) magnetic strength on the south pole and, (c) magnetic strength of the south pole of the same block in the permanent magnet configuration.....	13
Figure 2-4: Variation of the strength of the magnetic field (G) with the height (in.).....	13
Figure 2-5: Circuit with the matrix of Hall sensors.	14
Figure 2-6: Drift with time of the matrix of sensors inside a zero-Gauss chamber.	14
Figure 2-7: MetroLab MagVector™ MV2 (left) and Micronas HAL2425.....	15
Figure 2-8: Modifications to an earlier version of the magnet.	17
Figure 2-9: Magnetization configuration with modified magnet.	18
Figure 2-10: Strength of the residual magnetic field measured in (a) the central wire of one strand, (b) and in a group of ten strands measured in the central wire of the central strand.	18
Figure 3-1: Configuration of magnet 1.....	20
Figure 3-2: Configuration of magnet 2.....	21
Figure 3-3: Configuration of magnet 3.....	21
Figure 3-4: Measurement unit 1 with 4 sensors.....	22
Figure 3-5: Measurement unit 2 with 48 sensors.....	23
Figure 3-6: Final measurement units (a) 16 in. and, (b) 32 in. wide unit.	24
Figure 3-7: Sensor layout and DAQ for prototype unit 3b.	24
Figure 4-1: Laboratory test setup and sensor layout.	27
Figure 4-2: Test configuration 1 to 3.....	28
Figure 4-3: Result of test 1 to 3.	29
Figure 4-4: Test configuration 4.	29
Figure 4-5: MFL signal of transverse reinforcement only (test 4).....	30
Figure 4-6: Configuration and result of test 5.	31
Figure 4-7: Test configuration 6 and 7.....	32
Figure 4-8: MFL signal of PT rod with and without transverse reinforcement (test 5 to test 7). ...	32
Figure 4-9: Configuration and result of test 8.	33
Figure 4-10: Test configuration 9 and 10.....	34
Figure 4-11: Bridge segment.....	35
Figure 4-12: Location of transverse reinforcement and bundled strands in bridge segment.	35
Figure 4-13: Test configuration 11.....	36
Figure 4-14: Test configuration 12.....	37
Figure 4-15: Test configuration 13.....	38
Figure 4-16: Test configuration 14.....	39
Figure 4-17: MFL test setup.	40
Figure 4-18: Test configuration 15.....	40
Figure 4-19: Test configuration 16.....	42
Figure 4-20: Test configuration 17.....	42
Figure 4-21: Test configuration 18.....	43
Figure 4-22: Test configuration 19 and 20.....	43
Figure 4-23: MFL signal of a 55% defect under the transverse bars.....	44
Figure 4-24: MFL signal of a 55% defect in between the transverse bars.....	44

Figure 4-25: Test configuration 21 and 22.....	45
Figure 4-26: MFL signal of a 100% defect under the transverse bars.....	45
Figure 4-27: MFL signal of a 100% defect in between the transverse bars.....	45
Figure 4-28: Construction of specimen.....	46
Figure 4-29: Dimension and reinforcement detail of concrete block.	47
Figure 4-30: Testing on concrete blocks.....	47
Figure 4-31: Comparison of MFL signal for LST-1 & LST-2.....	49
Figure 4-32: Comparison of MFL signal for LST-3 & LST-4.....	50
Figure 4-33: Comparison of MFL signal for LST 5-7.....	50
Figure 4-34: Comparison of MFL signal for LST 8-9.....	51
Figure 4-35: Comparison of MFL signal for LST 10-11.....	51
Figure 4-36: Comparison of MFL signal for LST 12-14.....	52
Figure 4-37: Comparison of MFL signal for LST 15-16.....	52
Figure 4-38: Comparison of MFL signal for LST-17 & LST-18.....	53
Figure 4-39: Comparison of MFL signal for LST 18-20.....	53
Figure 4-40: Comparison of MFL signal for LST 21-22.....	54
Figure 4-41: Comparison of MFL signal for LST 23-26.....	54
Figure 5-1: Plan view of Bridge A.....	55
Figure 5-2: Marked locations for MFL testing on span 2.....	56
Figure 5-3: MFL signal of unmagnetized PT rod 1 (test I-S-1-1) (flux concentrator sensors).	58
Figure 5-4: MFL signal of magnetized PT rod 1 (test I-S-1-1-m) (flux concentrator sensors).	58
Figure 5-5: MFL signal taken between PT rods without magnetization (test S-1-0) (sensors with flux concentrators).	59
Figure 5-6: Test result of II-S-1-1 (regular sensors).....	59
Figure 5-7: Comparison of MFL signal from phase I and phase II on span 1 tendon 1 (sensors with flux concentrator).....	60
Figure 5-8: Comparison of MFL signal from phase I and phase II on span 1 tendon 2.	60
Figure 5-9: Test result of II-S-2-1 (regular sensors).....	61
Figure 5-10: Test result of II-S-3-2 (regular sensors).....	61
Figure 5-11: MFL signal of unmagnetized PT rod 2 (test I-S-4-2).....	62
Figure 5-12: MFL signal of tendon magnetized from the bottom (test II-S-4-2).....	63
Figure 5-13: Surface scan of S-4-2.	63
Figure 5-14: Comparison of MFL signal from phase I and phase II on span 4 tendon 2.	64
Figure 5-15: Area scan of span 1.	65
Figure 5-16: Area scan of span 2.	66
Figure 5-17: Area scan of span 3.	67
Figure 5-18: Area scan of span 4.	68
Figure 5-19: Area scan of span 5.	69
Figure A-1: Bridge A section through superstructure.	76
Figure A-2: Details of Bridge B.....	77
Figure A-3: GRP result for a depth of 3 in.–6 in.....	77
Figure A-4: GRP result for the line scan.....	77
Figure A-5: GRP test inside bridge for a depth of 3 in.–6 in.....	78
Figure A-6: GRP result for area scan of 44 in. x 12 in.	78
Figure A-7: Decommissioned box girder segments at FIU.....	79
Figure A-8: Empty ducts for testing.	79
Figure A-9: Location of transverse reinforcement and bundled strands in bridge.	79
Figure B-1: Span 1, PT rod 1 (test I-S-1-1).....	81
Figure B-2: Span 1, PT rod 1 (test I-S-1-1m).....	81
Figure B-3: Span 1 between PT rods (test I-S-1-0).	81

Figure B-4: Span 1, PT rod 2 (test I-S-1-2).....	82
Figure B-5: Span 2, PT rod 1 (test I-S-2-1).....	82
Figure B-6: Span 2 between PT rods (test I-S-2-0).	82
Figure B-7: Span 2, PT rod 2 (test I-S-2-2).....	83
Figure B-8: Span 3, PT rod 1 (test I-S-3-1).....	83
Figure B-9: Span 3 between PT rods (test I-S-3-0).	83
Figure B-10: Span 3, PT rod 2 (test I-S-3-2).....	84
Figure B-11: Span 4, PT rod 1 (test I-S-4-1).....	84
Figure B-12: Span 4 between PT rods (test I-S-4-0).....	84
Figure B-13: Span 4, PT rod 2 (test I-S-4-2).....	85
Figure B-14: Span 5, PT rod 1 (test I-S-5-1).....	85
Figure B-15: Span 5 between PT rods (I-S-5-0).	85
Figure B-16: MFL signal of unmagnetized PT rod 2 (I-S-5-2).	86
Figure B-17: MFL signal of PT rod 1 (II-S-1-1).	86
Figure B-18: MFL signal of PT rod 2 (II-S-1-2).	87
Figure B-19: MFL signal of PT rod 1 (II-S-2-1).	87
Figure B-20: MFL signal of PT rod 2 (II-S-2-2).	87
Figure B-21: MFL signal of PT rod 1 (II-S-3-1).	88
Figure B-22: MFL signal of PT rod 2 (II-S-3-2).	88
Figure B-23: MFL signal of PT rod 1 (II-S-4-1).	88
Figure B-24: MFL signal of PT rod 2 (II-S-4-2).	89
Figure B-25: MFL signal of PT rod 1 (II-S-5-1).	89
Figure B-26: MFL signal of PT rod 2 (II-S-5-2).	90
Figure B-27: Span 1, PT rod 1.	90
Figure B-28: Span 1, PT rod 2.	91
Figure B-29: Span 2, PT rod 1.	91
Figure B-30: Span 2, PT rod 2.	91
Figure B-31: Span 3, PT rod 1.	92
Figure B-32: Span 3, PT rod 2.	92
Figure B-33: Span 4, PT rod 1.	92
Figure B-34: Span 4, PT rod 2.	93
Figure B-35: Span 5, PT rod 1.	93
Figure B-36: Span 5, PT rod 2.	93
Figure B-37: Obtaining MFL signal from the bottom side.....	94
Figure B-38: Measurement area of test 1 & 2.....	95
Figure B-39: Measurement area of test 3.....	95
Figure B-40: Measurement area of test 4.....	95
Figure B-41: Area scan of test 1.....	96
Figure B-42: Area scan of test 2.....	96
Figure B-43: Area scan of test 3.....	96
Figure B-44: Area scan of test 4.....	96
Figure C-1: Numerical model of the magnet.....	97
Figure C-2: Schematic B-H curve.....	98
Figure C-3: B-H cure definition in ANSYS Maxwell.	98
Figure C-4: B-H curve defined for strands.	99
Figure C-5: Properties of Grade 35 NdFe magnet.....	100
Figure C-6: Magnetic properties of back iron.....	100
Figure C-7: The numerical setup for magnetizing a bar.....	101
Figure C-8: Analysis results for magnetizing a bar at 2.75 in. from the magnet.	102
Figure C-9: Analysis results for magnetizing a bar at 3 in. from the magnet.	103
Figure C-10: Analysis results for magnetizing a bar at 3.125 in. from the magnet.	104

Figure C-11: Analysis results for magnetizing a bar at 3.25 in. from the magnet.	105
Figure C-12: Analysis results for magnetizing a bar at 3.375 in. from the magnet.	106
Figure C-13: Analysis results for magnetizing a bar at 3.5 in. from the magnet.	107
Figure C-14: Analysis results for magnetizing a bar at 3.75 in. from the magnet.	108
Figure C-15: Analysis results for magnetizing a bar at 4 in. from the magnet.	109
Figure C-16: Analysis results for magnetizing a bar at 5 in. from the magnet.	110
Figure C-17: Analysis results for magnetizing a bar at 6 in. from the magnet.	111
Figure C-18: Analysis results for magnetizing a 96-in. bar at 3 in. from the magnet.	112
Figure C-19: Analysis results for magnetizing a 96-in. bar at 3.25 in. from the magnet.	113
Figure C-20: Analysis results for magnetizing a 96-in. bar at 3.5 in. from the magnet.	114
Figure C-21: Analysis results for magnetizing a 96-in. bar at 4 in. from the magnet.	115
Figure C-22: Stage 1 of bar passing 3 in. under the magnet.	116
Figure C-23: Stage 2 of bar passing 3 in. under the magnet.	116
Figure C-24: Stage 3 of bar passing 3 in. under the magnet.	117
Figure C-25: Stage 4 of bar passing 3 in. under the magnet.	118
Figure C-26: Stage 5 of bar passing 3 in. under the magnet.	118
Figure C-27: Stage 1 of bar passing 4 in. under the magnet.	119
Figure C-28: Stage 2 of bar passing 4 in. under the magnet.	119
Figure C-29: Stage 3 of bar passing 4 in. under the magnet.	120
Figure C-30: Stage 4 of bar passing 4 in. under the magnet.	120
Figure C-31: Stage 5 of bar passing 4 in. under the magnet.	121
Figure C-32: Stage 6 of bar passing 4 in. under the magnet.	121
Figure C-33: Results from 3-in. depth, no damage, bar only.	122
Figure C-34: Results from 3-in. depth, no damage, centered transverse.	123
Figure C-35: Results from 3-in. depth, no damage, offset transverse.	123
Figure C-36: Results from 3-in. depth, damaged, bar only.	124
Figure C-37: Results from 3-in. depth, damaged, centered transverse.	124
Figure C-38: Results from 3-in. depth, damaged, offset transverse.	125
Figure C-39: Results from 4-in. depth, no damage, bar only.	125
Figure C-40: Results from 4-in. depth, no damage, centered transverse.	126
Figure C-41: Results from 4-in. depth, no damage, offset transverse.	126
Figure C-42: Results from 4-in. depth, damaged, bar only.	127
Figure C-43: Results from 4-in. depth, damaged, centered transverse.	127
Figure C-44: Results from 4-in. depth, damaged, offset transverse.	128
Figure C-45: Plan of span 2 and the highlighted tendon of interest.	130
Figure C-46: Model of an individual unit with the PT tendons.	131
Figure C-47: Model of a slice of bridge showing 10 modules and a PT tendon.	131
Figure C-48: Close-up of the model.	132
Figure C-49: Magnetic field from the magnet around the bar (top) and in the bar (bottom).	133
Figure C-50: Magnetic field in models without stirrups.	134
Figure C-51: Results from the full model (magnetized from top measured on top).	135
Figure C-52: Results from model without stirrups (magnetized from top measured on top).	135
Figure C-53: Results from the full model (magnetized from top measured on bottom).	136
Figure C-54: Results of model without stirrups (magnetized from top measured on bottom). ...	136
Figure C-55: Results from model with magnet attached to ends of the PT tendon.	137
Figure C-56: Results from full model in a uniform magnetic field.	138
Figure C-57: Results from models without stirrups in a uniform magnetic field.	138
Figure D-1: Typical operation of MFL magnetizing and sensing system.	142
Figure D-2: Operation of MFL testing for (a) lab testing and (b) field testing.	143
Figure E-1: Effect of changing the magnetization direction for magnet 3.	145
Figure E-2: Difference between using the magnet 2 and 3.	145

Figure E-3: Change in the polarization of magnet 2.	146
Figure E-4: Results after several times of magnetization.....	146
Figure E-5: Effect of transverse reinforcement.	147
Figure E-6: Difference between the results when the polarization was changed.	147
Figure E-7: Results after several times of magnetization.....	147

LIST OF TABLES

Table 2-1. Principal characteristics of the MV2 Hall sensors	16
Table 2-2. Principal characteristics of the HAL2425 Hall sensors.....	16
Table 2-3. Polarity and strength of magnetic field at the central wire of one strand	19
Table 4-1. Test configuration 1 to 4.....	27
Table 4-2. Test configuration 5 to 10.....	30
Table 4-3. Test configuration 11 and 12.....	36
Table 4-4. Test configuration 13 to 14.....	37
Table 4-5. Test configuration 15.....	40
Table 4-6. Test matrix for the bottom magnetized strands.....	41
Table 4-7. Details of the ducts.....	46
Table 4-8. Lab tests details	48
Table B-1. Bridge measurement details	80
Table B-2. List of phase II MFL testing.....	86
Table B-3. Test detail on Bridge B.....	94
Table E-1. Summary of tests.....	144

LIST OF ABBREVIATIONS AND ACRONYMS

Acronym	Definition
AASHTO	American Association of State Highway and Transportation Officials
AC	Alternating current
ASTM	American Society for Testing and Materials
DAQ	Data acquisition
DC	Direct current
DOT	Department of Transportation
FDOT	Florida Department of Transportation
FE	Finite element
FHWA	Federal Highway Administration
FIU	Florida International University
HDPE	High density polyethylene pipe
GPR	Ground penetrating radar
HE	Hall effect
MFL	Magnetic flux leakage
NDT	Non-destructive testing
NdFeB	Neodymium Iron Boron
PCB	Printed circuit board
PI	Principal investigator
PSC	Prestressed concrete structure
PT	Post-tensioned
Reinf.	Reinforcement

1 INTRODUCTION

1.1 PRESTRESSED CONCRETE

The structural and durability performance of prestressed concrete (PSC) structures have improved since its inception in the early 1900s, mainly due to advancements in prestressing technologies, construction practices, and materials. Prestressing is applied to a structure either through pretensioning or post-tensioning. In pretensioning, the high-strength steel strands are tensioned prior to placing concrete in the form. After the concrete is cast, the steel strands bond directly with the concrete and transfer the force to the member. For internal post-tensioned (PT) applications, the tendons or bars are placed in ducts inside the concrete member. The post-tensioning is applied after the concrete has achieved a minimum compressive strength, and the ducts are filled with either grout or wax. Post-tensioned tendons can also be placed outside the concrete section, and the prestressing force is transferred to the concrete member through deviators and anchorages. Steel tendons, by virtue of their embedment, are not directly exposed to environmental conditions. Also, because of prestressing, the crack widths are reduced in concrete, which improves the durability of prestressed structures. Applications of PSC structures range from residential slabs, parking lots, silos, etc.

Prestressing technology has also been widely used in the bridge industry. The use of prestressing technique for concrete bridges is diverse and has been used for superstructure and substructure elements. These bridge elements are generally constructed using high performance materials and improved prestressing technologies. Prestressing has allowed the use of light and slender elements for long bridge spans. A typical example of tendons in a segment of a bridge segment is shown in Figure 1-1.

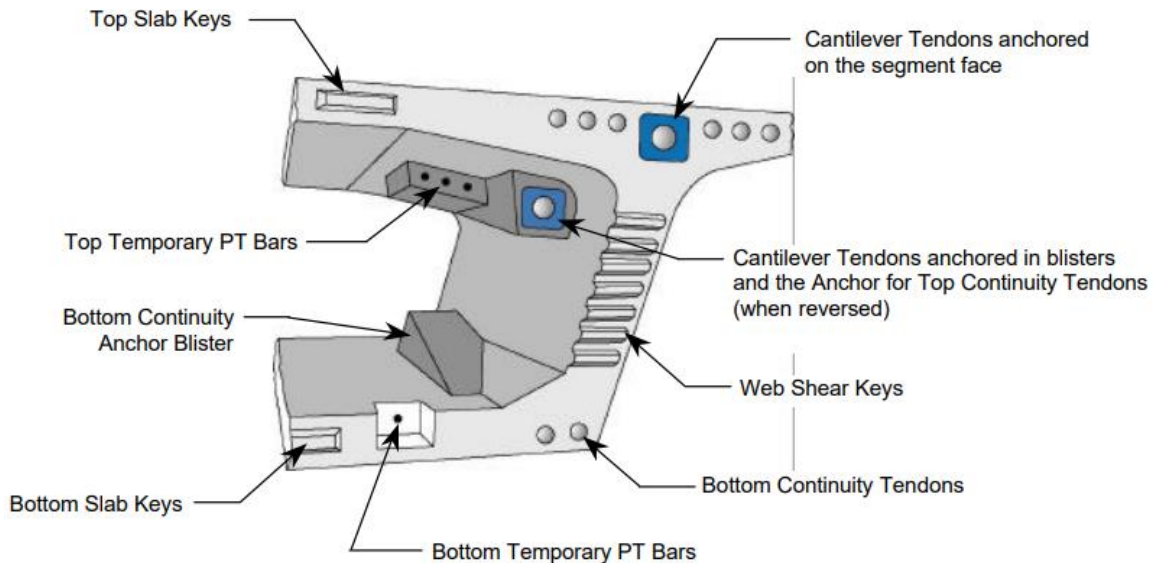


Figure 1-1: Typical cantilever segments with tendons (Corven and Moreton, 2013).

The current practices in prestressing technology have improved significantly over the past few decades and are documented in several guidelines and handbooks. The technological innovations and specification changes have introduced several different material and hardware components for application of prestressing technology. The

hardware components generally consist of anchorages, wedge plates, grout caps, ducts, duct couplers, etc.

1.1.1 Corrosion Problems in PSC Bridges

The corrosion mechanism of steel strands in prestressed concrete is generally similar to conventional reinforced concrete. However, the implications of failure of tendons are more consequential than failure of reinforcement in reinforced concrete (Poursaei, 2016). One of the main causes of corrosion is the ingress of chlorides and inadequate sealing of ducts especially at the anchorages. Severe corrosion has also been associated with deficient grout conditions. Also, the steel strands used in prestressed structures are under high stress which makes them susceptible to brittle failure. The fracture of these steel strands can lead to collapse of the bridge structure without ample warning.

Failure of high-strength tendon has become a serious problem as the deterioration of structures progresses due to aging. Despite advancement in prestressing technology, problems have been encountered in grouted PT ducts in Florida during the late 1990s and early 2000s. One of the early corrosion problems in PT structures was noticed during 1999 inspection of Niles Channel Bridge, the Mid-Bay Bridge, and the Sunshine Skyway Bridge in Florida. In 2005, Lake View Drive Bridge in Pennsylvania failed due to significant prestressing strand loss. More recently, the failure of two external post-tensioned tendons in the Ringling bridge was caused by corrosion of strands in deficient grout conditions (Azizinamini, 2017).

In pre-tensioned concrete structures, corrosion distress can be identified by concrete spalling, cracking of concrete, and bond reduction between concrete and steel strands. However, for PT applications the damages may be contained inside the ducts and surface distress may not be evident by visual inspection alone. In PT components, corrosion has been related to grout bleeding, grout voids, and grout segregation. Intrusion of moisture into the ducts can further aggravate corrosion conditions. The corrosion-induced structural damage of the concrete element and the strand metal loss can lead to brittle failure of the strand and significantly reduce the service life of the structure.

1.1.2 Practices to Assure Durable PT Systems

Because of observed corrosion issues with PT systems, state Departments of Transportation have made significant changes in their practice. Quality of grout, workmanship, and hardware used has improved significantly. Fortunately, the level of redundancies and safety factors used in design are high enough that the observed corrosion issues have not created significant public safety concerns. Florida Department of Transportation (FDOT) implemented new policies and procedures to enhance the long-term durability of their PT bridges in 2002. These policies and procedures were developed through extensive research highlighted in a ten-volume publication titled “New Directions for Florida Post-Tensioning Bridges” (Corven Engineering Inc., 2002). The following five strategies have been adopted for providing corrosion protection for PT bridges:

- Enhanced PT systems
- Fully grouted tendons
- Multi-level anchor protection
- Watertight bridges

- Multiple tendon paths

One of the major improvements from past practice is the use of plastic duct. Field performance and research has indicated that galvanized metal ducts offer little corrosion protection. Plastic ducts provide an added layer of protection. Further, plastic ducts are air and watertight.

Field observations indicate that one of the major areas of corrosion is at the anchorage areas. Similar to multiple protection layers for steel strands, recent practices are calling for multiple protection of anchorage regions. Thus, newer generations of anchorage systems are being developed, which are believed to resolve corrosion issues in the anchorage areas. It is worth mentioning that many states no longer permit use of older generation of anchorage devices.

The quality of grout prior to 2000 was not good. Use of new and proprietary grout types are now the norm with many DOTs. For present practice (in the future, use of un-grouted duct may be a feasibility as it will be easier to inspect and replace strands), the quality of grouting and workmanship is very important. The “Specification for Grouting of Post-Tensioned Structures”, by post-tensioning institute (PTI), provides comprehensive guidelines for grouting. This document is presently undergoing updates. The key elements for good grouting practices are: (1) being able to completely fill the duct, (2) low permeability, (3) appropriate bleed resistance, and (4) careful use of admixtures.

1.1.3 Field Inspection Challenges

Most of the bridges constructed in the U.S., constructed in middle of 20th century, have reached the end of their design life. The deterioration of some of these bridges has caused serious safety concerns which are reflected by poor bridge ratings in the national bridge inventory. Several durability problems have been documented in the past which has resulted into component failures and even catastrophic failure of these PSC bridges. Among the deterioration mechanisms corrosion is of foremost concern.

The inspection of post-tensioned bridges provides major challenges for the bridge (Dammika et al., 2014). The lack of proper and safe access to tendons adds difficulty to any inspection method. Additionally, these bridges generally have long spans, and the level of effort needed to inspect the entire bridge could be substantial. Visual inspections are supplemented with invasive methods, such as borescope, which have been used to assess the condition of strands in the PT ducts. However, these invasive methods are time consuming and costly and may compromise the durability of the tendons. Further, local corrosion damage to embedded steel elements does not generally result in visually noticeable changes to the external appearance of the bridge until it is too late. Therefore, an evaluation of these in-service bridges is important for safety and integrity of the bridge.

1.2 NON-DESTRUCTIVE TESTING METHODS

Non-destructive testing (NDT) methods represent techniques that are based on application of physical principles employed for the purpose of determining the characteristics of materials or components (Raj et al., 2002). These NDT methods allow detection of damages without impairing the serviceability of the structure. NDT technologies used for inspection of PT tendons are briefly described below (Azizinamini and Gull, 2012):

- **Visual methods:**

Visual inspection is the predominant method of inspection in bridges. The method involves using visual aid as a means for condition evaluation of a component. Cracking, fretting, surface corrosion, exfoliation, pitting, and intergranular corrosion can be detected visually when proper access to the inspection area is available. Visual inspection is relatively inexpensive and readily applicable when compared to most other NDT methods.

- **Magnetic methods:**

Magnetic methods make use of the interaction between magnetic fields and their interaction with matter. Magnetic flux leakage (MFL) is the principal magnetism-based NDT method that has been applied to inspect distress in ferrous materials. MFL is a contactless test and but the success of method relies on successful magnetization and measurement of flux signals from defect locations.

- **Mechanical wave/vibration methods:**

Mechanical wave methods make use of (small amplitude) mechanical motion that is set up in a material. Acoustic, ultrasonic, and vibrational methods fall into this category.

- **Electromagnetic wave methods:**

Infrared thermography (IT) and impulse radar (or ground penetrating radar represented by GPR) fall into the category of electromagnetic wave methods. IT method is primarily used to detect near-surface voiding in grouted PT ducts. GPR testing is used to detect the location of metal ducts in PT bridges.

- **Electrochemical methods:**

Electrochemical methods make use of electrochemical to monitor active corrosion. Due to limitations of the current testing technology, most of the studies have been carried out on detecting corrosion in PT tendons under laboratory conditions.

- **Penetrating radiation methods:**

Penetrating radiation method monitor the interaction of high energy electromagnetic radiation, such as x-rays and gamma rays, with matter to draw inferences about the material. The method can provide information about voids in ducts and wire breakages in strands. A primary drawback of this method is radiation exposure which is a safety hazard.

Each of the NDT methods explained above has its own benefits and limitations for a specific application. The inspections carried out using MFL method are highly repeatable and reproducible. MFL is a contactless and is robust in application. A brief overview of the principle of the MFL method is explained in the next section.

1.3 MAGNETIC FLUX LEAKAGE

MFL method is a magneto-static measurement technique and is based on the application of an external magnetic field in vicinity of a ferromagnetic (steel) material to create magnetic flux lines to pass through the steel. The principal components of the MFL are

comprised of a magnetic source and flux sensors. The application of MFL to concrete structures is possible since concrete medium does not affect the measurements unless ferromagnetic impurities are present in the concrete. MFL method works by magnetizing a strand under an exciting magnetic field and the magnetic flux predominantly remains within the strand. In the presence of a geometric discontinuity such as a part of a corroded strand with loss of cross-section, the magnetic flux is deviated (leakage) and can be detected by magnetic sensors such as Hall effect sensors (Figure 1-2).

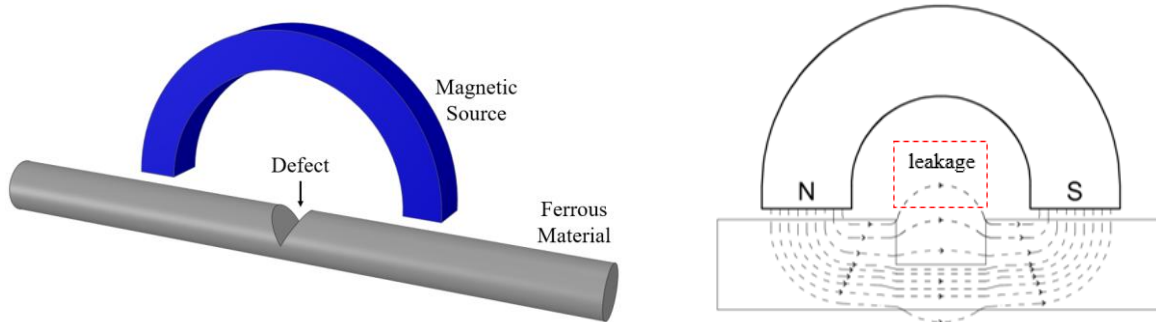


Figure 1-2: Principle of magnetic flux leakage method.

Excitation magnetic fields have been produced using a permanent magnet, an electromagnet or a solenoid depending on specific application. The Hall sensors are made with semi-conductor crystals which when excited by a passage of current perpendicular to the face of the crystal, responds by developing an output voltage proportional to the magnetic field strength. Analysis of the leakage flux output signals can be used to detect the location and the size of the defect. The extent of metal loss can be identified by the corresponding intensity of the defect leakage flux signals.

There are two primary methods for detecting the field anomalies using MFL. These methods are referred to as active and remanent (residual). In the active method, the specimen is magnetized initially and then the Hall sensors are placed above a target area and between the poles of the magnet. For the remanent method, the specimen is also initially magnetized, but the measurement is performed without further magnetization of the specimen. In both methods, the output voltage of the Hall sensors can be used to characterize the level of magnetization and changes in the magnetic field.

MFL method has been used as an NDT technique for a range of applications including bridges, pipelines, rail tracks, etc. In bridge structures, MFL has been used to carry out testing on PT tendons, suspension cables, etc. Recent research efforts have shown that the use of signal processing techniques can improve damage detection capabilities in the presence of secondary ferromagnetic sources (Azizinamini, 2017). Karthik et al. (2019) carried out MFL testing on full scale PT girder specimen with known metal defects and found that cross-sectional area greater than 5% was consistently identified. In another research correlation-based analysis was carried out to identify the position and intension of corrosion in steel (Elyasigorji et al., 2020, Elyasigorji and Ghorbanpoor, 2021). Recently, robotic rover was used by Azari et al. (2020) to carry out MFL testing on laboratory mockup girder and extended it to a field girder. The authors used experimental results and numerical models to disclose the corrosion zone. Chase and Balakumaran (2020) developed a MFL prototype unit and carried out laboratory and field study on

prestressed applications. Data processing and filtering techniques were used by Azizinamini (2017) to perturbances in MFL signal due to secondary ferromagnets.

1.3.1 MFL for External PT Systems

Due to their advantages, PT tendons are commonly used in PSC bridges for both substructure and superstructure elements. The MFL method has been widely used to detect the location and extent of corrosion of external PT tendons and stay cables. One common example of the use of MFL for external PT system is the clamped module, shown in Figure 1-3, which moves along the external PT tendons or cable stayed bridges. The advantage these modules provide is the ability to place the magnetic source and the Hall sensors as close as possible to the tendons. Based on the depth of the tendons from an accessible surface and damage sensitivity requirements, either an electromagnet or permanent magnets may be used. The choice of the magnetic source is dependent on many factors including availability of power source, safety requirements and logistical mechanism for supporting the system.



Figure 1-3: MFL of an external PT tendon (Lau and Azizinamini, 2018) and cable stays (Alpin Technik Leipzig accessed online 2020).

1.3.2 Application of MFL to Internal Tendons

The main challenge in extending the application of the method to internal tendons is the perturbation caused by reinforcement mesh. This mesh of reinforcement, common in reinforced or prestressed structures, can obscure the defect signal. Several analytical methods have been developed to characterize signal shape, amplitude, and slope of signals from the strands and reinforcement. However, the complex interaction of magnetic field between different ferrous materials inhibit meaningful result.

The application of MFL for internal tendons is dependent on many other factors including congestion of mild reinforcement and degree of defect to be detected. One of the key factors that affects the MFL signal is the presence of mild steel reinforcement which is located closer to the probing surface than strands, and therefore significantly affects the signals. Besides the challenges for practical application of MFL, the PT tendons in these structures are embedded in a mesh of mild reinforcement. Therefore, detection of defect using conventional MFL testing methodologies may not provide reliable results.

An example of tendon location in a typical box girder section is shown in Figure 1-4. The tendons are placed inside corrugated metal ducts, plastic, or high-density polyethylene

ducts. In these kind of bridge elements, the presence of blisters, diaphragms and deviators can complicate the magnetization and measurement of MFL signals. In addition, the internal tendons are typically placed in the PSC members in a straight, harped, or parabolic profile. This arrangement of these tendons increases the level of difficulty in implementing the MFL method. The complex profiles of these tendons limit the use of clamped, climbing assemblies and rotary systems.

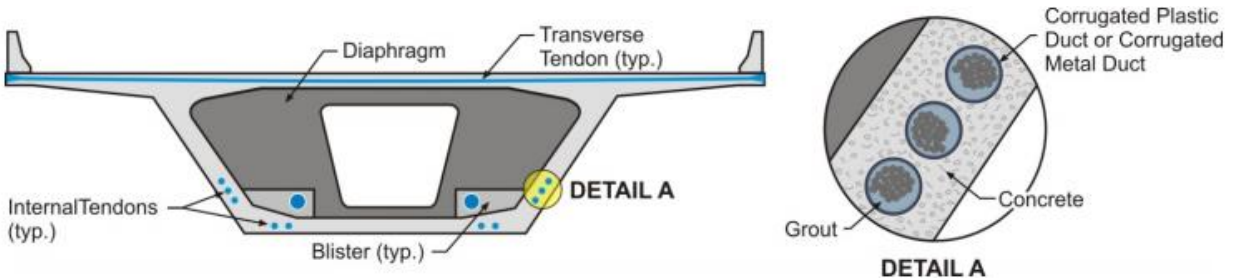


Figure 1-4: Balanced cantilever section showing location of internal tendons (Corven Engineering Inc., 2002).

1.4 PROJECT OBJECTIVES

Previous works at Florida International University (FIU) has shown that detection of wire breakages is possible for internal tendons (Sadeghnejad et al., 2017). However, the degree of damage detection was limited due to weak magnetization induced by the permanent magnet. The findings of these works emphasized the use of a more homogeneous magnetic field which can saturate internal tendons located at the depth of at least 8 inches or more. Also, the Hall sensors used in a previous hardware were primitive, demonstrated high fluctuations in measured MFL signals, and were not equipped with important features such as temperature drift corrections. Thus, the main objective of this project was to develop a modified magnetic NDT equipment which can be applied for internal tendons.

The main challenge in identifying damages in internal tendons depends on many practical constraints such as accessibility, depth of tendon, location of sensor with respect to sensor and presence of ferrous interferences such as metallic duct, mild reinforcements, etc. Besides practical constraints, the MFL method is also affected by the complex interactions of various elements of the bridge. It may be impractical to determine the effect of all individual elements; therefore, a numerical method is employed. The goal of the numerical analysis is to understand the behavior of magnetic field for different parameters. Based on outcomes of the study, a proof-of-concept testing will be conducted using the prototype unit, which will demonstrate the effectiveness of the equipment for section loss in internal tendons.

A key factor that effects the MFL signal is the degree of magnetic saturation induced by the magnetizing assembly. The magnetic saturation is mainly dependent on the strength of magnetic field and the depth of tendons. An increase in the distance can significantly reduce the magnetic saturation of the tendons which reduces the amplitude of MFL signal. Therefore, the modified MFL system should be designed to sufficiently magnetize the internal tendons. Also, the support system must be appropriately designed to reduce distance between the magnetizing assembly and depth of strands.

The objective of the project is to develop a concept that could facilitate field applications of the MFL system. Based on the testing results, modifications were made to the existing system in terms of magnetization scheme and sensing system. The support system was then developed which was intended to have the following characteristics:

- Portable unit
- Robust scanning of large areas
- Reliable data transmission to base station
- Capability to customize support system for various applications
- Pre-sessions of magnetization before measurement

1.5 RESEARCH APPROACH

The corrosion of prestressing tendons has resulted into major damages in many prestressed concrete bridges all over the world. There is a need to preemptively identify corrosion damages in the PT tendons and ensure proper mitigation measures are taken to avoid catastrophic failures. Compared to other NDT techniques, MFL method is suited for identifying section losses in steel. The principle of the MFL method is based on detecting flux leakage through discontinuity in the tendon. However, the test results are influenced by reinforcement mesh, duct type, etc.

Previous work was conducted at FIU using an earlier version of the equipment. The tasks carried out in this previous study were mainly focused on laboratory testing. The equipment developed under the previous work had limited capabilities both in terms of magnetization and measurement systems. A summary of the earlier version of the equipment is provided in Section 2. A modification of existing system was inevitable for application to internal tendons. A step-by-step modification was carried out on the existing magnet system to improve the depth of penetration of the magnetic field. Similarly, the existing Hall sensors exhibited high fluctuation which renders them impractical for scenarios where high resolution is carried. A new generation of sensors were introduced along with advanced electronics that are assembled in an experimental measurement unit. The experimental measurement and magnetization unit was further improved to develop a fully functional prototype unit, as described in section 3.

During the development of the system various laboratory experiments were conducted. The objective of the testing was to verify the capabilities of the developed system. Based on the results of these laboratory simulation, a novel testing protocol was developed which was able to identify the location of defect in steel strands. Additional laboratory testing was carried out on specimens which replicated conditions of an in-service bridge and segments of a decommissioned bridge located at FIU, as described in section 4.

An in-service bridge, located in Florida, was used as a test case. This bridge, consisting of prestressed hollow box sections with transverse PT rods, had been in service for more than 50 years. The field testing was carried out in multiple phases using developed measurement units. The developed testing protocol was implemented during the field tests and the results are provided in Section 5.

The conclusions made during development, laboratory and field testing are provided in Section 6. In addition, appendices are provided for miscellaneous detail related to the

project. An operation manual for measurement units and field inspection is also summarized in the appendices.

2 SYSTEM DEVELOPMENT AND TESTING

2.1 INTRODUCTION

A common MFL equipment for NDT is composed of two main systems: the magnetic excitation system and the magnetic measuring system (GangaRao, 1995). The magnetic excitation is the most important part of any magnetic NDT method, including MFL (Forster, 1986). The excitation can be accomplished using permanent magnets or electromagnets. The permanent magnet system does not require any external power source; therefore, the strength of its magnetic field is highly constant with time and temperature, together with a reduced size-to-maximum-strength ratio (Bozorth, 1993). However, it may not be possible to achieve strength values higher than 0.8 T (8,000 G) with permanent magnets. Conversely, electromagnets need an external power source, and in most cases, it should be coupled with a cooling system. However, this makes the system complex.

A magnetic measuring system can be made up of one or more sensors based on the following electromagnetic effects: inductive (coils), magnetoresistive (anisotropic magnetoresistance or giant magnetoresistance), or Hall (Hall sensors). While the inductive magnetic sensors are less affected by temperature, they are more suitable for sensing alternating magnetic fields rather than static magnetic fields. On the other hand, anisotropic magnetoresistance (AMR) and giant magnetoresistance (GMR) provide higher sensitivity, but lower magnetic range and larger variation with temperature (Lenz and Edelstein, 2006). Magnetic sensors based on the Hall effect can be used to measure magnetic fields from $\pm 1 \mu\text{T}$ (10 mG) up to $\pm 10 \text{T}$ (0.1 mG) for a wide temperature range (Popovic, 2003). Additionally, nanotechnology advancements have made it possible to manufacture Hall sensors with an embedded temperature sensor, amplifier, analog-to-digital converters, physical memory, and other features. These sensors are optimized for precision and accuracy of the sensors, as well as eliminating the use of external conditioning circuits.

In this report, an overview of the main parts of the previous MFL system at FIU, the capabilities of this system, and the required improvements to adapt the system to the field conditions are presented. Although the excitation and the measuring systems are discussed in this report, special considerations are given to the magnetic measuring system.

2.2 EARLIER MFL SYSTEM

The MFL method was first developed in late 1970s and has been subject to ongoing evaluation as sophistication of electronic instrumentation and data analysis techniques have improved. The principal investigator (PI) of the project developed several magnetic field sources and a best sensor arrangement, which were used for testing on tendons and PT rods (DaSilva et al., 2009). In 2016, an initial assessment of MFL for internal tendons was carried out by the PI under FDOT project BDV29-977-05 (Azizinamini, 2017). Preliminary testing was carried out on laboratory specimens, which was later extended to decommissioned bridge segments located at FIU. The components of the system are shown in Figure 2-1.

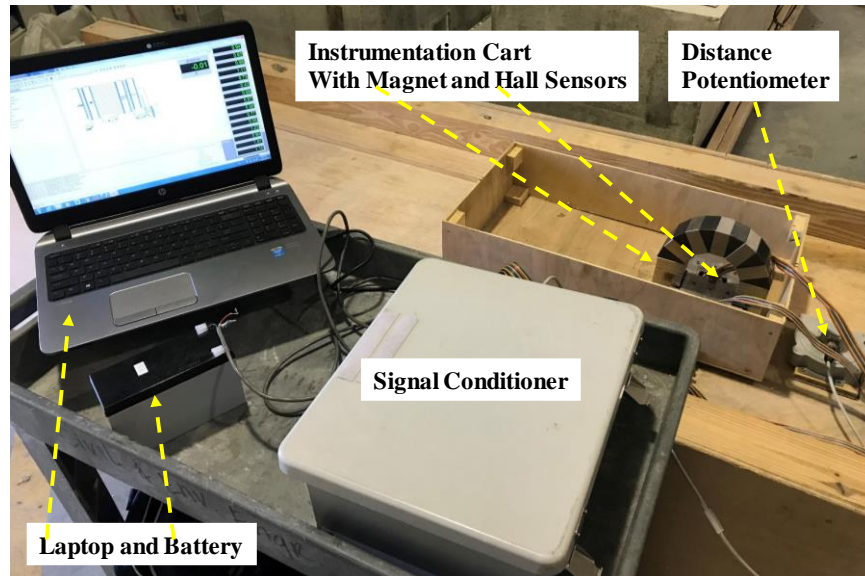


Figure 2-1: Components of the earlier MFL system.

These details of these individual components, shown in Figure 2-2, are tabulated as follows:

1. An array of HE sensors positioned between the magnet poles detected the flux leakage in the regions of steel section loss. Fifteen HE sensors were placed on a printed circuit board (PCB) in a 3 x 5 grid. The positions of these HE sensors were optimized for better detection of flux signals.
2. A U-shaped permanent magnet consisting of seven Grade 45 neodymium magnet blocks with alternating iron wedge yokes.
3. An aluminum cart for mounting the sensor array and permanent magnet. The carriage was made from aluminum due to its low magnetic permeability relative to steel. The wheeled carriage smoothly traversed the test specimen along a longitudinal path while maintaining a constant distance between the sensors and the test strands.
4. A strain potentiometer was used to measure the distance as the aluminum cart traversed along the strand.

The system was operated by magnetizing a group of tendons or PT rod in both an active and passive measurement setup. The system was powered externally either through a direct current (DC) or an alternating current (AC) power supply. Due to low resolution of the electronics, a signal conditioner was used for filtering of test results and a laptop was used for archiving and post-processing the data. The instrumentation of this system was designed to operate on a smaller scale for horizontal and vertical probing surfaces.

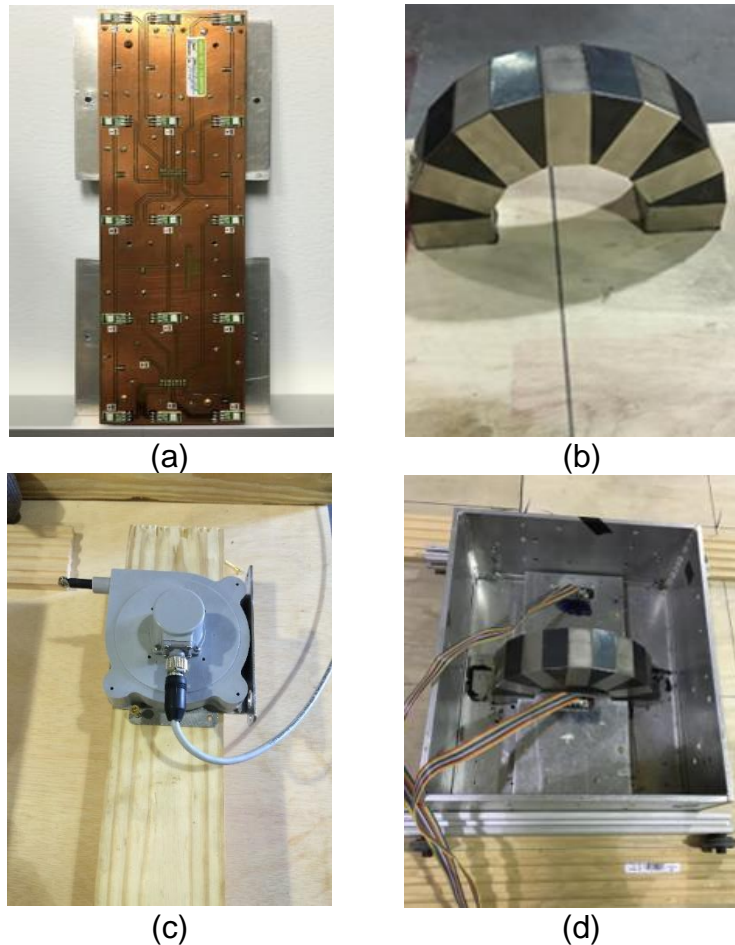


Figure 2-2: Instrumentation: (a) sensors, (b) magnet, (c) potentiometer and, (d) cart.

Before proceeding with the development of the new MFL system, a study was carried out to ascertain the deficiencies of the current MFL system.

2.2.1 The Permanent Magnet on the Earlier MFL System

The “U” shaped magnet of the earlier MFL equipment consists of seven 2 in. x 2 in. x 1 in. NdFeB magnet blocks of grade N45, and six wedges of low carbon steel AISI 1010, as shown in Figure 2-3(a). The strength of the magnetic field at the center of the face on a single block of permanent magnet was 0.43 T (4,348.2 G). The strength on similar face of end blocks in “U” shaped configuration was 0.6 T (6,062.8 G), as can be observed in Figure 2-3(b) and (c). It should be noted that the readings of the Gaussmeter are in Gauss.

The distance between the poles of permanent magnet was about 4 in. The magnetic field penetrates deeper as the separation of the poles gets smaller; however, smaller distance compromises the homogeneity of the magnetic field.

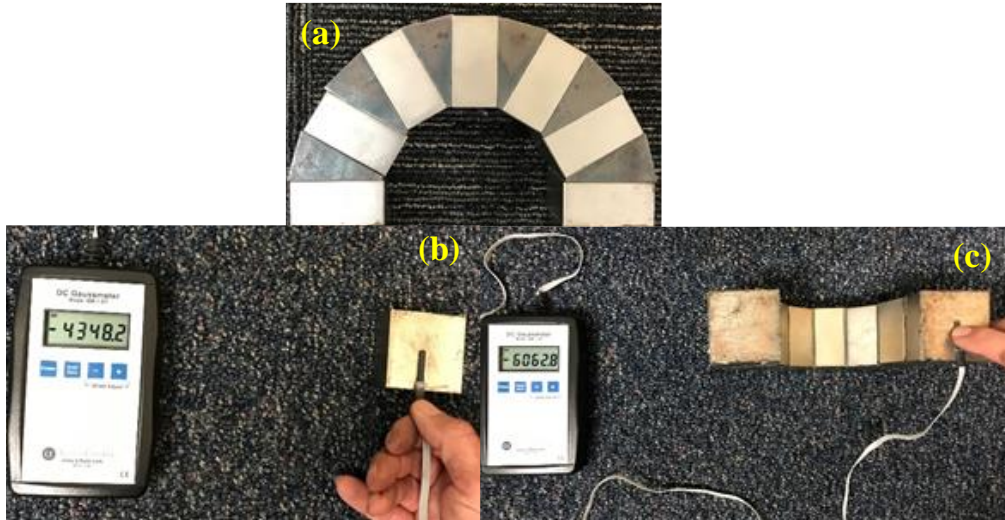


Figure 2-3: (a) Earlier magnet version, (b) magnetic strength on the south pole and, (c) magnetic strength of the south pole of the same block in the permanent magnet configuration.

The change in magnetic field strength of the permanent magnet at various distances, up to 10 in. away from the face of the magnet, were measured. As can be seen in Figure 2-4, the strength of the magnetic field drops roughly ten times when the gaussmeter probe is just taken 2 in. away from the north pole surface. The dashed line represents the strength at 2 in. It is worth to point out that the purpose of these measurements was to characterize the permanent magnet, avoiding the complexities of making the measurements with a ferromagnetic material.

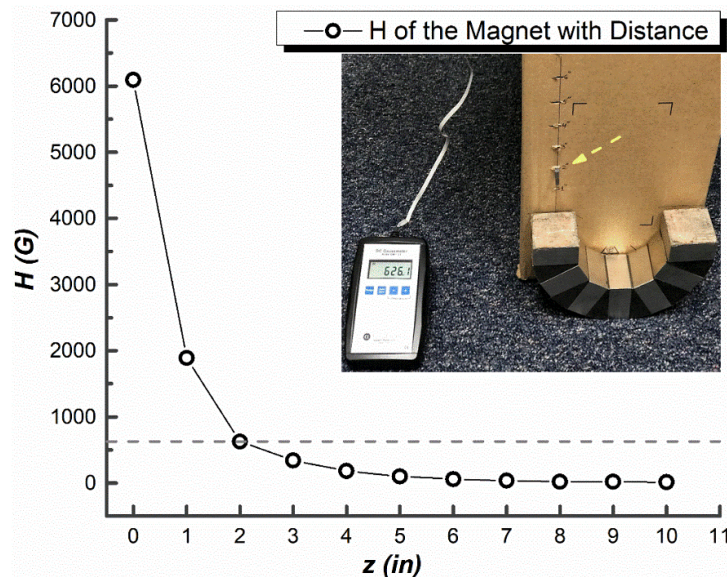


Figure 2-4: Variation of the strength of the magnetic field (G) with the height (in.).

2.2.2 The Magnetic Sensors of the Earlier MFL Equipment

The magnetic measuring system of the earlier MFL equipment consisted of a 3 x 5 matrix of SS94A2 Series, Noise Shielded-Ratiometric-Linear Hall sensors from Honeywell as

shown in Figure 2-5. These sensors only measure the magnetic field perpendicular to the plane of its surface, which is identified as B_z in this report.

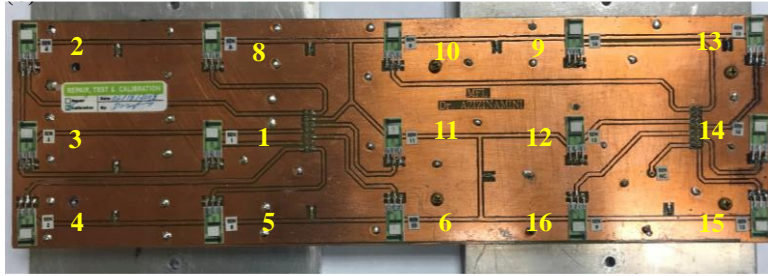


Figure 2-5: Circuit with the matrix of Hall sensors.

In the sensor layout, the distance between sensors in each row is about 3 in. and 1.5 in. in each column. For a typical case, if the center of this sensor layout is placed over a duct located at a distance of 4 in., the effective area for receiving the MFL signal will be limited. Considering its dipolar nature, the magnetic strength of a defect decay in space relative to the inverse cube of the distance. The larger the dispersion of the sensors in space, the higher the influence of the signals from the surroundings. Therefore, it was concluded that this sensor arrangement can complicate the comparison and interpretation of the MFL signal from sensors widely separated.

The scanning of a large area is one of the features expected from NDT equipment intended for bridge inspection. For this, the measuring system needs to have a stable behavior during relatively long periods of time. In the case of a multi-sensor system, all sensors should have almost similar response to the same stimulus.

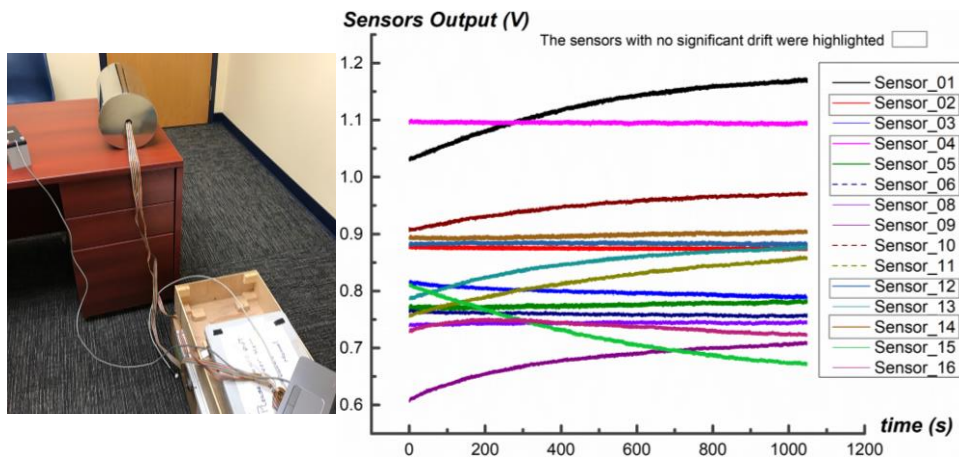


Figure 2-6: Drift with time of the matrix of sensors inside a zero-Gauss chamber.

To investigate how the response of each sensor, when exposed to the same stimulus scenario, the whole matrix of Hall sensors were placed in a zero-Gauss chamber as, shown in Figure 2-6. The sensors with no significant drift were highlighted with a dashed-line rectangle. At first glance, a big disparity in the output values can be seen. A major concern is that only 5 out of 15 sensors exhibit a constant behavior with time. These discrepancies were likely related to the age of the sensors.

2.2.3 Linear Encoder and DAQ of the Earlier MFL Equipment

The distance measurement in the earlier MFL system consisted of a string potentiometer. This mechanism requires attaching the string to a stationary reference point at the start of the test. Although the mechanism provided a fairly accurate results, but it was impractical for measurements on actual bridges. A military grade portable data acquisition (DAQ) system was used in the earlier MFL equipment; however, the system was outdated and heavy, which made it impractical.

2.3 DEVELOPMENT OF NEW MFL SYSTEM

The primary objective of this project was devoted to identifying deficiencies of this early version of the MFL system. With the advancements of new sensors, microelectronics and digital devices, the capabilities of the earlier MFL system can be improved and extended to a wide range of applications. These sensors are shown in Figure 2-7. A systematic study was carried out to improve the components and the details are provided in this section.

2.3.1 Modification to Measurement System

Modern Hall sensors bring important features such as temperature sensor for temperature drift corrections. Amplifiers and analog-to-digital converters eliminate the errors and the complexity of external circuit for signal conditioning, and physical memory to program the suitable magnetic range of the sensors. Regarding the complexity of measuring the MFL on bridge structures, the following Hall sensors were selected to be implemented as improvements to the current MFL system.

- MagVector MV2 Sensors
- Micronas HAL2425 Sensors



Figure 2-7: MetroLab MagVector™ MV2 (left) and Micronas HAL2425.

2.3.1.1 MV2 Hall Sensor

Magvector™ MV2 developed by MetroLab consists of a magnetometer on a chip which measures the field in three orthogonal directions. The principal characteristics of these sensors are summarized in Table 2-1.

A series of test were performed in the laboratory conditions on a single cut strand. The B_x and B_z component of the MV2 and B_z of the current sensor #11 (as shown in Figure 2-5) for active and residual were measured. It was observed that for the active mode that the peak-to-peak variation of the sensor #11 is 55 times the variation of MV2 sensor for B_z component. For the residual mode, the peak-to-peak variation of sensor #11 was only 6.45 times the variation of MV2 sensor for B_z component.

Table 2-1. Principal characteristics of the MV2 Hall sensors

Magnetic Actuation Type	Ratiometric
Sensitivity @ 25 °C and 100 mT	0.27 mV/mT
Operating Temperature Range	-40 °C to 125 °C [-40 °F to 257 °F]
Programmable magnetic detection range	±30000 G (±3 T) Programmable down to ±1000 G (±100 mT)

2.3.1.2 HAL2425 Sensor

HAL2425 sensors is part of the HAL 24xy series by Micronas. This series has a monolithic integrated circuit which provides an output voltage proportional to the magnetic flux through the Hall plate and proportional to the supply voltage (ratiometric behavior). The main feature of this sensor is the possibility of setting the magnetic range in eight (8) values, from ±4000 G (400 mT) to ±30 G (3 mT) using software. The principal characteristics of these sensors are summarized in Table 2-2. Testing was carried out on strands with a complete defect and results showed that in residual condition, the B_z component was most sensitive.

Table 2-2. Principal characteristics of the HAL2425 Hall sensors

Magnetic Actuation Type	Ratiometric
Sensitivity	±1% to ±0.8 % depending on the Magnetic range, the Voltage and Temperature
Operating Temperature Range	-40 °C to 150 °C [-40 °F to 302 °F]
Eight Programmable magnetic detection ranges	(1) ±4000 G (±400 mT) (2) ±2000 G (±200 mT) (3) ±1000 G (±100 mT) (4) ±500 G (±50 mT) (5) ±250 G (±25 mT) (6) ±120 G (±12 mT) (7) ±60 G (±6 mT) (8) ±30 G (±3 mT)

2.3.1.3 Flux Concentrators

Flux concentrators are devices that are added to intensify the magnetic flux in a specific direction. The flux concentrators were made with smooth iron shaft with a diameter of 1/16 in. and a length of 1 inch. These flux concentrators were affixed in a vertical direction on the top of the Hall sensors.

2.3.2 Modification to Magnetizing System

Previous studies using the earlier MFL system have shown capabilities to detect defects in active and residual modes in the presence of transverse reinforcement (Azizinamini, 2017). However, the earlier version of the permanent magnet was unable to magnetize tendons located far from the poles which severely limited the measurement system’s capabilities to identify damages. Therefore, modifications to the permanent magnets were required to allow uniform magnetization of tendons embedded at deeper locations.

As shown in Figure 2-8, different modifications were made to the earlier version of the permanent magnet. Initial modifications consisted of an addition of Neodymium Iron

Boron (NdFeB) Grade 52 blocks. The strength of the magnetic field increased by almost 600 G (60 mT) However, these modifications did not significantly improve the magnetizing capability of the earlier version of the magnet. This was mainly due to the proximity of the poles and the addition of more magnets caused non-uniformity in the field.

Additional modifications were made by inserting carbon steel bar on the top of the magnet (Figure 2-8c). The third change to improve the magnetic strength of the magnet was the addition of two magnet pieces with reduced geometry to concentrate the magnetic flux lines (Figure 2-8d). Note that the strength of the magnetic field at the surface of the poles increased by more than 1400 G (0.14 T) from the original magnet (i.e. from 6,062 G (0.6 T) to 7,486 G (0.74 T)).

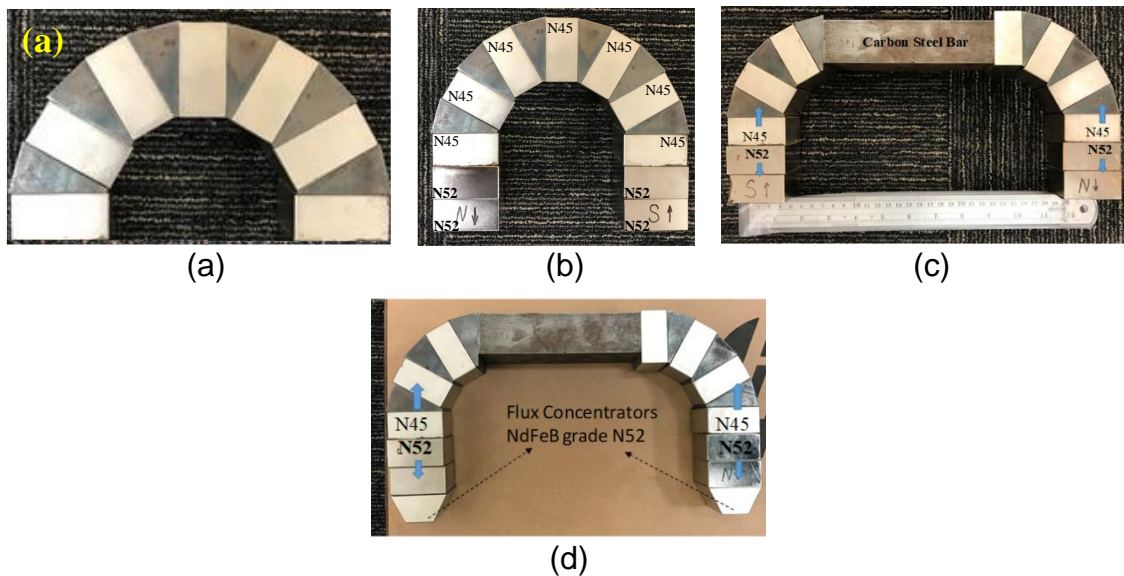


Figure 2-8: Modifications to an earlier version of the magnet.

A simple laboratory test was carried out to determine the effectiveness of the modified magnet in magnetizing the strands. The strands were magnetized by moving them at various distances from the modified magnet. The magnet was laid down and fixed on a table and a new strand measuring 8-ft long was displaced six times along the center line of its poles for four distances. A plastic board of ¼ in. thickness was used to keep the strand at an equal distance from magnet's poles. The details of the test are depicted in Figure 2-9.

It is important to highlight that all the strands (as received) had some level of residual magnetization. As can be observed in Figure 2-10, the residual magnetic field strength for the received strands was not insignificant when compared to the strength of magnetic field for the original magnet at 3 in. (341.3 G) and 4 in. (181.4 G) given in Figure 2-4.

The results are summarized in Table 2-3. As can be seen, there was a change in the polarity and the relative saturation of the strand. However, special attention was given to the result when the strand was slid on the table at a distance of 4 in. from the magnet's poles. Magnetizing the strand at 4 in. resulted in a bigger difference between the pole strength than the difference measured with 6 in. condition. This can be due to the non-homogeneous distribution of the magnetic field at these distances. On the other hand, at

the 2 in. and $\frac{1}{4}$ in. there was no change in the polarity and the residual magnetic field reached the maximum value of 270 G. It was clear that for these two distances, the magnetization conditions were optimum. A huge strength of the residual magnetic field (1047.7 G) of a $\frac{1}{8}$ in. defect on four strands which were magnetized at 2 in. from the magnet was observed.

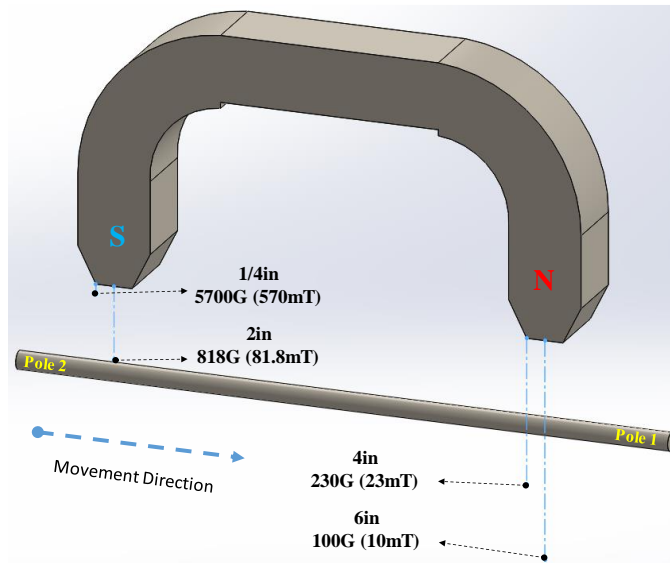


Figure 2-9: Magnetization configuration with modified magnet.

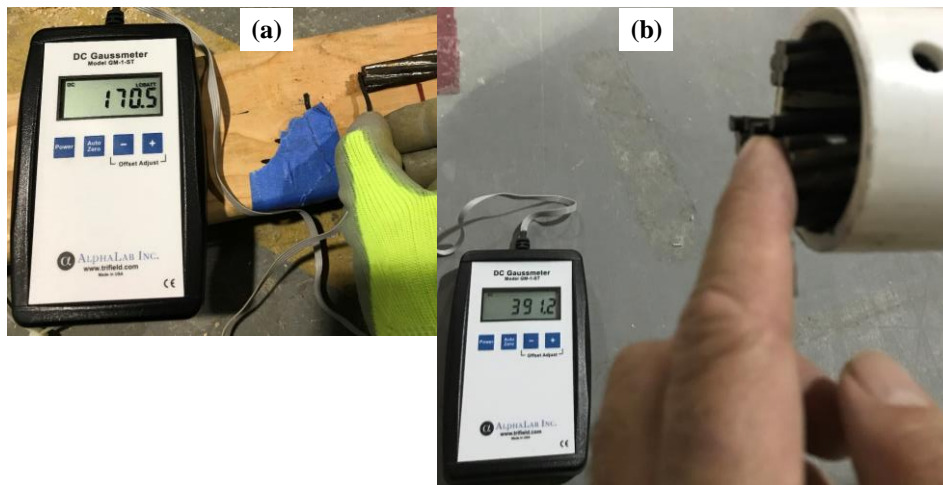


Figure 2-10: Strength of the residual magnetic field measured in (a) the central wire of one strand, (b) and in a group of ten strands measured in the central wire of the central strand.

Table 2-3. Polarity and strength of magnetic field at the central wire of one strand

Strand Condition	Magnetic Field Strength	Pole 1 Polarity	Pole 1 Strength	Pole 2 Polarity	Pole 2 Strength
As received	-	S	17 G	N	27 G
First run at 6 in.	100 G	N	50 G	S	118 G
Sixth run at 6 in.	100 G	N	47 G	S	112 G
First run at 4 in.	230 G	S	189 G	N	27 G
Sixth run at 4 in.	230 G	S	191 G	N	25 G
First run at 2 in.	812 G	N	270 G	S	270 G
Sixth run at 2 in.	812 G	N	270 G	S	270 G
First run at 1/4 in.	5700 G	N	270 G	S	270 G
Sixth run at 1/4 in.	5700 G	N	270 G	S	270 G

In this section, different modifications to the earlier version of the magnetizing system were studied. Although the changes to the earlier version of magnet improved the magnetizing capability, but due to proximity of the poles, the strength was not sufficient for applications where internal tendons are located at a larger depth. All magnets version presented here weigh less than 40 lbs. and can be operated with or without a mounting cart. Therefore, these magnets were primarily used for probing horizontal and vertical surfaces with near surface steel tendons.

From the systematic work that was carried out in this section, it was found that an increase in the magnetic strength cannot be achieved by addition of magnets only. For applications where internal tendons are embedded at a larger depth, further modifications were made to the system which are presented in Section 3. The aim of these changes was to develop a magnet which can magnetize steel strands at a larger depth.

3 FINAL MFL SYSTEM

3.1 MAGNETIZATION UNITS

This section presents the final set of magnets which were assembled for a range of applications. Three different magnet configurations are presented in this section, which can be used for internal tendons located up to a depth of 8 inches. The modifications to an earlier version of the magnet (referred to as magnet 1) which were developed in a previous section were designed for magnetizing specimens on a smaller scale. Considering the complexities of real structures where internal tendons are located deeper in a mesh of mild reinforcement, two new permanent magnets were assembled. These magnets, referred to as magnet 2 and magnet 3, consisted of a U-shaped yoke where the poles were spread out. These magnet systems with an improved geometrical configuration allowed the magnetic field to flow more uniformly between the poles. The following sections presents the characteristics of these magnets.

3.1.1 Magnet 1

As previously mentioned, magnet 1 was modified version of the earlier magnet. Two new blocks of NdFeB of Grade 52 were placed on each pole as shown in Figure 3-1. As a result of these modifications, the strength of the magnetic field increased by almost 600 G (60 mT). Since the penetration depth of the magnet is highly dependent of the distance of the two poles, this magnet was mainly suitable for shallow tendons and areas with limited access.

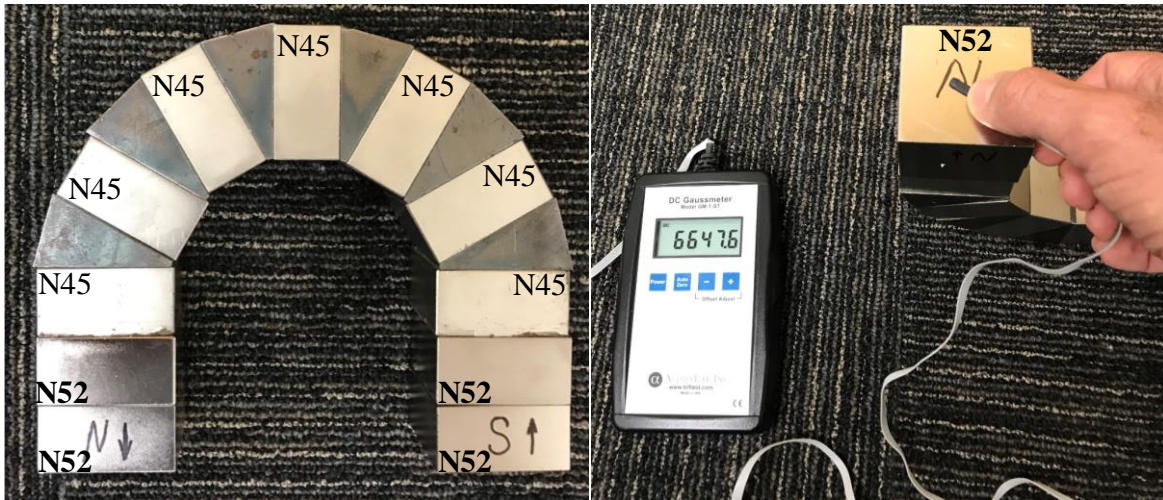


Figure 3-1: Configuration of magnet 1.

3.1.2 Magnet 2

A new magnet system was fabricated with an improved geometrical configuration that allows the magnetic field to flow more uniformly between the poles. For magnet 2, the “U” geometry was used with magnet poles spread out. The assembly consisted of a total of three permanent magnets on each side joined by a steel yoke. The six magnet blocks were made of grade 52 NdFeB material. The size of each block was 6 in. x 4 in. x 2 in. Note that the strength of the magnetic field at the surface of the poles increased to about 6000 G (0.6 T). This magnet was used for most of the laboratory and field testing. The weight of magnet 2 was about 140 lb. Although the complete magnet unit is compact, but

due to weight, this magnet configuration requires a mounting cart for operation. The magnet configuration is shown in Figure 3-2.

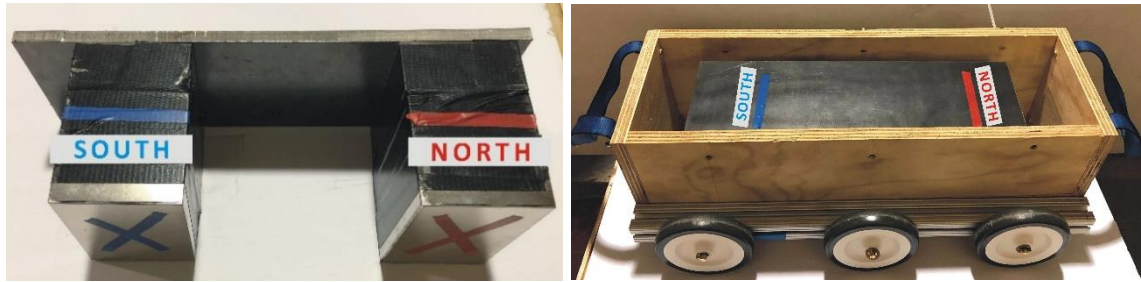


Figure 3-2: Configuration of magnet 2.

3.1.3 Magnet 3

The third magnet was configured to have lower weight and larger pole distance compared to magnet 2. This magnet is made from grade 52 NdFeB material. Magnet 2 is consisted of 13 permanent magnets of 2 in. x 3 in. x 4 in. and 4 magnetic wedges. The capability of this magnet was tested in the laboratory and was compared with magnet 2 through a series of experiment on steel strands at 10 in. from the magnet. The results of this study are presented in Appendix E. The weight of magnet 3 was 120 lb. Similar to magnet 2, the handling and operation of this magnet configuration requires a mounting device. The magnet configuration is shown in Figure 3-3



Figure 3-3: Configuration of magnet 3.

The separating distance between the tendon (or PT rod) and magnet is one of the most important parameters which affects the MFL signal. This is particularly important in case of internal tendons where it may be necessary to move the magnet assembly as close to the concrete surface as possible. For magnet 2 and 3, a cart assembly was fabricated with low clearance wheels. In both cases, the offset of the permanent magnet from a scanning surface was about 1-inch. The carts were made of non-ferromagnetic material to minimize disturbances in the magnetic field. The permanent magnets were not affixed to the cart and, if required, can be mounted on a different support system.

3.2 MEASUREMENT UNITS

The goal of modifications to the existing MFL system was to develop a prototype unit which can be used for internal tendons. Different prototype units were assembled which housed all main components of the measurement system. The following design considerations were taken into account to assemble the measurements units:

- To ensure portability, all units were wheel mounted. The size of the units was designed to allow operation in areas with limited access.

- The distance between sensors and probing surface was kept minimum. The sensors were arranged in a linear arrangement to allow area scan.
- Military-grade laptops were used with measurement units. The rugged laptops provide longer battery hours and a sturdy protective chassis that allows operation in extreme conditions.
- An external AC power source was used for powering the measurement units. Alternatively, DC power source can also be used.
- An incremental linear encoder was used with all units. Incremental encoders provide position information for a rotating shaft by producing a continuous series of pulses.
- Different compact DAQ were selected for collection and processing of the data from sensors and linear encoder.
- A sub-routine code was developed to plot the data in real-time. Also, the code was able to develop area plots for surface scans.

A set of prototype measurement units was developed at FIU. These units are capable of scanning internal tendons located on horizontal surfaces. However, these units can also be modified for other applications if railing and additional support mechanisms are provided. Few examples where these units can be used are the tendons in deck slabs, cantilever and continuity tendons of box girders, transverse PT rods in bridges, etc. The detail of different measurement units is presented below:

3.2.1 Experimental Measurement Units

Various prototype units were assembled for testing, validation, and demonstration of MFL for laboratory and field conditions. These units consisted different numbers of sensors ranging from 1 to 48. In all the units, the sensors were mounted on low clearance wheels to allow scanning to be carried out as close to the surface as possible. Figure 3-4 shows measurement unit 1 used for field measurement.

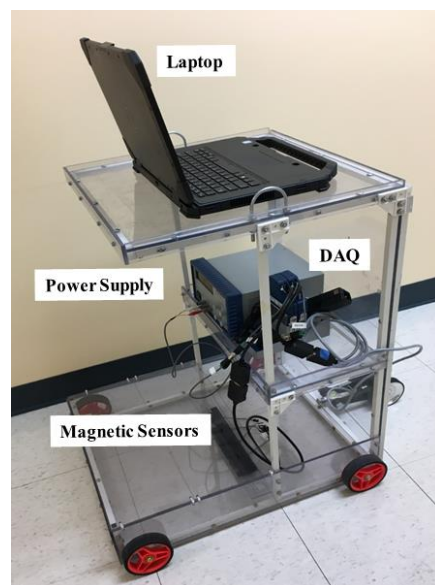


Figure 3-4: Measurement unit 1 with 4 sensors.

The components of sensing system were constructed using a lightweight Plexiglas ® mounted on an aluminum frame. This unit is lightweight and robust for probing horizontal surfaces. One of the drawbacks of this unit was its width which cannot scan more than 1.5 ft. width of the bridge component.

An improvement was made in the measurement unit 2 by increasing the width and using a compact housing to accommodate all DAQ and sensors. The measurement unit shown in Figure 3-5 was made with wood and contained two rows of sensor over a width of 36 inches. First array contained 32 HE sensors each at a spacing of 1-inch. The second array consisted of another 16 sensors with flux concentrators spaced at 2 inches. The portability of the unit was ensured by using lightweight wood. This unit can scan a surface area 31 inches wide. An incremental linear encoder was attached at the rear end to allow distance measurements.



Figure 3-5: Measurement unit 2 with 48 sensors.

3.2.2 Final Measurement Units

For the final measurement unit, two prototype units were developed. The primary difference in both the units is the width and number of sensors. These units are referred to as measurement unit 3a and 3b and are shown in Figure 3-6. These assemblies contain 16 and 48 sensors for unit 3a and 3b, respectively. The sensor lay out for the bigger unit is shown in Figure 3-7. The sensors were attached to a printed circuit board. Both units have shaft type linear encoders attached to the main. The DAQ is affixed in the housing and a more robust USB cable connection is use for the laptop. Due to large demand from a series of sensors, an external power is required for operation. The smaller unit can operate on the USB connection alone but using external power supply would provide a more reliable measurement. These units were fabricated using acetal polymer plastic. The advantages of this material are its superior mechanical strength, fatigue endurance, resistance to moisture and wide end-use temperature range. The other components of these units were mainly comprised of aluminum parts. These units were designed to accommodate the laptop for single user operation.



Figure 3-6: Final measurement units (a) 16 in. and, (b) 32 in. wide unit.

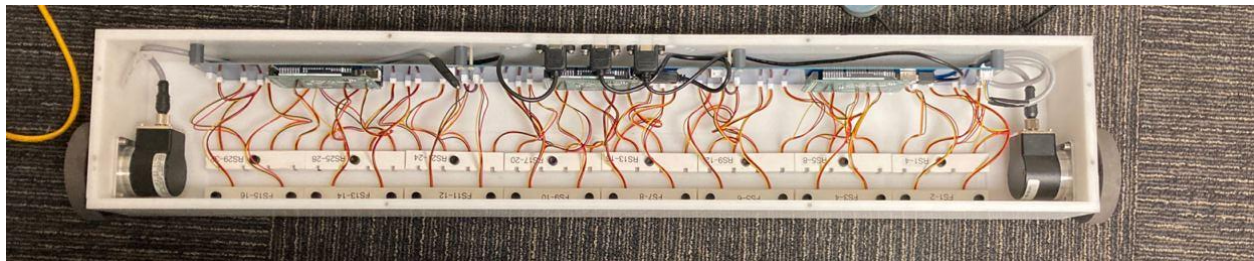


Figure 3-7: Sensor layout and DAQ for prototype unit 3b.

3.3 CAPABILITIES OF DEVELOPED SYSTEM

A series of modifications was made to the previous version of MFL for improvements in the magnetic and sensing system. The system has demonstrated improved capabilities which are summarized below.

3.3.1 Maximum Depth of Tendons

The efficiency of an MFL device for detection of defects in internal tendons is dependent on many factors including the density of reinforcement mesh, depth of tendons, and material of tendon ducts. In the prototypes developed under this task, the magnetic flux generated by the permanent magnet version 2 and 3 can be used for internal tendons which are embedded 8 inches inside the concrete. For magnet 1, the maximum penetration of flux signals is less than 4 inches.

3.3.2 Mild Reinforcement Density

The prototype measurement and magnetization units are capable of testing internal tendons in an environment with low to medium reinforcement ratios.

3.3.3 Access – Lane Closure Requirement

The lane closure requirements for MFL testing of bridges depends on the type of structure and location of the tendons. The operation of the MFL system is robust and does not require lane closure for extended periods of time.

3.3.4 Coverage Area

The final prototype units were used for testing of bridges. Based on these experiences it was found that an area of 1000 sq. ft., using measurement unit 2 and 3b, can be performed in a 15-minute time frame. However, this number can vary from bridge component being tested and the level of end user expertise. For magnetization using magnet 2 and 3, a cart or sliding assembly is required for field operation. The scanning time for along tendon measurement is about 1 hour per 1000 linear foot.

3.3.5 Weather Conditions

The MFL system consists of microelectronics such as sensors and laptop which can be affected by weather conditions. The design and material durability of acetal allows measurement unit 3a and 3b to be used in tough weather conditions.

3.3.6 End User Expertise

For a typical horizontal surface, the operation of the prototype unit requires minimal manpower, but end-user expertise is required to interpret and analyze the data. The manual for operation and setting up the software are provided in Appendix D.

4 LABORATORY AND SEGMENT TESTING

The objective of this research was to conceptualize a modified MFL system that is effective for internal tendons. Therefore, the effectiveness of the modifications to measurement and magnetizing systems needs to be demonstrated for field conditions. Based on consultation with the FDOT, a bridge with known defects was selected. Using the schematic drawings of the actual bridge, laboratory mock-up specimens were constructed. The details of the bridge are provided in Appendix A.1. The same bridge was investigated numerically in Appendix C.

The subject bridge (also referred to as Bridge A) presented a case where PT rods were used. Preliminary tests were carried out on laboratory mock-up specimens to better understand the effect of various testing parameters on defect signals. These parameters include the effect of transverse reinforcement, magnetization schemes, and the percentage of metal loss area.

The magnetization and measurement units were constantly modified and improved throughout the progress of this research. The capabilities of the new MFL systems were examined through laboratory testing. As a proof-of-concept, similar protocols were followed for testing on the bridge segments available at FIU. The details of laboratory and segment testing are provided in the following sections.

4.1 LABORATORY TESTING

Based on Bridge A conditions, a laboratory experiment was designed to perform sample measurements. The laboratory test setup consisted of a plywood unit, each 8-ft long. The units were designed to accommodate longitudinal tendons or PT rods and transverse reinforcement at different depths and spacing. Multiple units were joined to mimic different conditions and minimize end effects. In addition, the units were designed to allow magnetization and measurements from the top and the bottom. The mock-up test setup and sensor layout are shown in Figure 4-1.

Each test run was carried out by traversing the magnetization unit on the top or bottom of the mock-up units. At this stage, magnet 2 was used for all testing. Then, the experimental measurement unit was moved along the length of the prestressing tendons or rods. The data acquired by each run for sensor 1 to sensor 4 was displayed in real-time. The testing on these specimens do not necessarily represent real conditions but rather provides the researchers with an understanding of principles in MFL testing. The outcomes of these test schemes are refined to develop a new testing protocol.



Figure 4-1: Laboratory test setup and sensor layout.

4.1.1 Testing on the Unmagnetized System

The success of the MFL method for internal tendons is dependent on many factors, but the most important parameters include the density of reinforcement, depth of tendons and the minimum damage severity to be detected. The laboratory tests were carried out on a baseline condition where the transverse reinforcement and PT rod were all in an unmagnetized state. The objective of these readings was to understand the effect of unmagnetized transverse reinforcement on unmagnetized PT rod. The test matrix is given in Table 4-1.

Table 4-1. Test configuration 1 to 4

Test No.	Magnetization State	Inspected Tendon	Transverse Reinf. Top	Transverse Reinf. Bottom
1	Unmagnetized	PT rod	-	-
2	Unmagnetized	PT rod	Strand at 7 in. c/c Depth 4.5 in.	-
3	Unmagnetized	PT rod	Strand at 7 in. c/c Depth 4.5 in.	Strand at 5 in. c/c Depth 16 in.
4	Unmagnetized	-	Strand at 7 in. c/c Depth 4.5 in.	Strand at 5 in. c/c Depth 16 in.

The configuration of Tests 1 to 3 and arrangement of strands and transverse reinforcement is schematically shown in Figure 4-2. These tests were carried out on a PT rod with a 100% defect (2-in. gap). In test 1, only the signals from PT rods were measured. For test 2 and test 3, test runs were carried out in the presence of top and top/bottom transverse reinforcement, respectively.

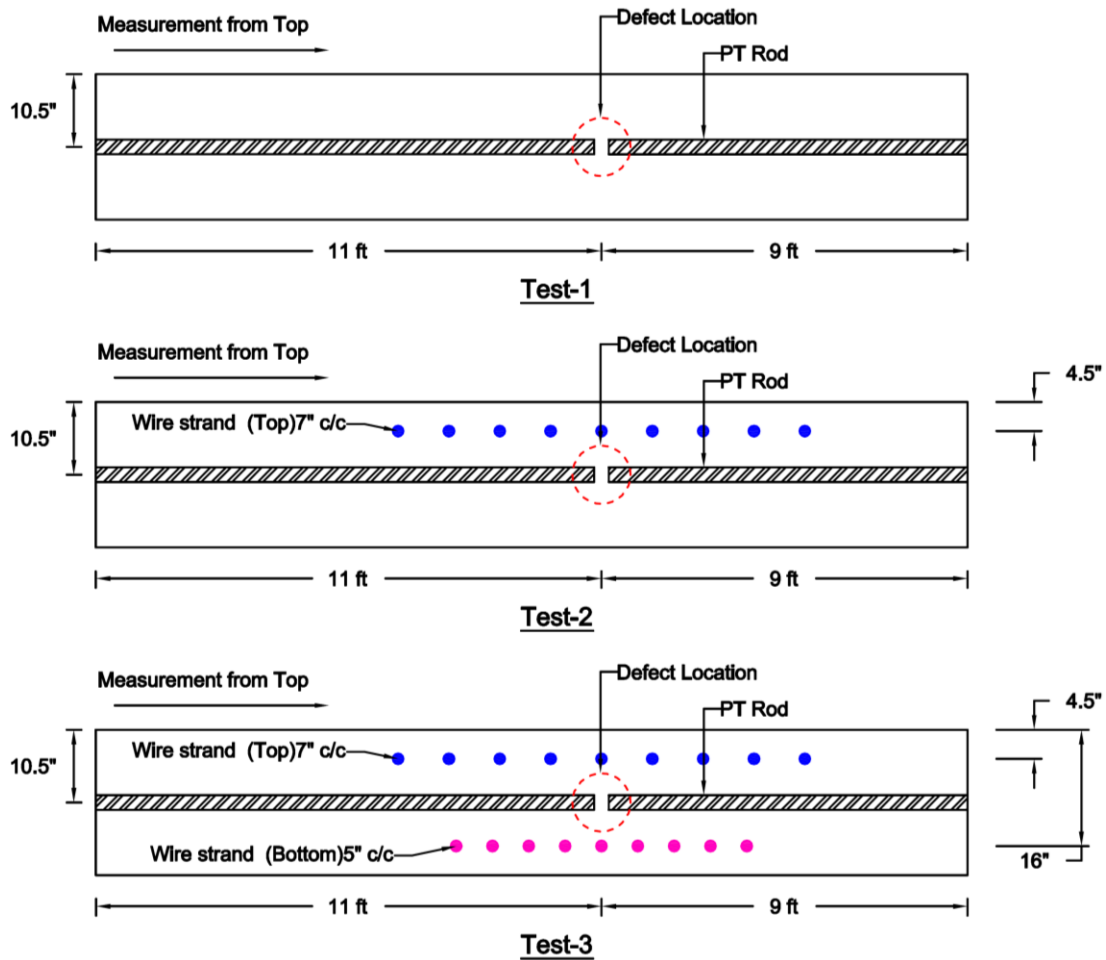


Figure 4-2: Test configuration 1 to 3.

The result in Figure 4-3 shows the measured signal for test 1 even in the presence of a complete defect. Also, the signal was unaffected by the presence of the top or bottom transverse reinforcement (test 2 and test 3). The signal measured in these tests does not follow any specific pattern. This concludes that an unmagnetized or insufficiently magnetized system cannot be used to locate a defect. Also, the signal shown in Figure 4-3 may not be considered as a baseline for all PT rods.

The signal of an unmagnetized strand shows the residual magnetization during the manufacturing process and may vary from one sample of the rod to another. Although a discontinuity in the PT rod will cause flux changes, however, these changes are not evident in the results. The quantification of residual magnetization along the length of the rod is complicated, and the test results do not capture the location of the defect. This implies that the PT rods must be saturated to some degree of magnetization before reliable signals can be observed.

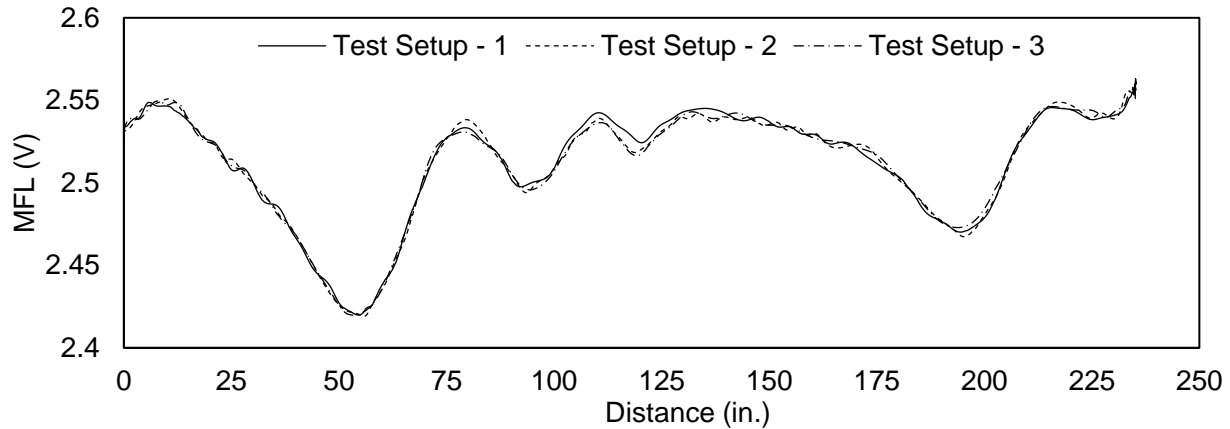


Figure 4-3: Result of test 1 to 3.

Test 1 to test 3 were performed on PT rods with and without the presence of transverse reinforcement. The effect of residual magnetization of the transverse reinforcement alone was not evident from these tests. Therefore, test 4 was carried out to understand the effect of transverse reinforcement only (Figure 4-4). No magnetization scheme was used before the measurements were taken.

Test results, shown in Figure 4-5, did not indicate any significant difference in MFL signals. The results from four different tests show that there is no residual magnetization of transverse reinforcement. Comparing these MFL signal of test 4 with the MFL signal from test 3, it is confirmed that the residual magnetization of PT rod causes more change in measured voltage (indicator of the magnetic field intensity) than the transverse reinforcement. Although the transverse reinforcement also has some degree of residual magnetic field, but it does not manifest in the measured signal.

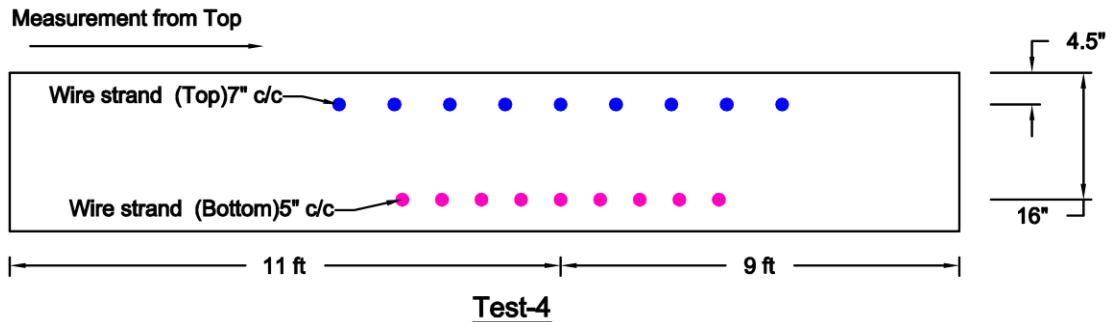


Figure 4-4: Test configuration 4.

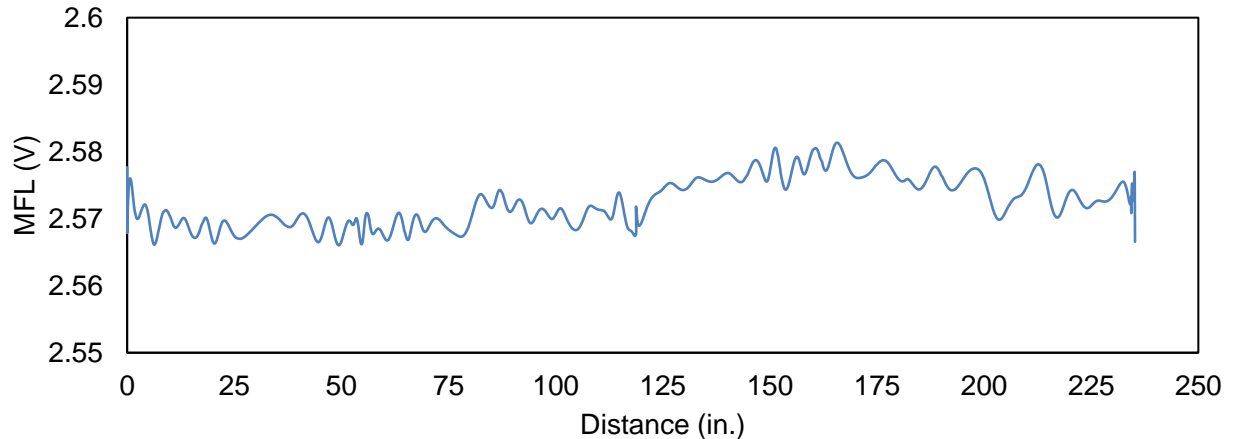


Figure 4-5: MFL signal of transverse reinforcement only (test 4).

4.1.2 Bottom Magnetization on Laboratory Mockup Specimen

Test 1 to test 4 replicated a case where both transverse reinforcement and PT rods were not magnetized during the testing. These four test cases were carried out to understand if a defect can be located using their residual magnetization of the tendons from their fabrication process. Test results indicated that magnetization is important to develop a more unified flux through the system. Therefore, the system was magnetized three times from the bottom and the sensor system was used on the top to measure the MFL signal. The magnetization from the bottom was carried out at 6 in. away from the bottom transverse reinforcement. The arrangement of the system and the magnetization scheme for test 5 is shown in Figure 4-6. The test matrix for the bottom magnetized strands is provided in Table 4-2.

Table 4-2. Test configuration 5 to 10

Test No.	Magnetization State	Inspected Tendon	Transverse Reinf. Top	Transverse Reinf. Bottom
5	Magnetized from Bottom	PT rod	Strand at 7 in. c/c Depth 4.5 in.	Strand at 5 in. c/c Depth 16 in.
6	Magnetized from Bottom	PT rod	-	Strand at 5 in. c/c Depth 16 in.
7	Magnetized from Bottom	PT rod	-	-
8	Magnetized from Bottom	-	Strand at 7 in. c/c Depth 4.5 in.	Strand at 5 in. c/c Depth 16 in.
9	Magnetized from Bottom	-	Strand at 7 in. c/c Depth 4.5 in.	-
10	Magnetized from Bottom	-	-	Strand at 5 in. c/c Depth 16 in.

The results of the MFL signal for test 5 is shown in Figure 4-6. Magnetizing from the bottom side provided a clear indication of a defect in the PT rod. The effect of transverse reinforcement is eliminated, and the peak and valley curve show the defect location. This is an important result indicating that the system behaves differently when magnetization scheme differs. The possible reason for the elimination of perturbances is that the

magnetization scheme saturates the near-surface ferromagnetic materials (i.e. the PT rod and the bottom reinforcement). However, the transverse reinforcement located on the top is not magnetized. Because the measurement was performed from the top, the unsaturated top reinforcement did not affect the MFL signal. Although the methodology adopted in this test follows magnetization from the bottom and measurement from top, the converse of this would also generate similar test results.

The near surface refers to the surface of the concrete slab closer to the magnetization source. For example, in test 5, the near surface is the bottom surface of the mockup setup. The far surface refers to the surface of the concrete slab opposite to the magnetization location. For example, in test 5, the far surface is the top surface of the mockup setup.

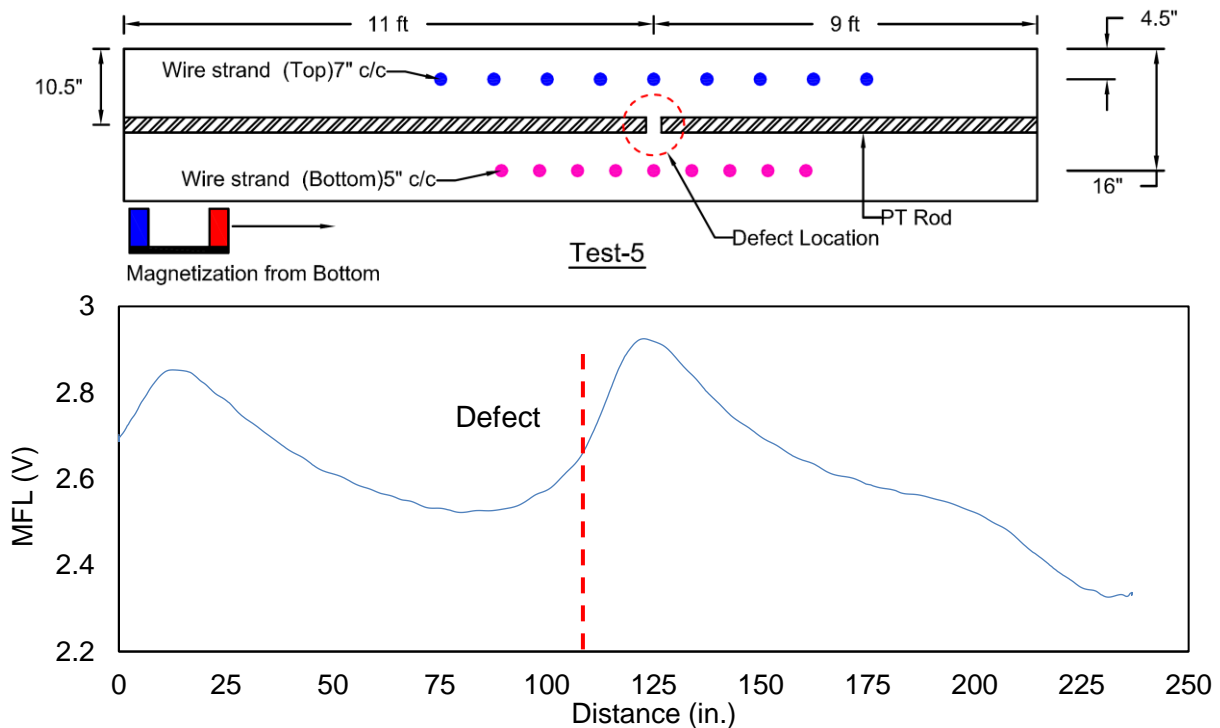


Figure 4-6: Configuration and result of test 5.

The results from test 5 show that the magnetization from the bottom and measuring MFL signal from the top side can predict the location of the defect. These signals can be affected by the arrangement of near-surface transverse reinforcement and remain essentially unaffected by the far-surface top transverse reinforcement. Test 5 was taken as a precedent and was used for the optimization of other test parameters.

To verify the effect of transverse reinforcement, two additional tests were carried out. In test 6, the top transverse reinforcement was removed while in test 7 both top and bottom transverse reinforcement was removed. Both the tests were carried out with a complete defect as shown in Figure 4-7. Like test 5, the magnetization was carried out from the bottom, and signal measurement was taken from the top. Test results were then compared to the signal obtained from test 5 shown in Figure 4-6 for sensor 1. The objective of these two tests was to isolate the parameters that potentially affect the signal.

Test results, shown in Figure 4-8, compares the MFL signal from test 5 to test 7. As expected, the MFL signal from test 6 was not affected when only the bottom reinforcement was present. However, for test 7 when no transverse reinforcement (top and bottom) was present, the MFL signal decreased. This suggested that the bottom transverse reinforcement was enhancing the signal reading making it easier to locate the defect. From the start point, all test cases from test 5 to test 7 plots were almost coincident. When the measurement system approaches the defect location, the signal for test 7 shifts downwards accompanied by softening of peaks. This implies that there was more dispersion of remanent magnetization when no transverse reinforcement was present.

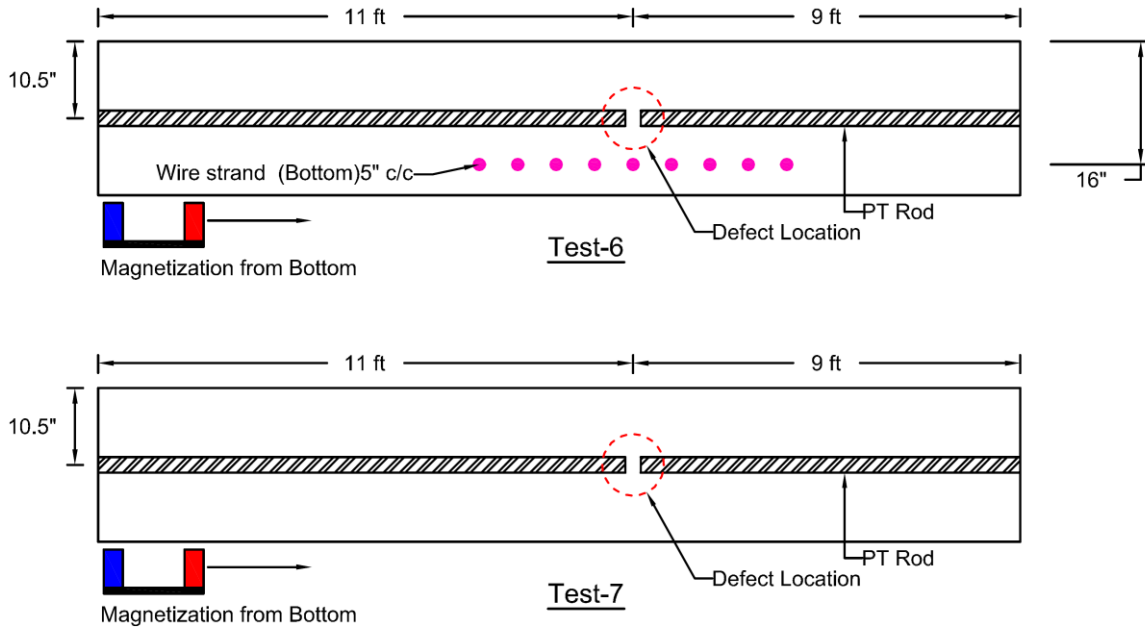


Figure 4-7: Test configuration 6 and 7.

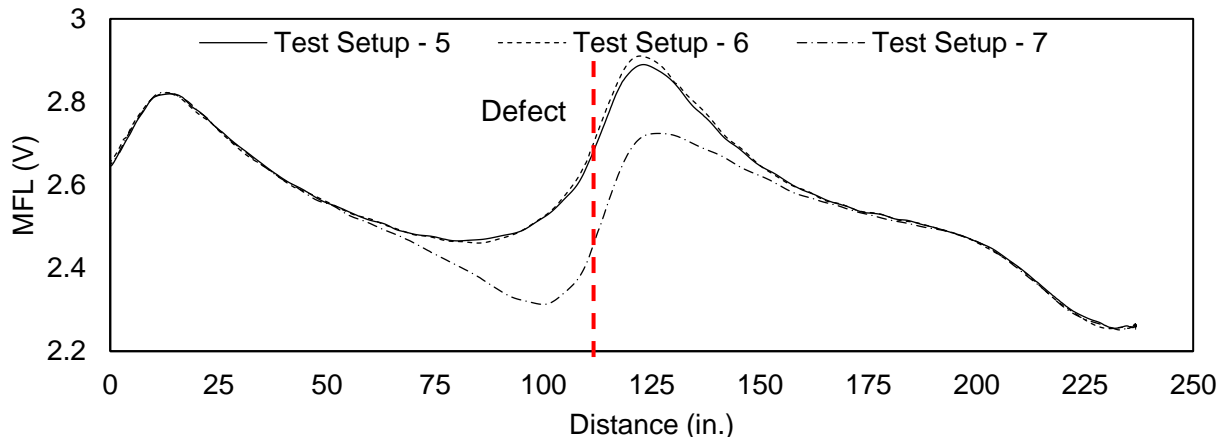


Figure 4-8: MFL signal of PT rod with and without transverse reinforcement (test 5 to test 7).

Previous tests 5 to 7 were carried out using the PT rod with and without the presence of transverse reinforcement. One additional test (test 8) was performed to check the effect of transverse reinforcement only when no PT rod was present (Figure 4-9). This

configuration was similar to test 4 but the system was in a magnetized state. The objective of the test was to evaluate the magnetized system with the similar unmagnetized system in test 4. The results from the MFL signal are shown in Figure 4-9 for four sensors. The top transverse reinforcement was located far from the magnet and was not saturated. Therefore, the plot shows a single peak from the bottom transverse reinforcement only. If the top transverse reinforcement was magnetized, the graph would have shown multiple peaks. The singular peak at this location which is an integration of MFL signals from the top transverse reinforcement. This MFL signal is fundamentally different from unmagnetized transverse reinforcement shown in Figure 4-5. This reiterates the need for magnetization before any measurement is taken.

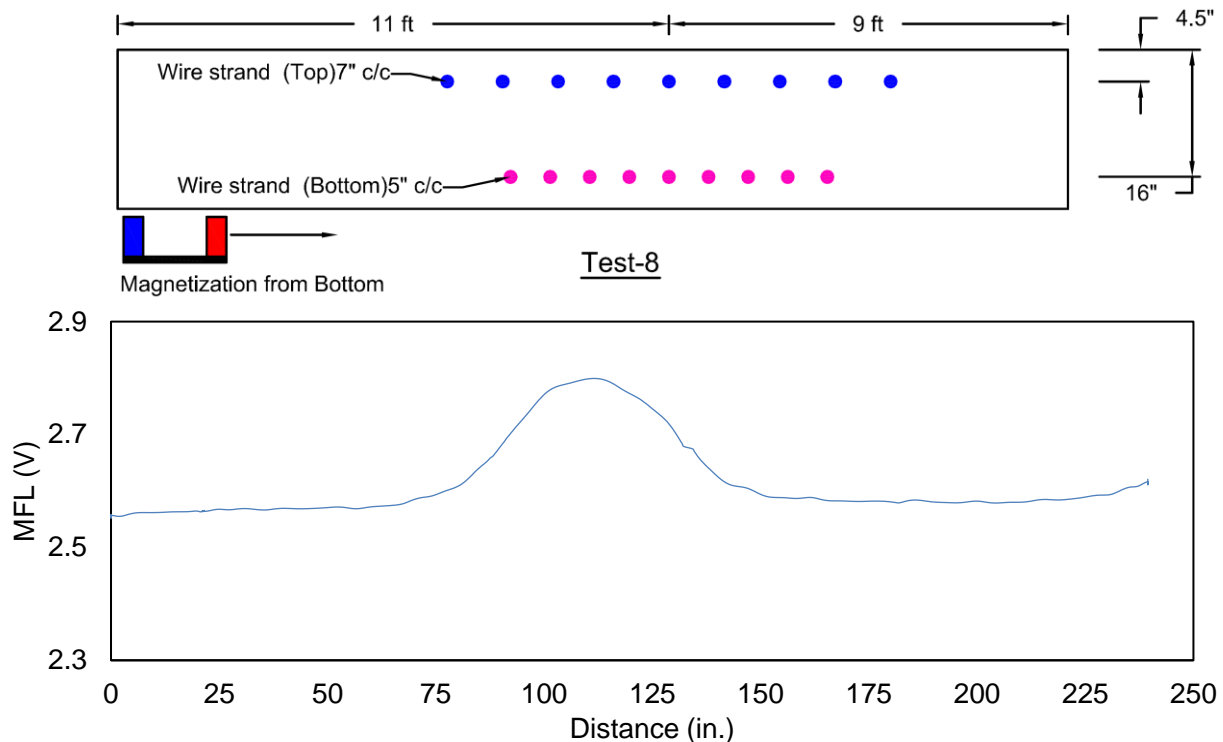


Figure 4-9: Configuration and result of test 8.

Following Test 8 where the effect of transverse reinforcement was evaluated, and results showed that only near-surface reinforcement was saturated. Test 9 and test 10 were carried out in the presence of either the top or bottom reinforcement only to verify findings of test 6 to 8. The configuration of test 9 and 10 are shown in Figure 4-10. The result indicates that the MFL signal does not change at the location of top transverse reinforcements and the trend is similar to unmagnetized strands shown in Figure 4-5.

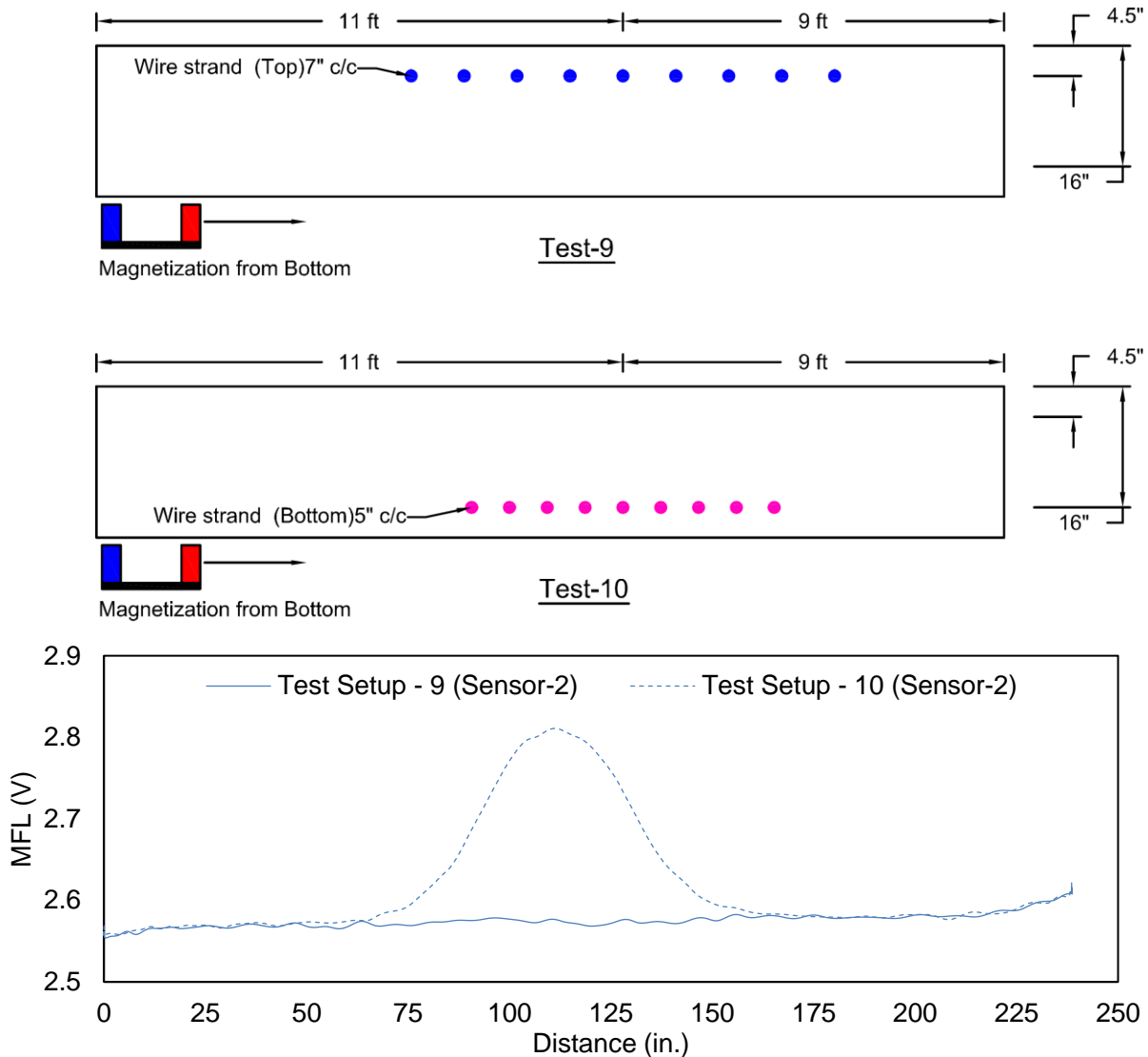


Figure 4-10: Test configuration 9 and 10.

However, for the bottom reinforcement (test 10), a single peak was observed again. These results show that there was no MFL signal in the top transverse reinforcement and the signal came only from the bottom transverse reinforcement.

4.1.3 Summary of Laboratory Tests

Different tests were carried out on mock-up laboratory specimens from test 1 to test 10. These tests considered magnetization scheme as described and the effect of transverse reinforcement. Based on the results, it was found that the magnetization method used resulted in a clear indication of defect signal even in the presence of transverse reinforcement. This result demonstrated a potential application for field usage. However, the laboratory mock-up specimens were built with a 100% section loss and presented an extreme test case but not necessarily indicative of the actual damage scenario. In the next phase of testing, the measurement unit and magnet 2 was used for testing on the bridge segment with different section loss scenarios.

4.2 TESTING ON BRIDGE SEGMENTS

4.2.1 Bridge Segments at FIU

In the next stage, the testing procedures developed on laboratory mock-up specimen were extended to the bridge segments at FIU. These bridge segments were salvaged from an existing bridge that was planned for demolition. The segments of this bridge were transported to FIU for NDT. The detail of the bridge segment is presented in Appendix A.3. Figure 4-11 shows the bridge segment with the arrangement of a platform for magnetization of the strands and the instrumentation cart on the top of the bridge segment.

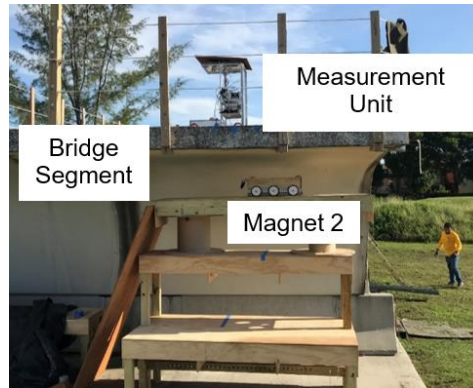
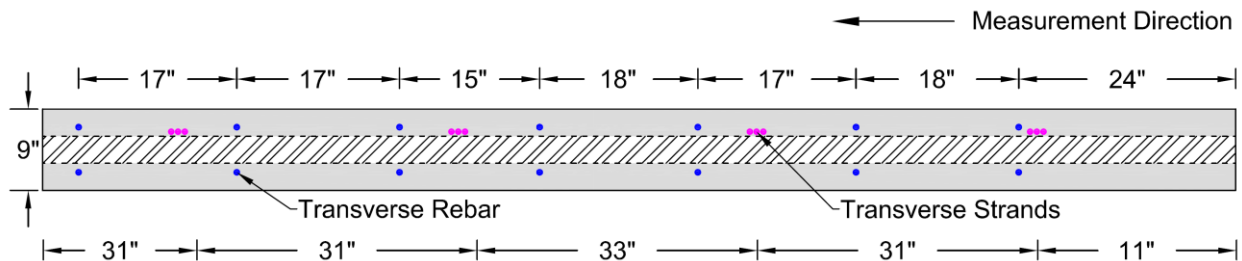


Figure 4-11: Bridge segment.

In the top slab of the bridge segment, there were top and bottom reinforcements that were perpendicular to the tendon ducts and were located intermittently along the length of the segment. In addition, there were bundled strands located transversely to the continuity tendon ducts. The location of these transverse reinforcements and tendons are shown in Figure 4-12. In addition, an empty duct was located in the top slab which provided an opportunity to testing different section loss configurations in a controlled environment.



Section of Bridge Segment

Figure 4-12: Location of transverse reinforcement and bundled strands in bridge segment.

Testing was carried out on the bridge segment to validate the capability of the modified MFL system and demonstrate its application to identify strand metal loss in internal tendons. Similar test protocols from laboratory testing were followed for the segment tests.

4.2.2 Preliminary Tests on Bridge Segment

Preliminary tests were carried out on the bridge segment to determine signals from unmagnetized strands. The empty ducts in the top slab were used to place bundled strands for a length of 10 feet. The grouped strands consisted of ten 7-wire strands (0.6-in diameter). The cross-section loss in the strands was simulated by saw cutting the wires of the strands. The objective of these preliminary tests was to understand the effect of residual unmagnetized strands on the defect signal.

Table 4-3. Test configuration 11 and 12

Test No.	Magnetization State	Section Loss	Defect Location
11	Unmagnetized	10%	Defect located under transverse reinf.
12	Laboratory magnetized	20%	Defect located under transverse reinf.

The configuration for test 11 and results are shown in Figure 4-13 where a 10% cross-section loss was placed in the bridge segment. The depth of the tendons was about 4.5 inches from the top slab. The measurement of the MFL signal was performed from the top slab along the length of the strands. It should be noted that the strands were unmagnetized.

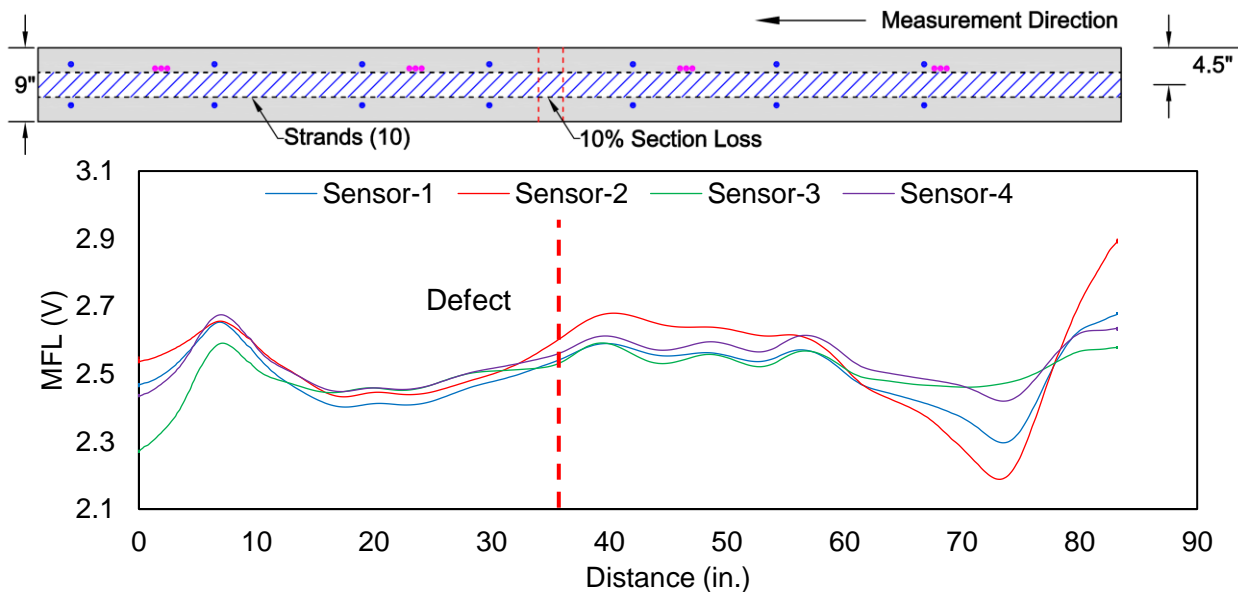


Figure 4-13: Test configuration 11.

The results shown in Figure 4-13 indicated that the residual magnetization of the strands does not allow the identification of the 10% section loss. The peaks at the start and end of the plot are indicative of the end effect. All the sensors indicate a similar trend and the location of defect could not be predicted. This result was similar to a 100% defect test on laboratory mock-up specimens shown in Figure 4-3. The residual magnetization causes some change along the length of the strands, but the defect location and percentage section loss were difficult to predict.

Using a similar approach for test 12, another set of strands, but with a 20% section loss which was magnetized in the laboratory and was placed in the duct (Figure 4-14). The MFL signal was observed from the top and the results are also plotted in Figure 4-14. The MFL signals from this test configuration show the location of defect. The transverse strands did not affect the signal.

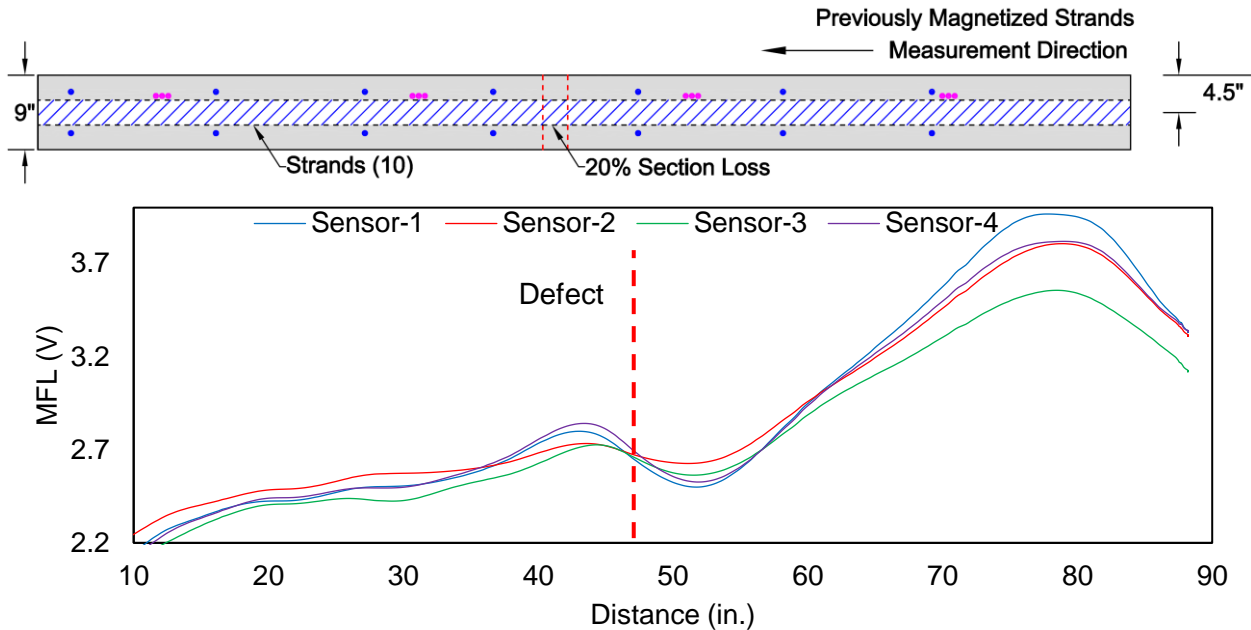


Figure 4-14: Test configuration 12.

The results of this test are promising as they were able to predict section loss of 20%. However, laboratory magnetized strands are not representative of in-field internal PT tendons. Therefore, additional tests were performed where the magnetization scheme was carried at the site from the top and bottom of the slab.

4.2.3 Top Magnetization Scheme

The field magnetization was carried out from the top slab followed by signal measurement from the same surface. Two tests were carried out as mentioned in Table 4-4.

Table 4-4. Test configuration 13 to 14

Test No.	Magnetization State	Section Loss	Defect Location
13	Top magnetization	10%	Defect away from transverse reinf.
14	Top magnetization	10%	Defect located under transverse reinf.

The simulated damage in the strands was 10% but the location of the defect was varied for test 13. Initially, the strands were magnetized three times from the top side and the MFL signal was observed as shown in Figure 4-15. It can be observed from the figure that the location of the defect is away from the transverse reinforcement. The magnetization scheme from the top causes the top reinforcement to be magnetized more than the tendons. This results in a stronger MFL signal from these top transverse reinforcements obscuring the location of the defect.

For Test 13, the transverse reinforcement was located away from the simulated damage. However, it is likely that the defect is located right underneath the transverse reinforcement. To simulate this condition, a test configuration (test 14) was setup as shown in Figure 4-16. The signal is strong at the location of the defect as the transverse reinforcement is also passing through it.

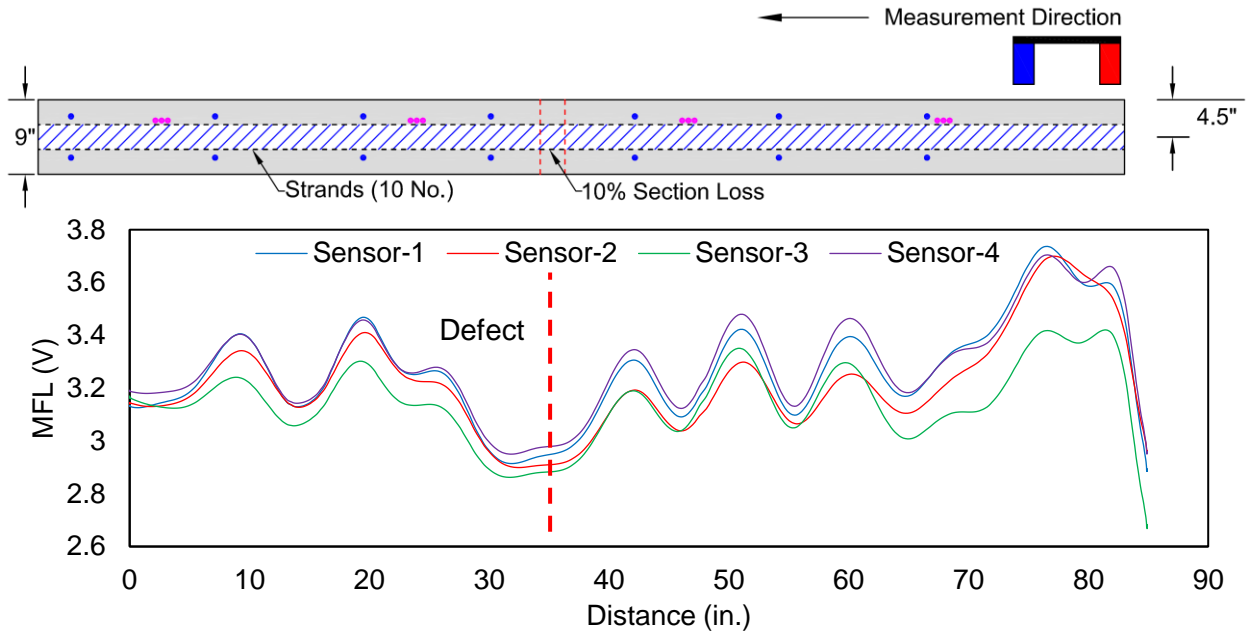


Figure 4-15: Test configuration 13.

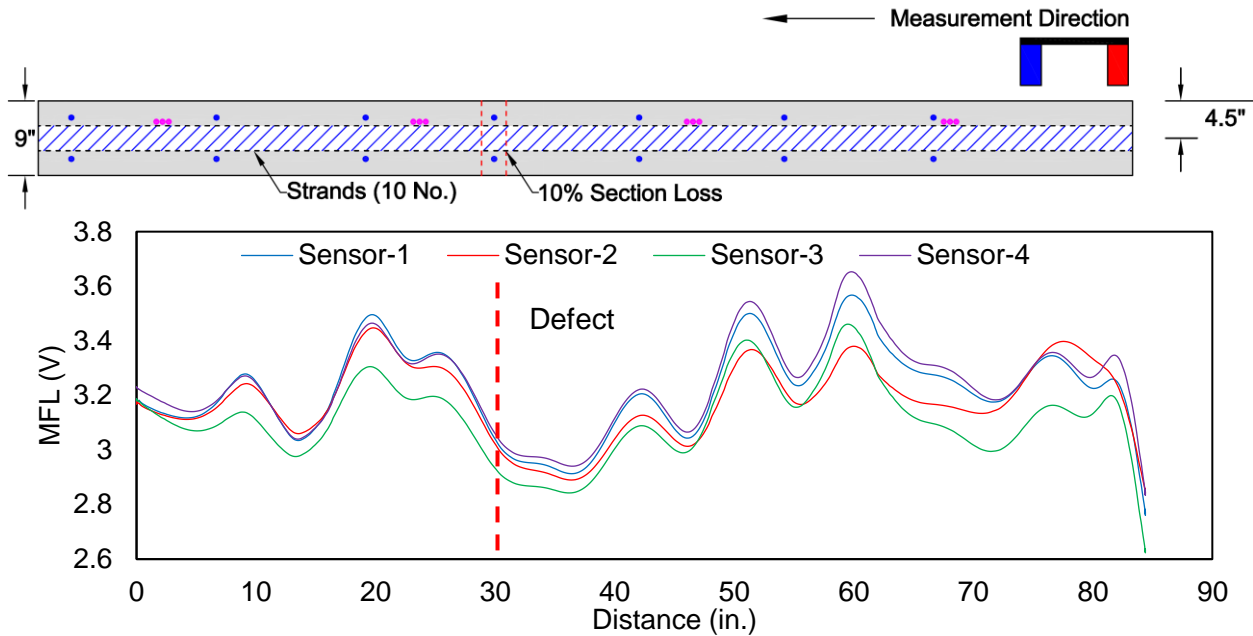


Figure 4-16: Test configuration 14.

4.2.4 Bottom Magnetization Scheme

The results from the top magnetization scheme showed that the section loss may not be ascertained with confidence when the defect was either located away or directly under the transverse reinforcement. Based on the magnetization scheme developed in laboratory mock-up specimens, additional tests were run where the strands were magnetized at the site from the soffit of the girder. The strands were magnetized from the bottom using a modified assembly where the magnet poles faced upward direction. The distance between the poles of the magnet and the bottom surface of the segment was varied from 7 in. down to 3 in. The magnetization procedure was repeated three times to get a stronger signal from the sensors and to see the effect of transverse reinforcement.

The segment has three main tendons, one in the center and two on either side in the longitudinal direction. These tests were performed on the tendon located at the right side of the segment in the longitudinal direction. This tendon contained ten number 0.6-inch strands. The MFL tests were performed with a 10%, 55%, and 100% defect in the strands. The defect was positioned 1) between two transverse reinforcements and, 2) just below the transverse reinforcement. The measurement of the MFL signal was performed from the top slab, as shown in Figure 4-17.

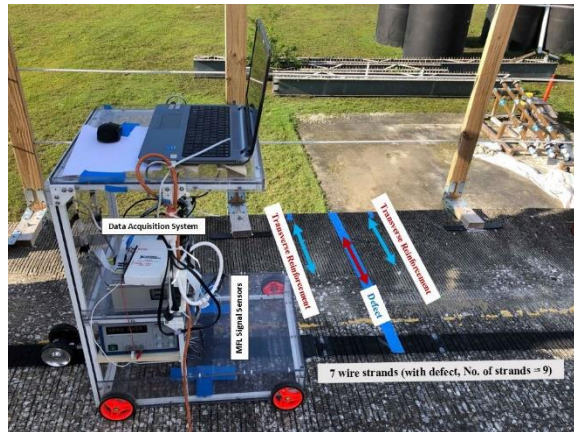


Figure 4-17: MFL test setup.

Before magnetization was performed, a test was run to check the residual magnetization in the strands (Table 4-5). Figure 4-18 shows the configuration and results for test 15 where the section loss was 10%. The result shows that the defect did not cause a change in flux at the location of the defect. This test configuration was similar to test 11 but a different duct was used for measurement of the signal. For both cases, the defect location was not clear.

Table 4-5. Test configuration 15

Test No.	Magnetization State	Section Loss	Defect Location
15	Unmagnetized	10%	Defect away from transverse reinf.

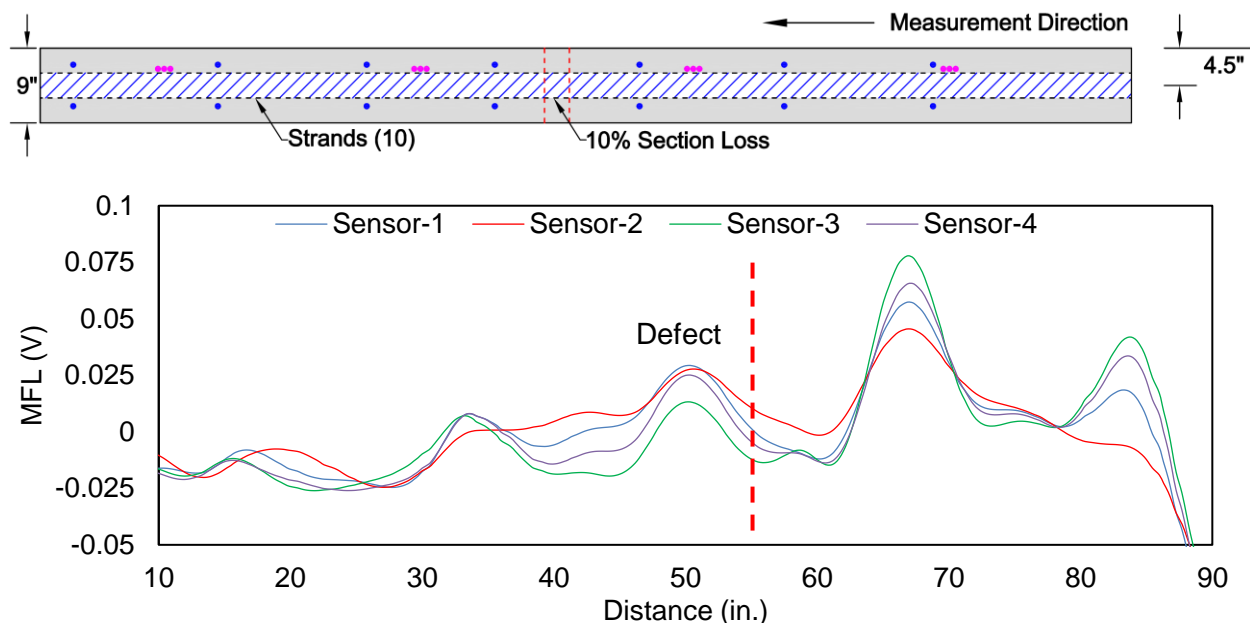


Figure 4-18: Test configuration 15.

Following this test, the strands were magnetized from the soffit of the girder. A test matrix was developed with different defect location and depth of magnet which is listed in Table 4-6. The variables in the test matrix represent different levels of section loss of 10%, 55%,

and 100%. Initially, the magnetization was carried out at 7 in. depth from the bottom of the soffit of the top slab. However, results indicated that the strands were not sufficiently magnetized. Therefore, the depth of magnetization was lowered to 3 in. Another variable that affects the test results is the location of the defect adjacent to other ferromagnetic materials. For bridges in the field, the defect location may extend along the length of the tendon. In many cases, the damage is not localized, and the exact nature and severity may also differ. It may not be possible to replicate the full spectrum of test cases; therefore, three simplified cases are considered for the test segments. These cases consider the following:

- The defect is located between two transverse reinforcements.
- The defect is located directly below the transverse reinforcement.
- The defect is located between transverse reinforcements but away from prestressing strand.

The details of test configurations 16 to 18 are explained below. All these tests consider a 10% section loss while the damage location and depth of magnetization differed. Test 16 was carried out with a 10% defect but due to insufficient magnetization, the MFL signals were not strong. The plot of the result, shown in Figure 4-19, indicates four possible points at the defect location. The signal from each sensor is not concurrent at the location. Also, sensor 2 shows a softened peak when compared to other sensors. This indicates that the magnetization scheme was not sufficient to allow a more reliable signal to be obtained.

Table 4-6. Test matrix for the bottom magnetized strands

Test No.	Depth of Magnetization	Section Loss	Defect Location
16	7 inches	10%	Defect located under transverse reinf.
17	3 inches	10%	Defect located under transverse reinf.
18	3 inches	10%	Defect away from transverse reinf.
19	3 inches	55%	Defect located under transverse reinf.
20	3 inches	55%	Defect located between transverse reinf. and away from strands
21	3 inches	100%	Defect located under transverse reinf.
22	3 inches	100%	Defect located between transverse reinf. and away from strands

Test 17 was carried out using a similar configuration as test 16, but the magnetization was then carried out from a depth of 3 in. This allowed a more uniform magnetization of the bundled strands. The results of the test are plotted in Figure 4-20. The lower depth of magnetization removed the non-coincident peaks which were observed in test 16. All sensors show a common location where the defect was located. The magnetization from a closer range improved the resolution and accuracy of damage detection, but this also increased the magnetization of secondary ferromagnetic materials. This can be observed by an increase in the magnitude of the measured signal.

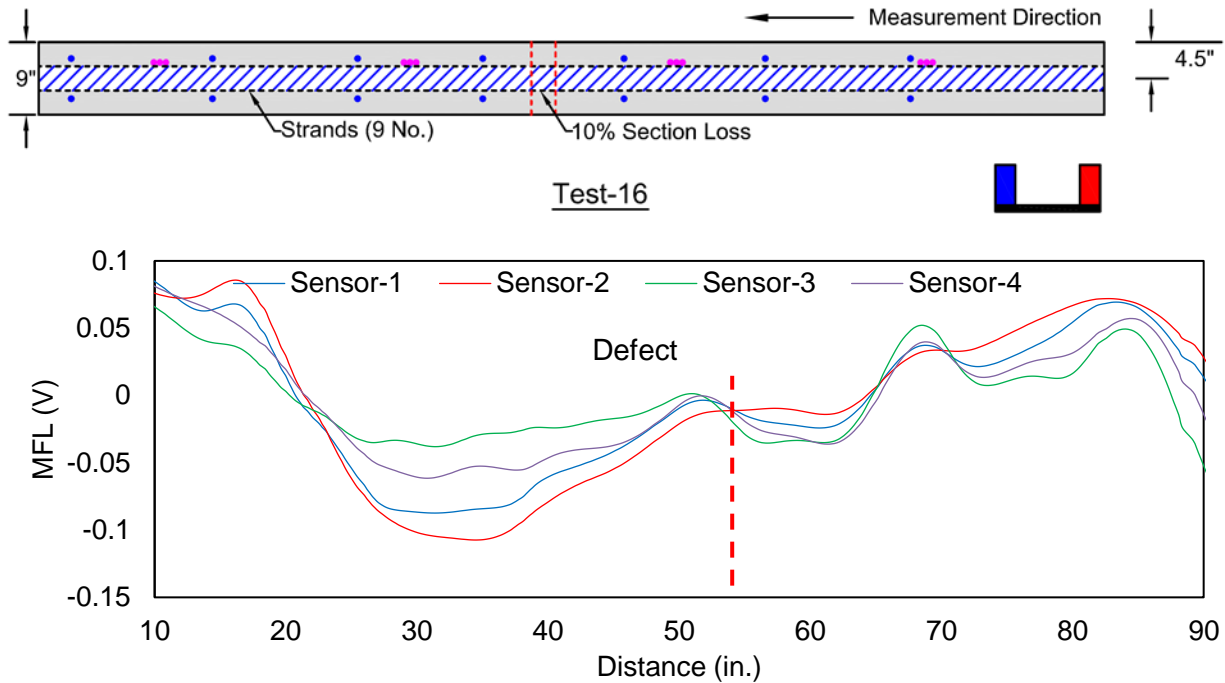


Figure 4-19: Test configuration 16.

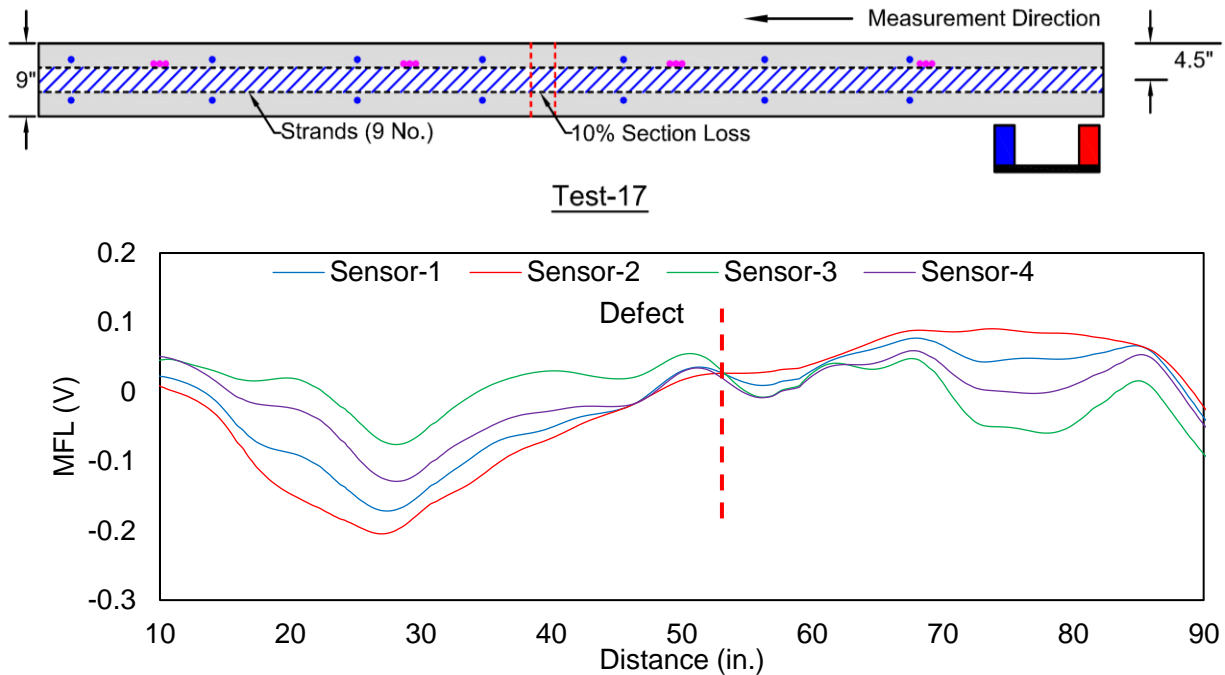


Figure 4-20: Test configuration 17.

For test 16 and test 17, the damage was located between the two reinforcement. To confirm if the change in signal represented the defect location, another test (test 18) was run where the defect location was moved 5 in. away from its original position. The MFL signal of this case is shown in Figure 4-21. The MFL signal for test 18 was similar to tests 16 and 17 which confirms that the change is caused by the defect.

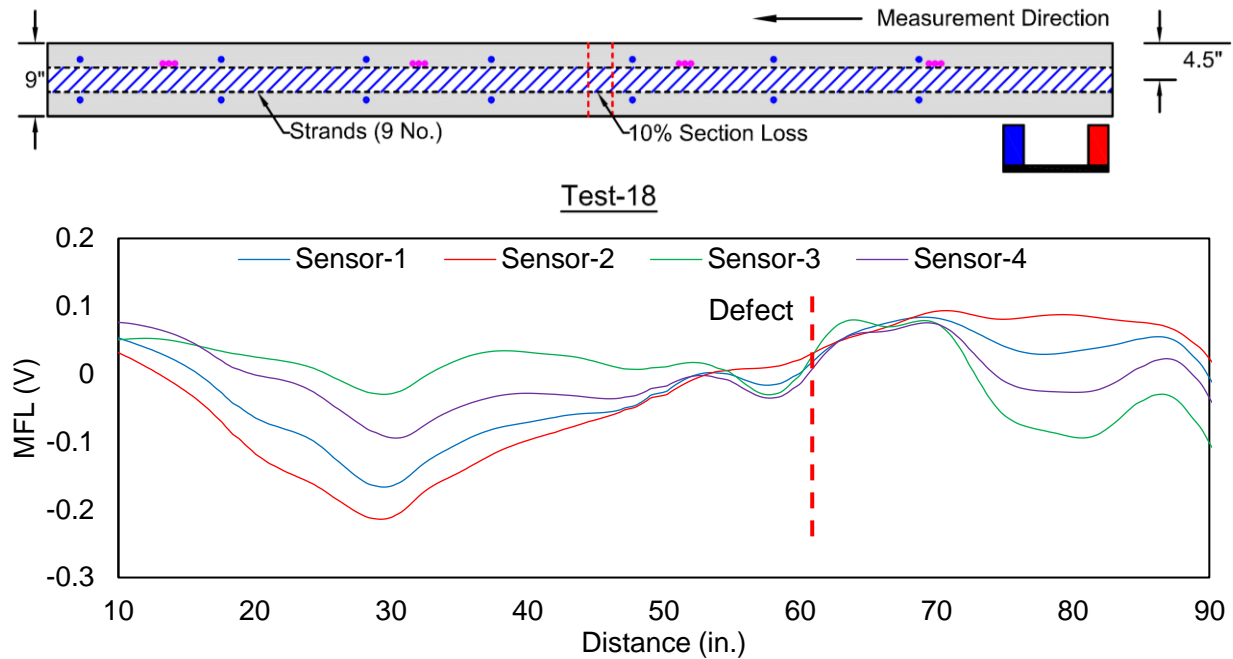


Figure 4-21: Test configuration 18.

The bottom magnetization was able to locate the section loss of 10% with limited accuracy. Additional tests were carried out where an increased section loss of 55% was simulated in the strands. Also, the defect was located in such a way that the transverse reinforcement was passing just above and below the defect. The two test cases (test 19 & test 20) are shown in Figure 4-22.

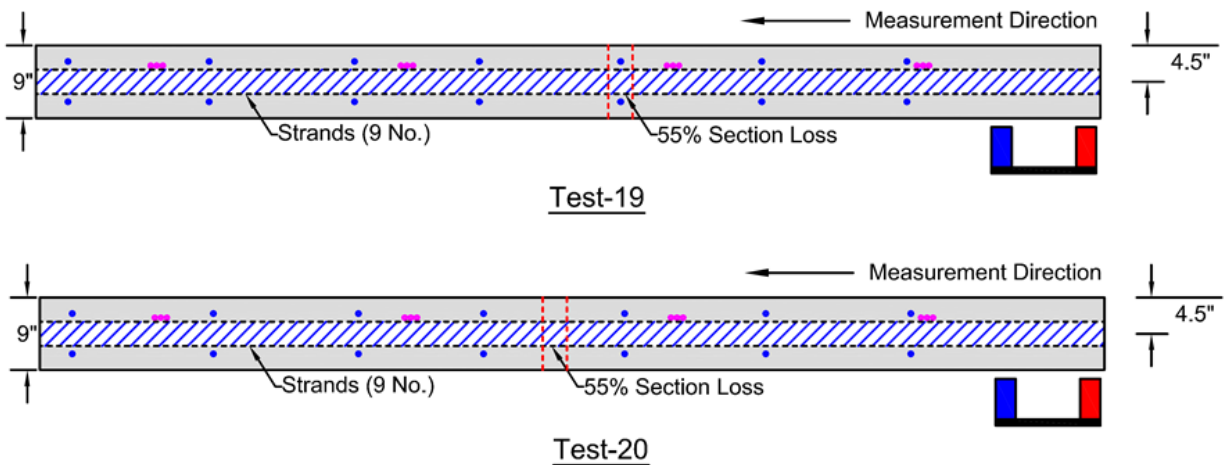


Figure 4-22: Test configuration 19 and 20.

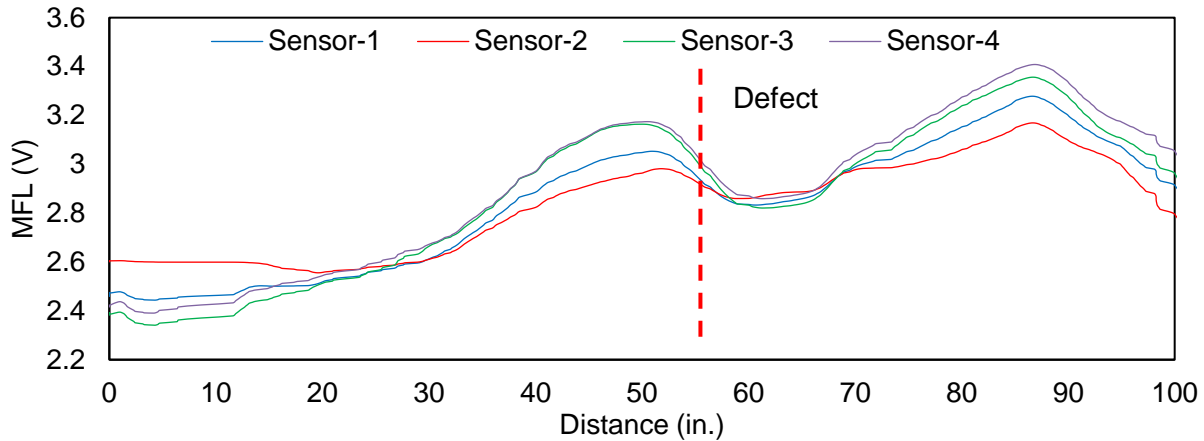


Figure 4-23: MFL signal of a 55% defect under the transverse bars.

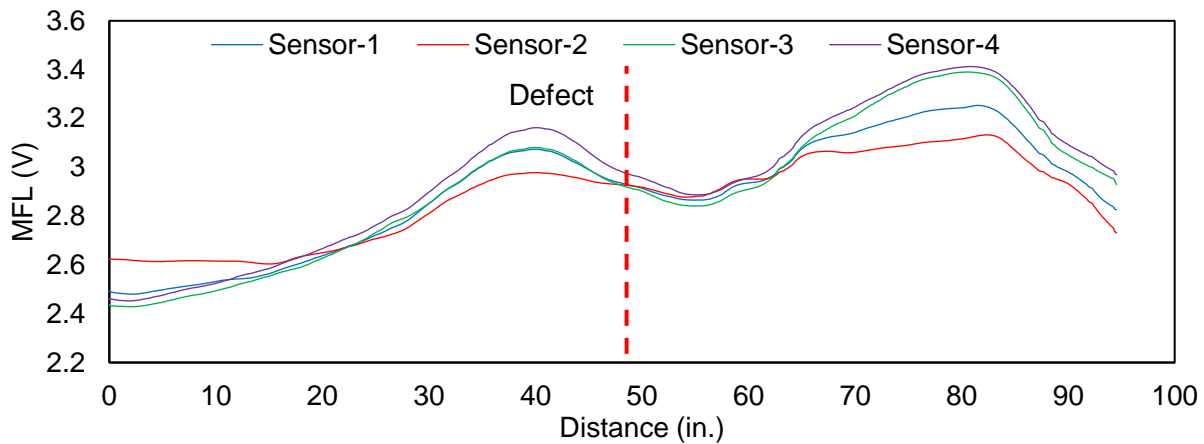


Figure 4-24: MFL signal of a 55% defect in between the transverse bars.

Figure 4-23 and Figure 4-24 show that the defect is clearly visible, and the transverse reinforcement does not affect the signal. It can be observed from the figures that the shift in defect location also causes a shift in the signal. Since the transverse reinforcement does not affect the result, its location between or below the reinforcement is trivial.

Testing using the bottom magnetization scheme was carried out with incremental section loss from test 16 to test 22. The MFL signal improved with an increase of section loss from 10% to 55%. Figure 4-25 shows Tests 21 and 22 were carried out with a 100% section loss when the defect is located underneath or adjacent to transverse reinforcement, respectively. The objective of the test was to check the effect of the total section loss on the MFL signal.

The results of these tests, shown in Figure 4-26 and Figure 4-27, indicates that the MFL signal is quite strong at the location of the defect and all sensors are showing same location of the defect which means that transverse reinforcement is not affecting the signal from the sensors. Also, there is slight variation in the signal when transverse reinforcement is present just above and below the defect. Comparing the results of different defect percentage indicates that the magnitude of MFL signal increases when the section loss increases.

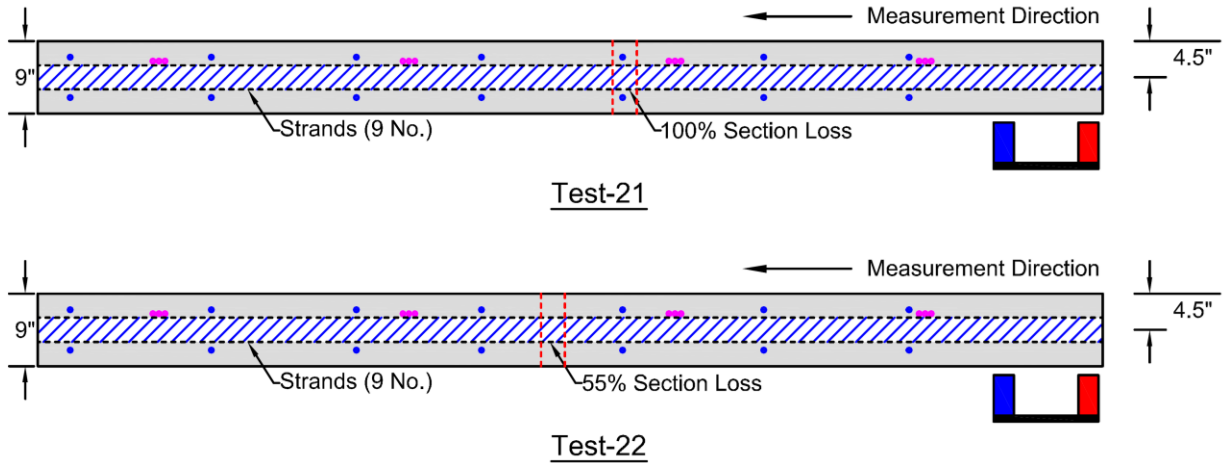


Figure 4-25: Test configuration 21 and 22.

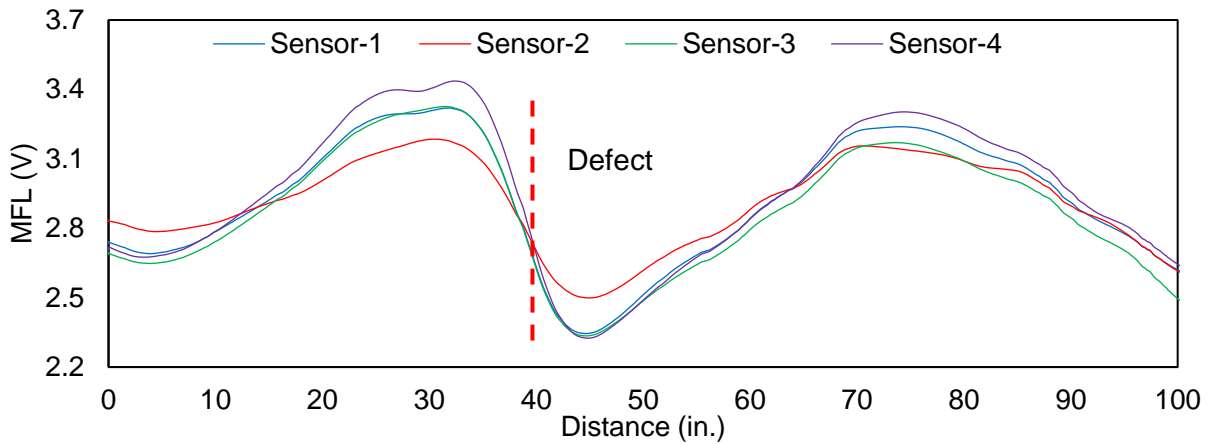


Figure 4-26: MFL signal of a 100% defect under the transverse bars.

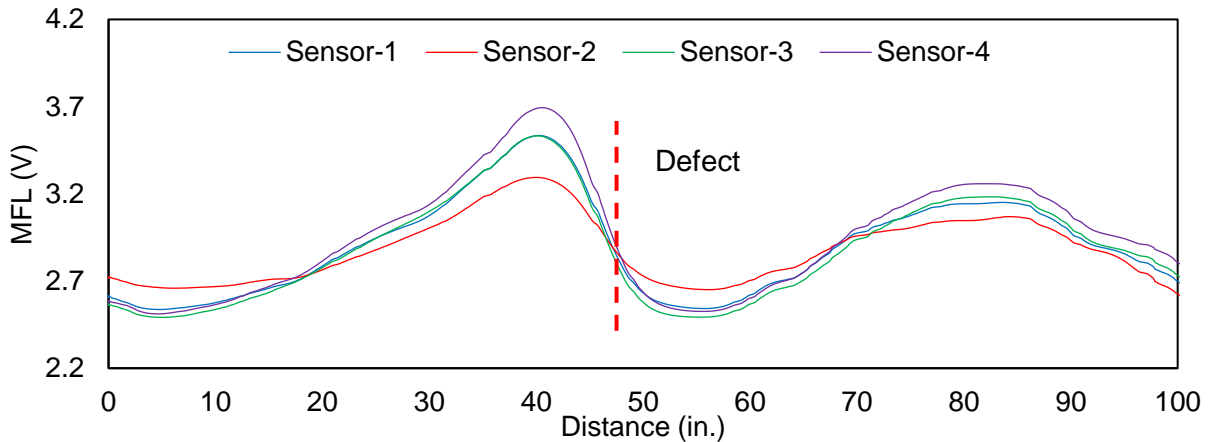


Figure 4-27: MFL signal of a 100% defect in between the transverse bars.

4.2.5 Segment Testing Summary

A series of testing was carried out on the bridge segment at FIU. Different magnetization schemes were used to magnetize a group of strands placed in an empty duct. The test

variables also considered the effect of magnetization depth, section loss and location of transverse reinforcement. The test results were similar to laboratory mockup specimen where the bottom magnetization scheme resulted in a clear indication of defect signal even in the presence of transverse reinforcement. An increase in section loss improves the signal magnitude and an accurate prediction of defect. Near-surface magnetization is more effective in saturating the strands and improves the MFL signal taken from the far-surface.

4.3 BRIDGE A MOCKUP SPECIMEN

Preliminary laboratory testing was carried out on wooden specimens which allowed simulation of different testing conditions. However, these specimens did not replicate Bridge A condition. It was decided that a more realistic test setup needs to be developed. The dimension and reinforcement details of Bridge A were used to construct the concrete blocks. These concrete blocks represent a five feet wide longitudinal section of the bridge. The concrete blocks, shown in Figure 4-28, were constructed each six feet in length which replicated the width of the actual pretensioned hollow slab sections. The width of the specimen was designed to furnish a platform wide enough for the measurement units to be operated from the top or bottom of the blocks. The construction drawings were used to determine the location of mild reinforcement and tendons as shown in Figure 4-29.



Figure 4-28: Construction of specimen.

The depth of bridge slabs was 18-in with a 1.5-inch overlay; therefore, the concrete blocks were also constructed with a total thickness of 19.5 inch. No pretensioning was applied to the strands during casting of concrete. In actual bridge the tendons were located at a uniform depth of nine inch from the bottom side. However, to provide more options for the research team, three ducts were embedded in the slabs. The details are as follows:

Table 4-7. Details of the ducts

Sr. No.	Depth from soffit of blocks	Distance from center	Material	Diameter of duct
Duct-1	9 in.	10.0 in	Corrugated Metal	4 in.
Duct-2	12.5 in.	0.0 in.	Voided	4 in.
Duct-3	9 in.	10.0 in.	Voided	4 in.

The slabs were placed on concrete blocks which were constructed to provide a clearance of 15 inches from the floor. The tendons in each block were anchored to the formwork to prevent any movement during the casting of concrete. Also, the location of the transverse reinforcement was marked on the concrete blocks for easy identification during the MFL measurement.

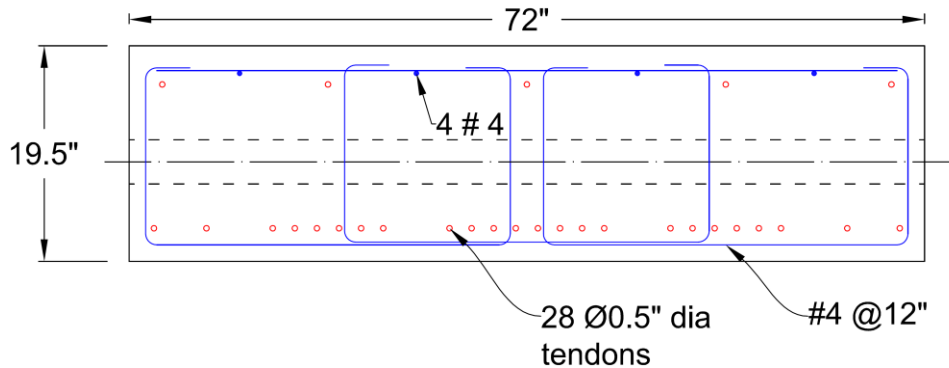


Figure 4-29: Dimension and reinforcement detail of concrete block.

The three concrete blocks were placed in a series to obtain a working platform with a total length of 18-ft. The blocks were constructed with a matching interface at the top to allow smooth traversing with the prototype unit. The PT rod or strands were placed in one the ducts and the magnet assembly was used for magnetizing the rod from the bottom. Using the prototype unit-2, readings were taken from the top surface. The test platform and photographs during testing are shown in Figure 4-30.



Figure 4-30: Testing on concrete blocks.

The summary of the tests is provided in Table 4-8. In this table the duct used for placement of the PT tendon, type of the PT tendon, the signal measurement scheme, type of the defect, and magnetization used are defined. Only tests with results from duct 1 and 3, where the duct has the same depth as Bridge A are reported here. The PT tendon material used in Bridge A was PT rods, however a few cases with bundle of 10 strands were also tested. MFL signal was measured either from the top or bottom of the slab. In

some of the tests, flux concentrators were used to magnify the sensor reading. The type of the defect used for PT rods were complete discontinuity with a 0 to 6-in. gap. Magnet 2 was used for all the magnetizations.

Table 4-8. Lab tests details

Test No.	Duct No.	Material	MFL Signal Taken	Defect	Magnetization
LST-1	Duct-3	PT rod	Top	100%	No Magnetization
LST-2	Duct-3	PT rod	Bottom	100%	No Magnetization
LST-3	Duct-3	PT rod	Top	100%	Bottom
LST-4	Duct-3	PT rod	Bottom	100%	Bottom
LST-5	Duct-3	PT rod	Top	100% (2")	Bottom
LST-6	Duct-3	PT rod	Top	100% (6")	Bottom
LST-7	Duct-3	PT rod	Top	100% (10")	Bottom
LST-8	Duct-1	PT rod	Top	100%	No Magnetization
LST-9	Duct-1	PT rod	Bottom	100%	No Magnetization
LST-10	Duct-1	PT rod	Top	100%	Bottom
LST-11	Duct-1	PT rod	Bottom	100%	Bottom
LST-12	Duct-1	PT rod	Top	100% (2")	Bottom
LST-13	Duct-1	PT rod	Top	100% (6")	Bottom
LST-14	Duct-1	PT rod	Top	100% (10")	Bottom
LST-15	Duct-3	PT rod	Top (w/o flux concentrator)	100%	Bottom
LST-16	Duct-3	PT rod	Top (with flux concentrator)	100%	Bottom
LST-17	Duct-3	PT strands	Top (w/o flux concentrator)	100%	Bottom
LST-18	Duct-3	PT strands	Top (with flux concentrator)	100%	Bottom
LST-19	Duct-3	PT strands	Top (with flux concentrator)	50%	Bottom
LST-20	Duct-3	PT strands	Top (with flux concentrator)	30%	Bottom
LST-21	Duct-3	PT rod	Top (with flux concentrator)	100% (6")	Bottom
LST-22	Duct-3	PT rod	Top (with flux concentrator)	Defect connected with rebars	Bottom
LST-23	Duct-3	PT rod	Top (with flux concentrator)	100%	Bottom
LST-24	Duct-3	PT rod	Top (with flux concentrator)	75%	Bottom
LST-25	Duct-3	PT rod	Top (with flux concentrator)	50%	Bottom
LST-26	Duct-3	PT rod	Top (with flux concentrator)	25%	Bottom

4.3.1 Comparison of MFL Signal with No Magnetization

The first test was conducted in the non-metallic duct by placing the PT rod with a 100% defect in the middle (at 100 in.). The MFL signal was taken from the top of the specimen without doing any magnetization and then compared with the MFL signal taken from the bottom of the specimen. The MFL signal is shown in Figure 4-31. LST-1 shows MFL signal from the top surface in which a small peak at the location of the defect is obtained due to residual magnetization available in the PT rod. LST-2 shows MFL signal from the bottom. The many peaks in the signal shows transverse reinforcement and the MFL signal in inconclusive.

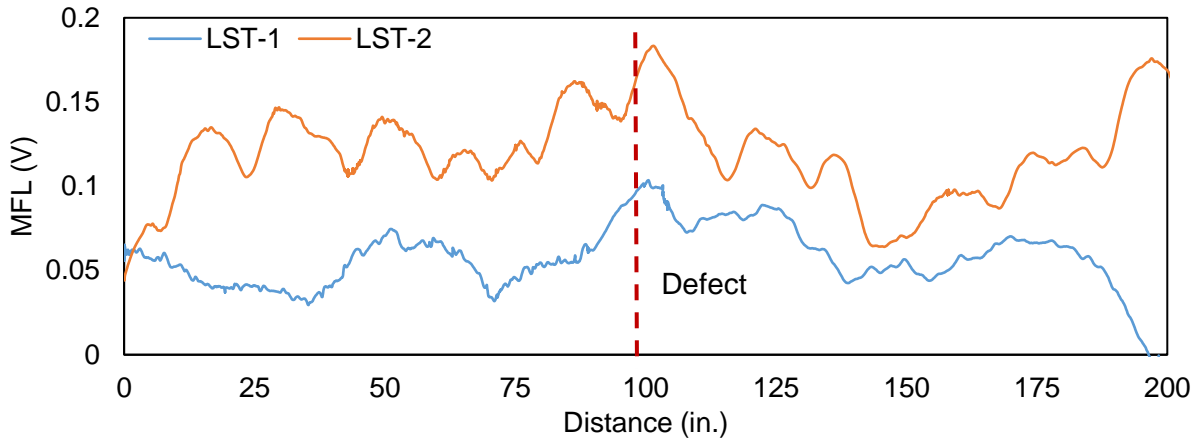


Figure 4-31: Comparison of MFL signal for LST-1 & LST-2.

4.3.2 Comparison of MFL Signal with Magnetization from Bottom Side

LST-3 and LST-4 tests were conducted in the non-metallic duct by placing the PT rod with a 100% defect in the middle (at a distance of 100 in.) and the MFL signal was taken from the top of the specimen without any magnetization and then compared with the MFL signal taken from the bottom of the specimen. The MFL signal is shown in Figure 4-32. LST-1 shows MFL signal from the top surface in which a small peak at the location of the defect is obtained due to residual magnetization available in the PT rod. The LST-2 shows MFL signal from the bottom. The many peaks in the signal shows transverse reinforcement and the MFL signal in inconclusive.

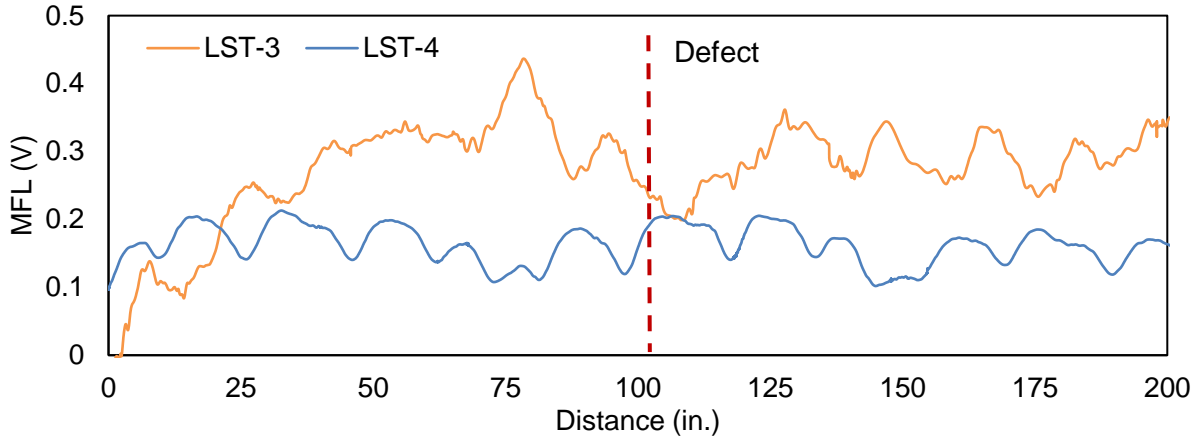


Figure 4-32: Comparison of MFL signal for LST-3 & LST-4.

4.3.3 Effect of Gap Width on MFL Signal (Non-metallic duct)

Test LST-5 to LST-7 were carried out on the non-metallic duct. A complete defect was simulated by two pieces of dywidag rods. The distance between these dywidag rods was varied from 2 inches to 10 inches to see the effect on signal strength. The defect can be observed by the peak-and-valley pattern at the location of defect. The results showed that the MFL signals are not affected by the gap width between the dywidag rods. This reinforces the effectiveness of the MFL method as it can locate localized discontinuities or fractures in the internal tendons.

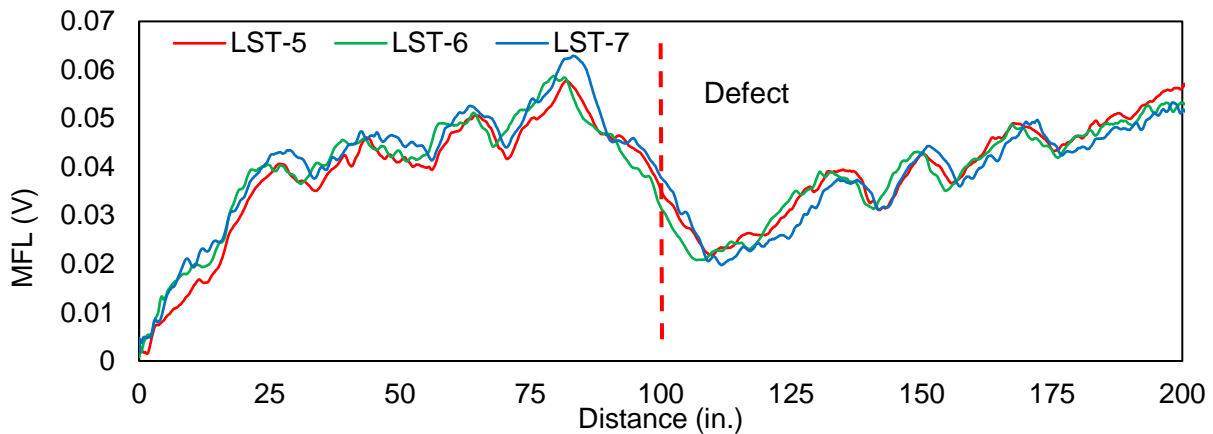


Figure 4-33: Comparison of MFL signal for LST 5-7.

4.3.4 Metal Duct without Magnetization

During the construction of the specimen, a metal duct was embedded in the deck panels at the same height as the non-metallic ducts. A complete defect in PT rod was positioned midway and the readings were taken without magnetization. The results plotted in Figure 4-34. The metallic ducts were disjointed at the interface between two continuous slabs which causes a change in flux signal even though the PT rods are in an unmagnetized state.

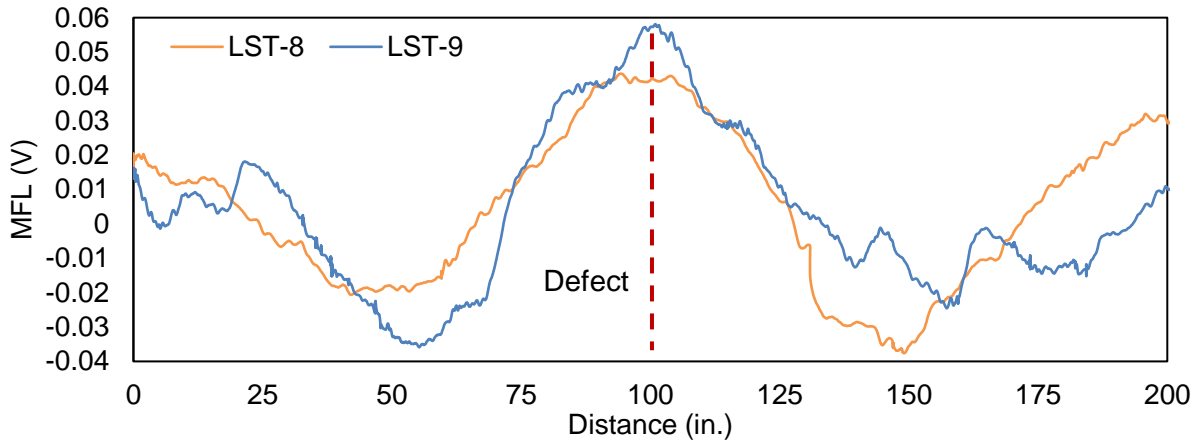


Figure 4-34: Comparison of MFL signal for LST 8-9.

4.3.5 Metal Duct with Magnetization

A complete defect in PT rod was positioned midway which was placed in the metallic duct and the readings were taken without magnetization as shown in Figure 3-8. LST-10 represent signal from the top and LST-11 represent signal taken from the bottom side of specimen. The several peaks in the signal from the bottom side represent the transverse reinforcement hence making it difficult to get exact location of the defect. The defect from the signal from the top surface can be observed by the peak-and-valley pattern of signal. Also, as metallic ducts were disjointed at the interface between two continuous slabs hence causing a change in flux signal.

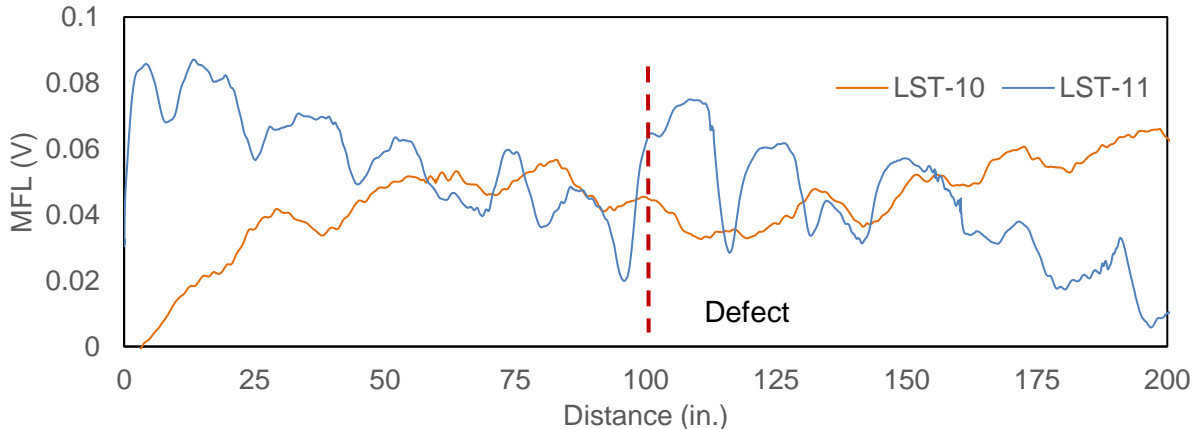


Figure 4-35: Comparison of MFL signal for LST 10-11.

4.3.6 Effect of Gap Width on MFL Signal (Metallic duct)

Test LST-12 to LST-14 were carried out on the metallic duct. A complete defect was simulated by two pieces of dywidag rods. The distance between these dywidag rods was varied from 2 inches to 10 inches to see the effect on signal strength. The defect can be observed by the peak-and-valley pattern at the location of defect. The results showed that the MFL signals are not affected by the gap width between the dywidag rods. This also

reinforces the effectiveness of the MFL method as it can locate localized discontinuities or fractures in the internal tendons.

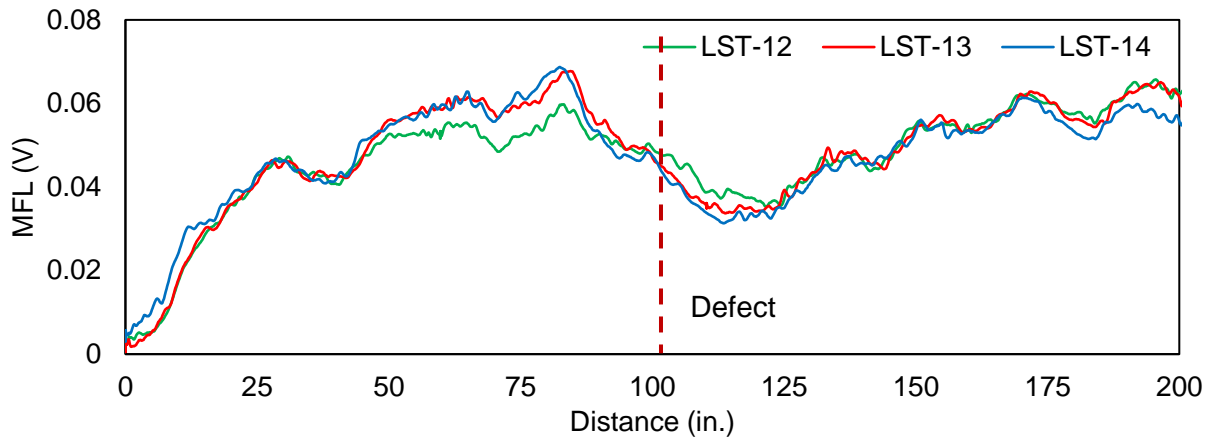


Figure 4-36: Comparison of MFL signal for LST 12-14.

4.3.7 Effect of Flux Concentrator on Signal of PT Rod

Test LST-15 and 16 were carried out to visualize the effect of flux concentrator on the signal of PT rod. Both tests were conducted on non-metallic duct by introducing defect in the middle of a PT rod. LST-15 shows signal obtained by a regular sensor while LST-16 shows signal obtained by a sensor with flux concentrator as shown in Figure 3-10. The signal shows a huge peak in the signal obtained with flux concentrator making it easy to get the location of the defect.

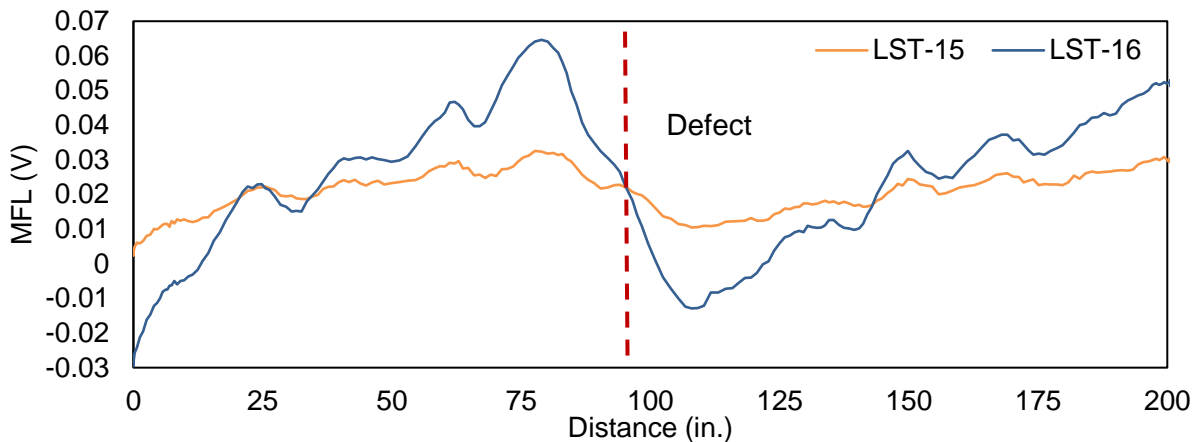


Figure 4-37: Comparison of MFL signal for LST 15-16.

4.3.8 Effect of Flux Concentrator on Signal of Strands

LST-17 and 18 were carried out to visualize the effect of flux concentrator on the signal of strands. These tests were also conducted on non-metallic duct by introducing defect in the middle of strands. LST-17 shows signal obtained by a regular sensor while LST-18 shows signal obtained by a sensor with flux concentrator as shown in Figure 3-11. The signal shows a huge peak in the signal obtained with flux concentrator making it easy to get the location of the defect.

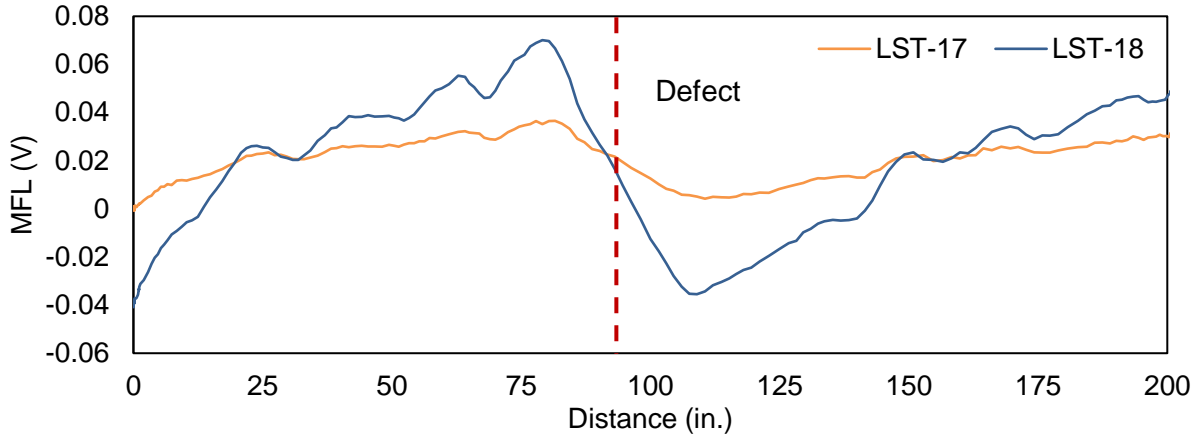


Figure 4-38: Comparison of MFL signal for LST-17 & LST-18.

4.3.9 Effect of Percentage of Defect on MFL Signal of Strands

These tests were conducted on non-metallic duct by introducing a 30%, 50% and 100% midway defect in the strands. LST-18 represents a 100% defect; LST-19 represents a 50% defect while LST-20 represents a 30% defect. The signal shown in Figure 3-12 shows that in all three cases, it is possible to obtain the location of the defect but there is difference in the peaks of the signal. A 30% defect has lower peak than 50% defect which has a lower peak than a 100% defect.

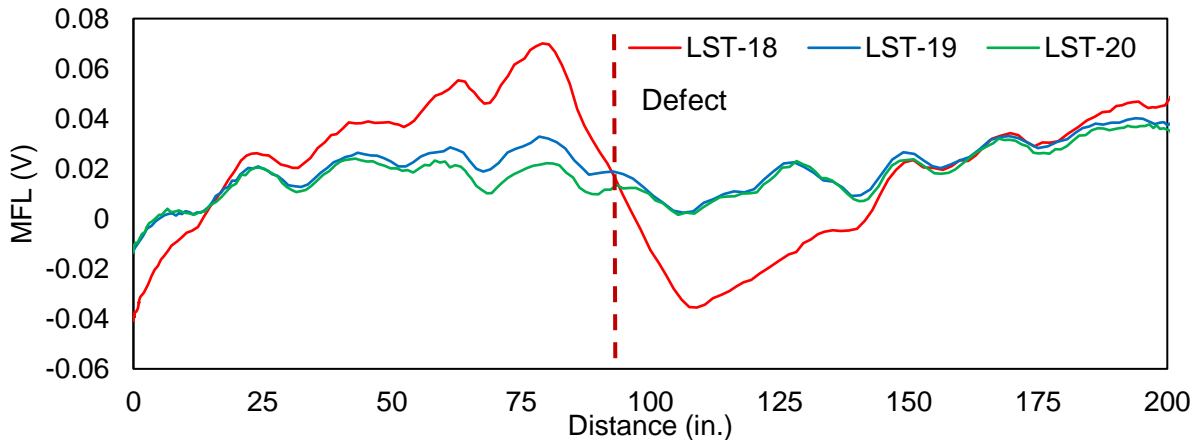


Figure 4-39: Comparison of MFL signal for LST 18-20.

4.3.10 Effect of Defect with Clear Gap & Connected with Rebars

These tests were conducted on non-metallic duct with a PT rod. LST-21 was conducted by introducing a 6 inch midway defect in the PT rod while LST-22 was conducted on the same PT rod but connected with No.5 rebars at the location of the defect. The signal shown in Figure 3-13 shows that there is not much difference in the signal obtained in both cases. So, the presence of other reinforcement bars at the location of the defect do not contribute much and the defect can be located from the MFL signal.

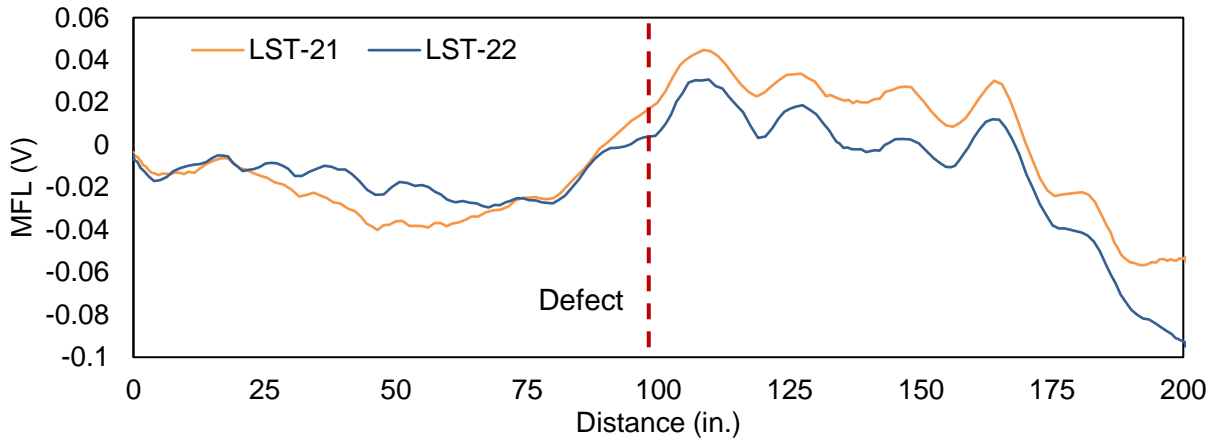


Figure 4-40: Comparison of MFL signal for LST 21-22.

4.3.11 Effect of Percentage of Defect on MFL Signal of PT Rod

These tests were conducted on non-metallic duct by connecting the PT rod with reinforcement bars at the location of the defect with a 25%, 50%, 75% and 100% area of the PT rod. LST-23 represent a 100% defect (no connecting rebar); LST-24 represent a 75% defect (2#5 rebars equal to 25% area of PT rod); similarly, LST-25 represent a 50% defect and LST-26 represent a 25% defect. The signal is shown in Figure 3-14 shows that in all four cases, the MFL signals are not affected by the presence of reinforcement bars between the PT rod and defect can be located by the peak-and-valley pattern at its location.

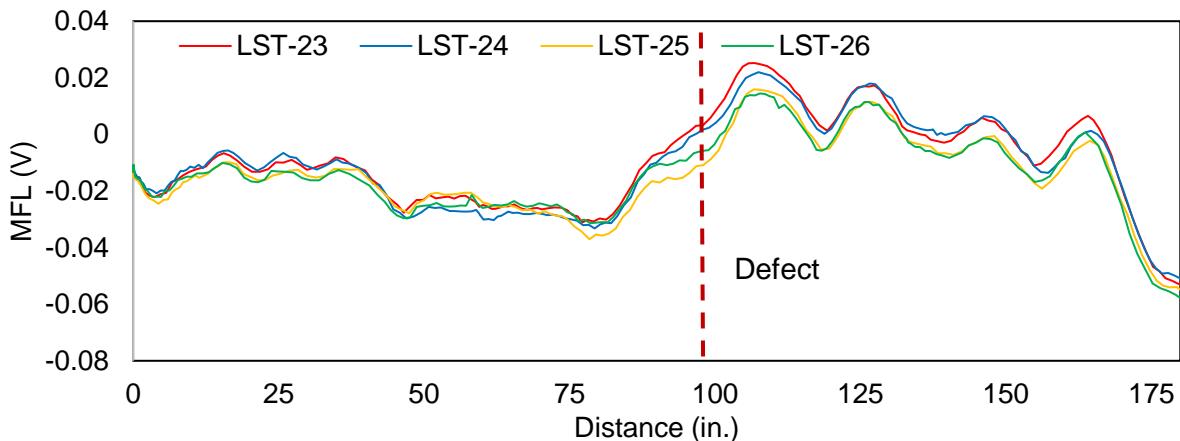


Figure 4-41: Comparison of MFL signal for LST 23-26.

4.3.12 “Bridge A” Mockup Testing Summary

A series of testing was carried out on the bridge segment build to mockup Bridge A conditions in the laboratory. Bottom magnetization scheme was used to magnetize a PT tendon placed in an empty duct. The test variables also considered the effect of duct type, section loss, and gap width of a defect. The test results were similar to laboratory mockup specimen where the bottom magnetization scheme resulted in a clear indication of defect signal even in the presence of transverse reinforcement.

5 FIELD TESTING

5.1 BRIDGE A

Bridge A consisted of prestressed hollow slab sections which were post-tensioned in the transverse direction. The nomenclature of the strands and the plan of Bridge A is shown in Figure 5-1. It shows the dimensions and location of PT rods in the bridge. Each span of the northbound bridge consisted of two PT rods at about one-third of the span length. The spans and PT rods are numbered moving from south to north direction. As an example, S-3-2 refers to span 3 and rod 2. The bridge has been in service for more than 50 years, and it is possible that, due to environmental conditions, the bridge might have developed corrosion in the PT system. Routine inspection and findings of bore-scope testing on the bridge has prompted the bridge owners to carry out a more extensive probe into the condition of the PT rods in the bridge.

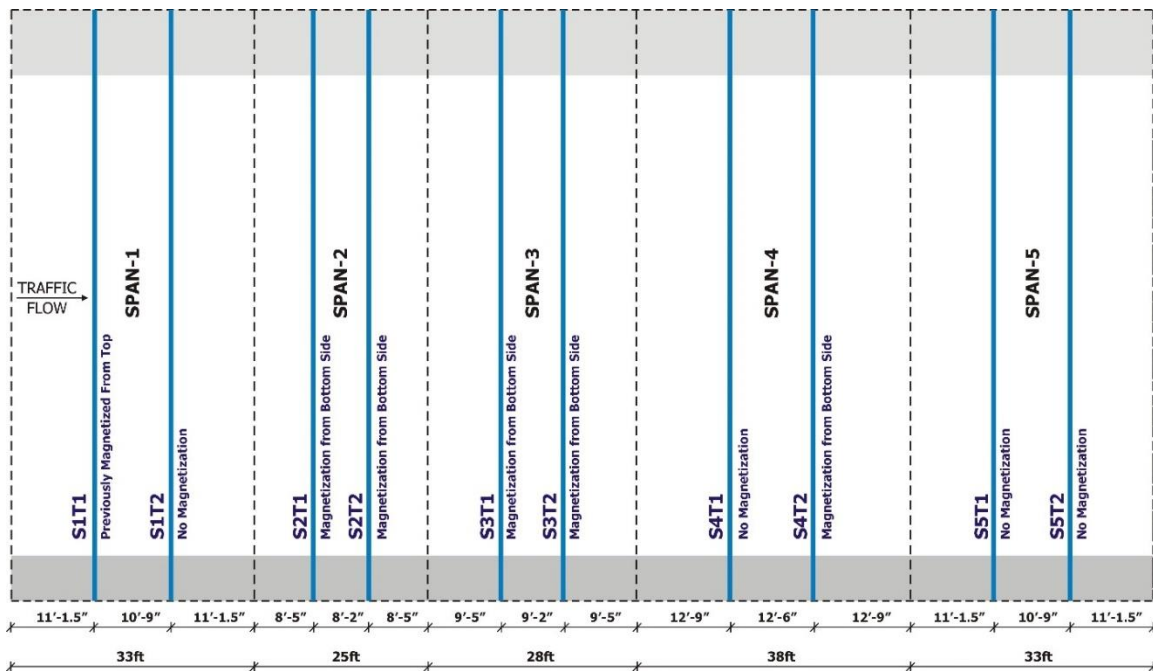


Figure 5-1: Plan view of Bridge A.

Testing on Bridge A was carried out in three phases. In the first phase, the bottom magnetization scheme was not carried out due to accessibility issues. In the next phase, an arrangement was made for magnetizing the tendons from the bottom. The last phase was similar to phase II, but no additional magnetization was performed. The MFL readings for all the phases were taken from the top at night when the traffic volumes are low. A summary of these test results is presented in the following sections, and complete test results are attached as Appendix B.

5.1.1 Phase I Testing

A series of MFL testing was carried out on all PT rods in June 2019 to obtain a baseline measurement. The MFL measurements were taken on both PT rods along the marked lines shown in Figure 5-2. In addition, testing was also carried out midway between these two PT rods. Before testing was carried out, the exact orientation of the embedded PT rods was marked on the deck slab. This procedure ensured that the measurement system

ran parallel to the marked lines. The objective of the testing was to establish a baseline signal which can be used as a reference for future testing. Although this undermines the research methodology developed earlier but helps in establishing a database for subsequent phases of testing.

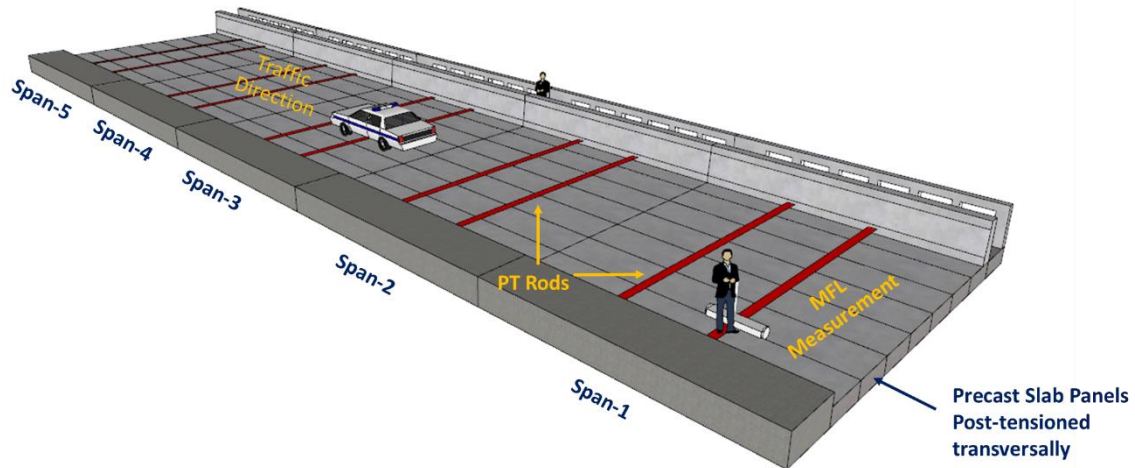


Figure 5-2: Marked locations for MFL testing on span 2.

The signal measurement was carried out by moving along the marked lines using sensors with flux concentrators. At the start of the testing, each strand was measured in its in-situ condition i.e. no magnetization scheme was involved. For span 01 only, the first PT rod (S1-1) was magnetized using magnet 2 from the top. Also, the readings between rod S1-1 and S1-2 were also taken with and without magnetization. However, results showed extensive perturbances due to magnetization and it was decided to take subsequent readings on raw tendons.

5.1.2 Phase II Testing

The testing performed in June 2019 was carried out on unmagnetized PT rods except one PT rod S-1-1. These MFL readings served as baseline signals for the modified testing protocol developed in the lab. In August 2020 a new set of MFL readings was performed on select PT rods. The magnetization was performed from underneath the bridge. A sliding assembly was attached at the bottom of the bridge along the length of the PT rod. The bottom magnetization was carried out by moving the permanent magnet (version 04) along this assembly. The clearance between the magnet and the soffit of the slab was about 1-inch. Since the bridge is located over a waterway, a floating barge was used to move along the length of the rods. Each PT rod was magnetized unidirectionally for three times. The approximate time for each set of magnetizations was about 10 minutes. Out of the 10 PT rods, the sliding assembly was installed for only five PT rod locations.

The signal measurement was carried out from the top of the bridge. Similar to phase I, the orientation of the PT rod was marked across the width of the bridge including the sidewalk. Using the prototype unit, MFL readings were taken from all PT rod locations. The prototype testing unit was consisted of two arrays of 32 regular sensor and 16 sensors with flux concentrators. The complete results are included in the Appendix B.2.

5.1.3 Phase III Testing

In phase I and II, the MFL readings were performed along the direction of PT rod. These measurements provided MFL signals on a limited area in the vicinity of the rod. Additional testing (phase III) on the bridge was carried out in October 2020. In this phase, a complete area scan of the entire bridge span was carried out. The scan was carried out on the northbound bridge between the barrier and the median. The observations made during phase II of the testing showed that the magnetization is retained over time; therefore, prior magnetizations carried out in phase I and II were deemed adequate for phase III. The area scan was carried out by taking consecutive readings along the width of the bridge for every 30 inches width. Depending on the width of the bridge and intermittent traffic closures, the scanning of a complete span took almost 45 minutes.

5.1.4 Discussion on Test Results

Phase I and phase II of the bridge testing were not carried out to compare progression of damages in the PT system. The objective of these testing was to draw a comparison of signal when the PT rod is in an unmagnetized and magnetized state. Selected test results from the two testing phases are described and discussed in this section. A complete set of results is provided in Appendix B.

The comparison of signals amplitude from unmagnetized and magnetized tendon for five PT rods show that the bottom magnetization scheme was able to penetrate to a depth of 9 inches. The measurement from the top surface showed intermittent peaks at the location of the reinforcement.

5.1.4.1 Span 1 – Tendon 1

Test I-S-1-1 was carried out in span 1 of the bridge on PT rod 1. At the time of testing (June 2019), no magnetization was carried out before measuring the signal. Figure 5-3 shows the MFL signal from the rod. The signal had high levels of noise which was attributed to unmagnetized state of tendon. However, a peak-and-valley signal with parallel extensions is found which may be an indicator of anomalous signal at the location. It should be noted that during the laboratory tests performed on un-magnetized dywidag rods, the signal was arbitrary and with peak-and-valleys of various intensity. This may be attributed to the rods getting magnetized during the manufacturing process. Another explanation for the disturbance in the signal shown in Figure 5-3 could be presence of a PT rod coupler at that location. At the coupler location, although the load is transferred completely, but due to the existing magnetic field the magnetic flux may leak.

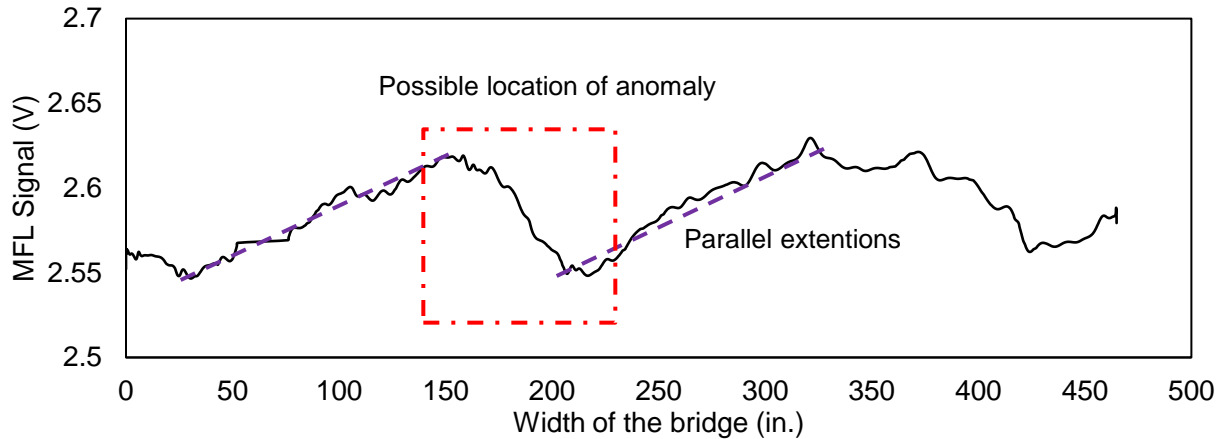


Figure 5-3: MFL signal of unmagnetized PT rod 1 (test I-S-1-1) (flux concentrator sensors).

In the next test, the same rod (S-1-1) was magnetized from the top using magnet version 04. The magnetization was carried out three times. Figure 5-4 shows the effect of magnetization on the signal. It can be observed that the magnetization scheme saturated the secondary ferromagnets thus, impairing the signal with excessive perturbances. The dotted lines in red represents the point of contact between two adjacent slab section.

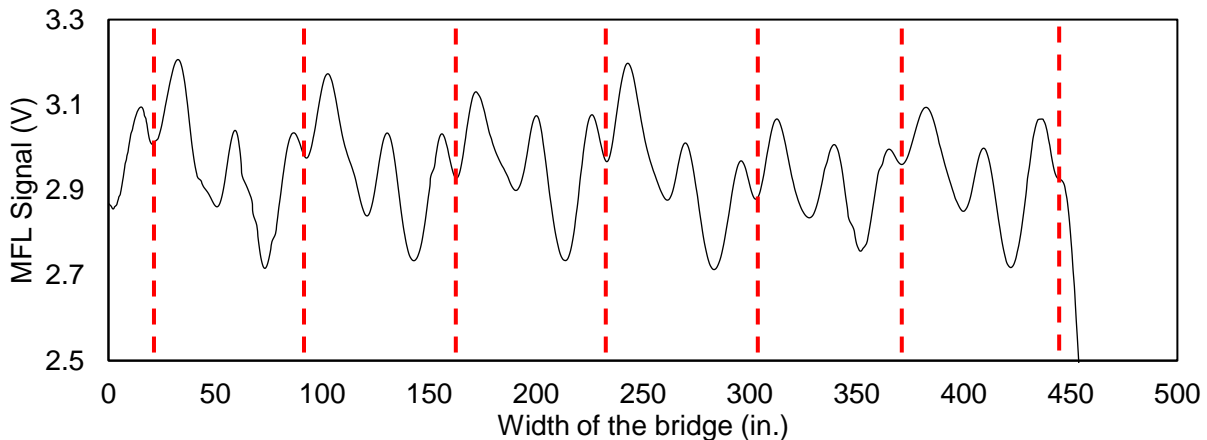


Figure 5-4: MFL signal of magnetized PT rod 1 (test I-S-1-1-m) (flux concentrator sensors).

Testing with no magnetization was carried out for locations where there was no PT rod. For this test, the exact center of two PT rods was selected as a test case (I-S-1-0). The field test results shown Figure 5-5 do not show any significant change in the MFL signal. Similar trend was observed for test 4 results given in laboratory testing. Although, a direct comparison of field and laboratory test is not intended, but similarity in signal trend and strength verifies the merits of laboratory mockup specimens.



Figure 5-5: MFL signal taken between PT rods without magnetization (test S-1-0) (sensors with flux concentrators).

Figure 5-6 shows the measurement taken from the same tendon in the phase II testing. The MFL measurement was performed from the top slab. Results are plotted for three sensors located in the middle and at the ends of prototype unit 3. The sensors at the ends are 16 in. away from the centerline of PT rod. The signals from the top magnetization in one of the PT rods (II-S-1-1) strands remained largely unaffected over time (Figure 5-7). This is an interesting observation and can assist periodic inspection teams to carry out future MFL measurements directly without the need for re-magnetization of same tendons or PT rods. However, it should be ensured that no other magnetization scheme may have ensued between the periodic inspections.

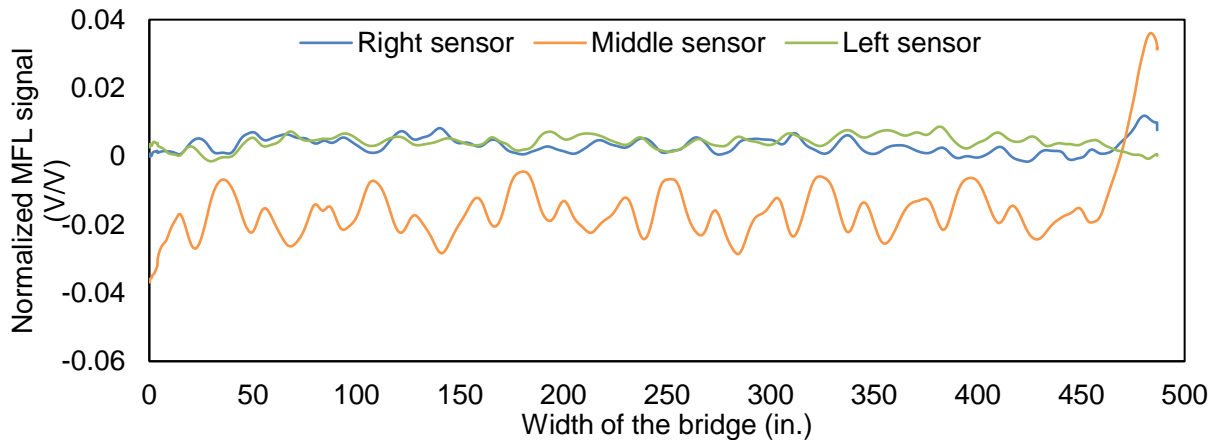


Figure 5-6: Test result of II-S-1-1 (regular sensors).

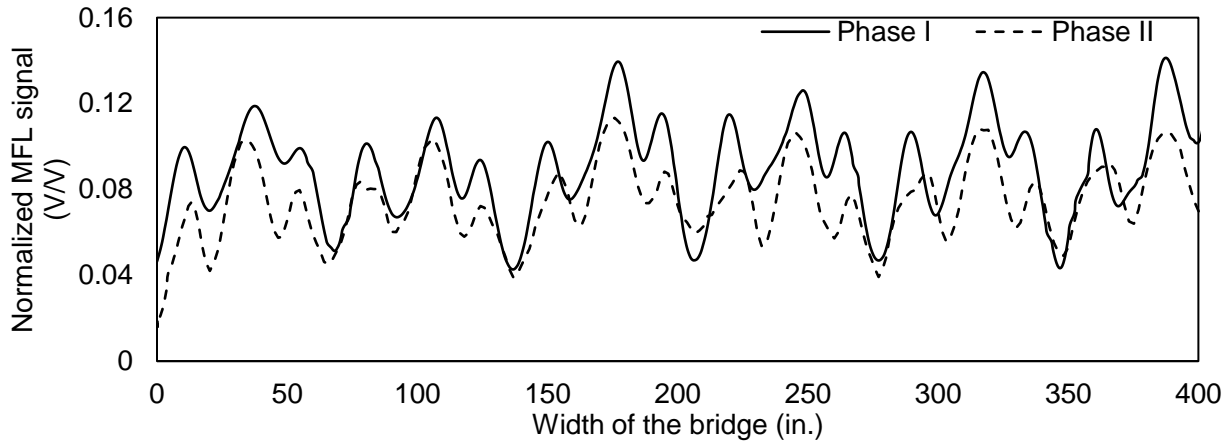


Figure 5-7: Comparison of MFL signal from phase I and phase II on span 1 tendon 1 (sensors with flux concentrator).

5.1.4.2 Span 1 – Tendon 2

The second tendon of first span was one of the tendons that was not magnetized in the two phases. The normalized signal taken with sensor with flux concentrators from both phases are shown in Figure 5-8. The magnitude of the signal is very low which is indicative of non-magnetized state of the tendon. This signal has not changed significantly between the two testing phases. The results from this tendon are inconclusive in detection of any anomalies as the signal magnitude is very small. Similar trends were observed in span 4 tendon 1, span 5 tendon 1, and span 5 tendon 2.

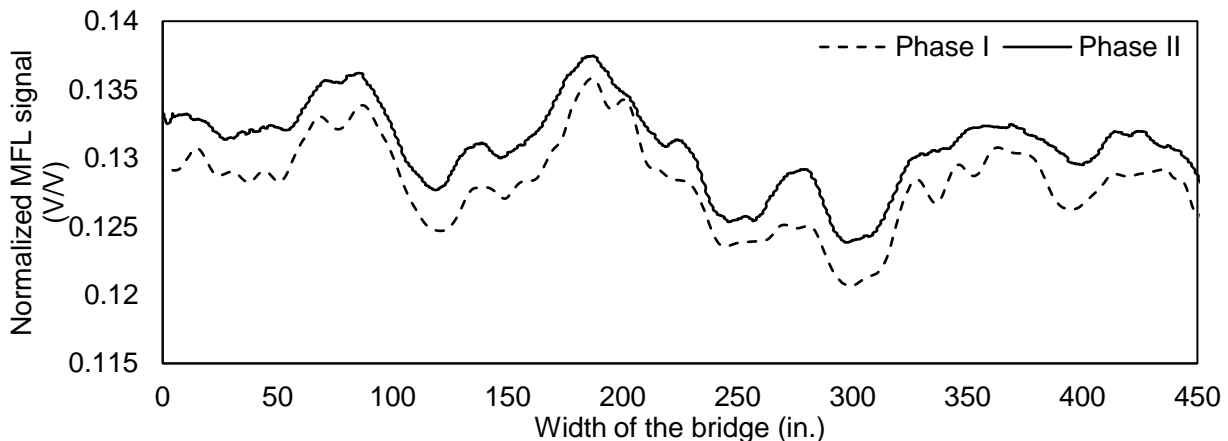


Figure 5-8: Comparison of MFL signal from phase I and phase II on span 1 tendon 2.

5.1.4.3 Span 2 – Tendon 1

A periodic inspection of the bridge in 2019 identified a failed PT rod which was replaced. Although new, the PT rod was magnetized from the bottom. The results of the measurement from the top of the bridge are plotted in Figure 5-9. The right and left sensors on the prototype unit are located 16 in. from the strand. The signal generated at these locations are indicative of a typical defect signal which is in fact a location of discontinuity of transverse stirrups from one slab unit to the next (marked by dotted red line). The signal from the middle sensor shows a minor amplitude when compared to the

other sensors. The tendon is currently in good condition and the signal does not show in anomalies.

Similar conclusions can be made from test II-S-2-2 on span 2 tendon 2. This tendon was also replaced in 2011 and it is fairly in a good condition. The results from this test is included in appendices.

Span 3 tendon 1 also has similar signal measurement. This tendon as well as the two tendons on span 2 was magnetized from the bottom during the second phase, but the signal has low amplitude and no further conclusions can be made on the condition of the tendon.

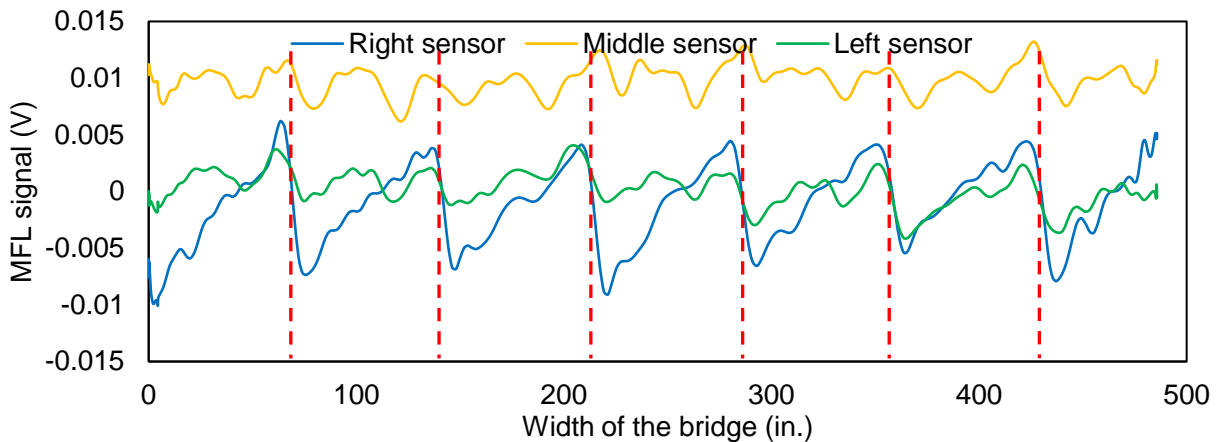


Figure 5-9: Test result of II-S-2-1 (regular sensors).

5.1.4.4 Span 3 – Tendon 2

This tendon was one of the tendons that was magnetized in the second phase from the bottom. A peak signal with high magnitude was observed at around 220 in. distance along the width of the bridge (Figure 5-10). Although there is a possibility of an anomaly at this location, this location coincides with the end of the panel.

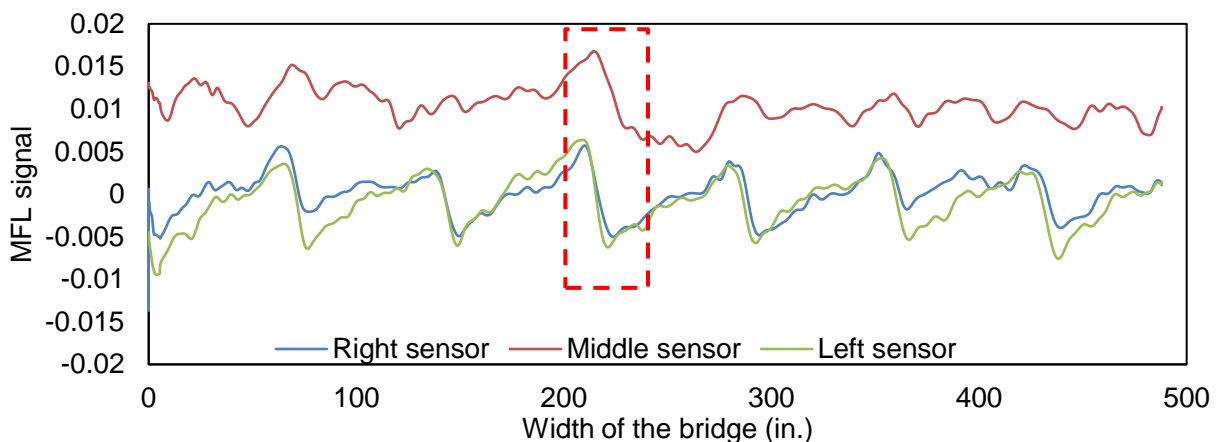


Figure 5-10: Test result of II-S-3-2 (regular sensors).

The end of the panels can be observed by peak-and-valley signal on right and left sensor signal. An out of place steel in the panel on the left of this location could make such peak, and absence of the steel in the right panel can obscure the valley. However, water can

leak between the panels into the PT duct and this location might be a possible location of corrosion initiation.

5.1.4.5 Span 4 – Tendon 2

Testing on unmagnetized rod was carried out on span 4 (test I-S-4-2). The results showed a peak and valley curve at the mid-distance of the plot shown in Figure 5-11. Although the tendon was not magnetized the magnitude of the disturbance in the signal is significant and indicated an anomaly at this location. The anomaly could be due to presence of corrosion, a coupler, or an out of place secondary reinforcement or steel.

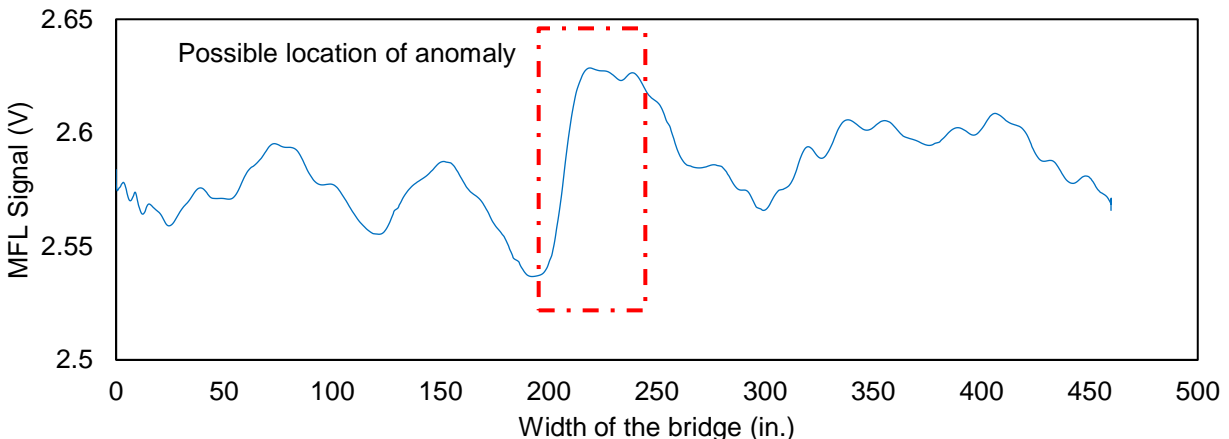


Figure 5-11: MFL signal of unmagnetized PT rod 2 (test I-S-4-2).

In phase II, the same tendon was magnetized from the bottom. Figure 5-12 shows line scans of the PT rod-2 in span-4 (II-S-4-2). The MFL measurement was performed from the top slab. Results are plotted for three sensors located in the middle and at the ends of prototype unit 3. The sensors at the ends are 16 in. away from the centerline of PT rod. The results of right and left sensors show a series of periodic peaks and valleys which are attributed to discontinuity of mild reinforcement when traversing from one slab unit to the next. The middle sensor is located directly on the top of PT rod.

The magnetization was performed exactly under the tendon location, so the scanned line 16 in. away from tendon (right and left sensors) should have a similar shape. This can be observed on some locations similar to the light blue dashed square highlighted in Figure 5-12. The disturbances on the main signal (middle sensor) may be an indicator of anomalies in the tendon. However, the presence of secondary reinforcement will also induce disturbance to the signal. It is important to compare the three lines to reach conclusions. For instance, the dark blue square highlighted in the graph shows a disturbance in the main signal. If the side signals at this location are compared to the light blue square, the disturbance can be seen in the difference between the two side signals. This may indicate that the change in the main signal is due to a secondary steel which affects all 3 signals. Also, the location of this disturbance on the signal (dark blue dashed square) is exactly at between two panels. This may indicate an out of place mild reinforcement which is parallel to the main tendon and is very close to the tendon (middle sensor) and top of the slab, which produces such signal at that location.

The line graph shows an anomalous signal at about 260 in. This location is not coincident with the end of a slab panel and it may be worthy to further investigate the location.

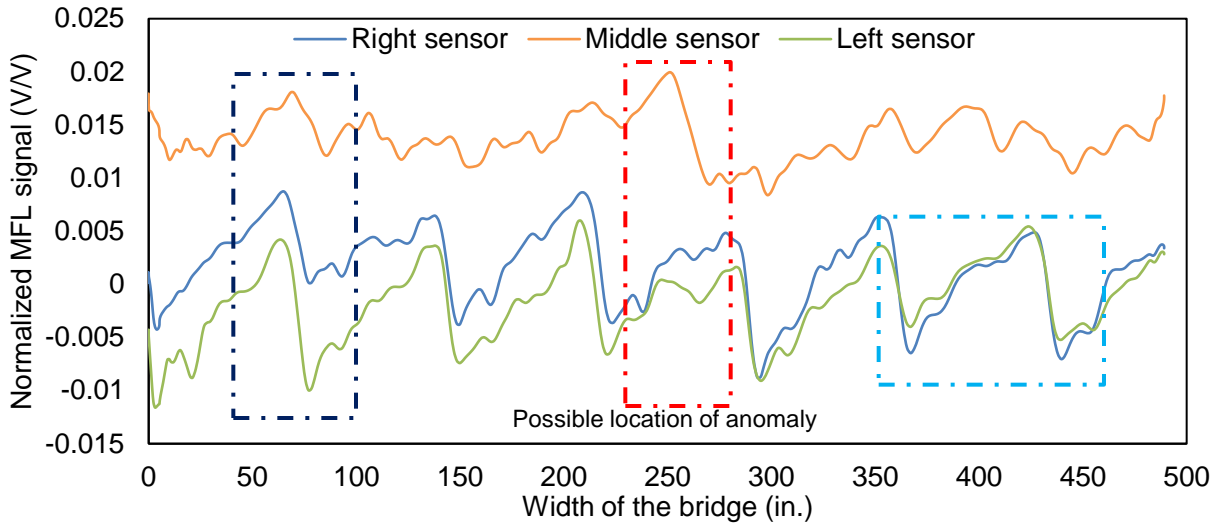


Figure 5-12: MFL signal of tendon magnetized from the bottom (test II-S-4-2).

The line measurements from all 32 sensors of prototype unit were used to regenerate the line graph as a surface scan plot. The surface scan provides a two-dimensional contour for the scanned area as shown in Figure 5-13. The transition from lighter to darker bands along the width of the bridge are indicative of slab panel discontinuities. The location of the anomaly shown in the line signal (Figure 5-12) can also be observed in this figure, as the pattern of the signal in the panels are changing. The signal at this location shows both lighter and darker signal, which is indication of bigger change in the signal. The dashed lines show the precast panels.

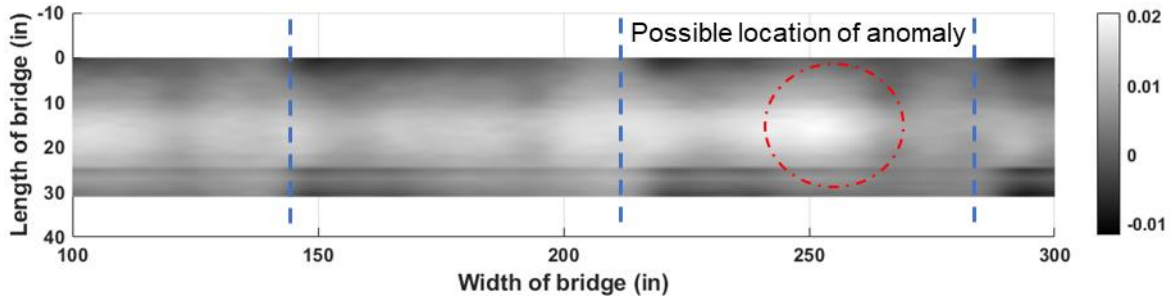


Figure 5-13: Surface scan of S-4-2.

Figure 5-14 shows the comparison of the two signals measured before (phase I) and after (phase II) magnetization. As can be seen, the disturbance in the signal occurs in the same location before and after magnetization. This strengthens the conclusions made above.

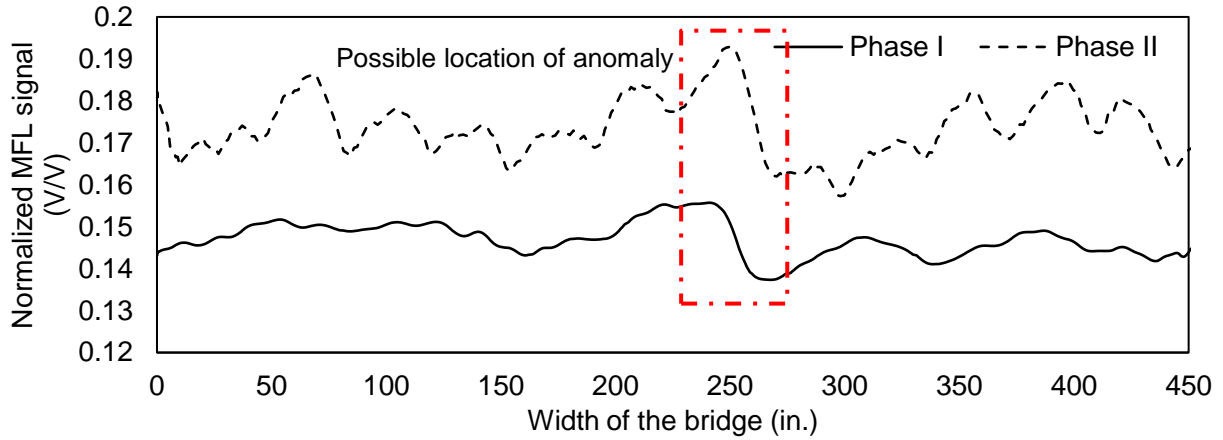


Figure 5-14: Comparison of MFL signal from phase I and phase II on span 4 tendon 2.

5.1.4.6 Area Scans

In phase I and II, a total of eight locations were magnetized. Among these, five PT rods were magnetized from the bottom, one rod was magnetized from the top and another top magnetization was carried out in between the two PT rods of span 1. The area scans of these five spans are shown below.

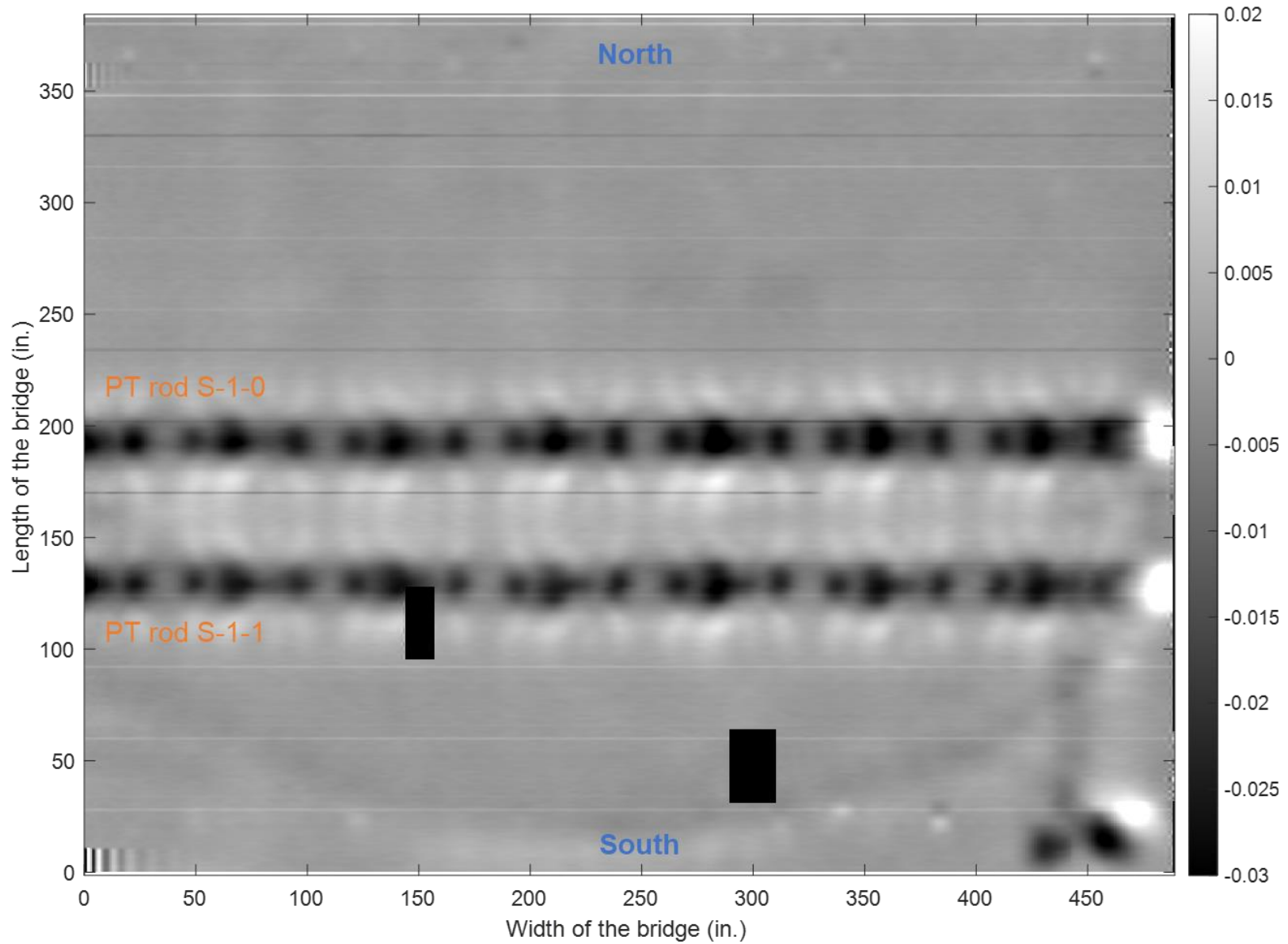


Figure 5-15: Area scan of span 1.

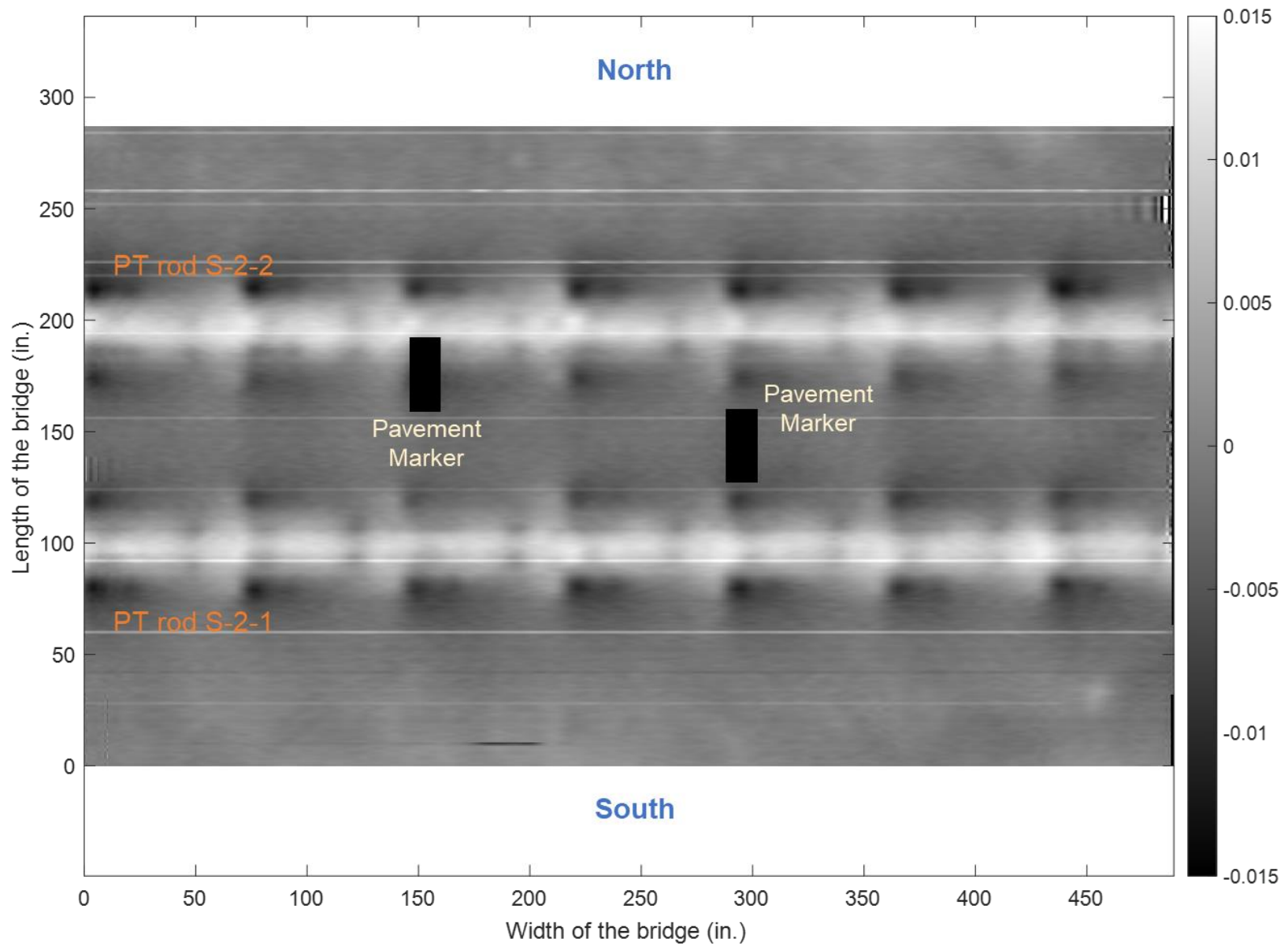


Figure 5-16: Area scan of span 2.

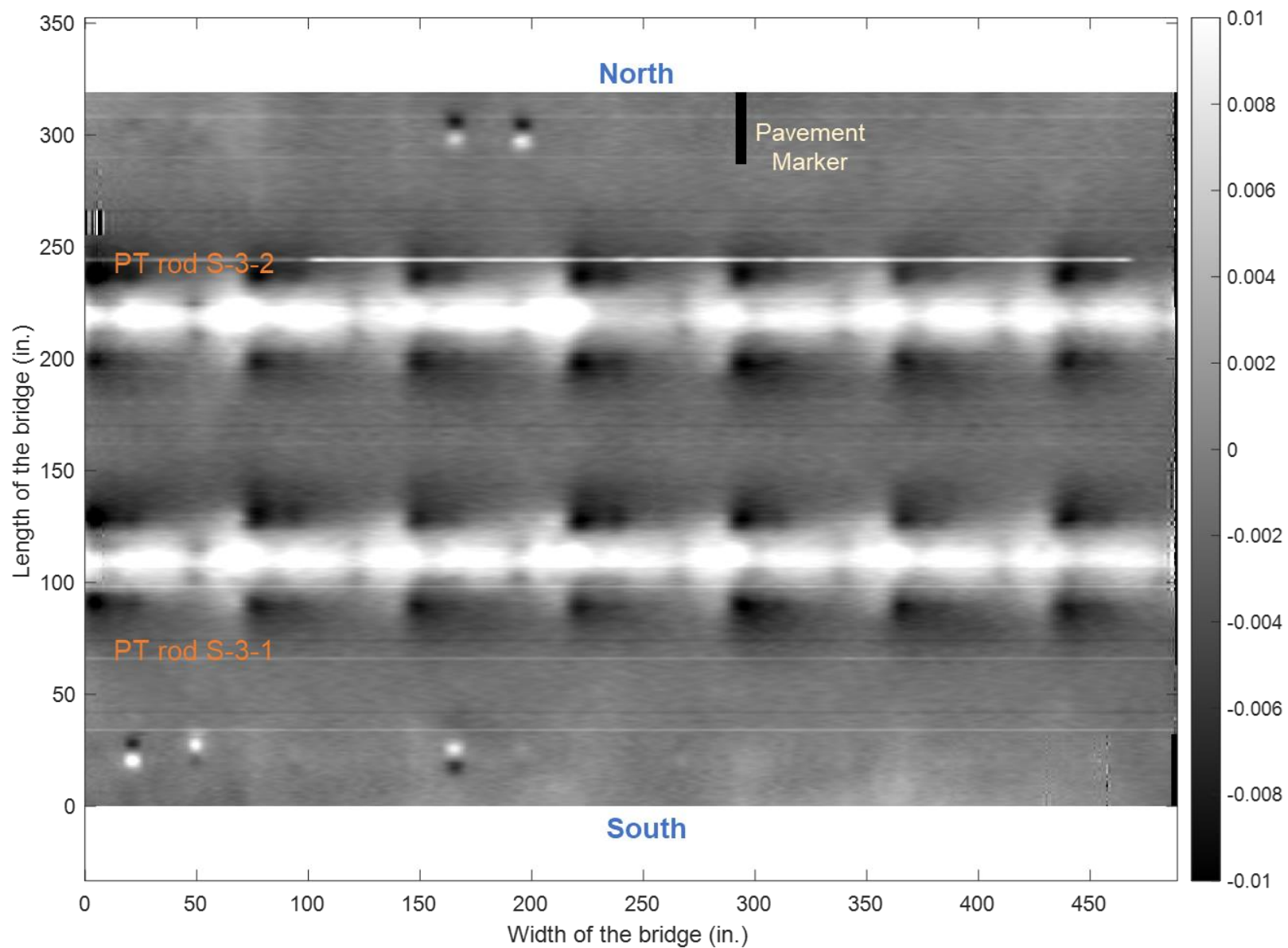


Figure 5-17: Area scan of span 3.

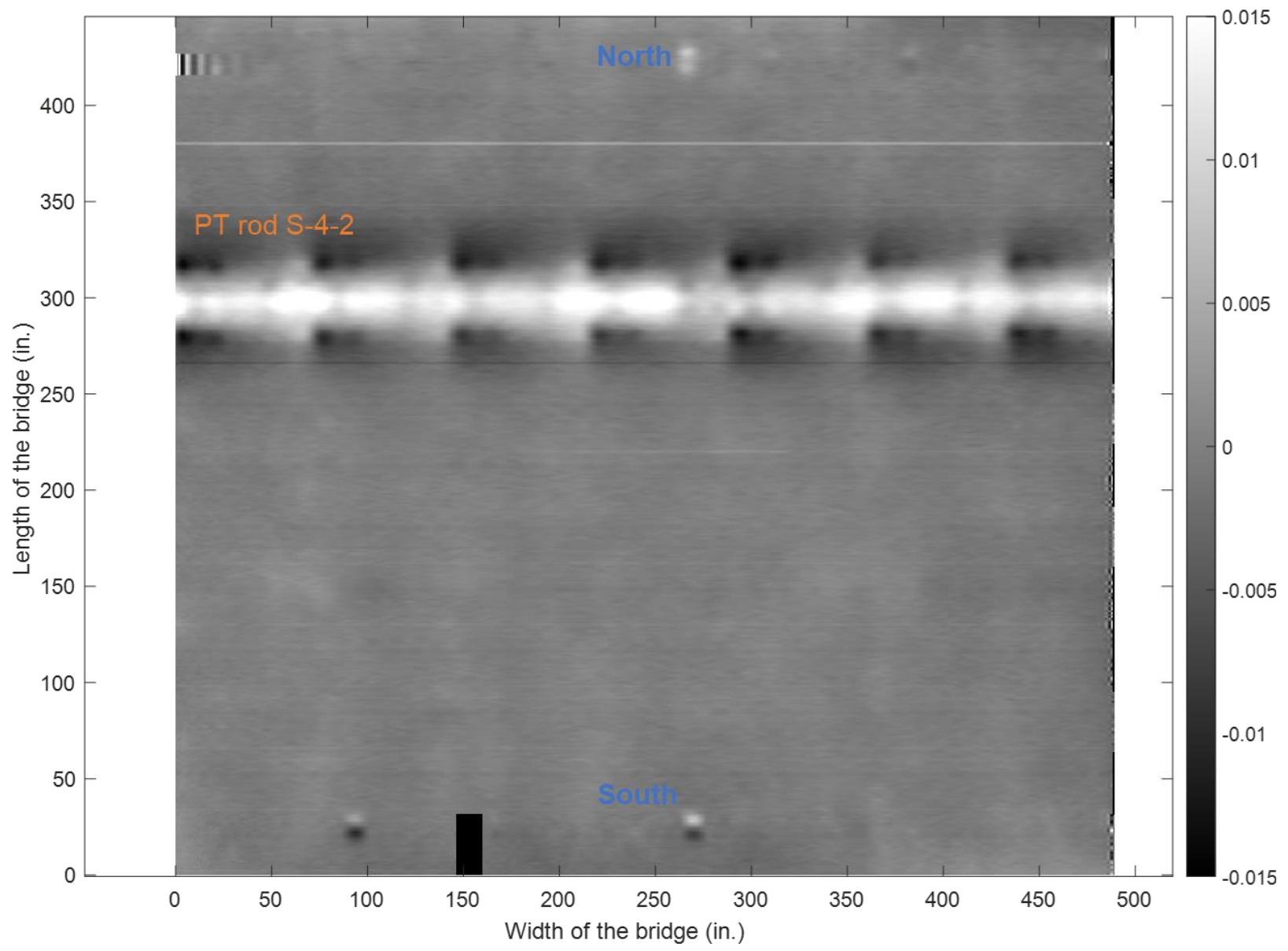


Figure 5-18: Area scan of span 4.

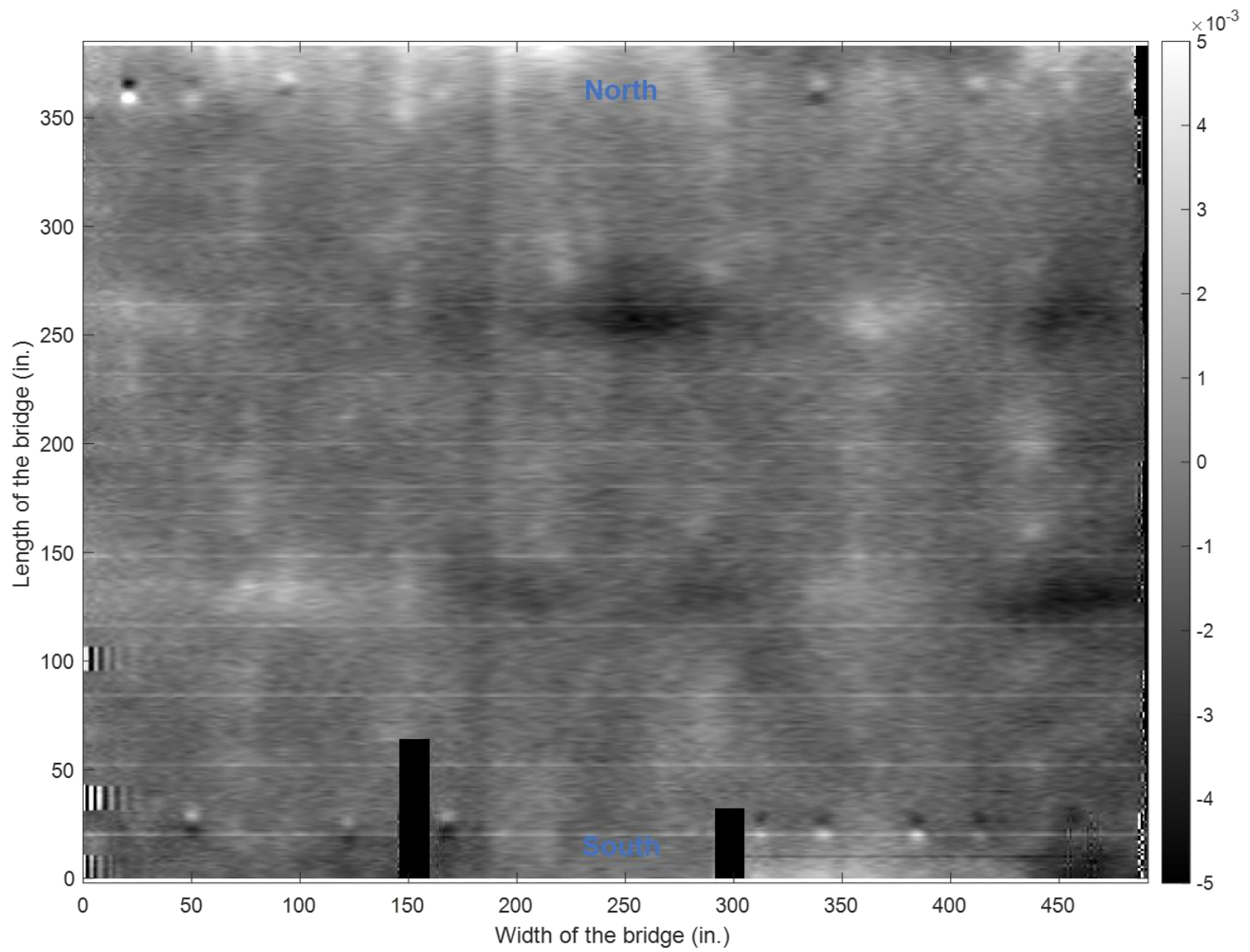


Figure 5-19: Area scan of span 5.

5.2 SUMMARY OF FIELD TESTING FOR BRIDGE A

Field testing was carried out on Bridge A which had been in service for more than 50 years. The bridge consisted of prefabricated sections of hollow slab with transverse reinforcement on the top and bottom. Two field testing were carried out on the subject bridge in June 2019 and August 2020. Testing was carried out on the PT rods located perpendicular to the direction of the traffic. The measurement of the signals was carried out from the top using the prototype units developed for this project. The phase I of the project provided a baseline signal with most of the readings taken without magnetization. The results of phase I indicated that the signals from the unmagnetized PT rods were mostly random. One of the tendons in span-1 (I-S-1-1) was magnetized from the top and the measurement showed that the peaks emanating due to the transverse reinforcement dominated the signal plot.

Following phase I, additional testing was carried out under phase II on a select number of tendons which were magnetized from the bottom. The magnetization was carried from the bottom using a floating barge and a sliding assembly. Prior installment of sliding assembly allowed robust and effective measurement of signals. This magnetization caused a change in magnetic field in the PT rods which provided a confirmation of the capability of the magnet (version 4) to saturate a ferromagnetic material embedded 9-in. inside the concrete. MFL readings on all PT rod were taken from the top. From a comparison of signals from phase I and phase II for the select tendons, showed that the bottom magnetization was able to saturate the PT rod. The PT rod (II-S-4-2) showed an anomalous signal at one location which may be indicative of corrosion, coupler, or a misplaced transverse reinforcement. The MFL measurement on the top magnetized rod (I-S-1-1) in phase I and phase II showed that the amplitude does not vary over a course of 14 months. The magnetization is retained over time unless otherwise affected with a disturbing magnetic field. This shows a promising tool for periodic inspection which can eliminate the need for magnetization of same tendon.

Area scans over the entire length of the bridge were carried out under phase III. Although the width of the magnet version 4 was 6 inches, the area plots showed a dispersion of magnetic field over an area about 5 feet wide. The results also showed that the MFL signal from magnetized PT rods can be distinguished in an area plot. The peak-and-valley in the line graphs for the bottom magnetized rods, which represented the discontinuity in the reinforcements of adjacent deck panels, appear intermittently as colored bands.

6 SUMMARY OF IMPORTANT FINDINGS AND CONCLUSIONS

This project was planned to be carried out in two phases. Original thinking was as follows:

“...This project will produce full functional prototype equipment that will detect the condition of internal tendons. It is intended that the project will be executed in 2 phases. By the end of phase 1 functional equipment that can detect corrosion in internal tendons at a minimum depth of 8 inches from the top of the concrete will be developed. Phase 2 of the project will focus on investigating the possibilities of detection at greater depths and the development and fabrication of the prototype version of the equipment and a copy will be provided to FDOT...”

As a result, the objective of the project was to develop practical and effective magnetic NDT equipment for condition assessment of internal tendons and associated testing procedure. The MFL testing system has been identified as an effective magnetic method to detect section loss in metals. In bridge inspection, MFL method has been successfully implemented for detection of defects in external PT ducts, stay cables and near-surface tendons. However, the existing MFL technology has shown limited merit for internal PT tendons. This is primarily due to field challenges which impede the magnetization of the internal tendons. Contrary to external tendons which are near-surface and accessible, the internal tendons are generally embedded deep and are inaccessible. Also, there is mesh of reinforcement in the vicinity of the internal tendons which attenuates the magnetization process. Of foremost importance is the improvement of existing MFL technology that can induce a magnetic field in the embedded internal tendons and employing advanced sensing technologies which can measure the signals from potential defect locations.

Previous work at FIU showed promising results of MFL method for detecting metal loss in internal tendons. However, the reliability and success of the method was influenced by magnetization protocol and sensing system. Therefore, the first part of the project started by identification of deficiencies in existing MFL equipment; based on these findings, the existing system was modified and improved. Different configurations for permanent magnets were investigated which were practical and efficient for magnetizing internal tendons. A set of new modified magnets was fabricated with an improved geometrical configuration and advanced neodymium magnets. Similarly, the sensing system was improved using a new generation of Hall sensors. The goal of these modifications was to develop a fully functional prototype unit. To this end, a set of units was developed which housed all the main components of the MFL system. The units were designed to perform scans primarily on horizontal surfaces, but the system can be customized for other applications as well. The developed prototypes were designed for efficiency and portability during field operation.

Based on consultation with FDOT, a bridge (also referred to as the selected bridge) with known defect was selected as a test case for laboratory and numerical simulations. The subject bridge had been in service for more than 50 years and presented a test case which was used for laboratory mockup specimen and numerical study. The purpose of simulating bridge conditions in laboratory was to simplify the system and allow a better understanding of the effect of various parameters on the MFL signal.

Using the schematic drawings of the actual bridge, laboratory mock-up specimens were constructed. These tests were carried out on plywood units which were designed to accommodate longitudinal tendons or PT rods at different depths and spacing. New method of magnetization methodology was also developed where the magnetization was carried out from the near-surface and measurement was performed from the far-surface. Near-surface refers to the surface of the slab where the magnetization is performed.

The new methodology developed for laboratory specimens was extended to segments of a salvaged bridge located at FIU. These segments consist of a box girder section with empty ducts in top slab. Testing was carried out on these segments to validate the capabilities of the modified MFL system and demonstrate its effectiveness for internal tendons. Different magnetization depths were used and as expected, near-surface magnetization was more effective in saturating the strands. The percentage section losses of 10%, 55% and 100% in a group of strands were used for the tests. The strands were magnetized from the soffit of the box girder and measurement was taken from the top. The results showed that the 55% and 100% section loss were clearly identified but a 10% section loss was relatively obscured due to perturbances in the MFL signal.

The methodology adopted for laboratory and segment testing was extended to the selected bridge. The tests were carried out on PT rods on all five spans of the bridge. The objective of the testing was to establish a baseline signal which can be used in future to check the progression of any corrosion. The tests were carried out on PT rods on all five spans of the bridge in three phases. In the first phase, measurements were performed mainly on unmagnetized PT rods to establish a baseline signal. Due to limitations on the site, the top magnetization was carried out on only select rods in span 1. The top magnetization on rods in span 1 saturated the transverse reinforcement resulting in a signal with multiple perturbances. In phase II, support railings were installed on the underside of the bridge to allow near side magnetization. The results from this phase showed that the modified magnet was able to magnetize the embedded PT rods. Anomalous signals were obtained for rods in span 3 and span 4 which may be indicative of a defect, construction deficiency, or a bar coupler. In phase III, only measurements were performed without any additional magnetization. The results showed that the magnetization is retained over time and the results are repeatable.

To complement the laboratory and field tests, a numerical study was performed to study the parameters that affect the magnetic field. The study was carried out using Ansys Maxwell for passive sensing. The purpose of the study was to attempt to better understand the effect of the depth of magnetization, transverse reinforcement, and damage severity. The results showed that the depth of magnetization effects the development of the magnetic field in the rod. The damage in the rod was evident in results when no transverse reinforcement was present. However, when a transverse reinforcement was located in the vicinity of the rod, the behavior became complex. Finite element analysis was also carried out on the selected bridge superstructure configuration. To limit the computation time only a segment of the bridge was modeled with PT rod, transverse reinforcement, and ties. Different simulations were considered but results show that there is a complex interaction of various elements and valid conclusions could not be strangely drawn.

In summary this project has successfully resulted in development of a prototype functional equipment and associated procedure for inspection of internal tendons, as Phase I of the investigation.

6.1 FUTURE RESEARCH

As mentioned before the original thinking in undertaking this project was as follows:

“...This project will produce full functional prototype equipment that will detect the condition of internal tendons. It is intended that the project will be executed in 2 phases. By the end of phase 1 functional equipment that can detect corrosion in internal tendons at a minimum depth of 8 inches from the top of the concrete will be developed. Phase 2 of the project will focus on investigating the possibilities of detection at greater depths and the development and fabrication of the prototype version of the equipment and a copy will be provided to FDOT.”

As described in this report, extensive efforts, were carried out and needed experiments, some beyond, what originally promised in the proposal were carried out to develop an effective complete system for inspection of internal tendons. The very challenging objectives of the project were achieved, and fully functional prototype MFL equipment and associated testing procedure is now developed.

It is highly recommended to extend to start immediately the Phase II of the project with following objectives:

- Develop user friendly field magnetization method.
- Develop more robust system for handling heavy magnet needed for field testing, during magnetization.
- Further evaluate the length of time that magnetization can remain in the tendons. This will greatly reduce inspection of internal tendons.
- For Bridge A continue taking additional MFL signals to study long term changes in MFL signals. It is important to note that first magnetization of tendons for Bridge A was carried out in August 2020.
- Select one additional bridge, preferably for one of the spans for bridges between Miami and Key west and further assess the merits of the MFL technology developed under this project for assessing steel strands embedded within internal tendons.
- Complete the development of prototype equipment that is professional level, as originally envisioned.

REFERENCES

- Alpin Technik Leipzig. Accessed online 2020. <http://www.alpintechnik.de/>.
- Azari, H., Ghorbanpoor, A. and Shams, S. (2020). *Development of Robotic Nondestructive Testing of Steel Corrosion of Prestressed Concrete Bridge Girders using Magnetic Flux Leakage System*. Transportation Research Board, 99th Annual Meeting, Washington DC.
- Azizinamini, A. and Gull, J. (2012). *Improved inspection techniques for steel prestressing/post-tensioning strand: Volume I*. Department of Civil and Environmental Engineering, Florida International University, Miami, Florida.
- Azizinamini, A. and Atorod (2017). *Non-destructive testing (NDT) of a segmental concrete bridge scheduled for demolition, with a focus on condition assessment and corrosion detection of internal tendons*. Department of Civil and Environmental Engineering, Florida International University, Miami, Florida.
- Bozorth, R.M. (1993). *Ferromagnetism*. Wiley-IEEE Press.
- Chase, S.B. and Balakumaran, S.S. (2020). *Magnetic Flux Leakage Device for Evaluation of Prestressed Concrete Box Bridges*. Virginia Transportation Research Council, Charlottesville, VA.
- Corven Engineering Inc. (2002). *New Directions for Florida Post-Tensioned Bridges. Volume 1 of 10: Post-Tensioning in Florida Bridges*. Florida Department of Transportation, Tallahassee, Florida.
- Corven, J. and Moreton, A.J. (2013). *Post-tensioning tendon installation and grouting manual*. FHWA-NHI-13-026. Federal Highway Administration (US).
- Dammika, A.J., Sheharyar, R., Takanami, R., Yamaguchi, H. and Matsumoto, Y. (2014). *An investigation on modal damping ratio as an indicator of invisible damage in PC bridges*. Life-Cycle of Structural Systems: Design, Assessment, Maintenance and Management.
- DaSilva, M., Javidi, S., Yakel, A. and Azizinamini, A. (2009). *Nondestructive method to detect corrosion of steel elements in concrete*. Nebraska Department of Transportation Research Reports 81.
- Elyasigorji, A. and Ghorbanpoor, A. (2021). *Magnetic Flux Leakage Signal Characterization for Detection of Corrosion in Prestressed Concrete Girders*. Transportation Research Board, 100th Annual Meeting, Washington DC.
- Elyasigorji, A., Rezaee, M. and Ghorbanpoor, A. (2020). *Characterization of Corrosion in PS Concrete Girders by Correlation Analysis*. In Structures Congress 2020: American Society of Civil Engineers, Reston, VA.
- GangaRao, H.V. (1995). *Nondestructive Testing Methods for Civil Infrastructure*. American Society of Civil Engineers.
- Karthik, M.M., Terzioglu, T., Hurlebaus, S., Hueste, M.B., Weischedel, H. and Stamm, R. (2019). *Magnetic flux leakage technique to detect loss in metallic area in external post-tensioning systems*. Engineering Structures.
- Lau, K., and A. Azizinamini. (2018). *Development of quality assurance and quality control system for post-tensioned segmental bridges in Florida: Case of ringling bridge—Phase II*. Department of Civil and Environmental Engineering, Florida International University, Miami, Florida.
- Lenz, J. and Edelstein, S. (2006). *Magnetic sensors and their applications*. IEEE

Sensors Journal.

- Popovic, R.S. (2003.) *Hall effect devices*. CRC Press.
- Poursaee, A. (2016). *Corrosion of steel in concrete structures. In Corrosion of steel in concrete structures*. Woodhead Publishing.
- Raj, B., Jayakumar, T. and Thavasimuthu, M. (2002). *Practical non-destructive testing*. Woodhead Publishing.
- Sadeghnejad, A., Valikhani, A., Chunn, B., Lau, K. and Azizinamini, A. (2017). *Magnetic Flux Leakage Method for Detecting Corrosion in Post Tensioned Segmental Concrete Bridges in Presence of Secondary Reinforcement*. Transportation Research Board, 96th Annual Meeting, Washington DC.

APPENDIX A DETAILS OF FIELD BRIDGES

A.1 BRIDGE A DETAILS

A known, tendon failure within a Bridge A provided an opportunity to investigate an actual structure. The selected bridge was located in Florida. The five-span bridge consist of prestressed concrete hollow core slabs in each span. The hollow core concrete slabs were pre-tensioned longitudinally with pre-tensioning strands and transversely by using two PT rods in each span, as shown in Figure A-1. The PT rods were located at a depth of 10.5 in. in the roadway portion and 12 in. on the footpath section. The pre-tensioning strands in the deck were located at a depth of 4.5 in. and at 7 in. c/c distance from the top.

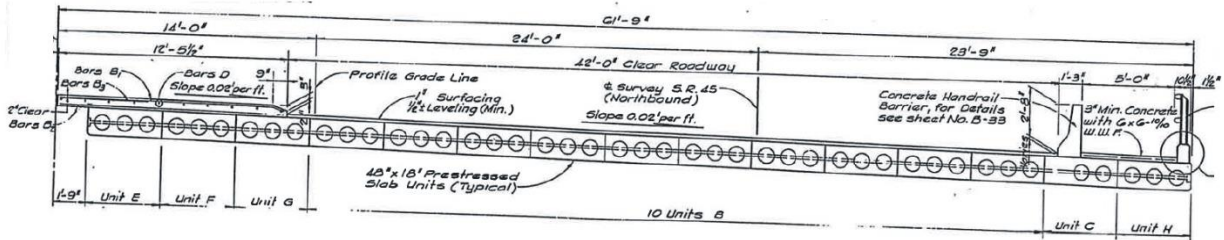


Figure A-1: Bridge A section through superstructure.

A.2 BRIDGE B DETAILS

Bridge B consist of a precast segmental single box girder bridge located at Florida. The section of the abutment span for Bridge B is shown in Figure A-2. A major part of the bridge structure is elevated and crosses a waterway which hindered the assembly of a support mechanism on pier spans. However, one of the abutment spans of the southbound bridge was partially accessible from the bottom and testing was carried out on a limited number of tendons located in the bottom slab. Prior to MFL testing, GPR was used to locate the exact position of tendons.

GPR is a non-invasive NDT technique that is commonly used to locate reinforcement and tendons in bridges. The method emits a pulsed electromagnet energy into a subsurface which is partly reflected which is evaluated by the GPR. It is a contactless technique and allows surface measurement at a fast rate. Depending on the use, most of the commercially available equipment can carry out both line scans and grid scans. The equipment generally consists of a sensor head and a computer to process the data.

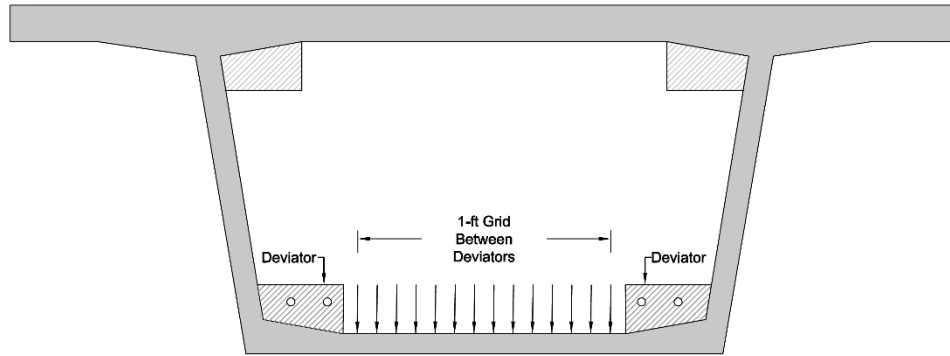


Figure A-2: Details of Bridge B.

The MFL measurement was preceded by GPR to precisely locate the tendons in the bottom slab. These measurements were taken from both the top and bottom of the slab. The first test was carried out underneath the bridge using area scan on a grid of 88 in. x 12 in. The test results from underneath the bridge is shown Figure A-3.

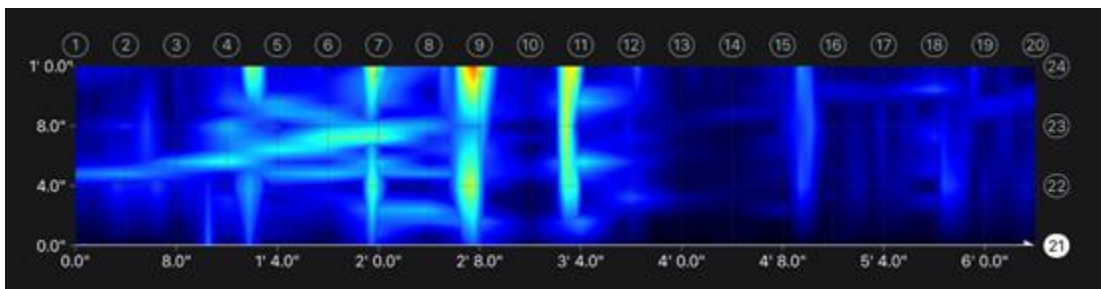


Figure A-3: GRP result for a depth of 3 in.–6 in.

The tendon locations are manifests on the plot as bright lines. However, a more reliable estimate of the location can be seen in a line view which is shown in Figure A-4.

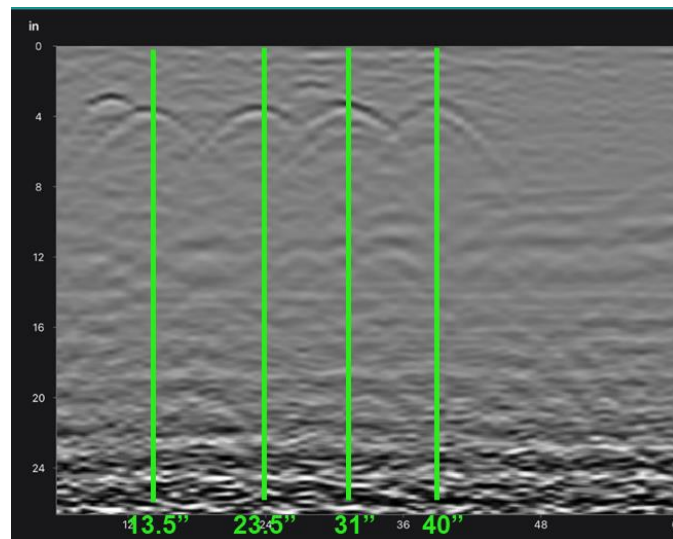


Figure A-4: GRP result for the line scan.

In addition to GPR testing from the bottom, additional measurements were made from inside the box girder. The test was carried out inside the bridge using area scan on a grid of 44 in. x 12 in. The test results are shown in Figure A-5.

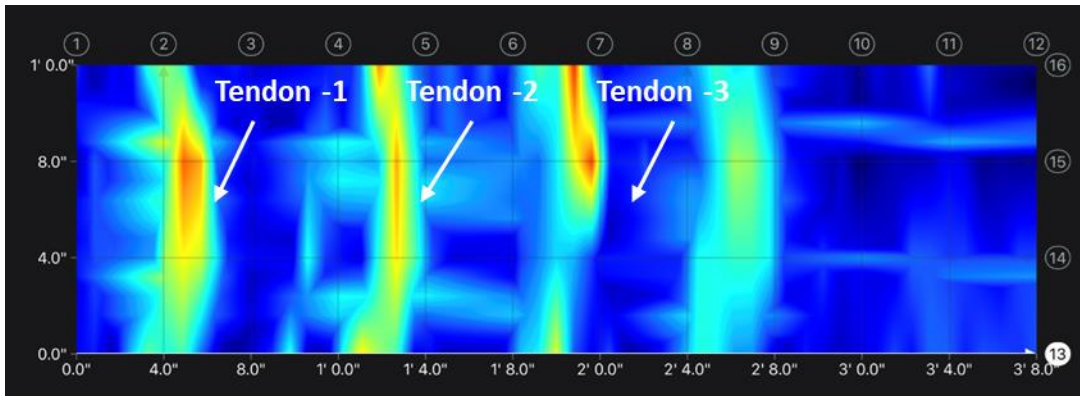


Figure A-5: GPR test inside bridge for a depth of 3 in.–6 in.

The location of tendons can be clearly seen in line scan shown in Figure A-6.

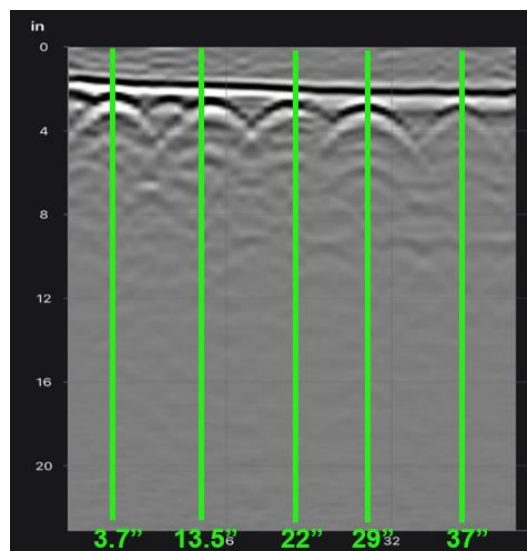


Figure A-6: GPR result for area scan of 44 in. x 12 in.

The GPR test results showed strong signals at three tendon locations and one obscure signal which is possibly an empty duct. These locations were marked on slab surfaces and subsequently used for magnetizing and MFL measurement.

A.3 BRIDGE SEGMENT DETAILS

An in-service bridge was scheduled for demolition due to necessary changes required for additional runway at the Fort Lauderdale Airport. The superstructure of the three-span bridge consisted of pre-cast segmented continuous box girder. Sequential demolition procedure was performed using a diamond impregnated cable wire saw to cut the bridge segments that were then removed by crane. The decommissioned bridge segments were transported to FIU to be used as a test bed. The bridge segments are shown Figure A-7.



Figure A-7: Decommissioned box girder segments at FIU.

These decommissioned bridge segments provided an opportunity to perform NDT tests which closely replicate field conditions. MFL testing was carried out on empty ducts located in the top slab of the box girder. The empty ducts allowed simulation of different controlled damage scenarios of PT tendons as shown Figure A-8.

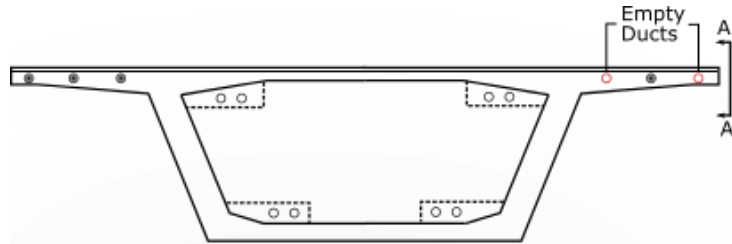
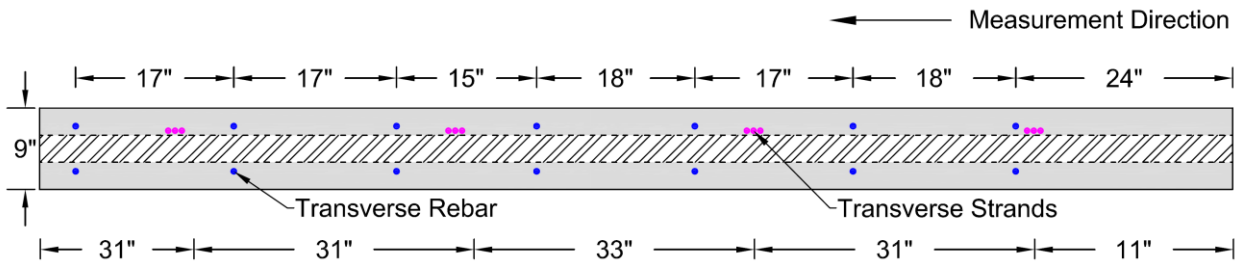


Figure A-8: Empty ducts for testing.

In the top slab, there were top and bottom reinforcements that were perpendicular to the tendon ducts and were located intermittently along the length of the segment. In addition, there were bundled strands located transversely to the continuity tendon ducts. The location of these transverse reinforcements (9 No.) and tendons (3 No.) are shown in Figure A-9. Testing was carried out on the bridge segment to validate the capability of the modified MFL system and demonstrate its application to identify strand metal loss in internal tendons.



Section of Bridge Segment

Figure A-9: Location of transverse reinforcement and bundled strands in bridge.

APPENDIX B FIELD TESTING RESULTS

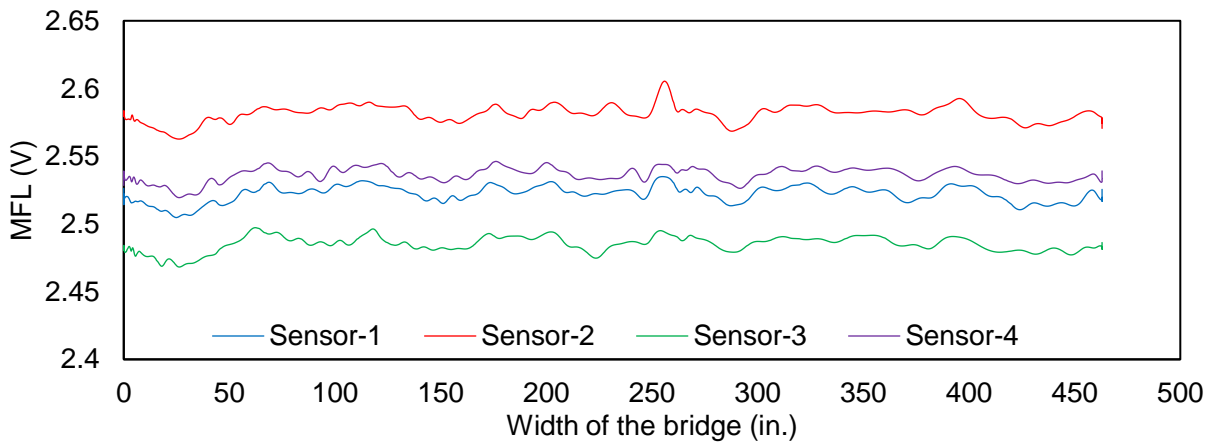
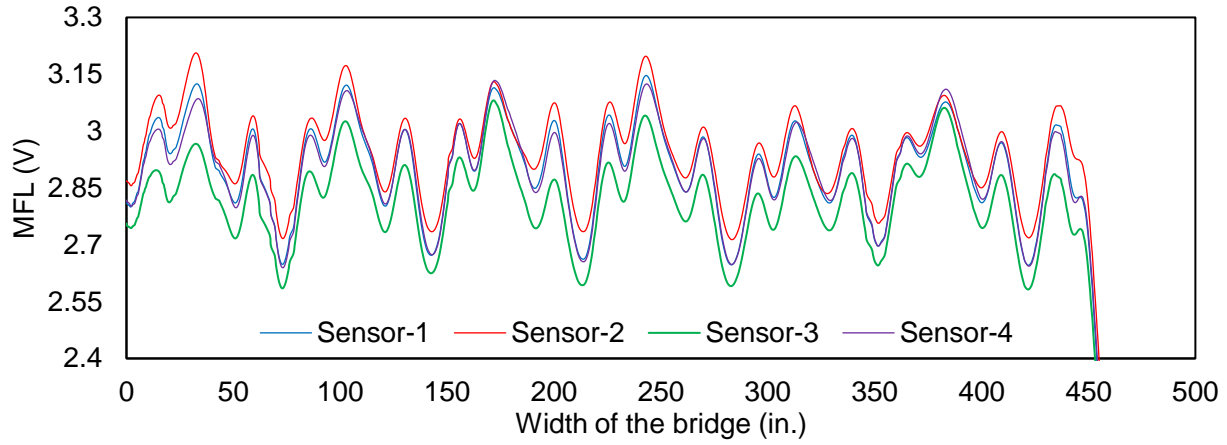
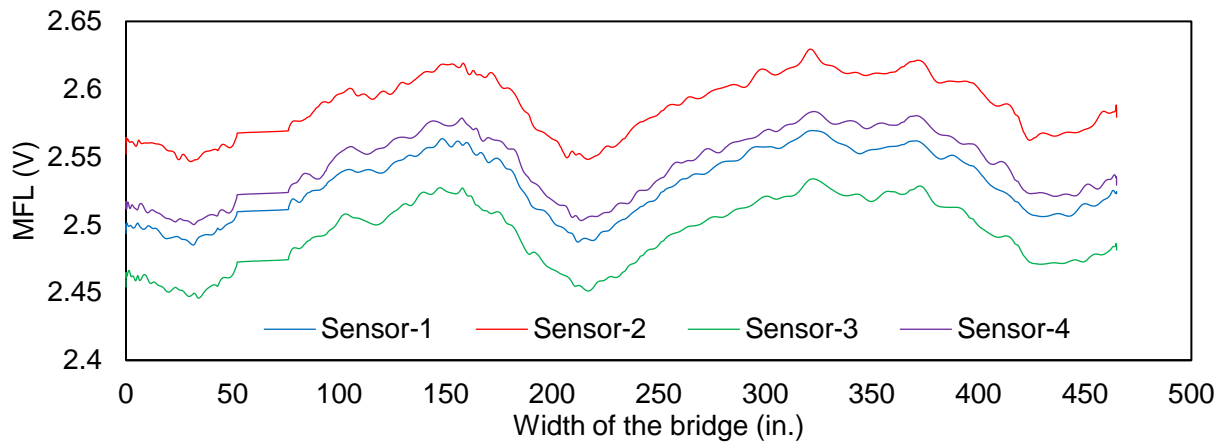
B.1 BRIDGE A PHASE I TESTING

For phase I, the testing was carried out on locations of all PT rods. All measurements were performed from the top of the bridge segment along the length of the PT rod. Table B-1 shows the details of tests conducted in all five spans of the field bridge. The test numbers are named by a four-letter name representing the test phase, bridge, span number and tendon number. PT rod 0 refers to reading taken midway between the rods of the subject span. Experimental measurement unit with four sensors was used for the testing and results are plotted for all four sensors.

Table B-1. Bridge measurement details

Test No.	Span No.	PT Rod No.	Magnetization Condition
I-S-1-1	Span 1	1	No Magnetization
I-S-1-1m	Span 1	1	Top Magnetized
I-S-1-0	Span 1	0	No Magnetization
I-S-1-2	Span 1	2	Magnetized
I-S-2-1	Span 2	1	No Magnetization
I-S-2-0	Span 2	0	No Magnetization
I-S-2-2	Span 2	2	No Magnetization
I-S-3-1	Span 3	1	No Magnetization
I-S-3-0	Span 3	0	No Magnetization
I-S-3-2	Span 3	2	No Magnetization
I-S-4-1	Span 4	1	No Magnetization
I-S-4-0	Span 4	0	No Magnetization
I-S-4-2	Span 4	2	No Magnetization
I-S-5-1	Span 5	1	No Magnetization
I-S-5-0	Span 5	0	No Magnetization
I-S-5-2	Span 5	2	No Magnetization

For span 1, magnetization from the top surface was carried out for PT rod 1 using magnet version 04. The measurement of the signal was also carried out from the top surface. For rest of the test segments, no magnetization was carried out. The objective of taking measurement between the two PT rods was to see the effect of transverse reinforcement only. Test results for all cases are presented in following sections. Note: all the results in this section are from regular sensors without flux concentrators.



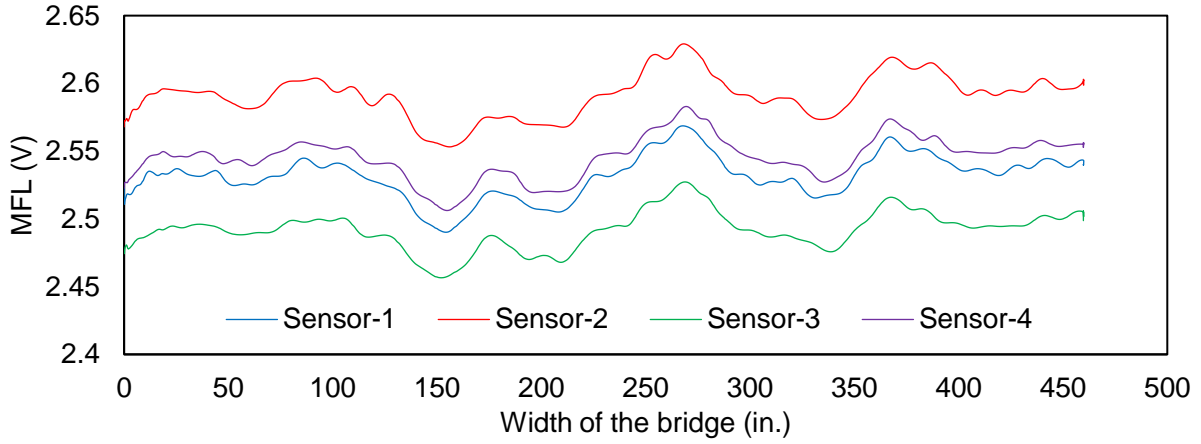


Figure B-4: Span 1, PT rod 2 (test I-S-1-2).

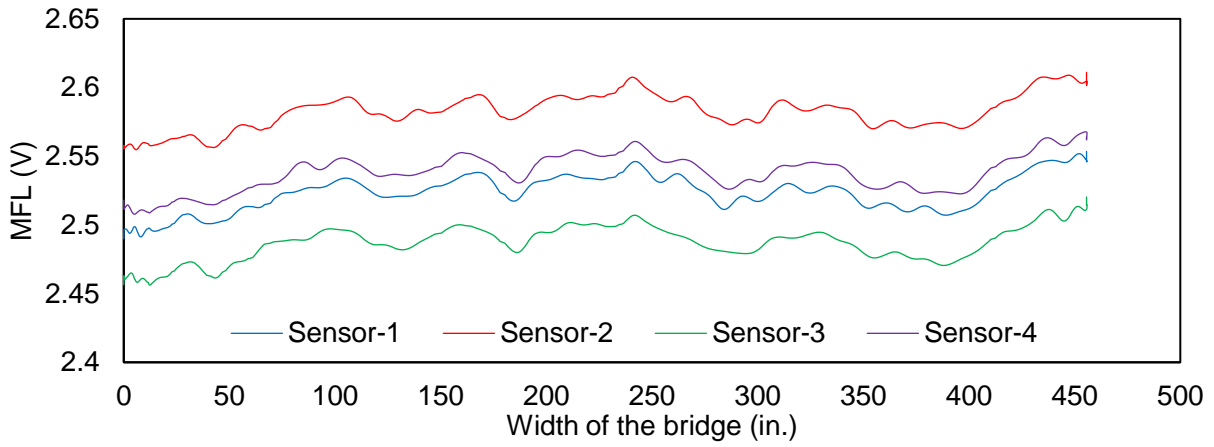


Figure B-5: Span 2, PT rod 1 (test I-S-2-1).

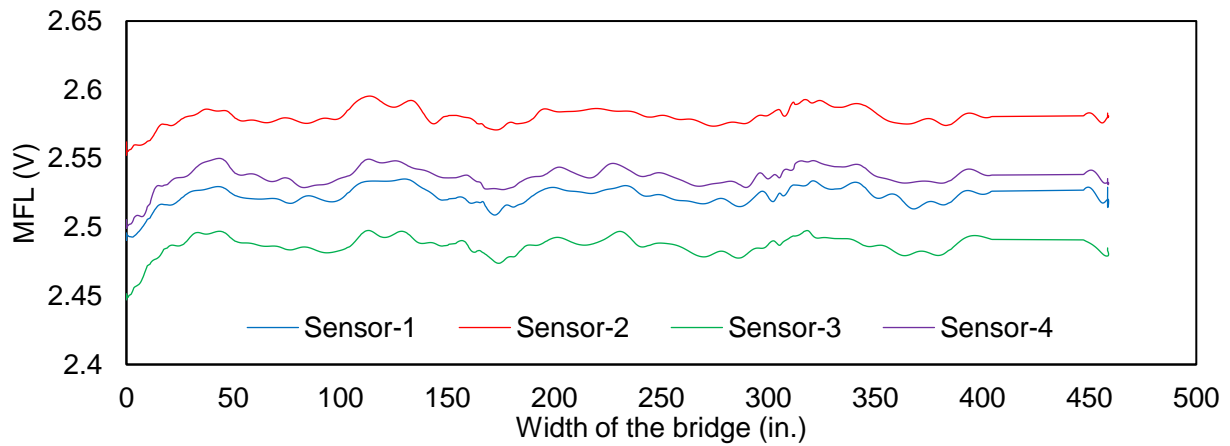
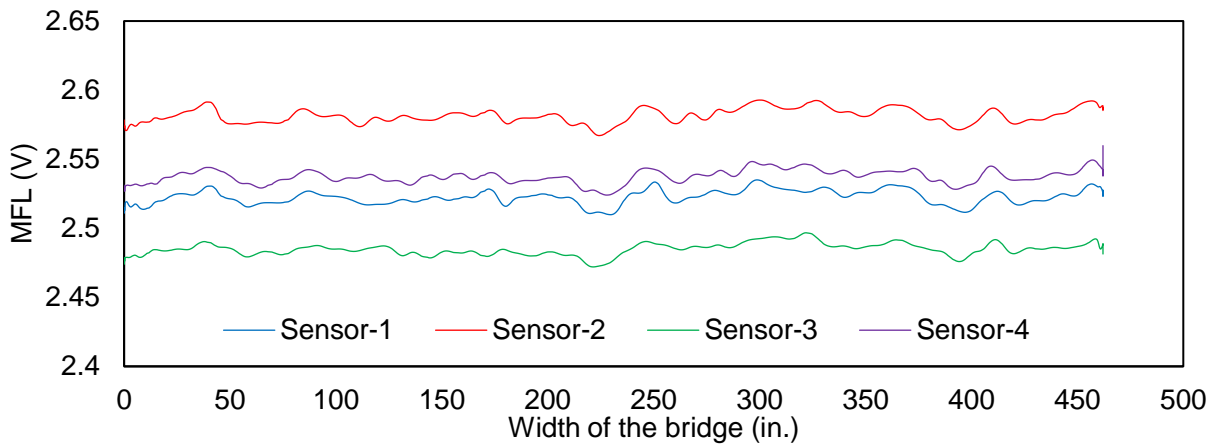
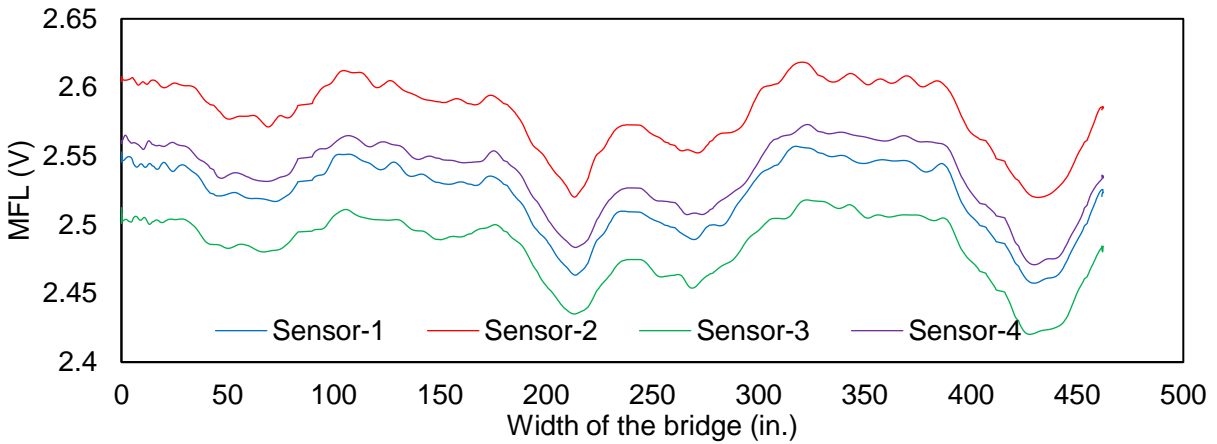
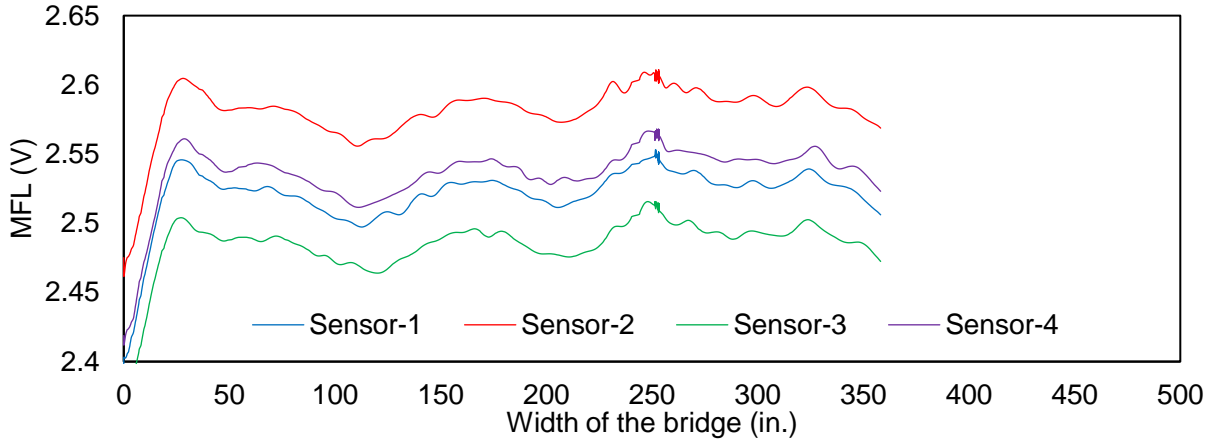


Figure B-6: Span 2 between PT rods (test I-S-2-0).



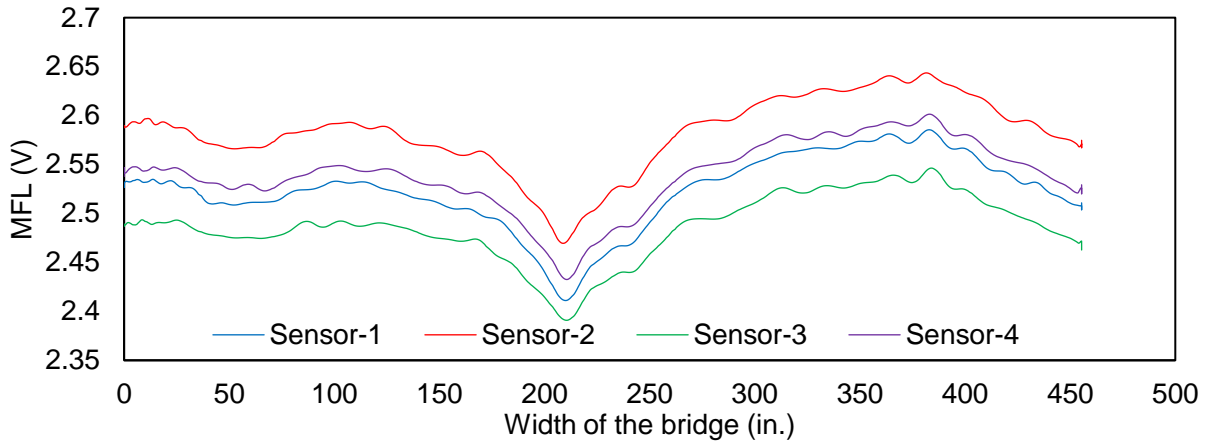


Figure B-10: Span 3, PT rod 2 (test I-S-3-2).

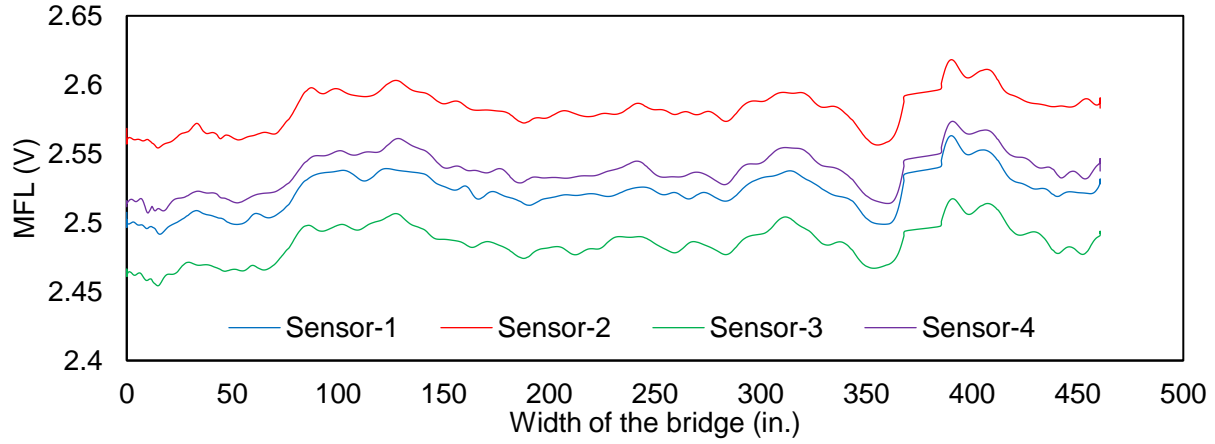


Figure B-11: Span 4, PT rod 1 (test I-S-4-1).

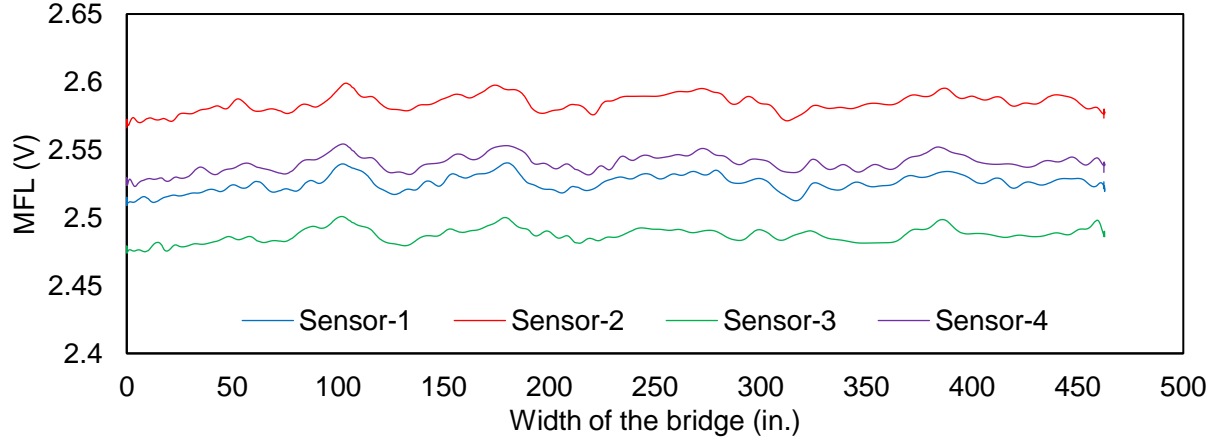


Figure B-12: Span 4 between PT rods (test I-S-4-0).

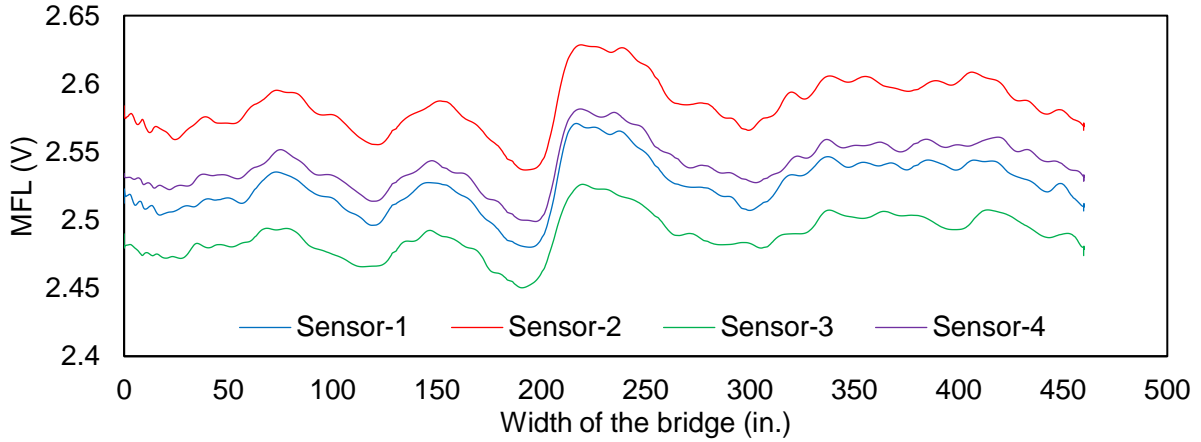


Figure B-13: Span 4, PT rod 2 (test I-S-4-2).

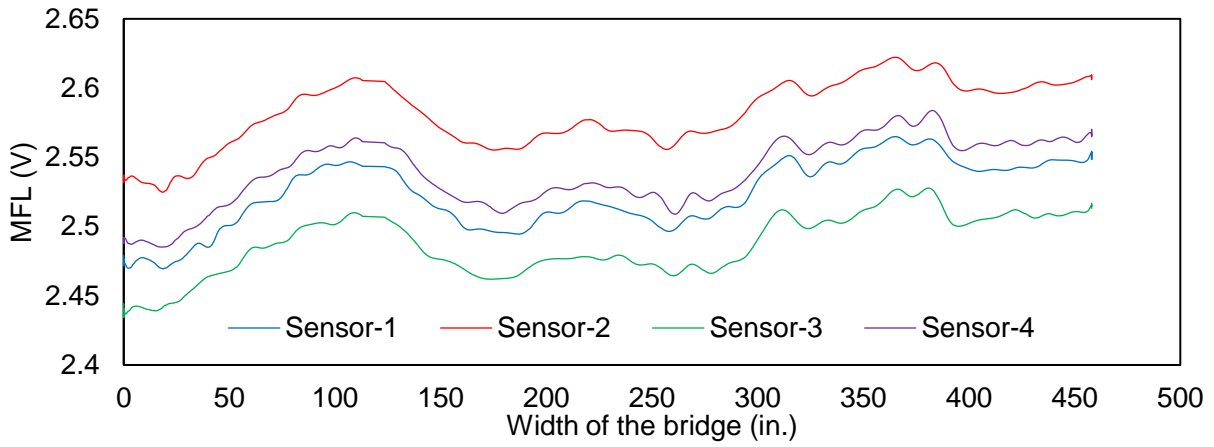


Figure B-14: Span 5, PT rod 1 (test I-S-5-1).

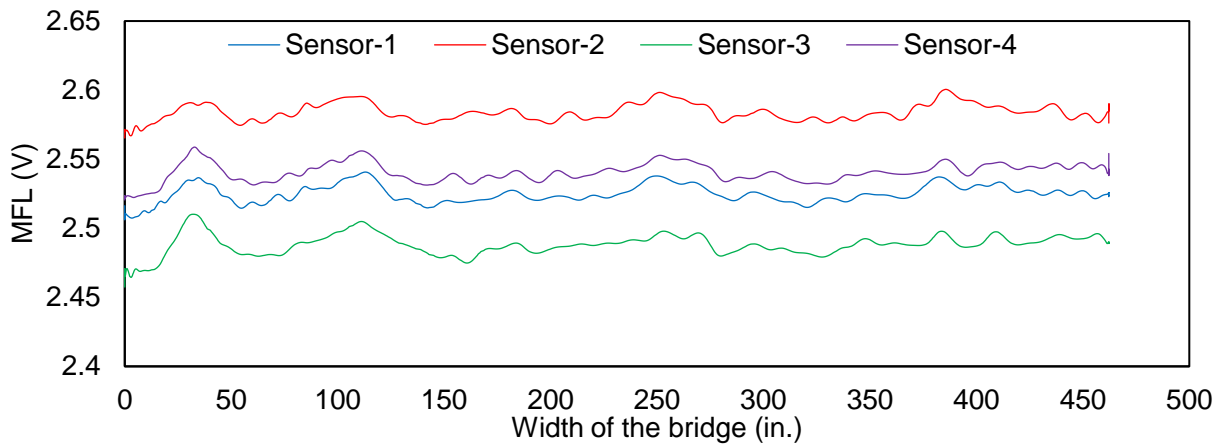


Figure B-15: Span 5 between PT rods (I-S-5-0).

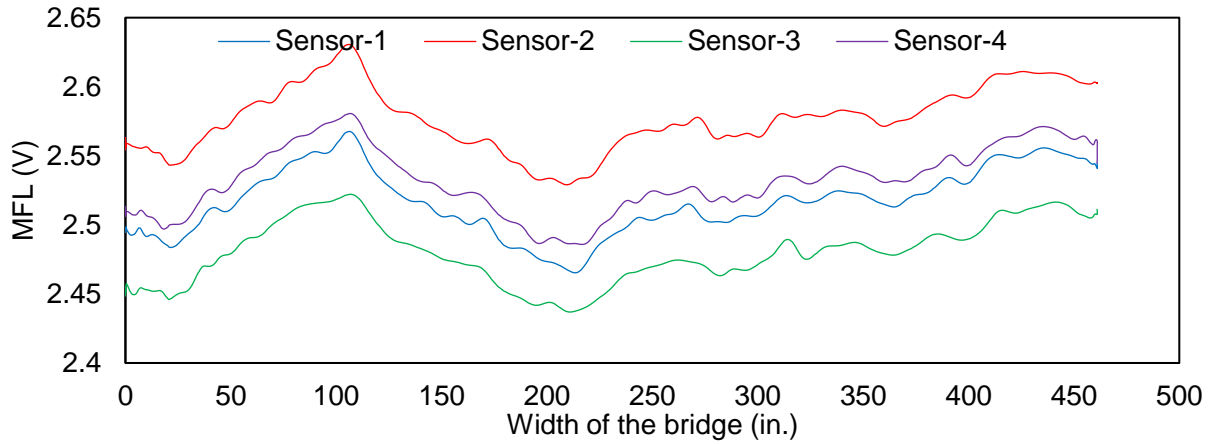


Figure B-16: MFL signal of unmagnetized PT rod 2 (I-S-5-2).

B.2 BRIDGE A PHASE II TESTING

Table B-2. List of phase II MFL testing

Test No.	Span No.	PT Rod No.	Magnetization Condition
II-S-1-1	Span 1	1	Top Magnetization (previously magnetized)
II-S-1-2	Span 1	2	No Magnetization
II-S-2-1	Span 2	1	Bottom Magnetization
II-S-2-2	Span 2	2	Bottom Magnetization
II-S-3-1	Span 3	1	Bottom Magnetization
II-S-3-2	Span 3	2	Bottom Magnetization
II-S-4-1	Span 4	1	No Magnetization
II-S-4-2	Span 4	2	Bottom Magnetization
II-S-5-1	Span 5	1	No Magnetization
II-S-5-2	Span 5	2	No Magnetization

Note: all the results in this section are from regular sensors without flux concentrators.

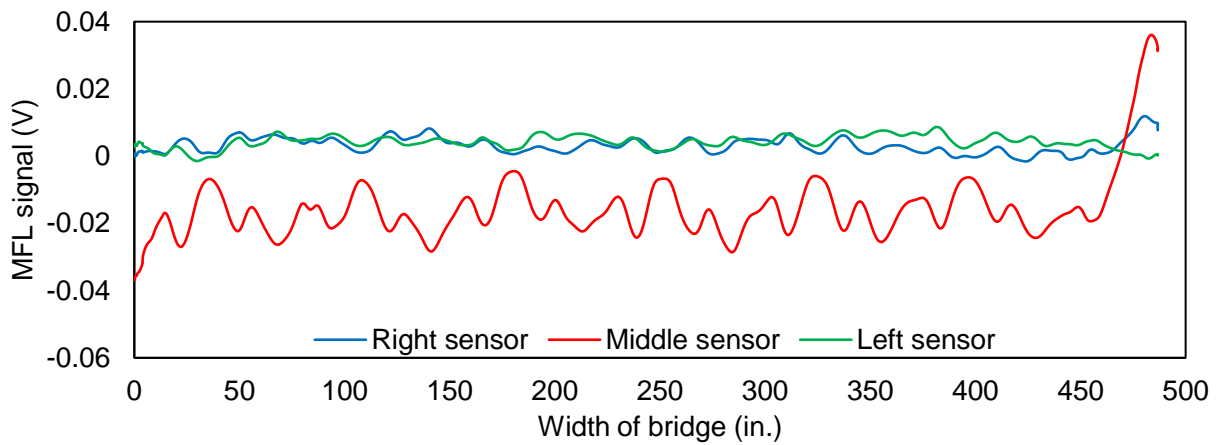


Figure B-17: MFL signal of PT rod 1 (II-S-1-1).

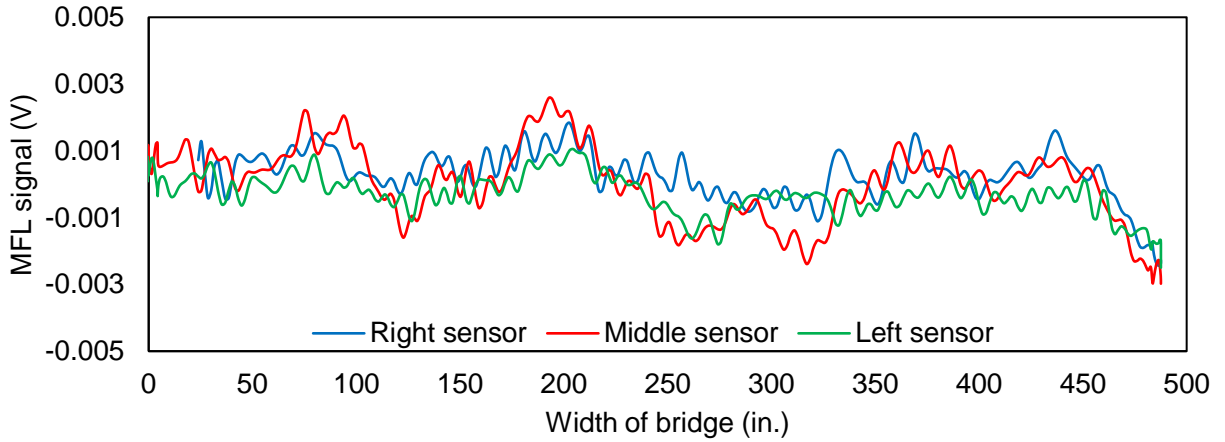


Figure B-18: MFL signal of PT rod 2 (II-S-1-2).

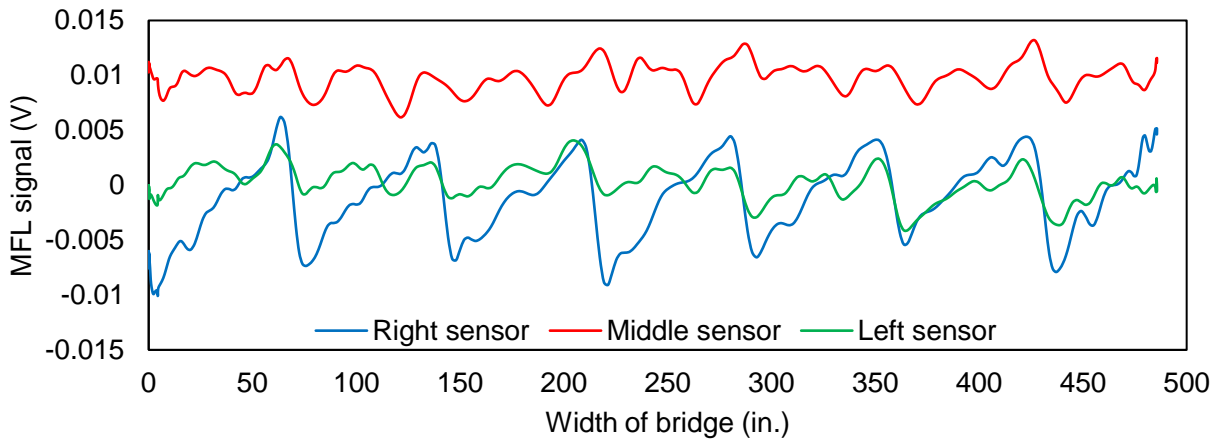


Figure B-19: MFL signal of PT rod 1 (II-S-2-1).

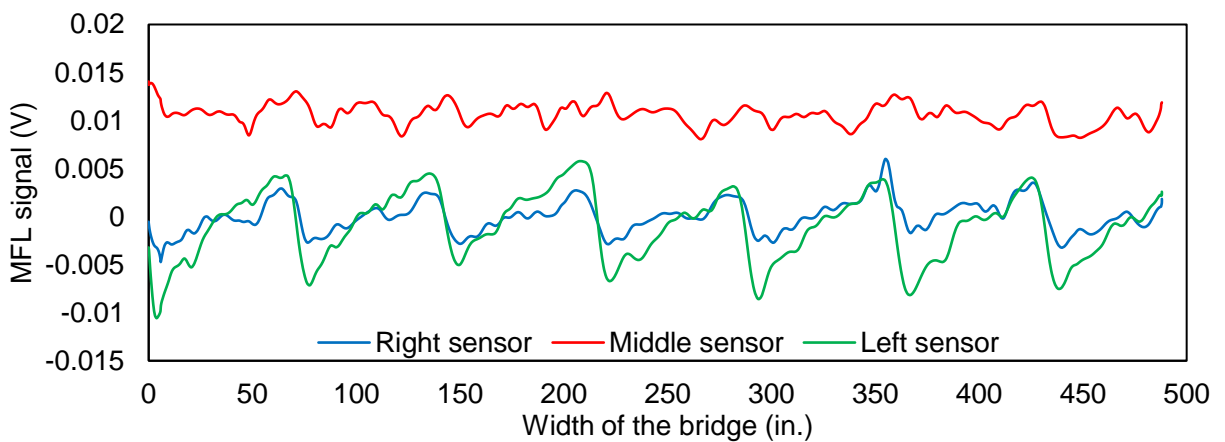


Figure B-20: MFL signal of PT rod 2 (II-S-2-2).

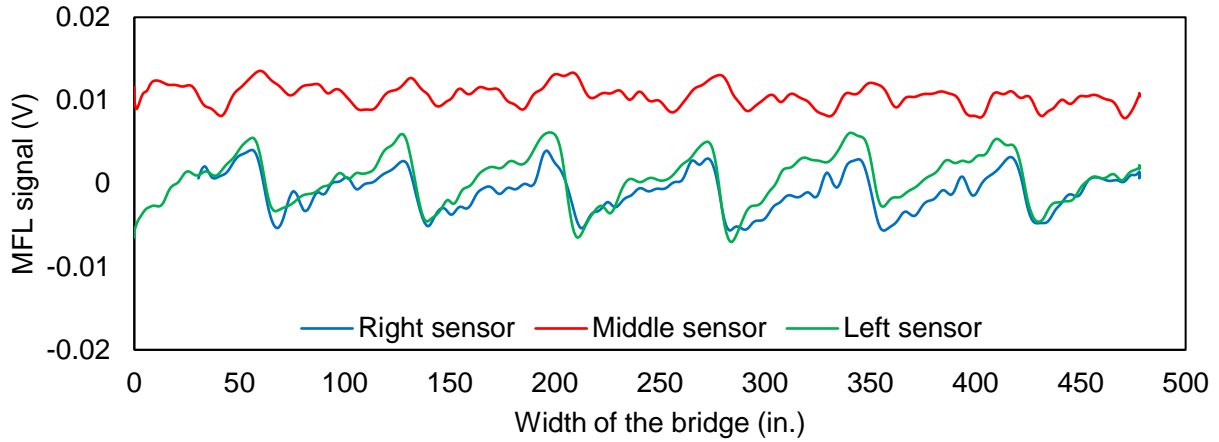


Figure B-21: MFL signal of PT rod 1 (II-S-3-1).

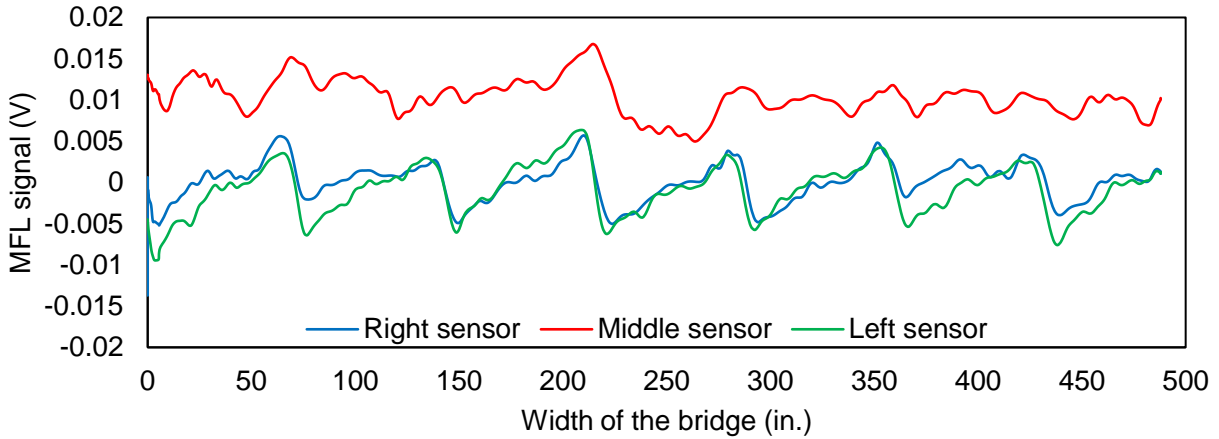


Figure B-22: MFL signal of PT rod 2 (II-S-3-2).

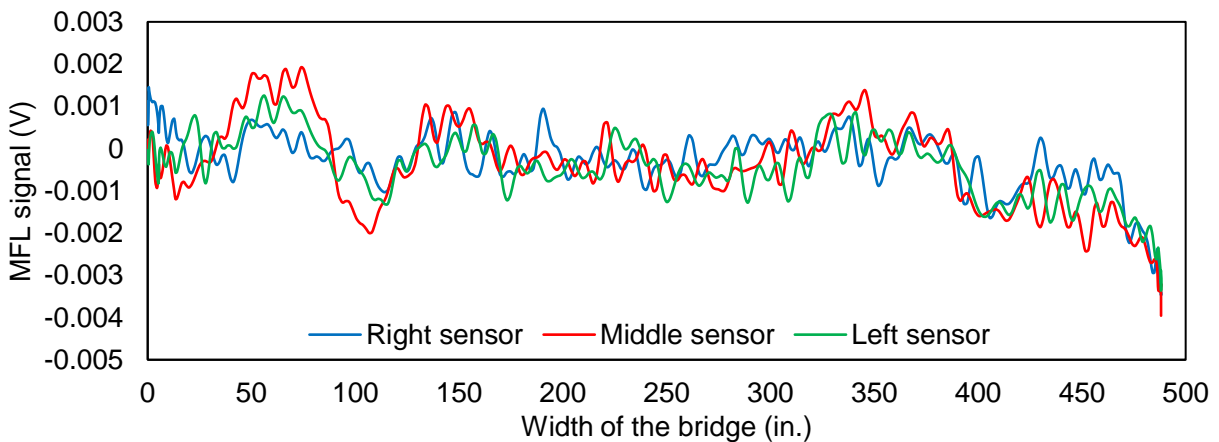


Figure B-23: MFL signal of PT rod 1 (II-S-4-1).

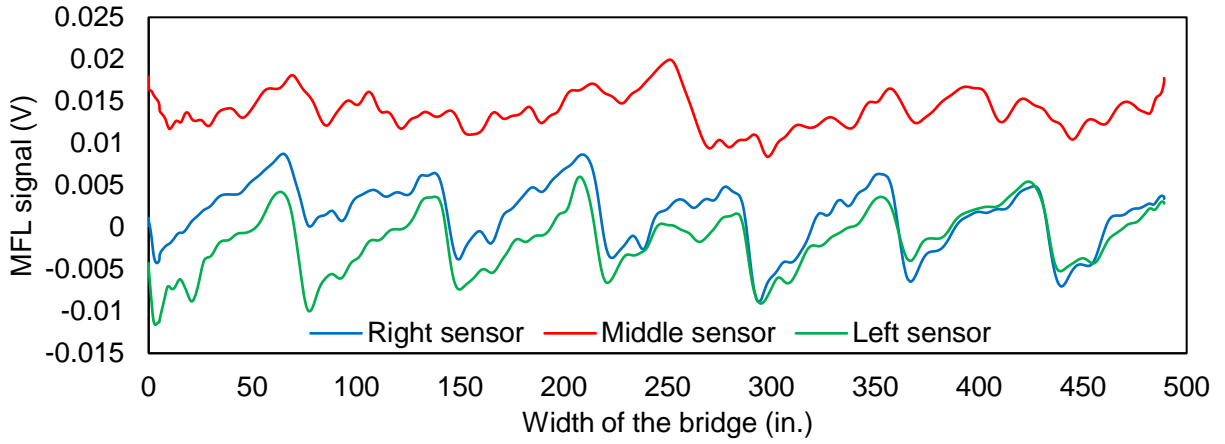


Figure B-24: MFL signal of PT rod 2 (II-S-4-2).

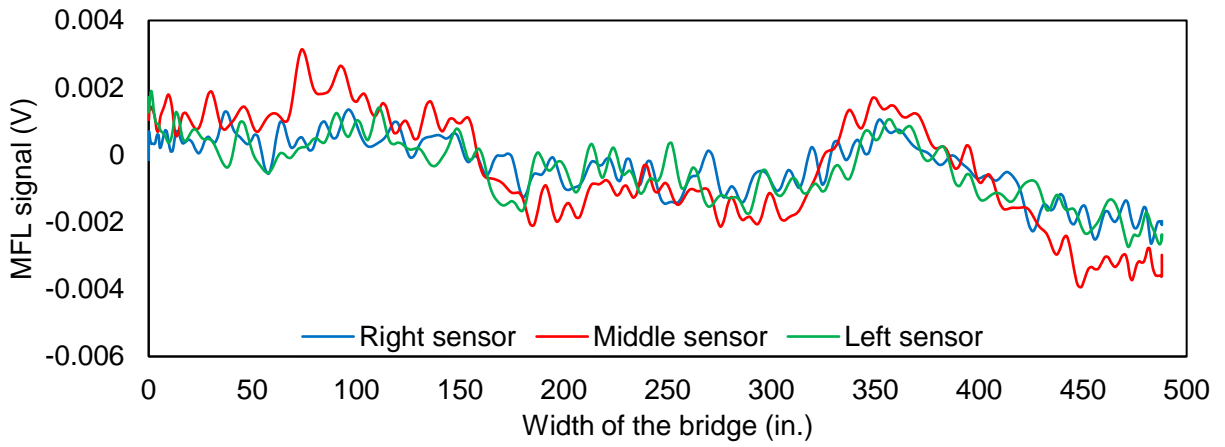


Figure B-25: MFL signal of PT rod 1 (II-S-5-1).

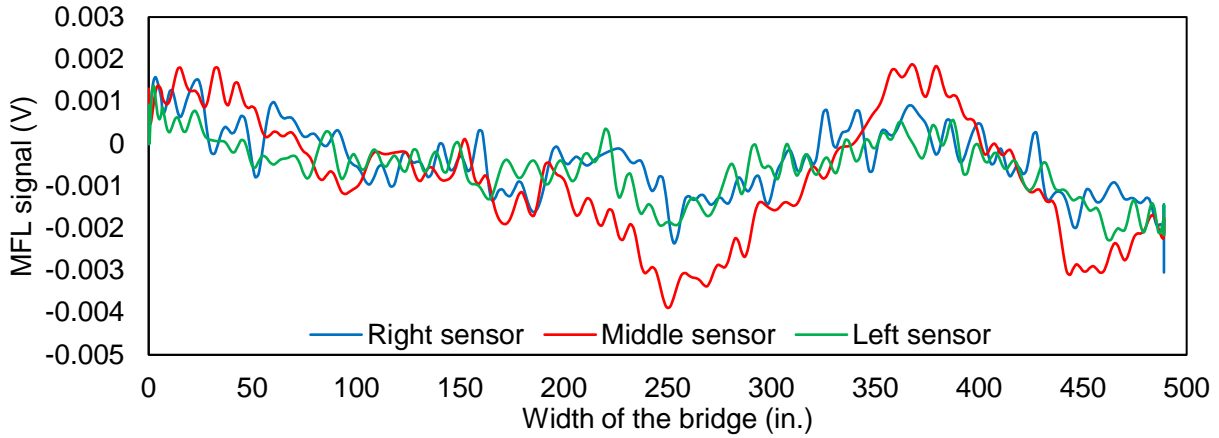


Figure B-26: MFL signal of PT rod 2 (II-S-5-2).

B.3 COMPARISON OF PHASE I AND II ON BRIDGE A

For sake of clarity, only results from sensor number 2 (experimental measurement unit 1) and middle sensor (experimental measurement unit 2) with flux concentrator are plotted.

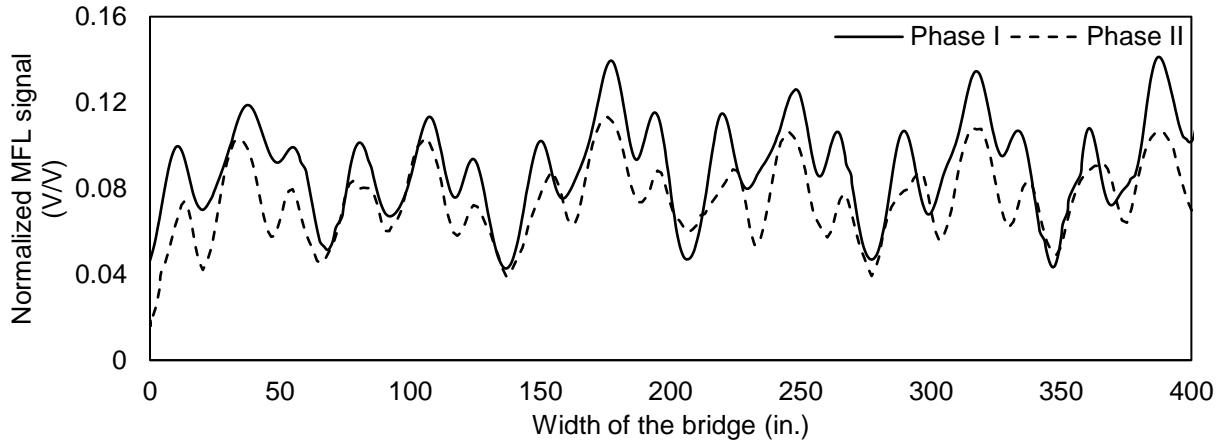


Figure B-27: Span 1, PT rod 1.



Figure B-28: Span 1, PT rod 2.

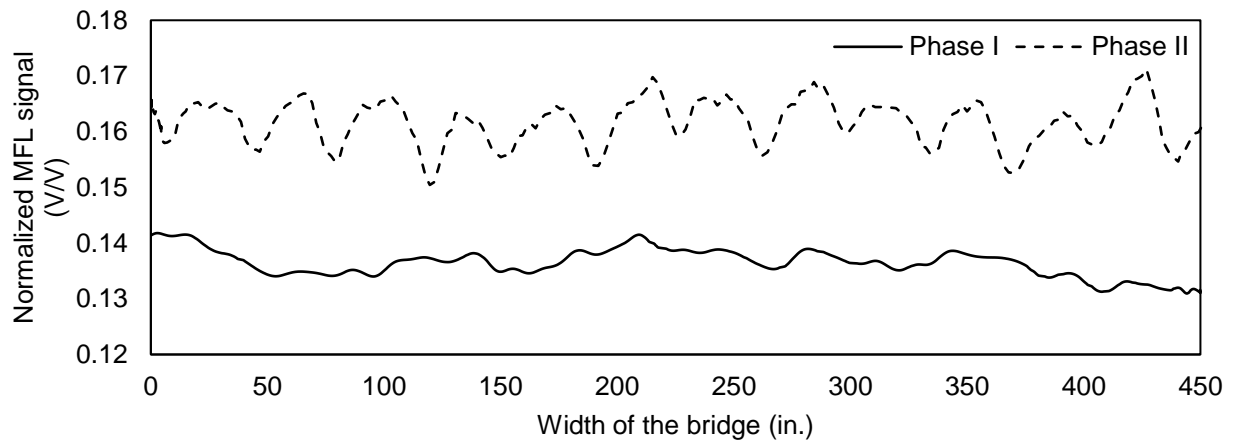


Figure B-29: Span 2, PT rod 1.



Figure B-30: Span 2, PT rod 2.



Figure B-31: Span 3, PT rod 1.

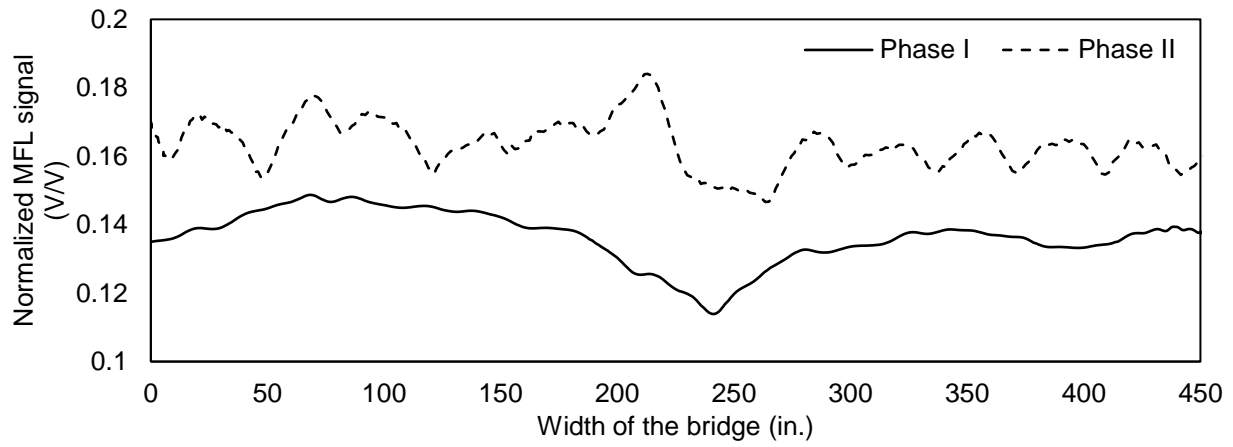


Figure B-32: Span 3, PT rod 2.



Figure B-33: Span 4, PT rod 1.

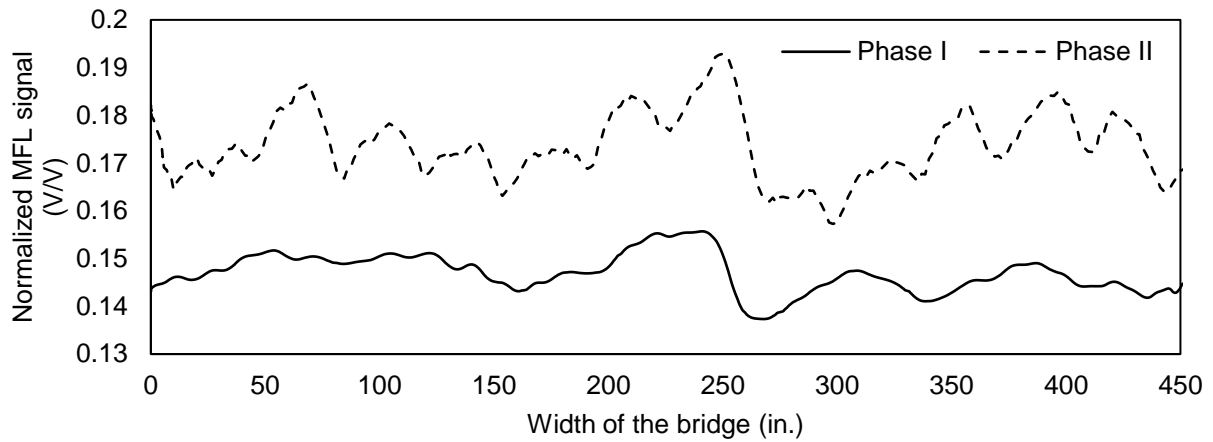


Figure B-34: Span 4, PT rod 2.

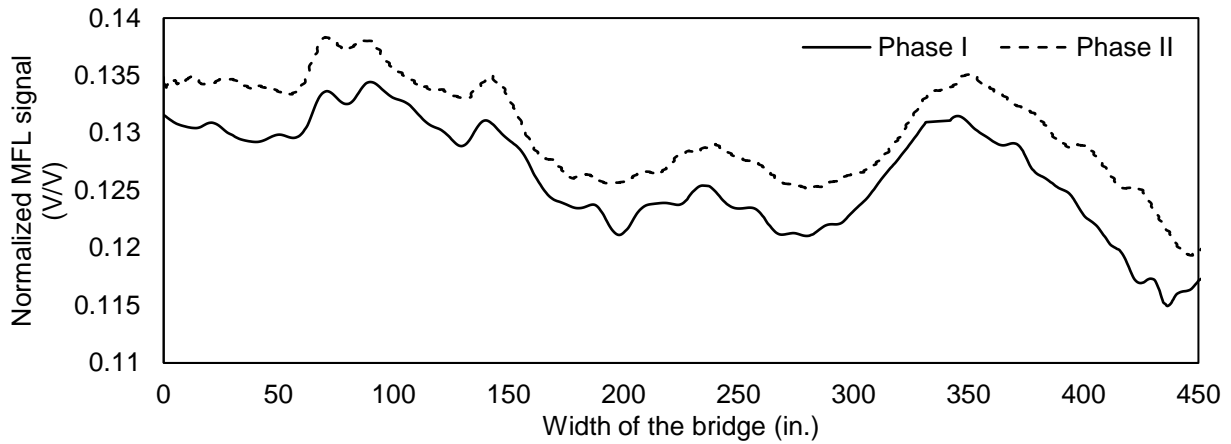


Figure B-35: Span 5, PT rod 1.

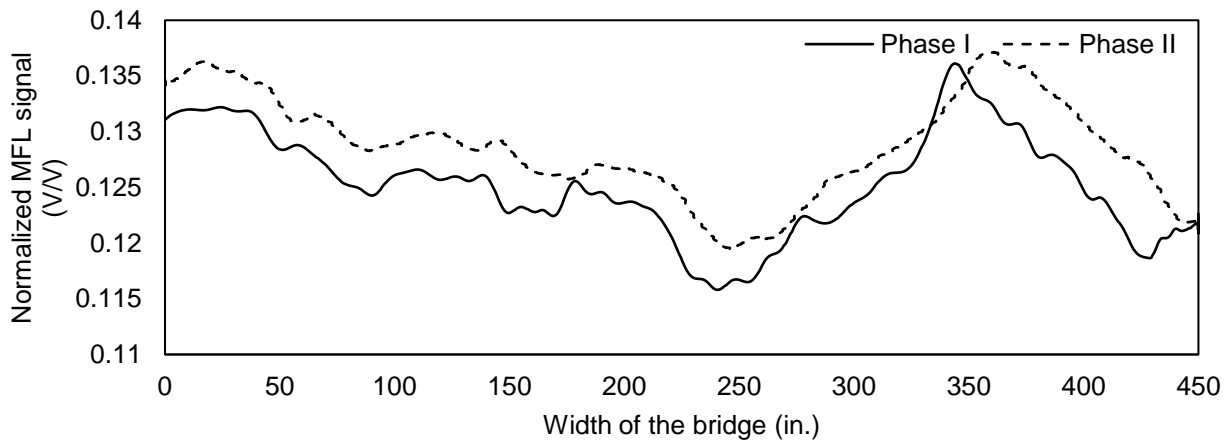


Figure B-36: Span 5, PT rod 2.

B.4 BRIDGE B TESTING

The testing protocol developed in the laboratory showed that the far side magnetization and near side measurement was able to locate the simulated damage in the tendons. Similar testing protocol was used for testing Bridge B. For the subject bridge, it was decided to test the bottom flange of the box girder for a select number of tendons. Initially, GPR was used for locating the tendon along the longitudinal direction of the box girder. The GPR readings were taken from the top and bottom of the slab. Based on the results from GPR mapping, the locations of tendons were marked at the soffit of the box girder. The details of the bridge and GPR testing is provided in Appendix A.2.

B.4.1 Test Methodology

A skyjack lift was used as a platform to magnetize along the marked location of the tendons. Out of a total of 14 segments in abutment span, testing was only carried out from segment 4 to segment 9. Figure B-37 shows a photograph of measurement from the bottom side of the slab. The thickness of the bottom flange was 8 inches.



Figure B-37: Obtaining MFL signal from the bottom side.

The test matrix is provided in Table B-3. Before magnetizing the slab tendons, an area scan was performed on the hatched area shown in Figure B-38. Then the tendons were magnetized from the bottom using magnet 2. The position of the magnet was along tendon 1. Then MFL signal was obtained for the hatched area also shown in Figure B-38. For test 3, another magnetization was performed using magnet 1 along tendon 3. The area shown in Figure B-39 was scanned during test 3. The last scan was performed on from the top on the hatched area shown in Figure B-40 without any additional magnetization.

Table B-3. Test detail on Bridge B

Test	Magnetization	Magnet	Tendon	Measurement
1	None	N/A	N/A	Area scan from the bottom
2	Bottom	2	1	Area scan from the bottom
3	Bottom	1	3	Area scan from the bottom
4	N/A	N/A	N/A	Area scan from the top

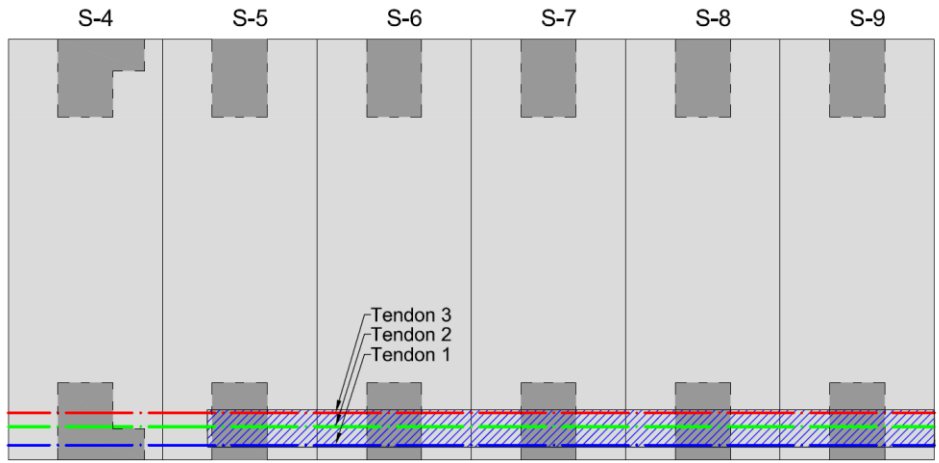


Figure B-38: Measurement area of test 1 & 2.

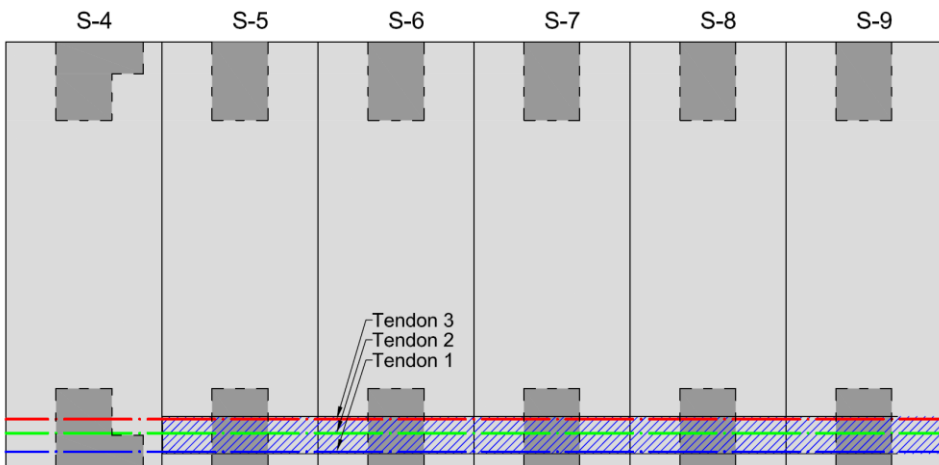


Figure B-39: Measurement area of test 3.

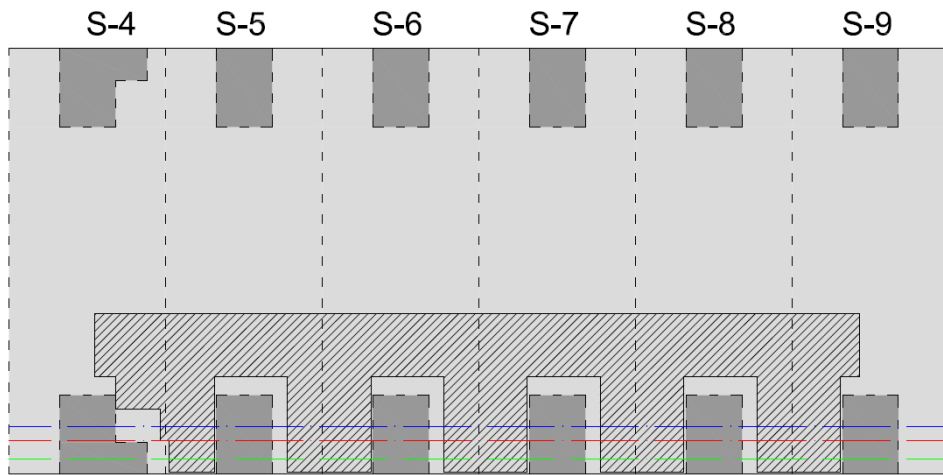


Figure B-40: Measurement area of test 4.

B.4.2 Test Results

As shown in Figure B-41, the area scan of test 1 does not show any significant signal from unmagnetized tendons. After magnetization, the area scan shows the location of transverse mild reinforcement which is plotted in Figure B-42. The mild reinforcement was located very near to the scanning surface and the magnetization scheme was very strong. Therefore, the mild reinforcement masks the signal from the tendon. To overcome this challenge, magnet 1 was used for tendon 3. The signal for test 3, shown in Figure B-43, but due to discontinuous magnetization the signal was unclear. Testing was also performed between the deviators. The area scan of test 4 is shown in Figure B-44. The location of the tendon can be seen in this figure but due to inaccessibility the signal were inconclusive.

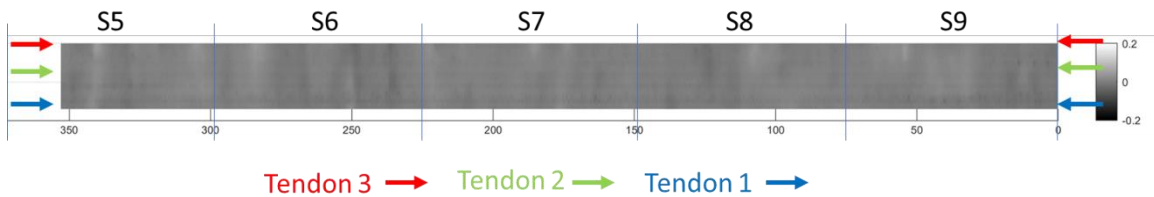


Figure B-41: Area scan of test 1.

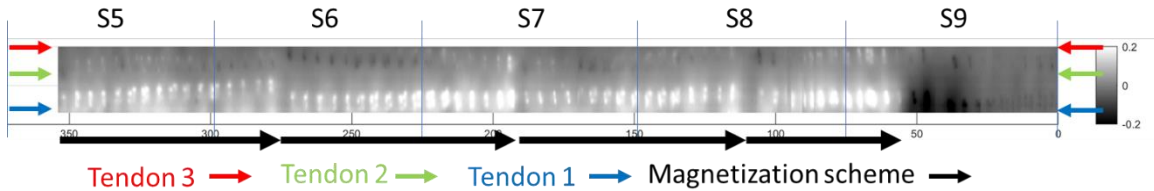


Figure B-42: Area scan of test 2.

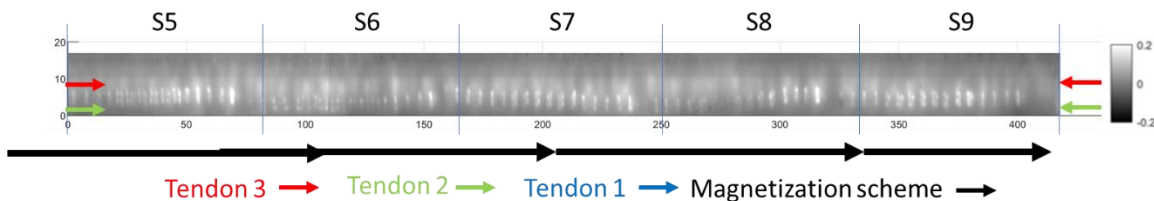


Figure B-43: Area scan of test 3.

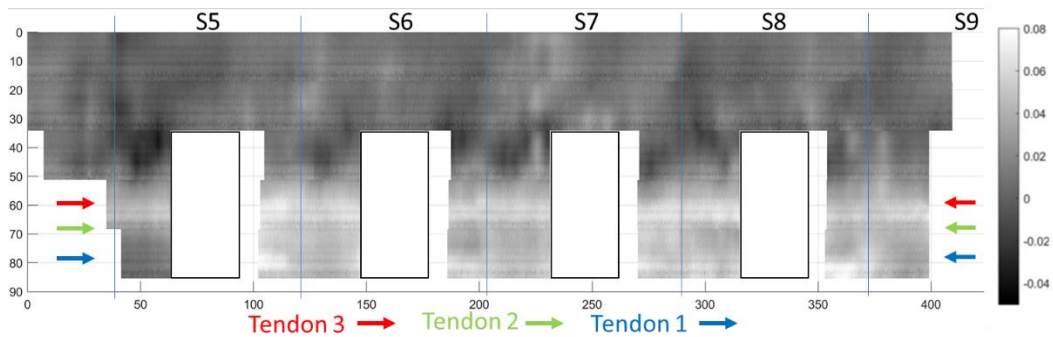


Figure B-44: Area scan of test 4.

APPENDIX C FINITE ELEMENT ANALYSIS OF MFL SYSTEM

C.1 PARAMETRIC STUDY ON MAGNETIZATION AND RESIDUAL MAGNETIC FIELD

To simulate the passive method of sensing, the residual (remanent) magnetic field that remains after the magnet has passed must be determined. Remanent magnetization (hysteresis) calculations can only be performed in transient analyses. Therefore, full transient analysis was used for all the models being presented. Note that if only the active method were to be simulated, this can be achieved with static analysis. Ansys Maxwell software was used for these analyses.

The numerical model of the magnet is shown in Figure C-1. The yoke is composed of two neodymium magnets (vertical poles) connected by a piece of iron (back iron) that completes the magnetic circuit.

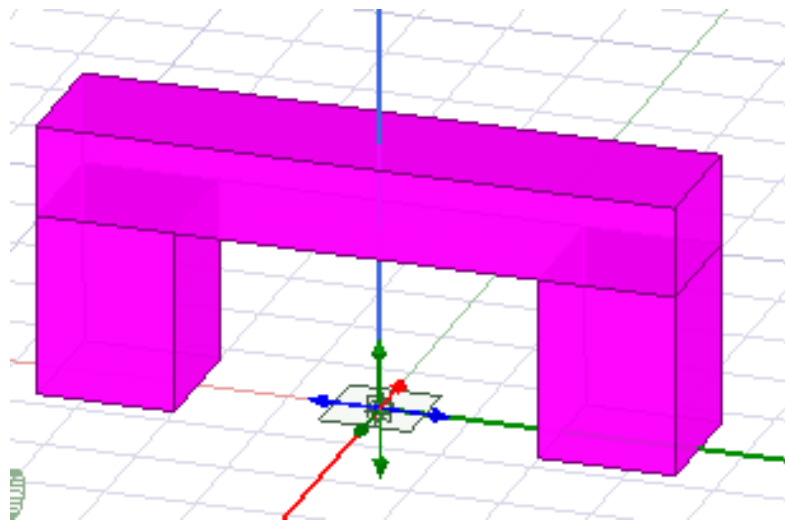


Figure C-1: Numerical model of the magnet.

C.1.1 Material Properties

To perform the demagnetization calculations, a B-H curve (flux density against magnetic field strength), as shown in Figure C-2, must be provided to define the hysteresis of the material.

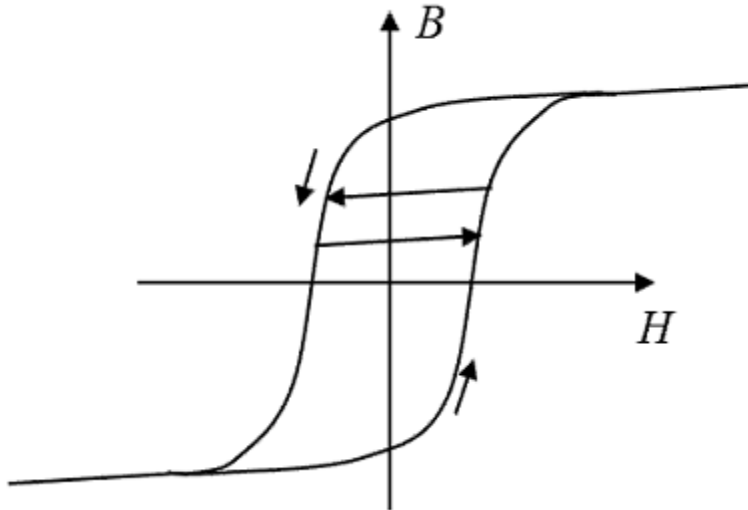


Figure C-2: Schematic B-H curve.

The information supplied is the coordinates for the upper branch of the saturation curve (Figure C-3). The descending branch is taken as the mirror. Note that the supplied curve necessarily must not go through the origin and the ascending branch of the initial magnetization is determined to be the average of the ascending and descending legs. The magnetic coercivity is determined from the curve as the value along the x-axis where the ascending branch passes through.

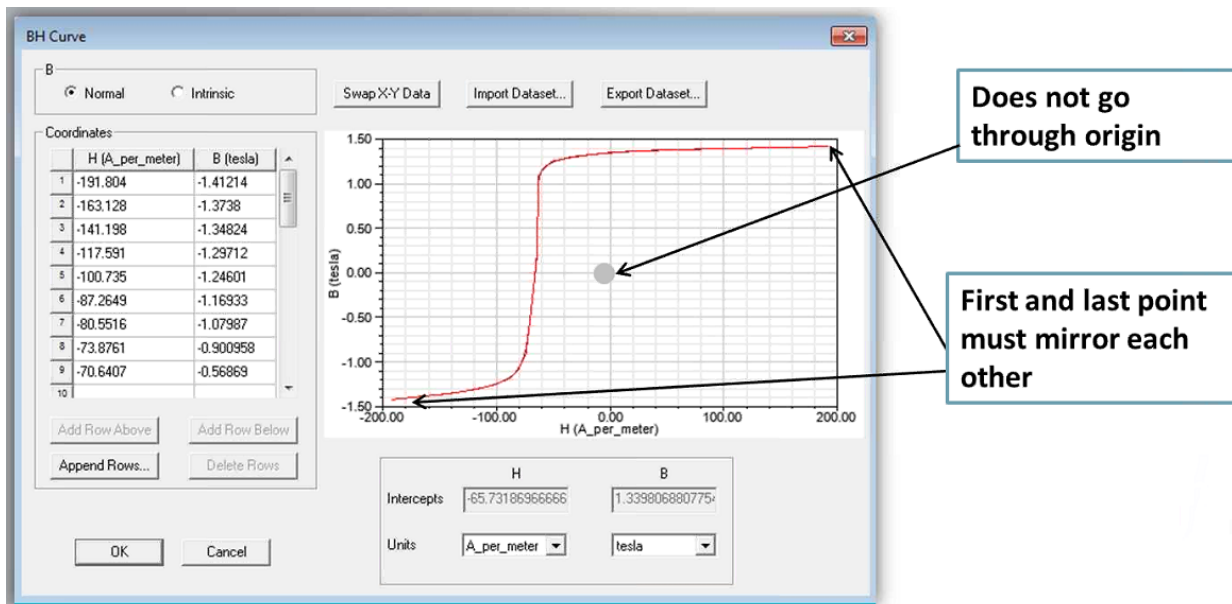


Figure C-3: B-H cure definition in ANSYS Maxwell.

C.1.1.1 Strand Material

The B-H curve for the strand material is given below and the calculated magnetic coercivity equals -272.3 A/m. This curve was obtained from literature as representative of mild steel (Figure C-4). This is sufficient for the purpose of the analyses performed in

this study. For each specific application, this information should be obtained for the specific material being investigated.

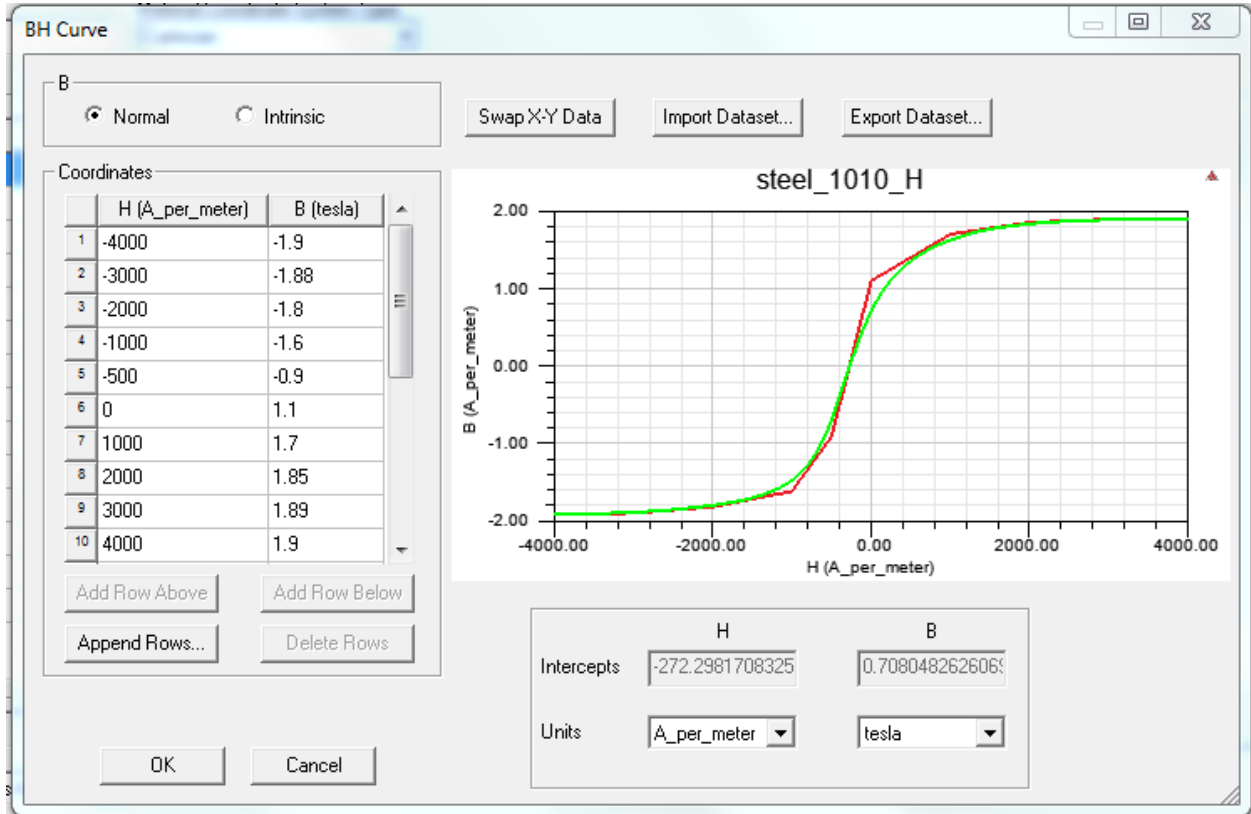


Figure C-4: B-H curve defined for strands.

C.1.1.2 Magnet Grade 35 NdFe

The properties for a basic Grade 35 Neodymium magnet obtained from the Ansys material library was used for the permanent magnets (Figure C-5). The magnetic coercivity of this magnet equals -890,000 A/m.

Material Name: NdFe35 Material Coordinate System Type: Cartesian

Properties of the Material

Name	Type	Value	Units
Relative Permeability	Simple	1.0997785406	
Bulk Conductivity	Simple	625000	siemens/m
Magnetic Coercivity	Vector		
- Magnitude	Vector Mag	-890000	A_per_meter
- X Component	Unit Vector	1	
- Y Component	Unit Vector	0	
- Z Component	Unit Vector	0	
Core Loss Model		None	w/m^3
Mass Density	Simple	7400	kg/m^3
Composition		Solid	
Young's Modulus	Simple	147000000000	N/m^2
Poisson's Ratio	Simple	0	
Magnetostriction	Custom	Edit...	
Inverse Magnetostriction	Custom	Edit...	

Notes: _____

Calculate Properties for: _____

Reset OK Cancel

Figure C-5: Properties of Grade 35 NdFe magnet.

C.1.1.3 Back Iron

Properties for the back iron of the magnetic yoke were again taken from the Ansys material library (Figure C-6). The relative permeability was taken to be 4000 (unitless).

Material Name: Iron Material Coordinate System Type: Cartesian

Properties of the Material

Name	Type	Value	Units
Relative Permeability	Simple	4000	
Bulk Conductivity	Simple	10300000	siemens/m
Magnetic Coercivity	Vector		
- Magnitude	Vector Mag	0	A_per_meter
Core Loss Model		None	w/m^3
Mass Density	Simple	7870	kg/m^3
Composition		Solid	
Young's Modulus	Simple	195000000000	N/m^2
Poisson's Ratio	Simple	0.28	
Magnetostriction	Custom	Edit...	
Inverse Magnetostriction	Custom	Edit...	

Notes: _____

Figure C-6: Magnetic properties of back iron.

C.1.2 Depth Study – Bar Only

C.1.2.1 Short Rod

A suite of analysis was performed to examine the process of magnetization as the magnet passed longitudinally over a bar with the bar at varying distance from the magnet. A transient analysis was performed to enable remanent magnetization calculations. The model in these analyses consisted of the magnetic yoke described previously. The grade 35 NdFe magnets are 3 in. x 3 in. square and 4 in. tall (stacked 1 in. magnets). The back iron is 3 in. wide by 2 in. high and 14 in. long. This geometry results in a clear space between the pole magnets of 8 in. The bar is modeled as a 1 in. diameter rod (24-sided polyhedron) made of 1010 steel, as shown in Figure C-7. The material curve is given in Section 2.1. In these analyses, there is no damage induced to the rod. After the bar had passed under the magnet, it continued to travel far away to ensure there was no longer any influence from the magnet itself.

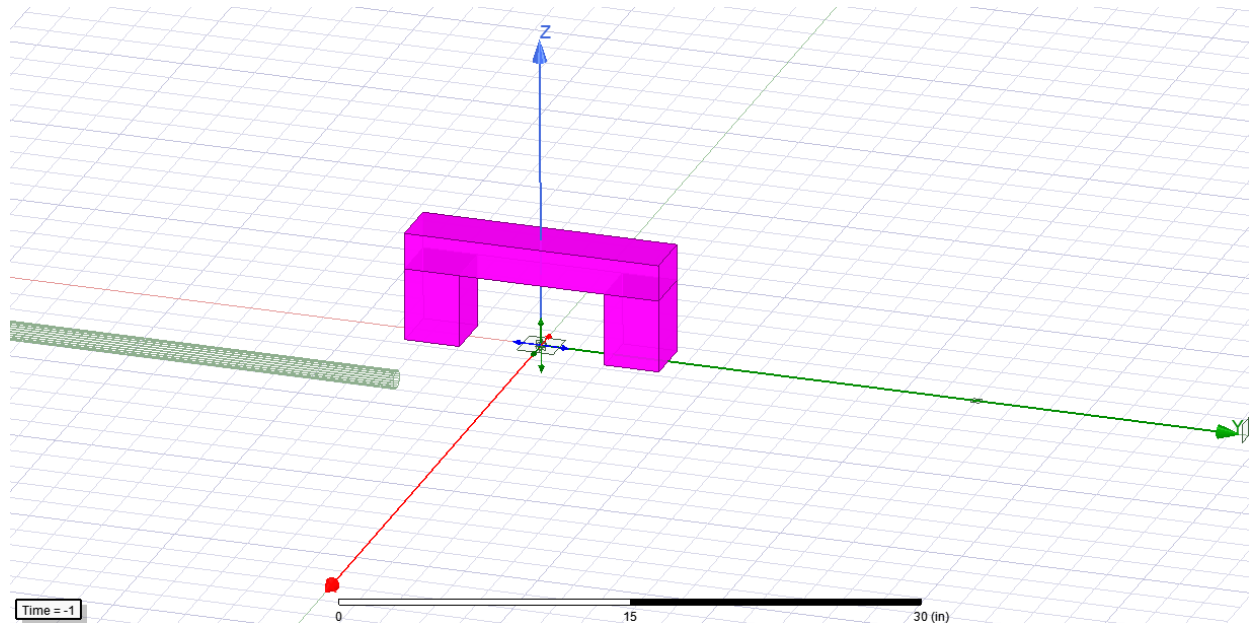


Figure C-7: The numerical setup for magnetizing a bar.

In the first suite of analyses, the rod length was 48 inches. As discussed later, this dimension was determined to be just barely long enough to examine the phenomenon occurring and several subsequent runs were made with longer rods to verify the observations. The following figures show the results of the short rod analyses. The indicated dimension (chart title) is the distance from the face of the magnet to the centerline of the rod. A total of 10 runs were performed at the following depths (inches): 2.75, 3, 3.125, 3.25, 3.375, 3.5, 3.75, 4, 5, and 6. Initially, runs were made at full inch increments. Additional depths were then added based on observations as described hereafter.

For each analysis there are two figures (Figure C-8 to Figure C-17). The first figure plots the measured flux in three directions against time. The rod is set to move at 1 in. per second, so time is equivalent to position. These plots examine the remanent field that remains in the bar after it has moved away from the magnet. The point of observation is

54 in. (to the right) from the centerline of the magnetic yoke and the leading tip of the rod was located 8 in. to the left (-8 in.). Therefore, the tip passes below the sensor at a time of 62 sec. In each of these plots, the red line is the vertical flux (B_z), the blue line is the longitudinal flux (B_y), and the brown line is transverse (B_x).

The second figure (vector plot) for each depicts the flux in the y-z plane at the end of the analysis when the rod is far from the magnet. This is the remanent field induced in the rod as a result of passing under the magnet.

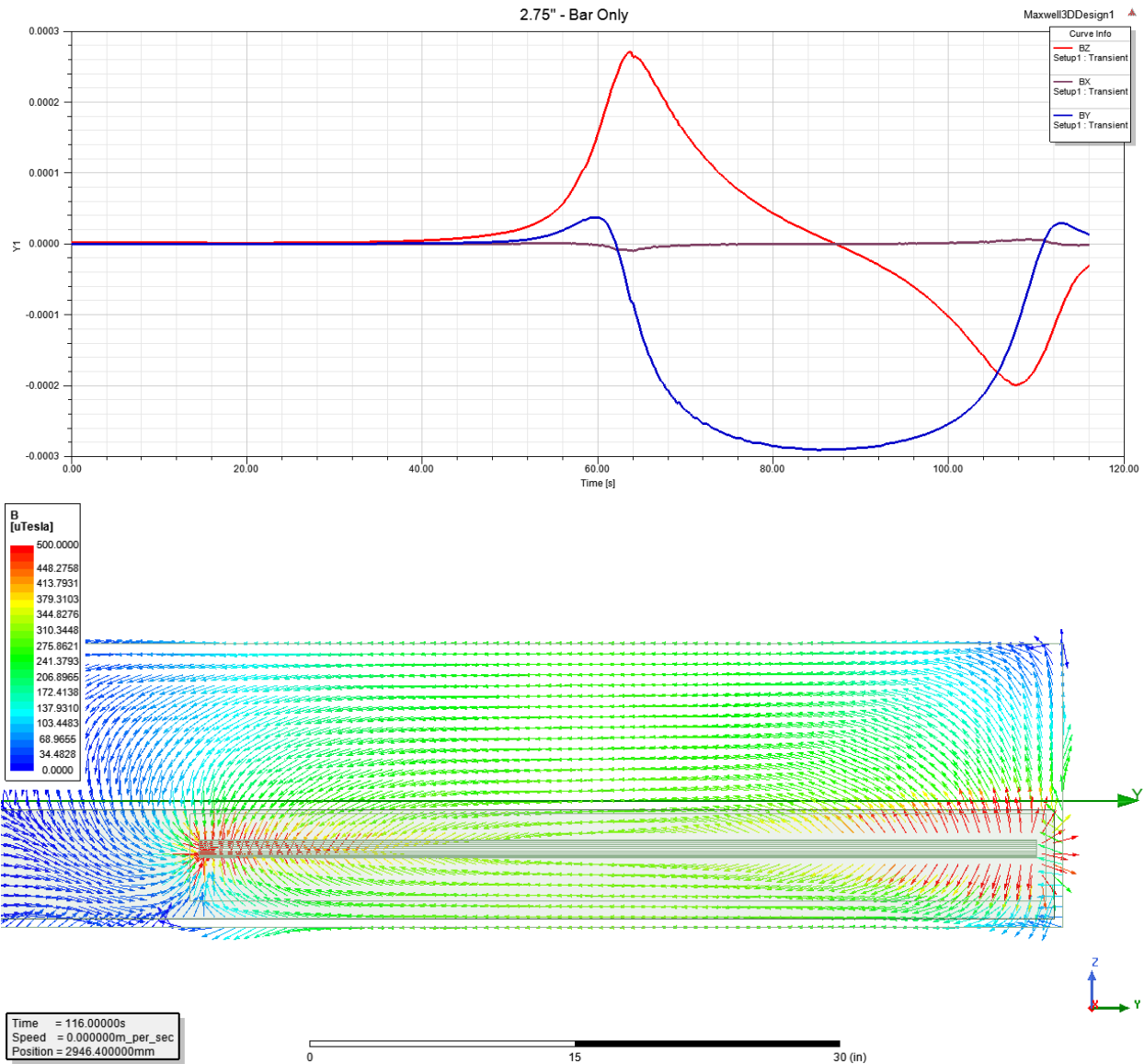


Figure C-8: Analysis results for magnetizing a bar at 2.75 in. from the magnet.

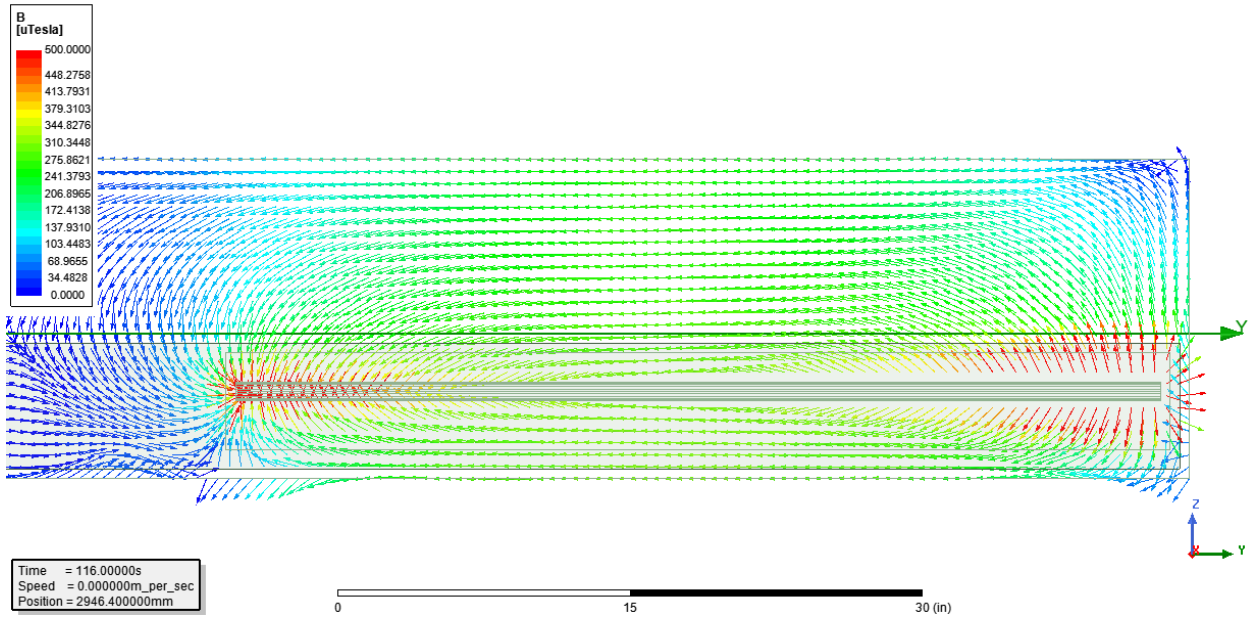
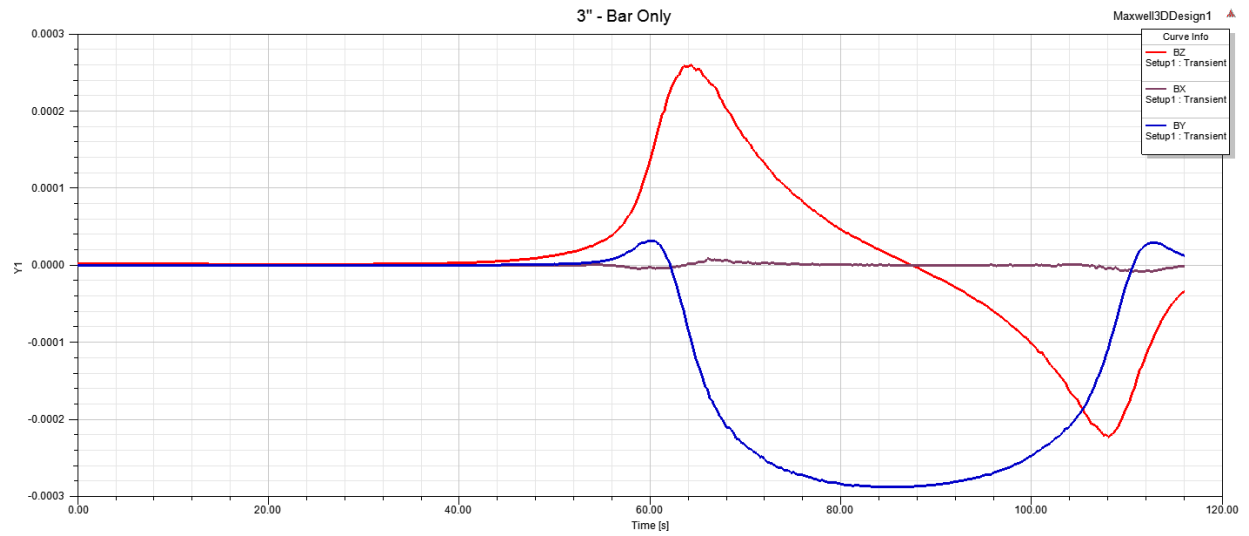


Figure C-9: Analysis results for magnetizing a bar at 3 in. from the magnet.

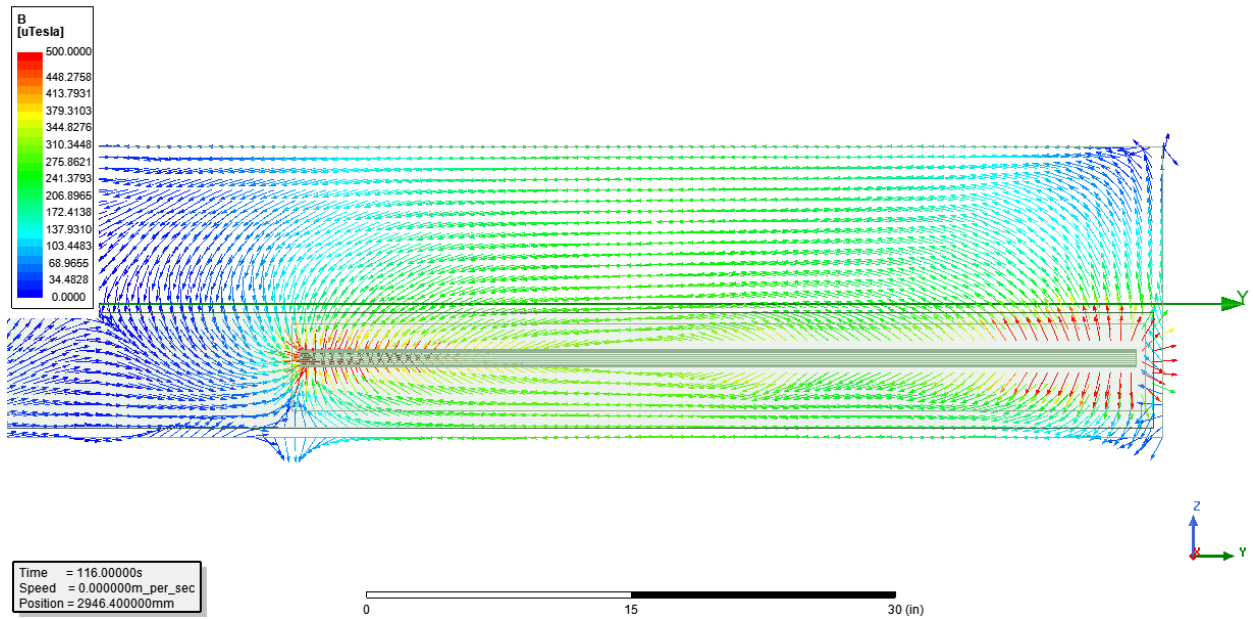
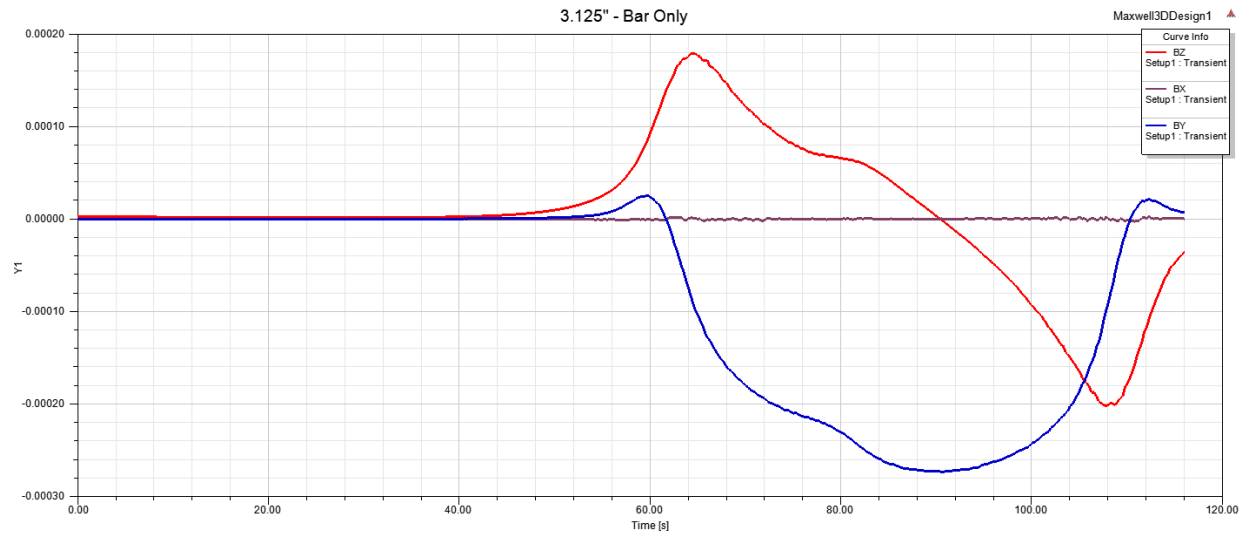


Figure C-10: Analysis results for magnetizing a bar at 3.125 in. from the magnet.

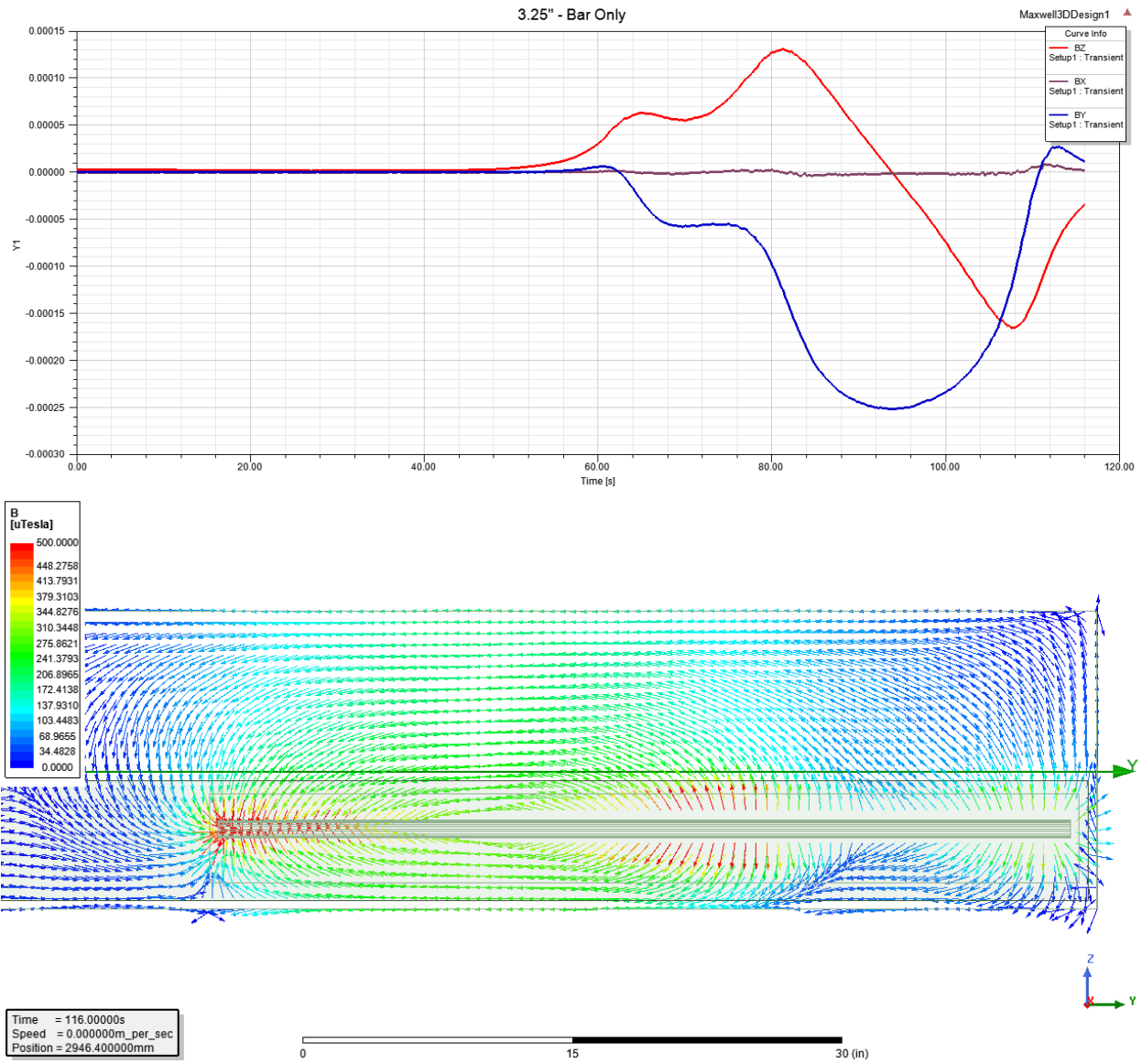


Figure C-11: Analysis results for magnetizing a bar at 3.25 in. from the magnet.

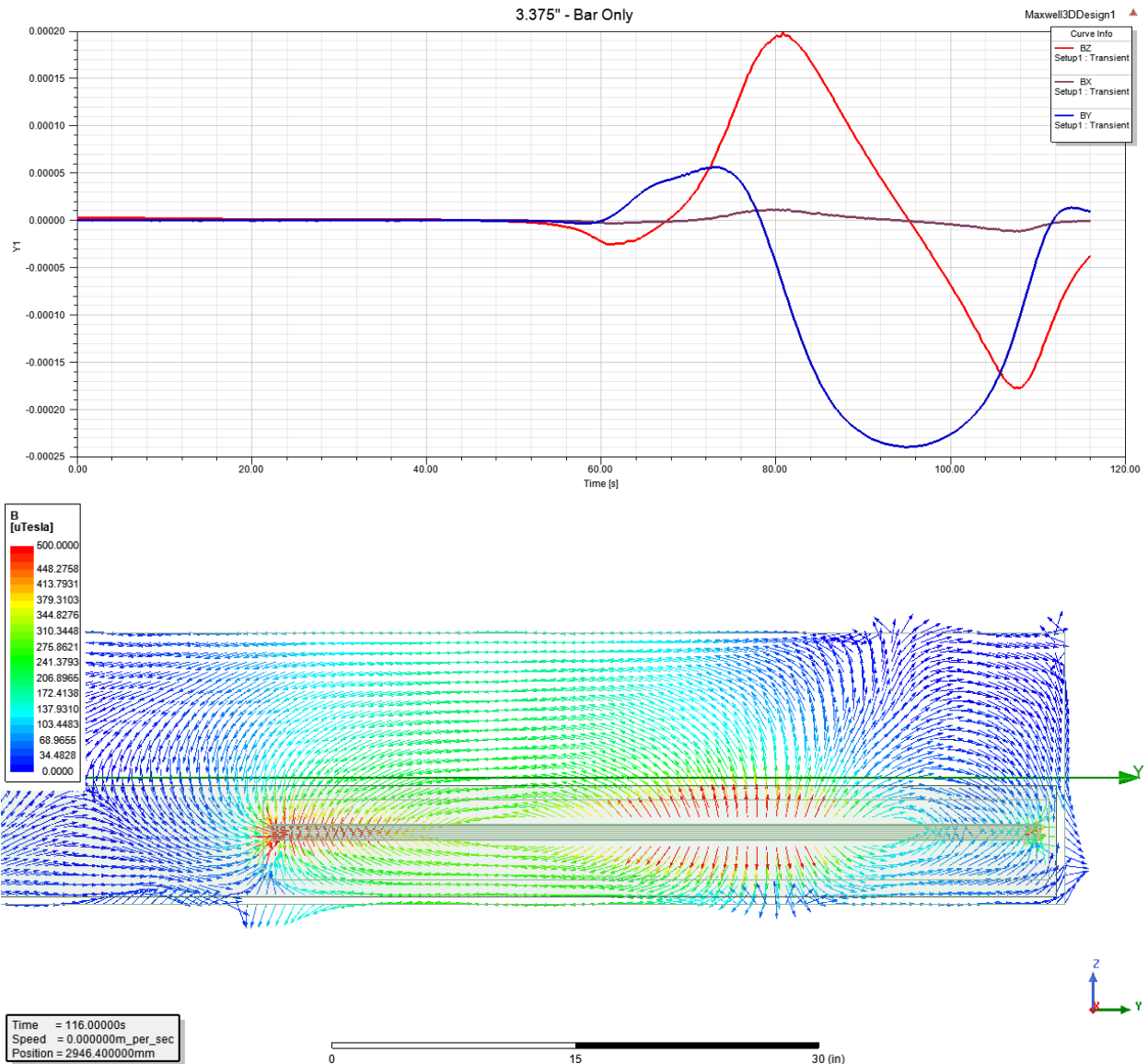


Figure C-12: Analysis results for magnetizing a bar at 3.375 in. from the magnet.

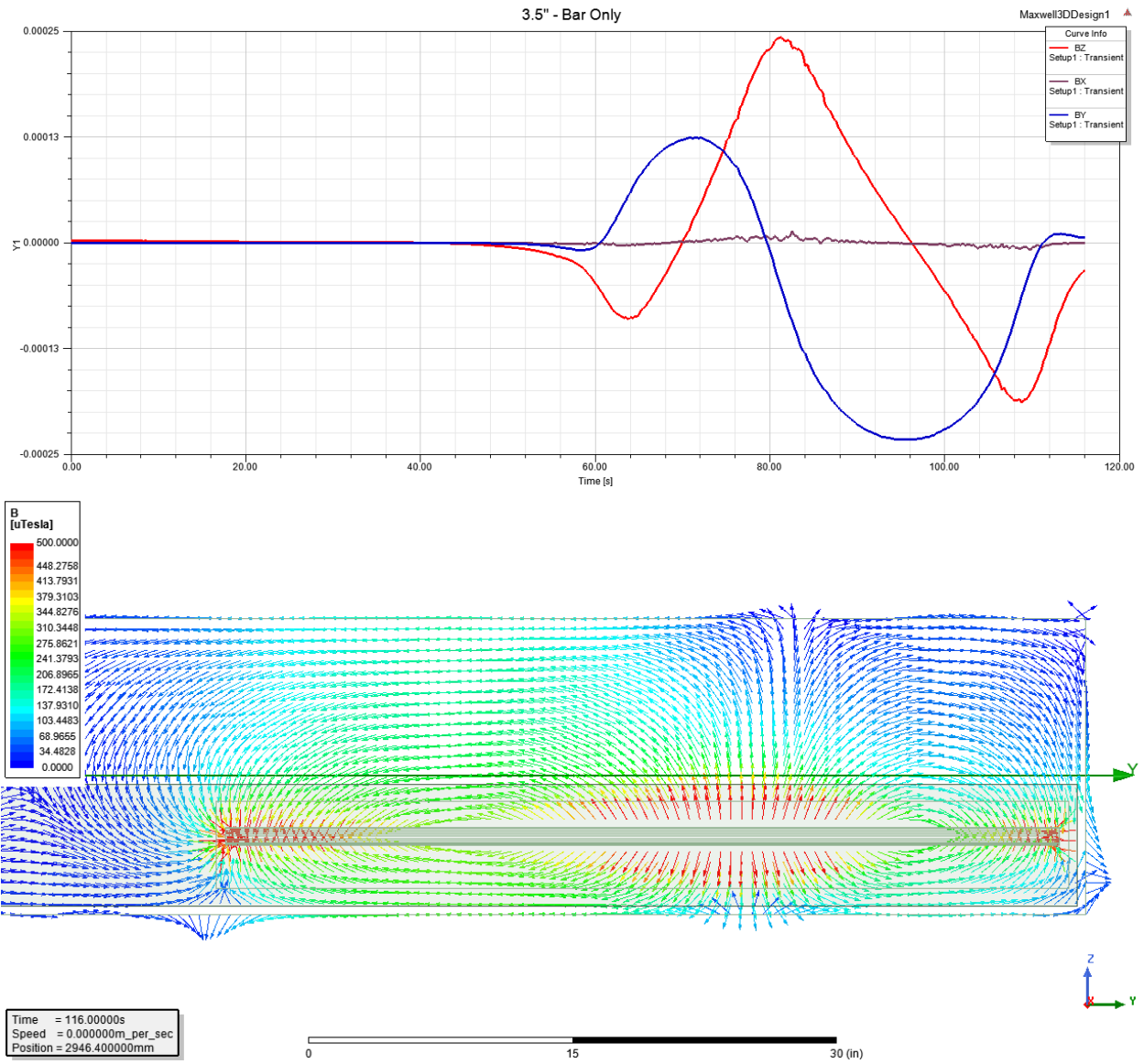


Figure C-13: Analysis results for magnetizing a bar at 3.5 in. from the magnet.

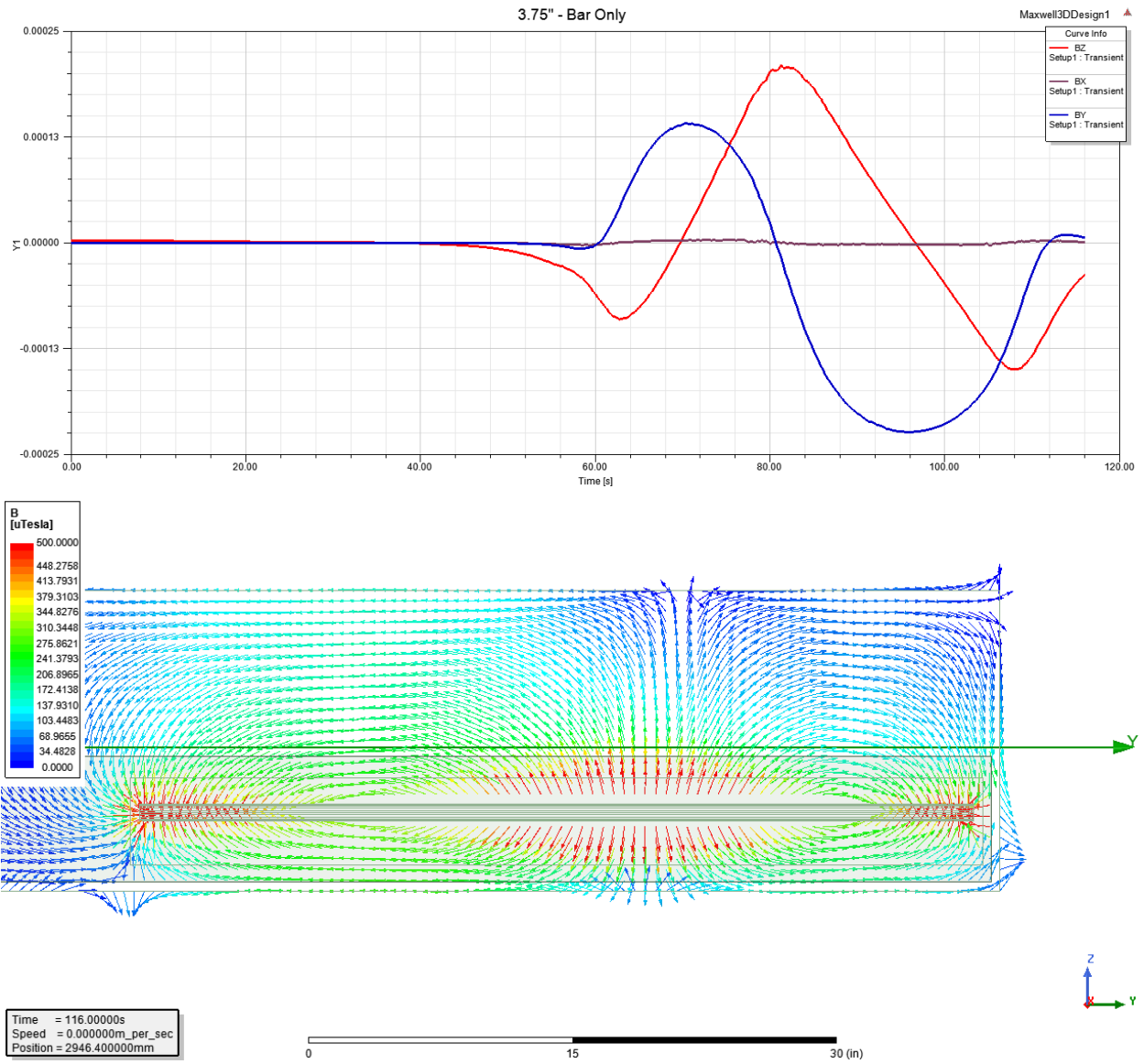


Figure C-14: Analysis results for magnetizing a bar at 3.75 in. from the magnet.

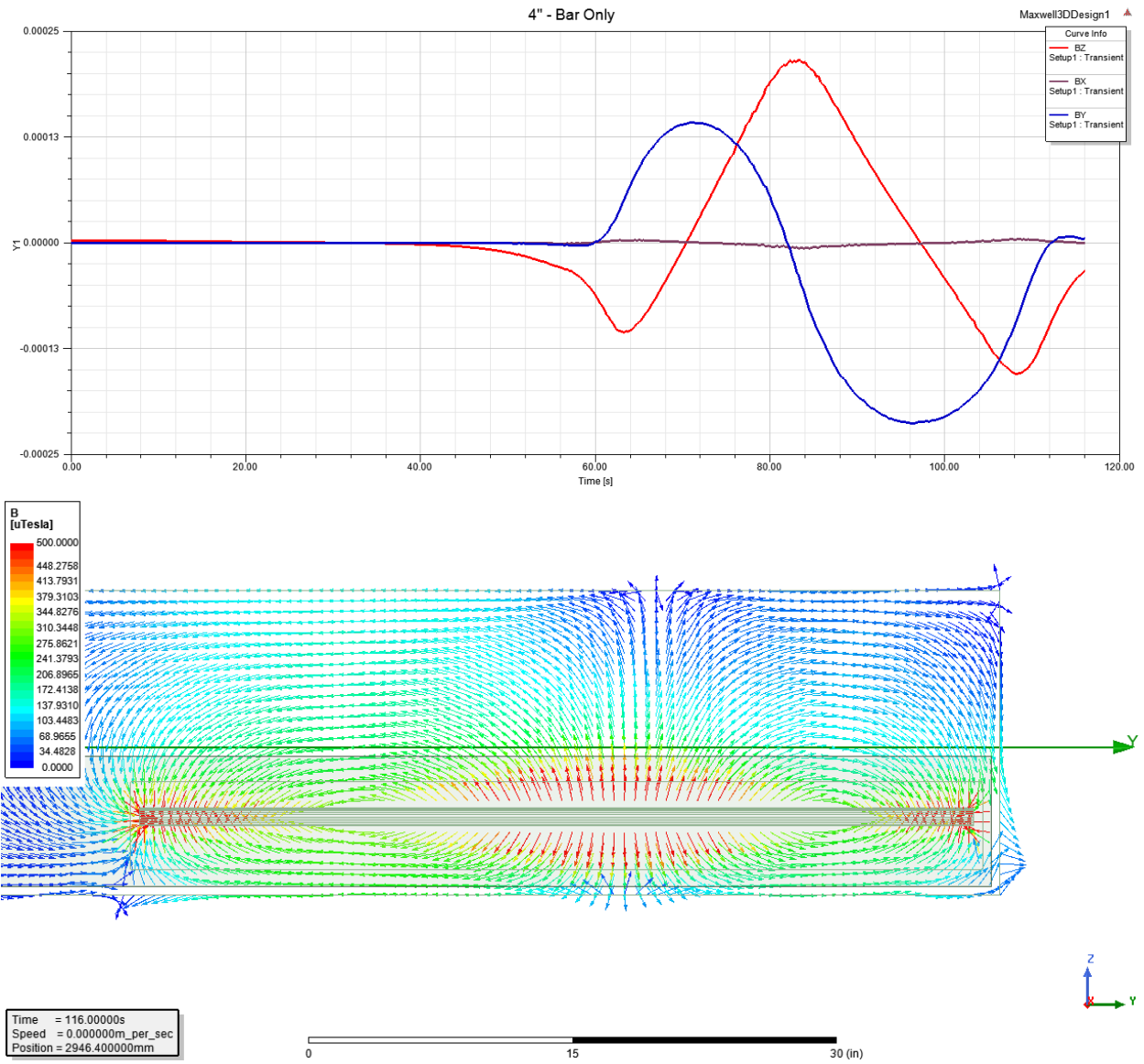


Figure C-15: Analysis results for magnetizing a bar at 4 in. from the magnet.

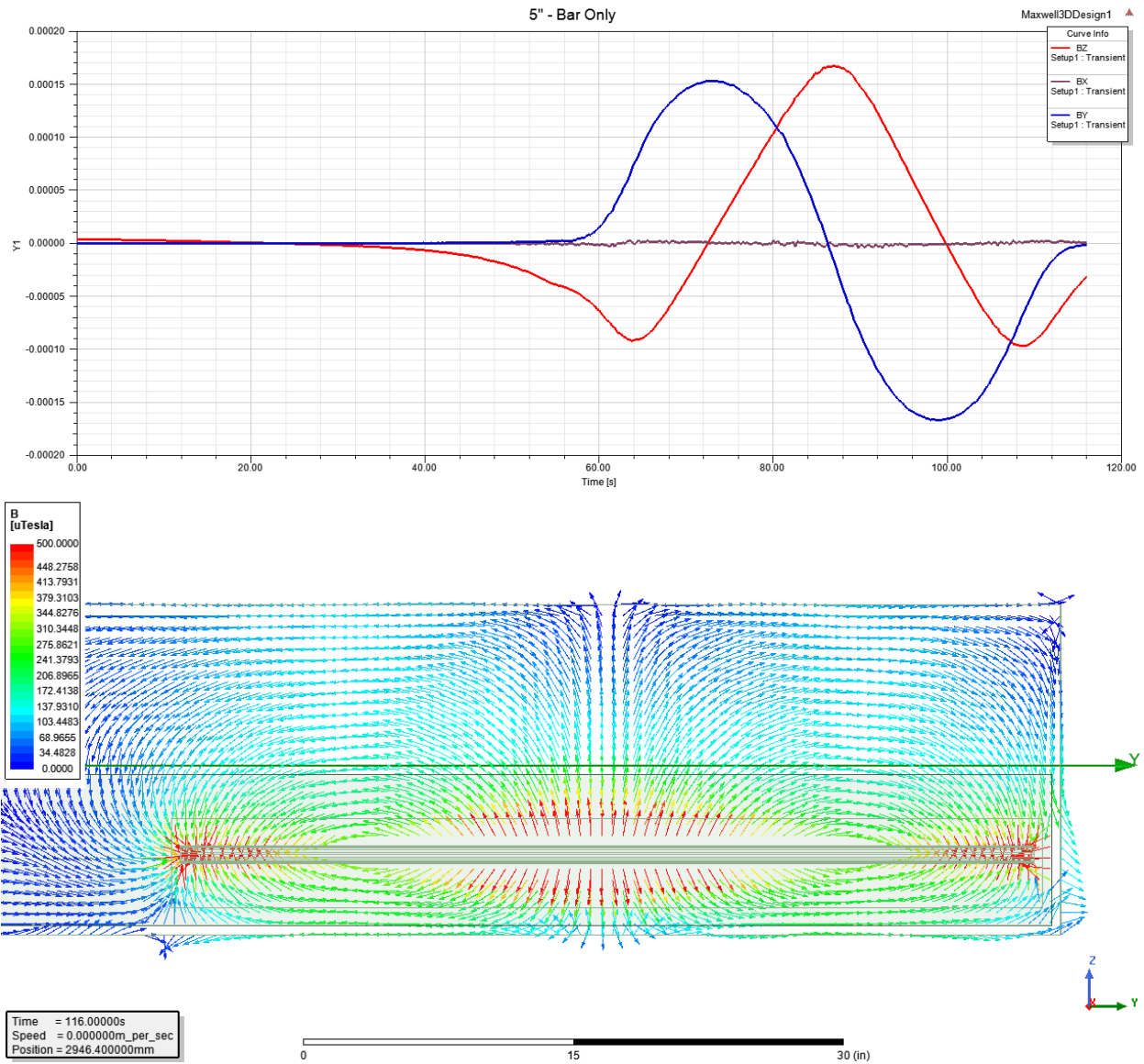


Figure C-16: Analysis results for magnetizing a bar at 5 in. from the magnet.

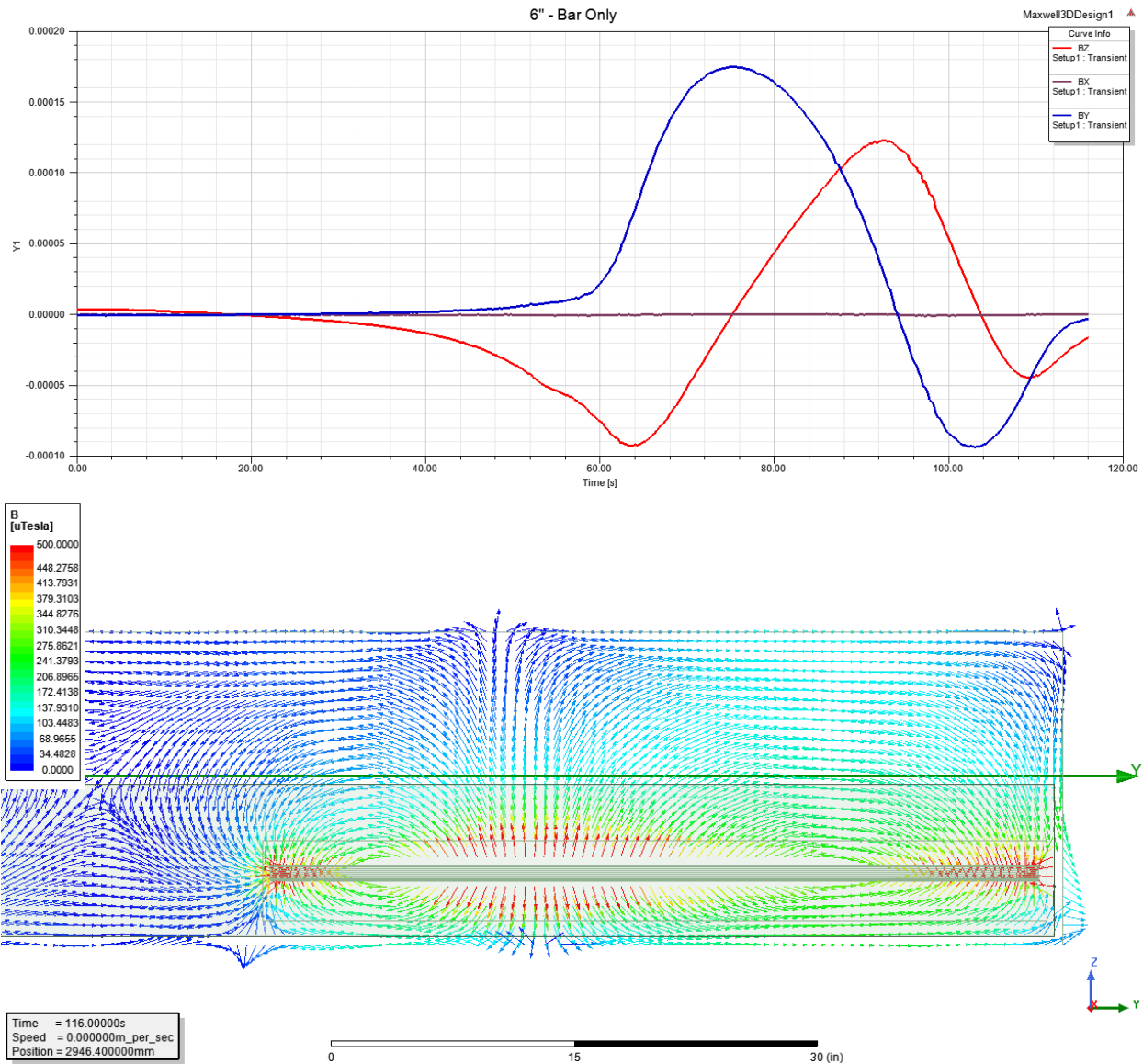


Figure C-17: Analysis results for magnetizing a bar at 6 in. from the magnet.

There is a significant difference in the results when the rod is far from the magnet compared to when it is near the magnet.

At shallow depths (consider 3 in.), the field resembles that of a simple bar magnet with a pole at each end. Looking at the plot of vertical flux over time, one sees a sharp positive signal as the tip of the bar passes under the sensor and a sharp negative signal as the trailing end passes. While the bar is under the sensor, the longitudinal flux is relatively uniform.

When the rod is deep (consider 4 in.), there appear to be three poles, one with outward flux in the middle and inward flux at the two ends. Looking at the plot of flux versus time, the signal is negative as tip of the bar passes the sensor (opposed to positive at shallow depths). The signal then goes positive as the central (outward) pole passes below the sensor and then returns negative as the trailing edge of the rod passes. The longitudinal flux signal flips from positive to negative as the central pole passes below the sensor.

Results from analyses at depths between these extremes show a complex transition with the change generally occurring at a depth of 3.3 in. An attempt to explain these observations will be presented in the following section.

C.1.2.2 Longer Rod

Several additional analyses were performed to determine the effect the rod length on the results. The rod length was increased to 96 in. with the tip located 24 in. left of center and the sensor at 144 in. right of center. The tip passes under the sensor at 168 seconds and the trailing edge passes at 264 sec. The following figures (Figure C-18 to Figure C-21) show the results from these runs.

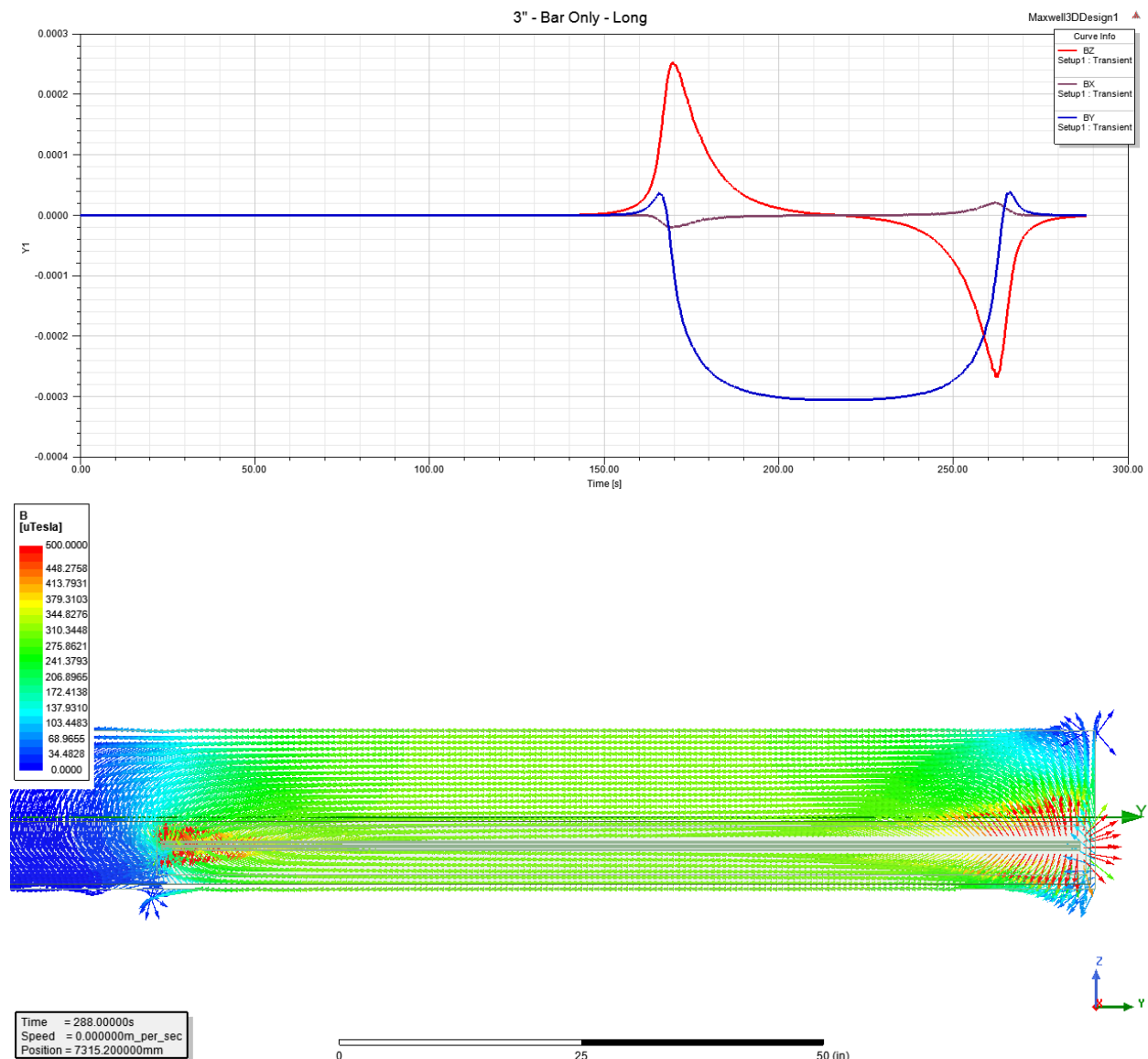


Figure C-18: Analysis results for magnetizing a 96-in. bar at 3 in. from the magnet.

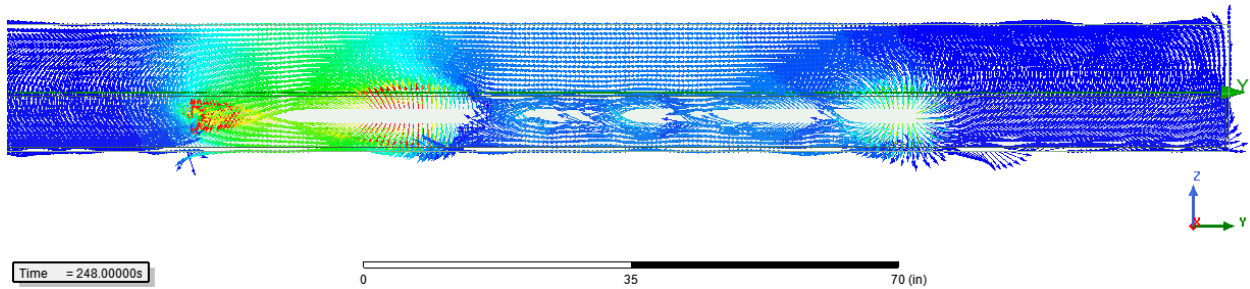
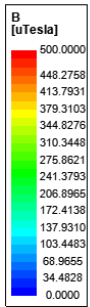
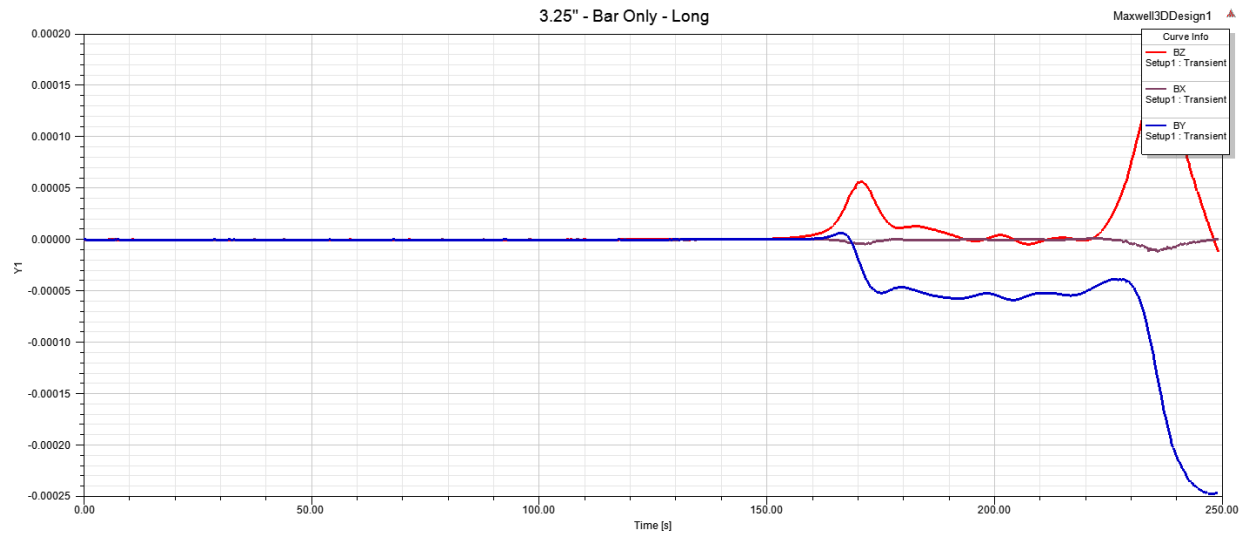


Figure C-19: Analysis results for magnetizing a 96-in. bar at 3.25 in. from the magnet.

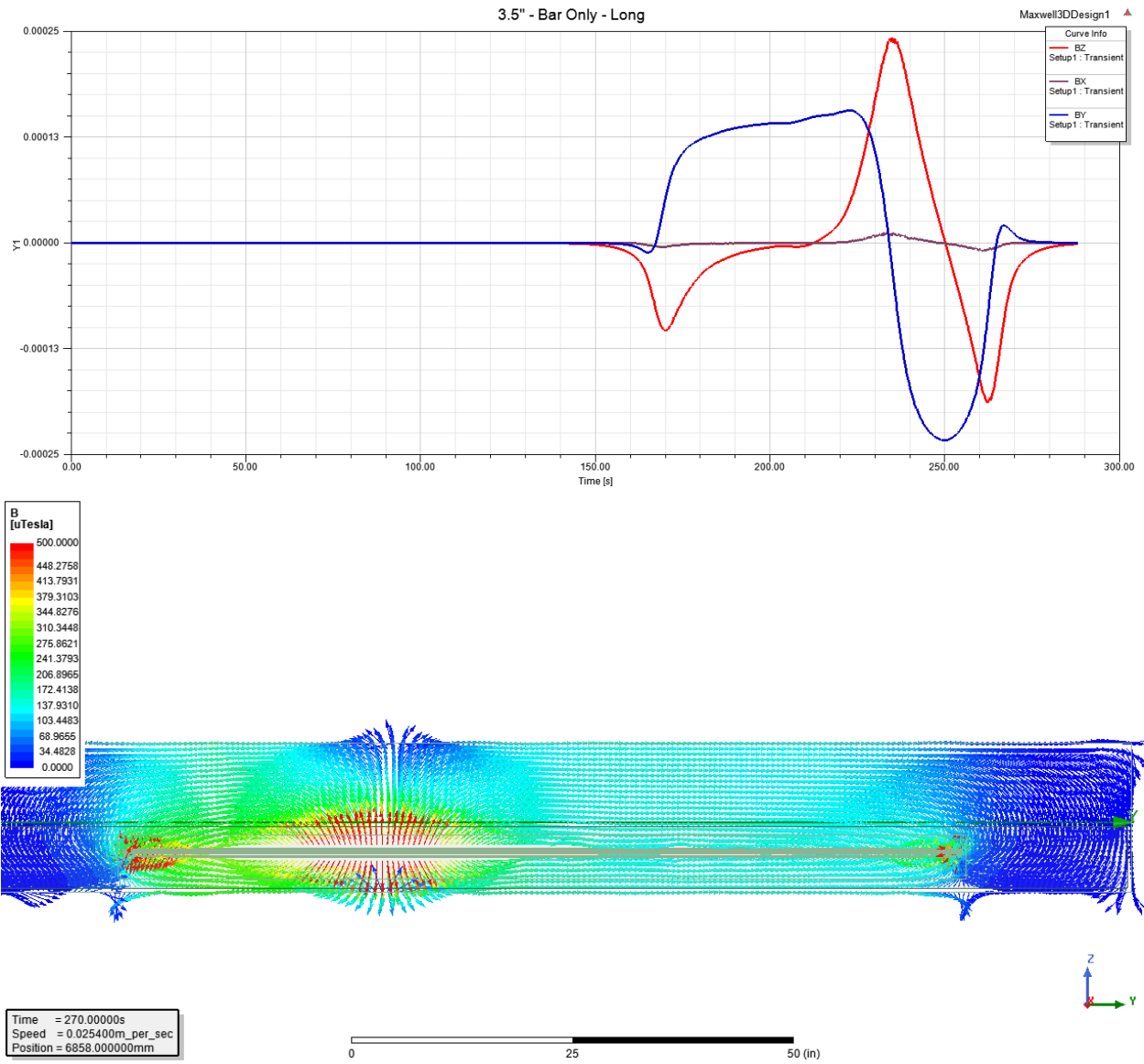


Figure C-20: Analysis results for magnetizing a 96-in. bar at 3.5 in. from the magnet.

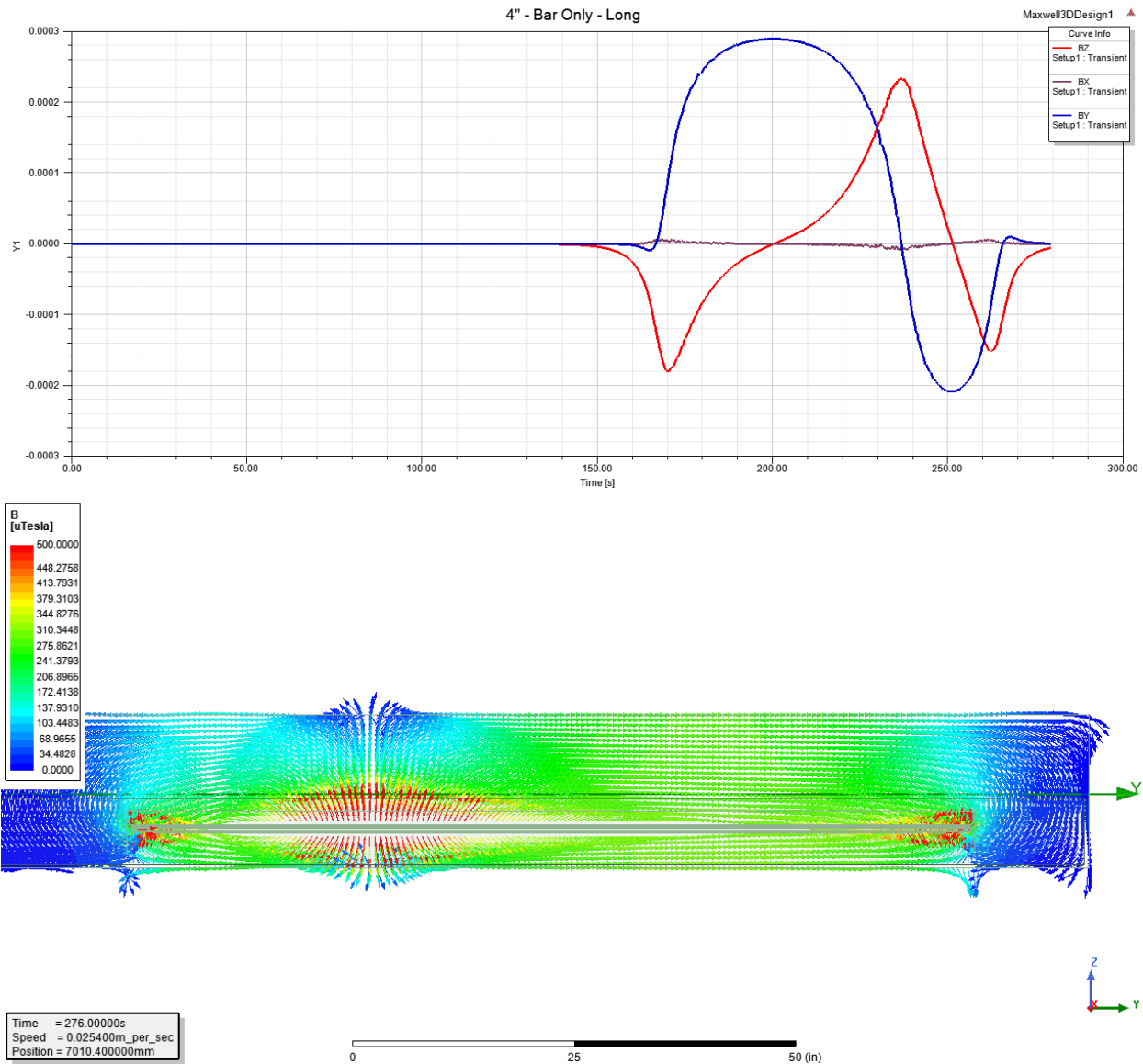


Figure C-21: Analysis results for magnetizing a 96-in. bar at 4 in. from the magnet.

For the case of the shallow bar, the results are similar to the short bar analysis and resemble a simple bar magnet with poles at each end. The primary observation to be made is that for the deep case, the interior pole occurs near the trailing edge of the bar. Note that the same distance, from the trailing edge to the pole, was observed in the short bar analysis as well, but just happened to coincide with the midpoint of the bar. The conclusion is that the apparent interior pole is simply an end effect that can be expected to occur for all lengths of the bar.

C.1.2.3 Depth Effect

The magnetic field created by the magnet (the orientation used in this analysis) points from right to left. The field flows out of the right pole and into the left pole. Below is a series of images showing the flux in the bar as the bar passes below the magnet (Figure C-22 to Figure C-26).

Figure C-22 shows the first stage of the bar passing under the magnet. At this point, tip of the rod is still to left of magnet and flux in bar points from left to right, flowing towards the inward left pole of the magnet.

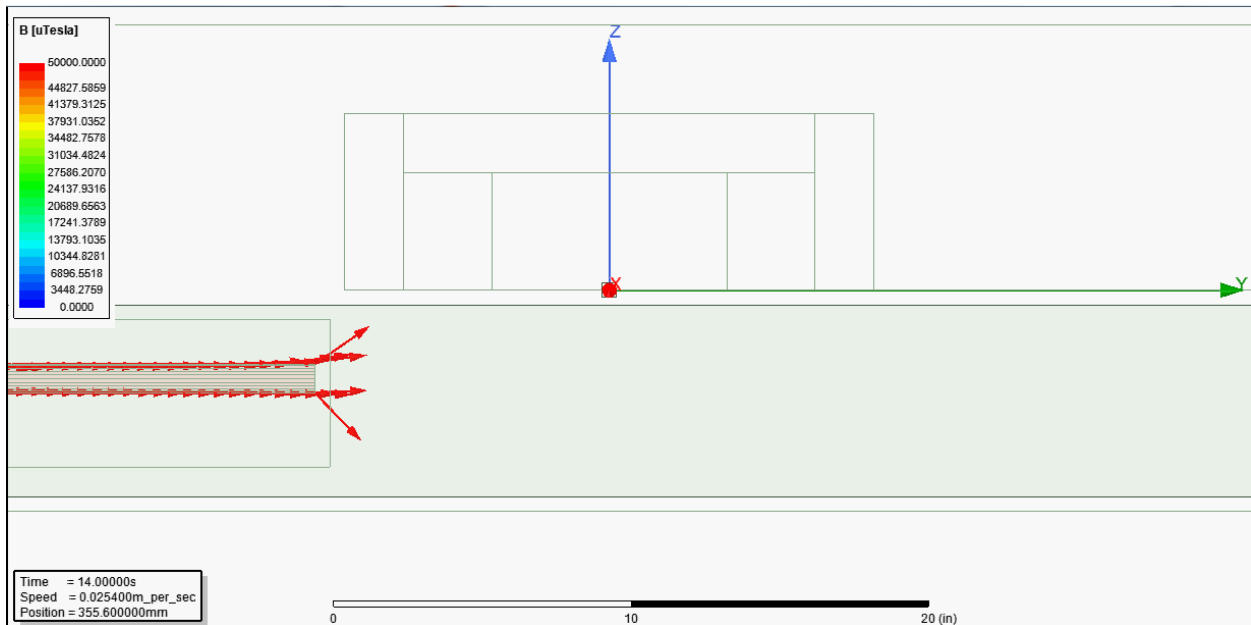


Figure C-22: Stage 1 of bar passing 3 in. under the magnet.

Figure C-23 shows the second stage, where the tip of the rod is between the poles of the magnet. Flux in the rod to the left of the left pole still flows from left to right, but flux in the rod between the poles now flows from right to left, matching the field that flows from the right pole towards the left pole

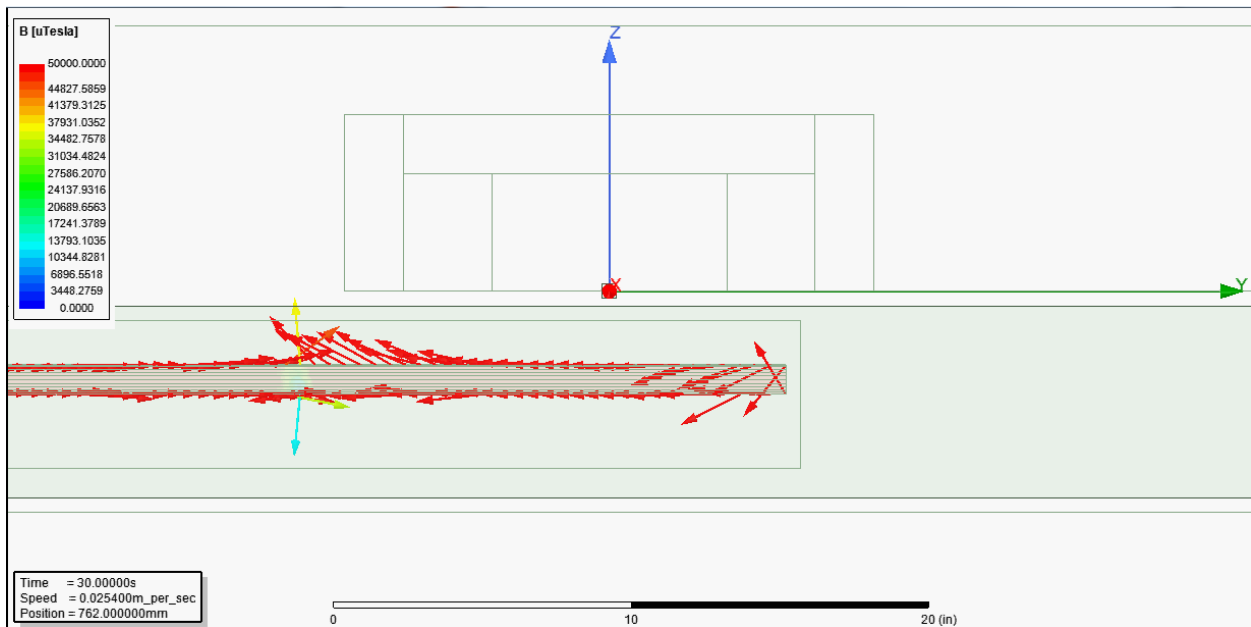


Figure C-23: Stage 2 of bar passing 3 in. under the magnet.

In Figure C-24, the leading tip has now passed beyond the right (outward) pole. It should be noticed that the flux lines directly below the pole deviate downward being pushed away

from the pole. Flux in the rod between the poles, and to the left of the magnet, are similar to what was seen in the previous observations. However, flux in the rod to the right of the magnet has changed direction and then flows to the right, away from the outward pole.

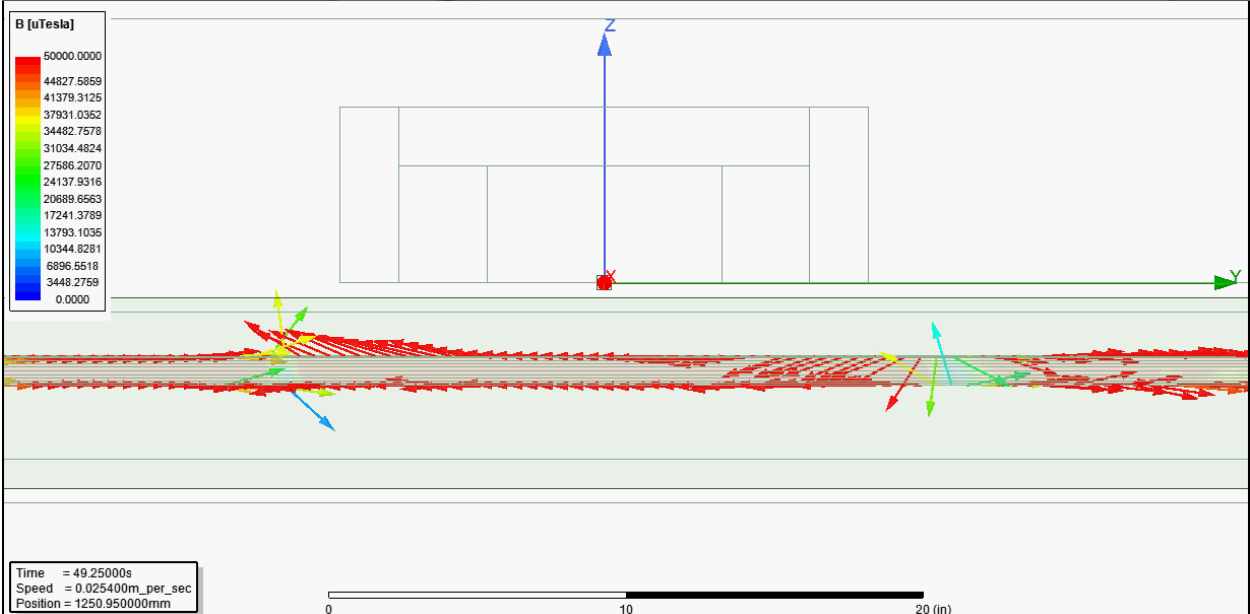


Figure C-24: Stage 3 of bar passing 3 in. under the magnet.

In Figure C-25, Stage 4, the trailing edge is now between the poles. Finally, Figure C-26 shows the trailing edge has cleared the right edge of the magnet. The final flux in the rod is pointing from left to right along the entire length of the rod.

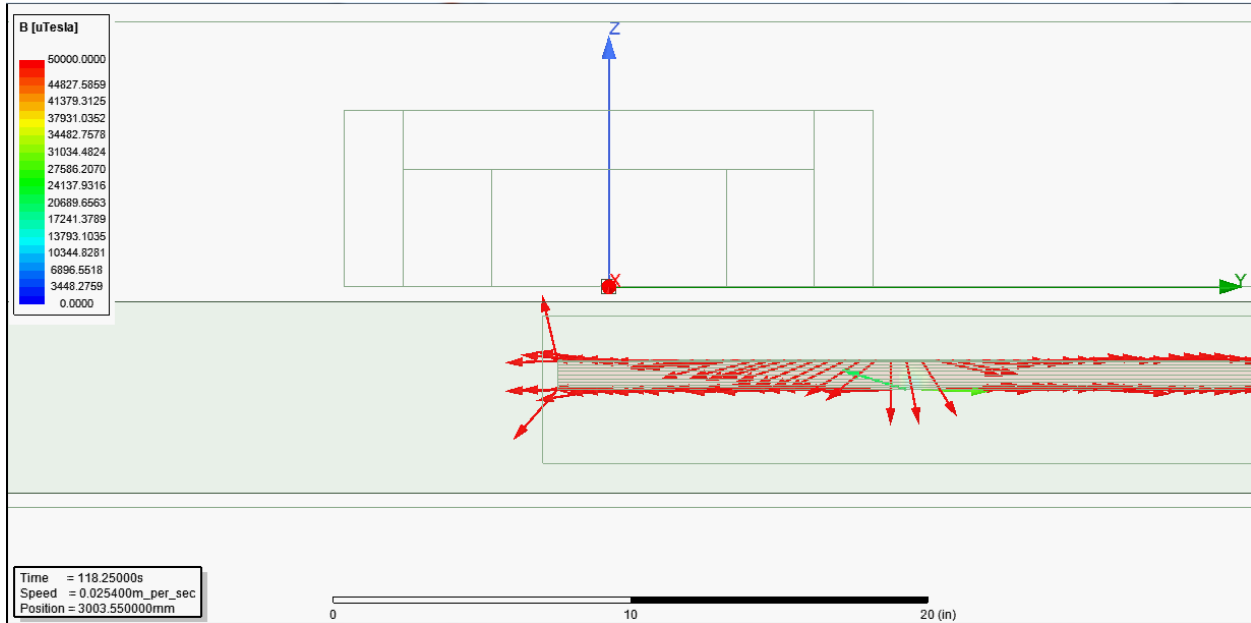


Figure C-25: Stage 4 of bar passing 3 in. under the magnet.

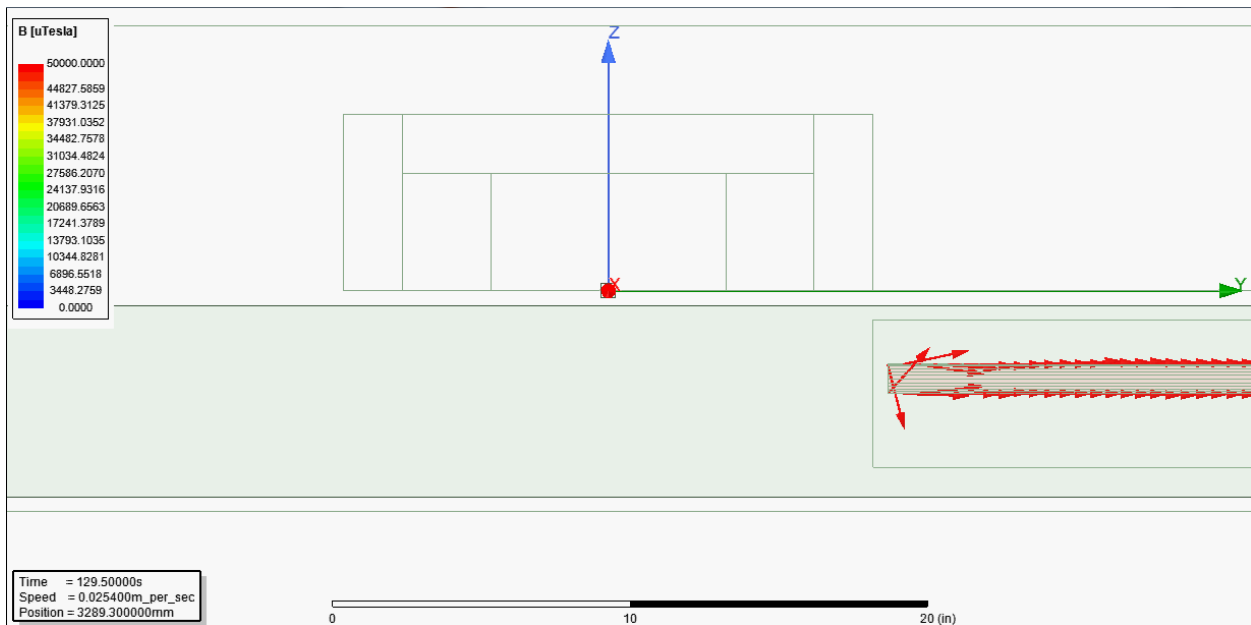


Figure C-26: Stage 5 of bar passing 3 in. under the magnet.

This gives rise to the observations in the previous section where the rod had the appearance of a simple magnet with a pole at each end and uniform field. A similar sequence is presented for the case of a deeper rod. Figure C-27 shows the first stage, where the tip of the rod is to the left of the magnet, the resulting flux in the bar is similar to previous section, pointing from left to right (towards the inward pole).

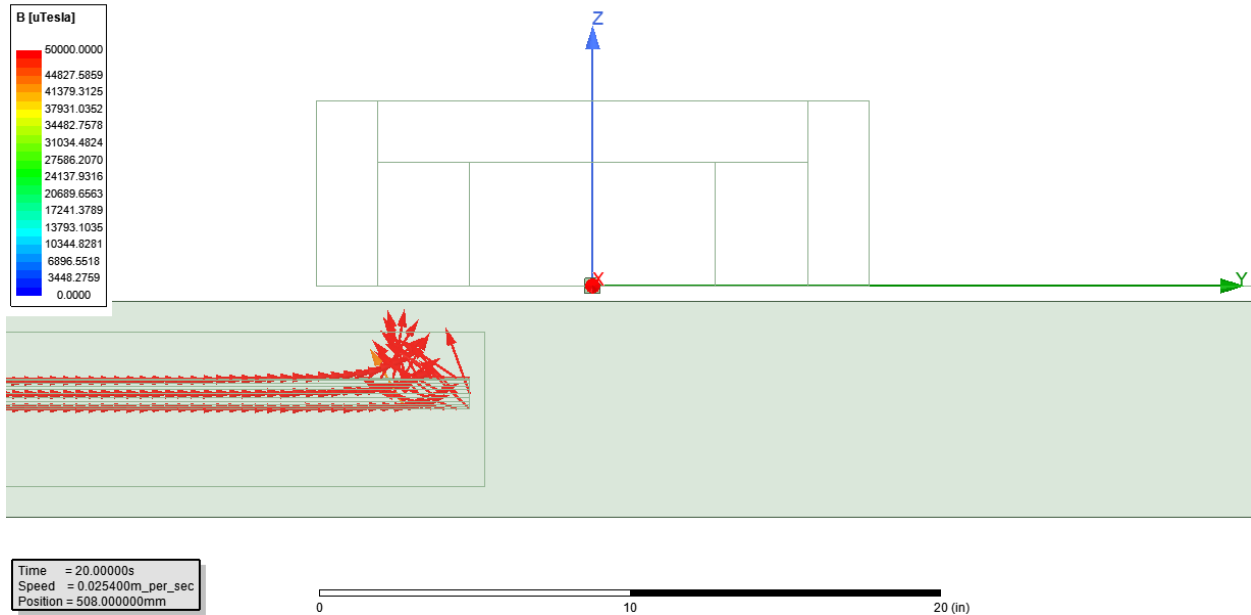


Figure C-27: Stage 1 of bar passing 4 in. under the magnet.

In Figure C-28, The tip is between poles with flux in the rod changed direction to match the field flowing from the right pole towards the left pole (similar observation).

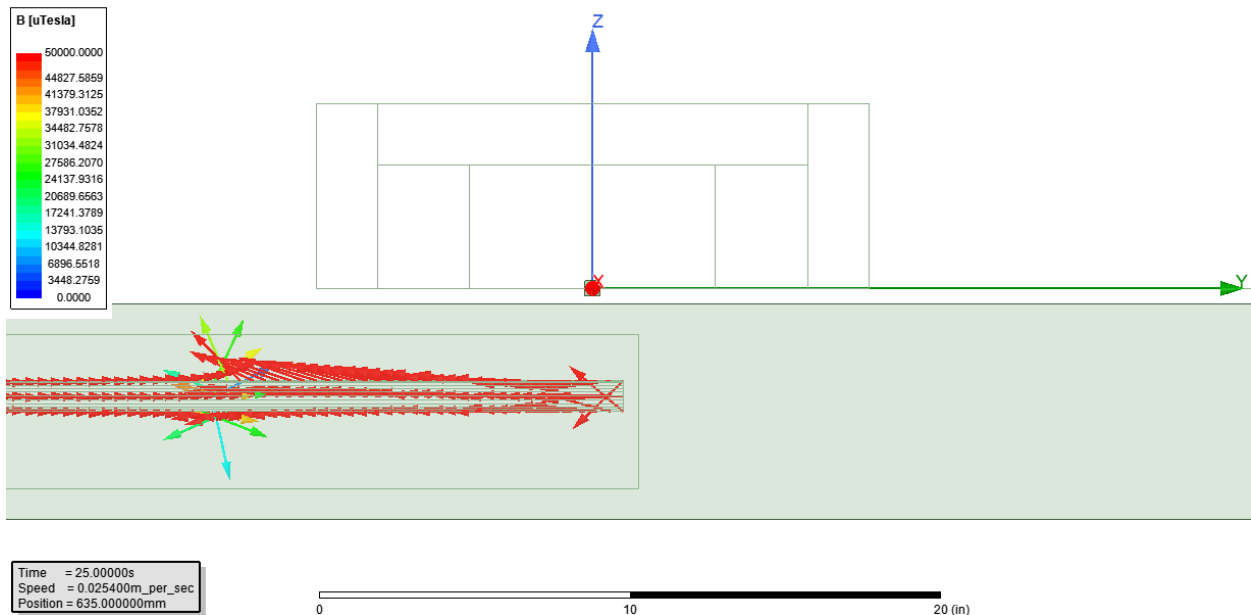


Figure C-28: Stage 2 of bar passing 4 in. under the magnet.

The difference occurs when the tip has passed beyond the right (outward) pole (Figure C-29). Rather than pointing from left to right, the flux still points from right to left, albeit with a lower magnitude than the flux in the rod between the poles. The suggested explanation is that at greater depths, the field (outward field from right pole) is not great enough to totally overcome and reverse the remanent magnetization that was introduced into the rod when it was between the poles. Rather than reversing the direction of the flux, it simply reduced its magnitude.

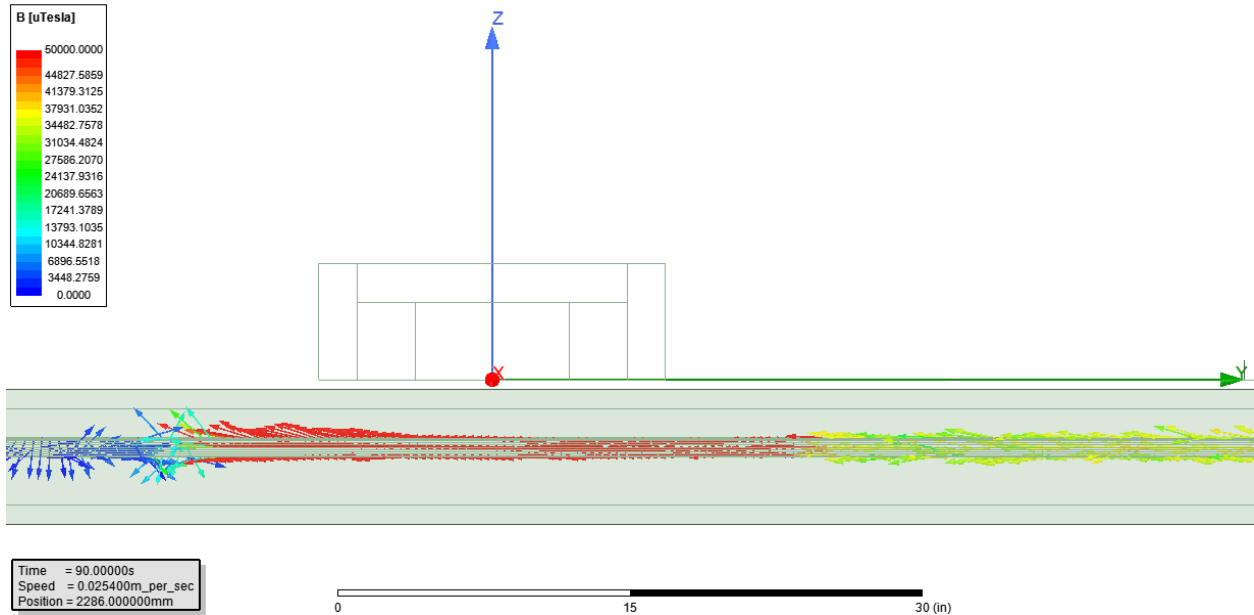


Figure C-29: Stage 3 of bar passing 4 in. under the magnet.

As the trailing end of the rod leaves the influence of the left pole (Figure C-30), the right pole begins to have greater influence over the flux in the rod. Note the "pile-up" that is beginning to occur to the right of the magnet.

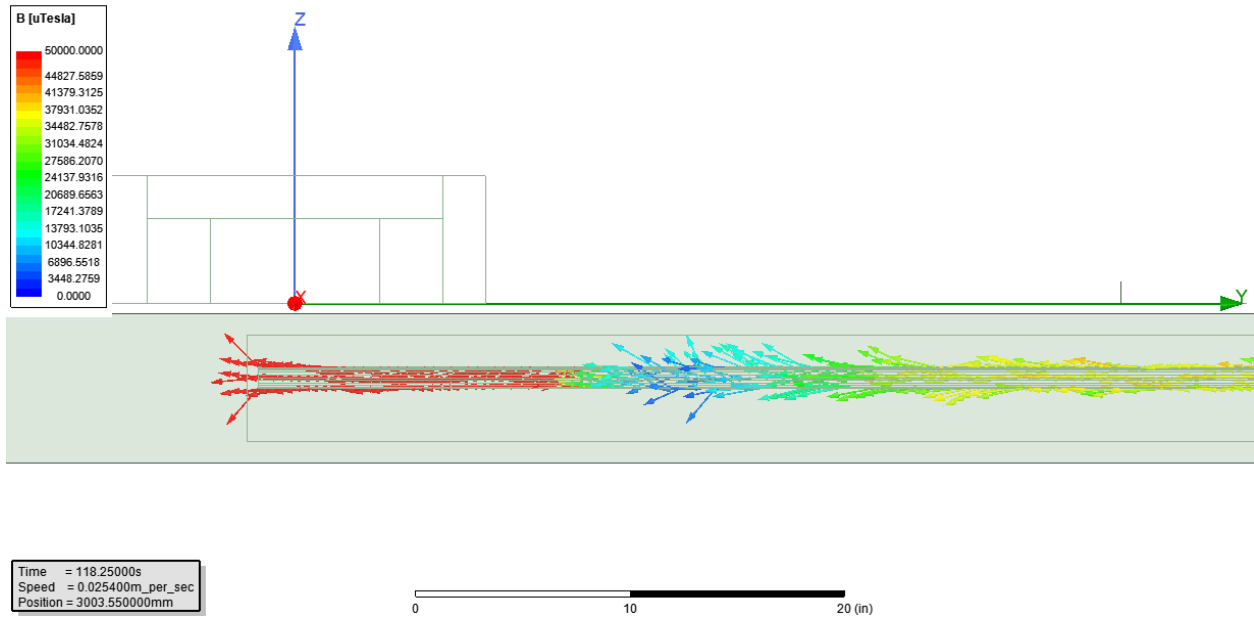


Figure C-30: Stage 4 of bar passing 4 in. under the magnet.

As the rod continues, the flux eventually reverses direction as the trailing edge gets far enough away from the influence of the left pole (Figure C-31). This situation is similar to that observed when the rod was shallow, and the right pole had greater influence due to its closer proximity.

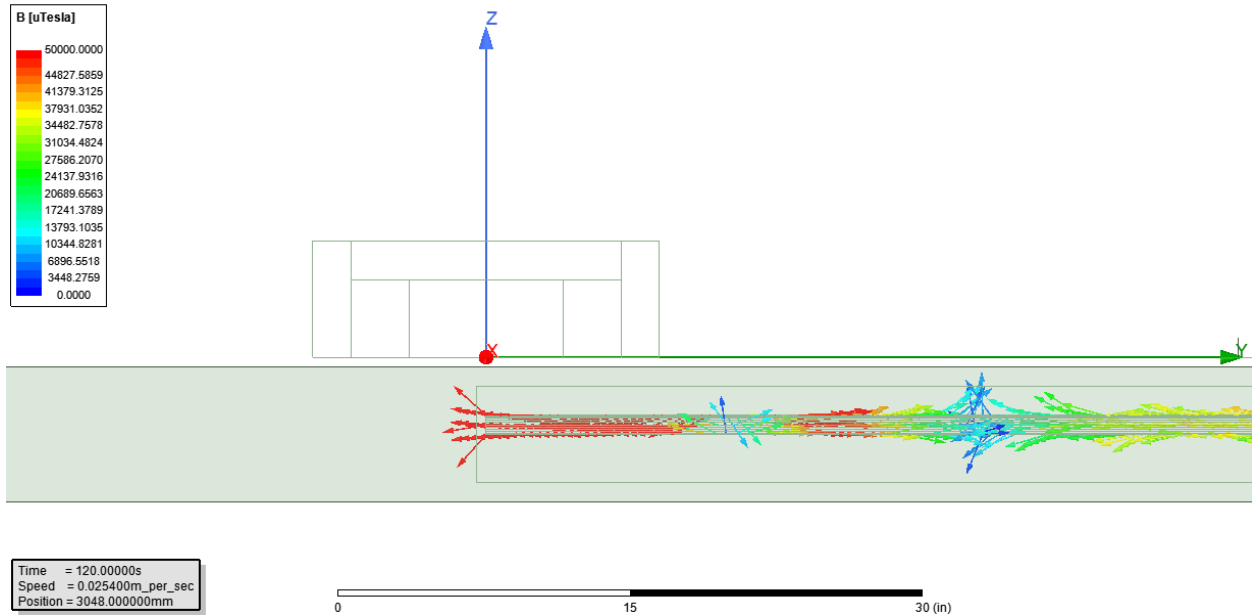


Figure C-31: Stage 5 of bar passing 4 in. under the magnet.

Finally, the trailing edge has passed the magnet entirely and flux in a short region of the rod near the trailing edge is pointing from left to right while the flux in the remainder of the rod points from right to left and there is an outward region of flux established where this change in direction occurs. This is the final remanent field that was observed in the previous section (Figure C-32).

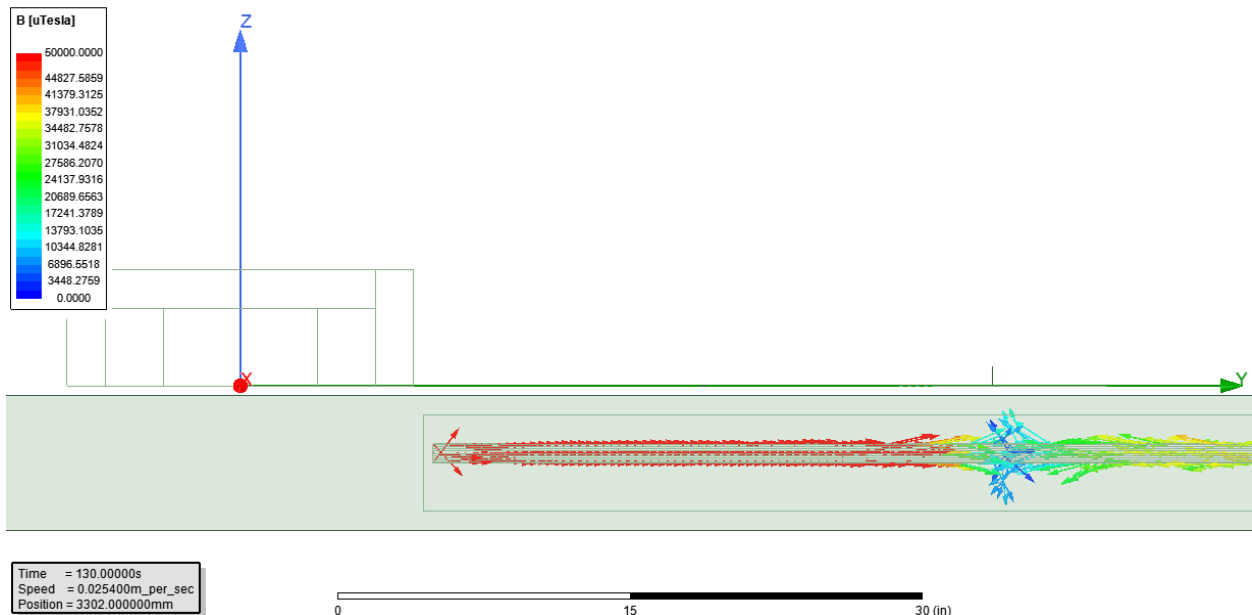


Figure C-32: Stage 6 of bar passing 4 in. under the magnet.

C.1.3 Damage Study

The previous study only considered solid undamaged reinforcement all alone. The ultimate goal is to recognize damaged prestressing reinforcement with the existence of additional bars in an actual structure. Therefore, a suite of analyses was run to have a

cursory look at the response under various conditions. The variables considered were damage (yes / no), depth (3 in. / 4 in.), transverse bars (none, centered, offset). A full factorial study was performed, and the results are presented in the following figures. For each combination, the resulting plots of flux (in three directions) versus time are presented similar to the charts presented in the plain bar depth study (Figure C-33 to Figure C-44).

The damage consisted of a 3/4 in. deep notch with 45-degree sides. The transverse bars are 3/8 in. diameter, 16 in. long, and spaced at 6 in. apart. There is a 1/4 in. clear gap between the main bar and transverse bar. For the case of the offset transverse bars, 7 in. is cut off from one side meaning the transverse bar extends 1 in. on one side and 8 in. on the other side of the main bar. Simple observations are provided after each plate and a more comprehensive discussion of results is provided in the section after all plots.

C.1.3.1 Depth – 3 inches

This result is the baseline bar only result from the previous with no damage induced to the strand.

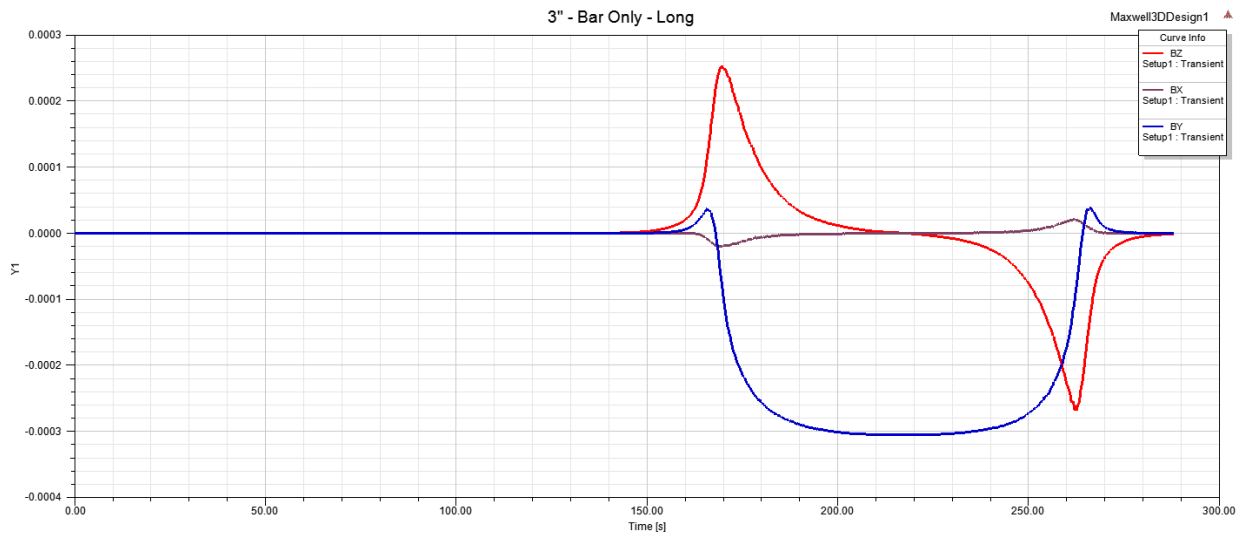


Figure C-33: Results from 3-in. depth, no damage, bar only.

The two transverse bar can be seen as ripples when transverse bars are centered with no damage induced to the strand.

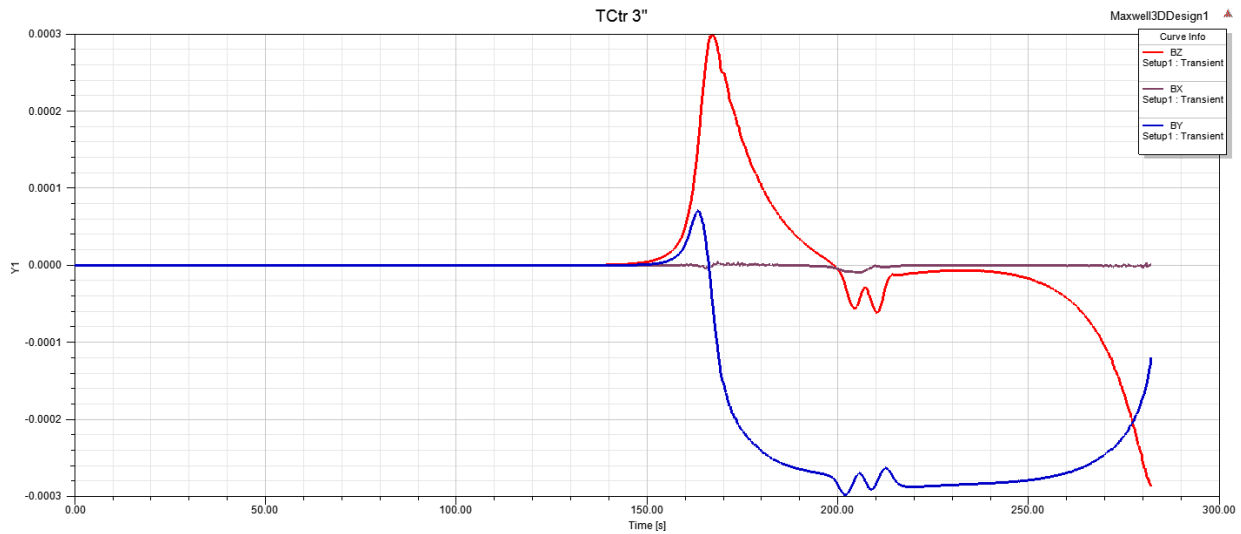


Figure C-34: Results from 3-in. depth, no damage, centered transverse.

Due to the proximity of the ends of the transverse bars, there is some flux in the transverse direction when transverse bars are on offset with no damage induced to the strand.

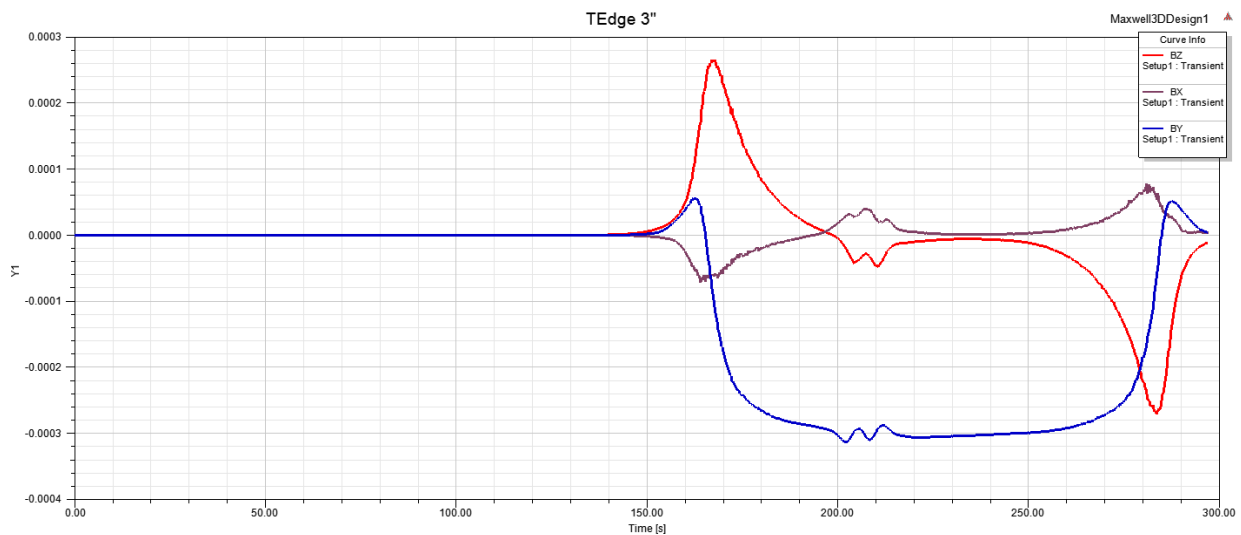


Figure C-35: Results from 3-in. depth, no damage, offset transverse.

When damage was only induced to the strand with no transverse reinforcement, there is no discernible difference in these results compared to the no-damage case.

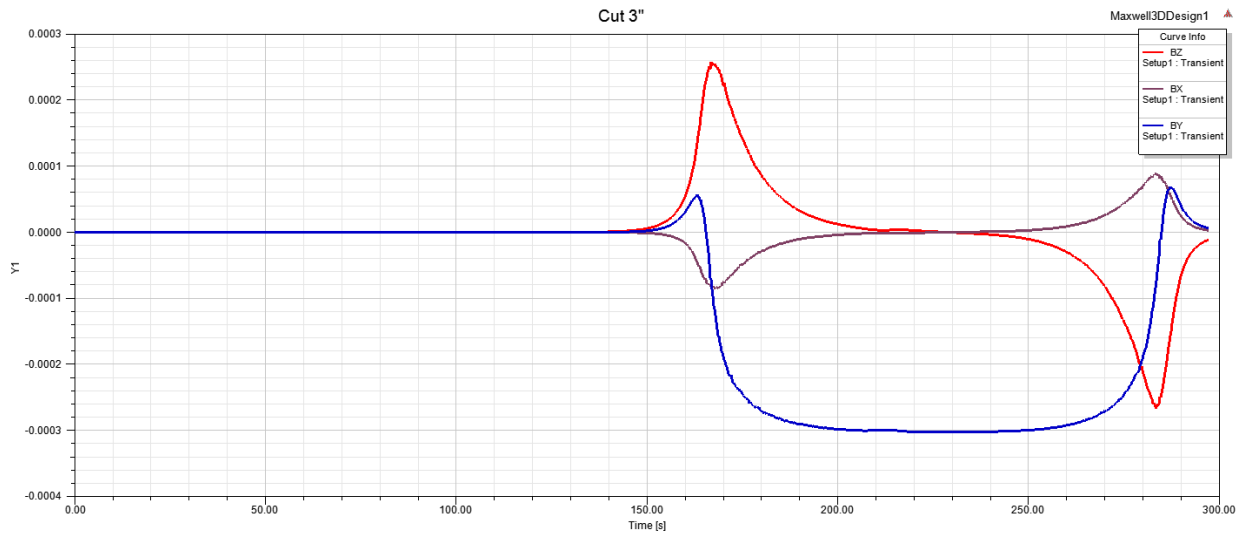


Figure C-36: Results from 3-in. depth, damaged, bar only.

When damage is induced, and transverse reinforcement is centered there is no discernible difference in these results compared to the no-damage case.

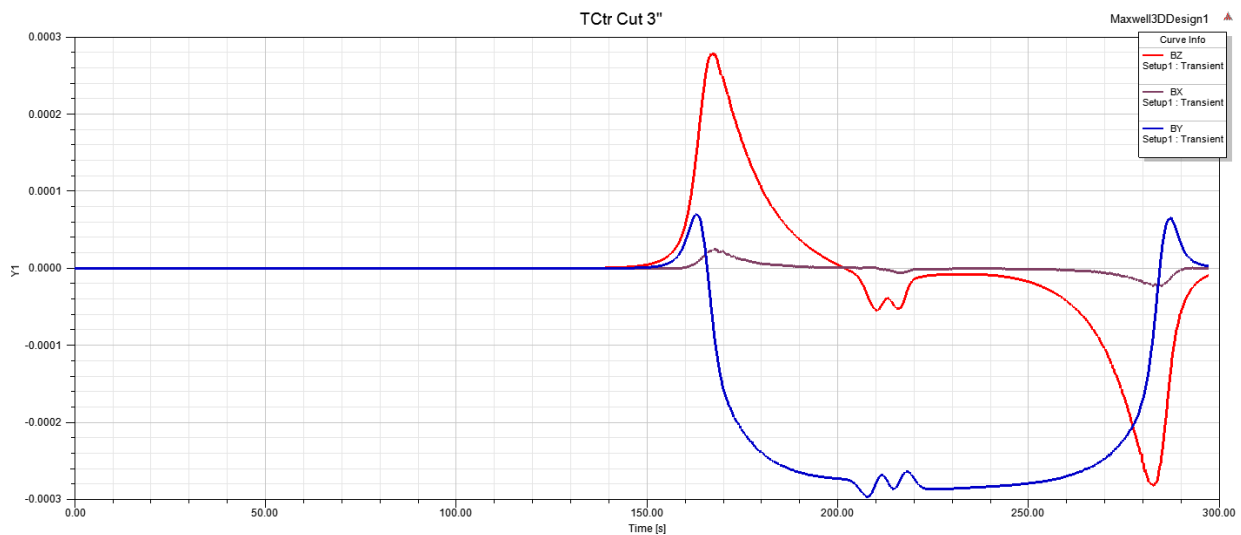


Figure C-37: Results from 3-in. depth, damaged, centered transverse.

When damage is induced to the strand and the transverse reinforcement is on offset, there is no discernible difference in these results compared to the no-damage case.

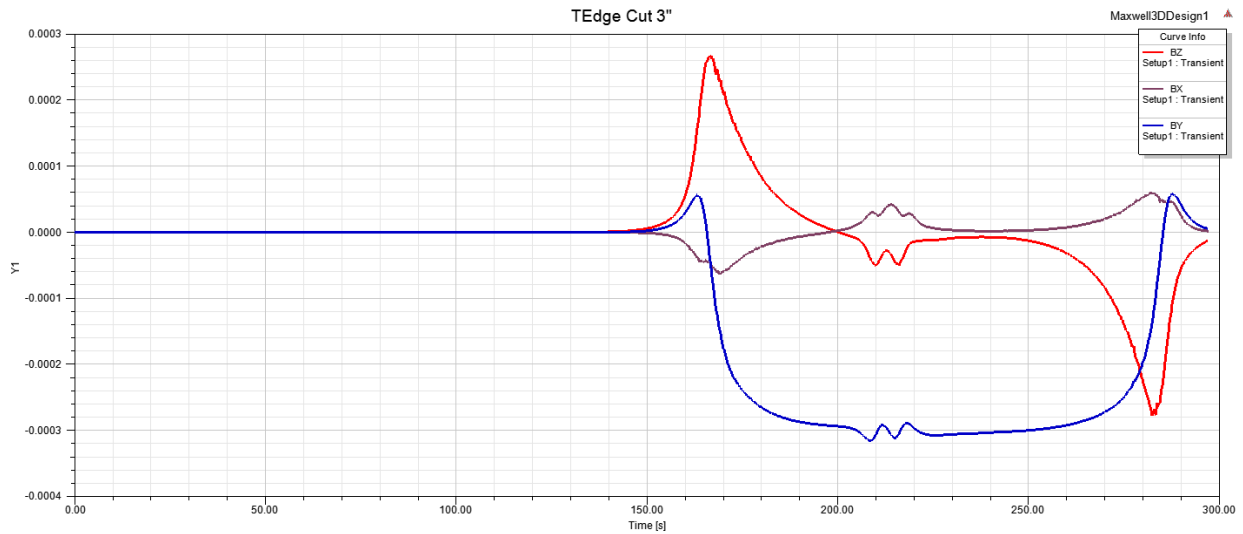


Figure C-38: Results from 3-in. depth, damaged, offset transverse.

C.1.3.2 Depth – 4 inches

This result is the baseline bar only result from the previous study. Note the difference in signal compared to the 3 in. depth. This difference was discussed at length in the Section C.1.2.

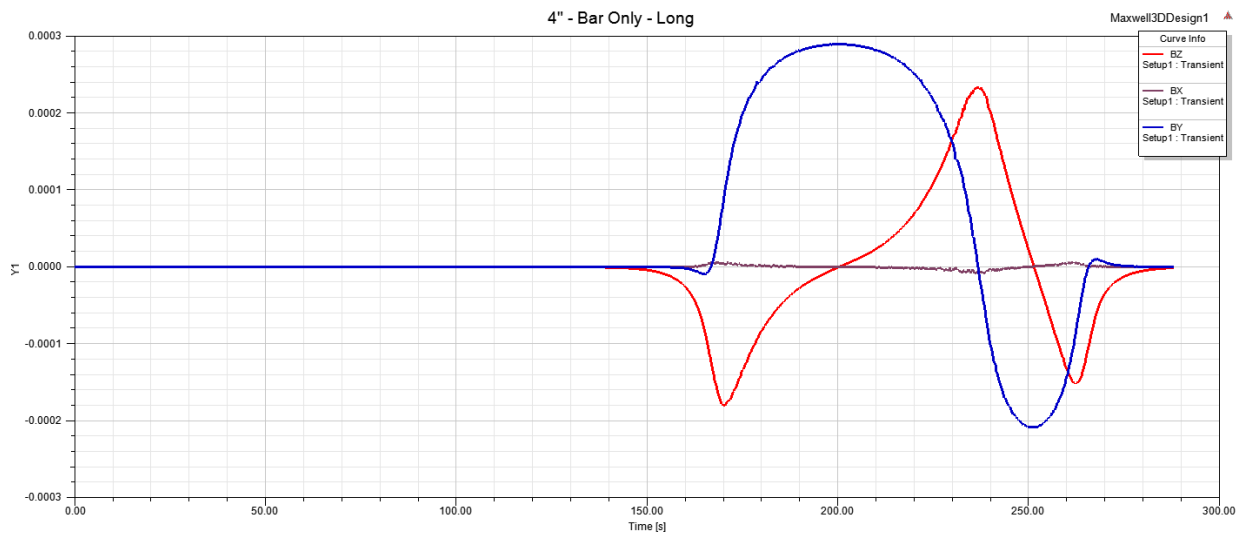


Figure C-39: Results from 4-in. depth, no damage, bar only.

The presence of the transverse bars can be seen as slight ripples in the response.

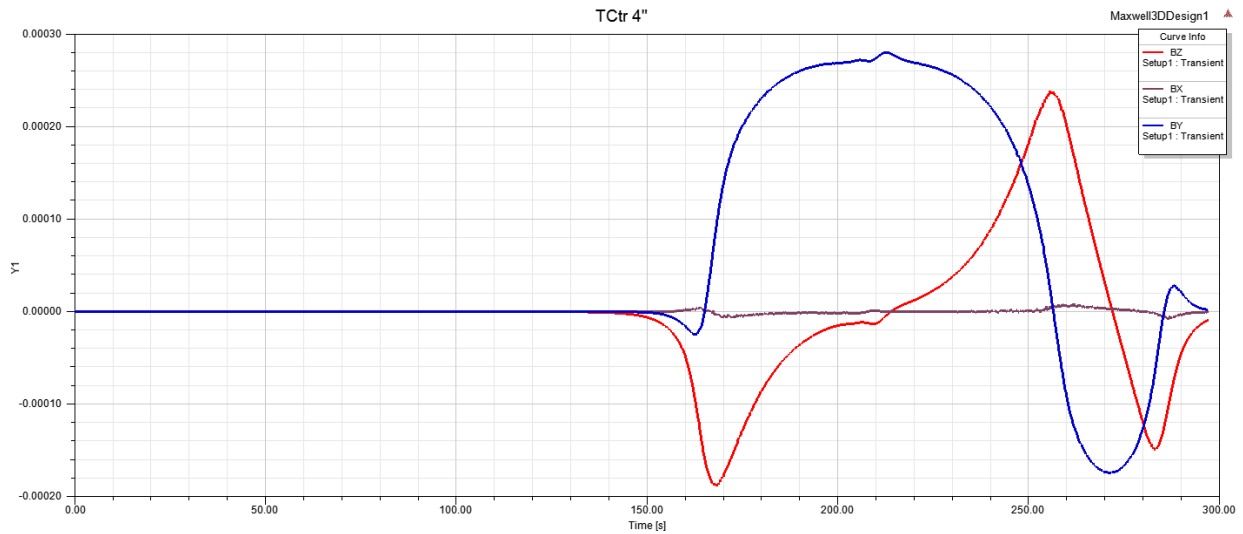


Figure C-40: Results from 4-in. depth, no damage, centered transverse.

In these results, it appears the proximity of the ends of the transverse bars has a significant and complex effect on the signals.

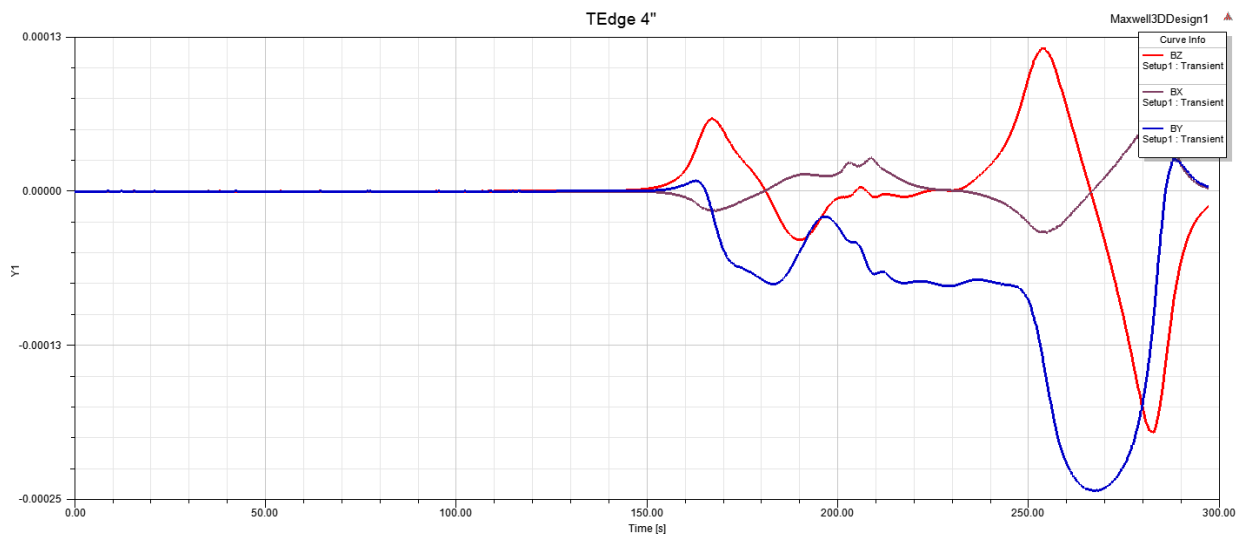


Figure C-41: Results from 4-in. depth, no damage, offset transverse.

The presence of damage has an obvious effect on the signal.

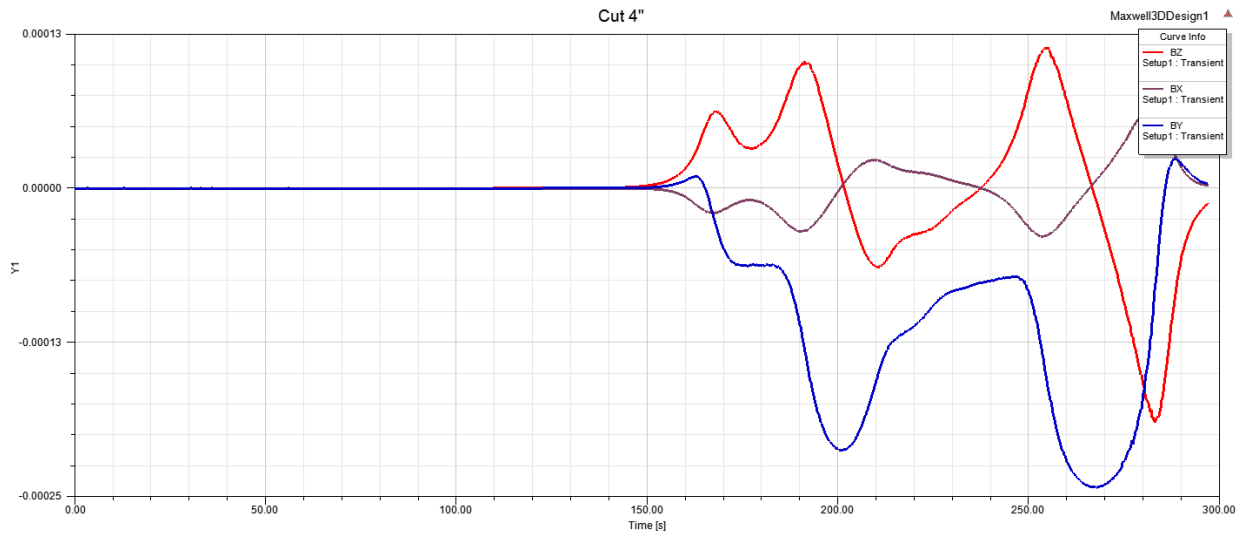


Figure C-42: Results from 4-in. depth, damaged, bar only.

The presence of transverse bars along with the damage changes the resulting signal.

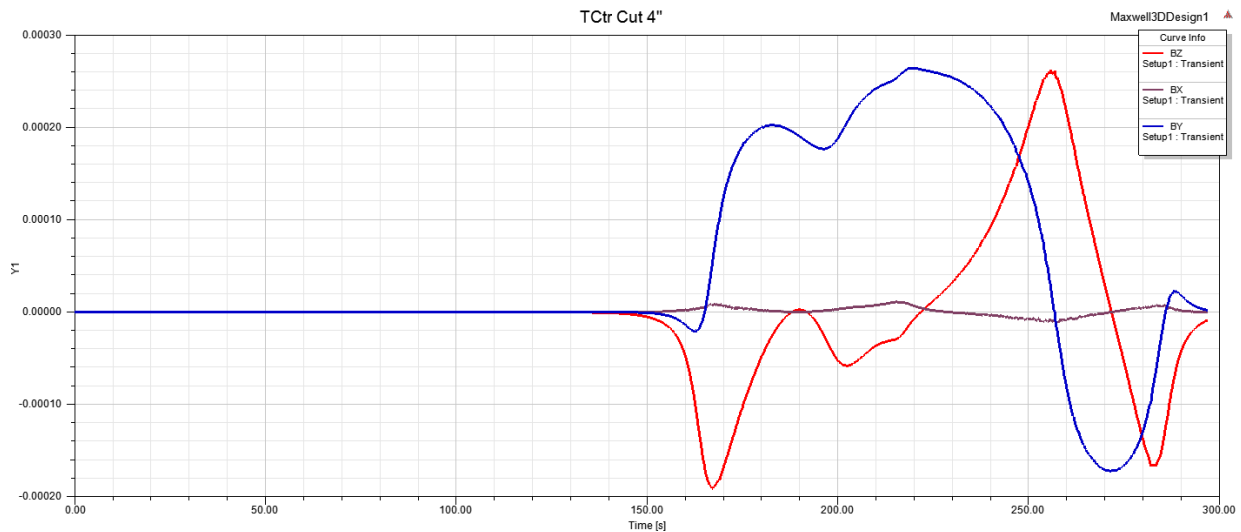


Figure C-43: Results from 4-in. depth, damaged, centered transverse.

Adding the end effects from the transverse reinforcement further complicates the response. At shallow depths, the damage is not evident in the response, the presence of transverse bars creates a slight ripple in the response, and end effects result in some transverse flux. When the strand is deep, the response gets very complex in the presence of damage and transverse reinforcement.

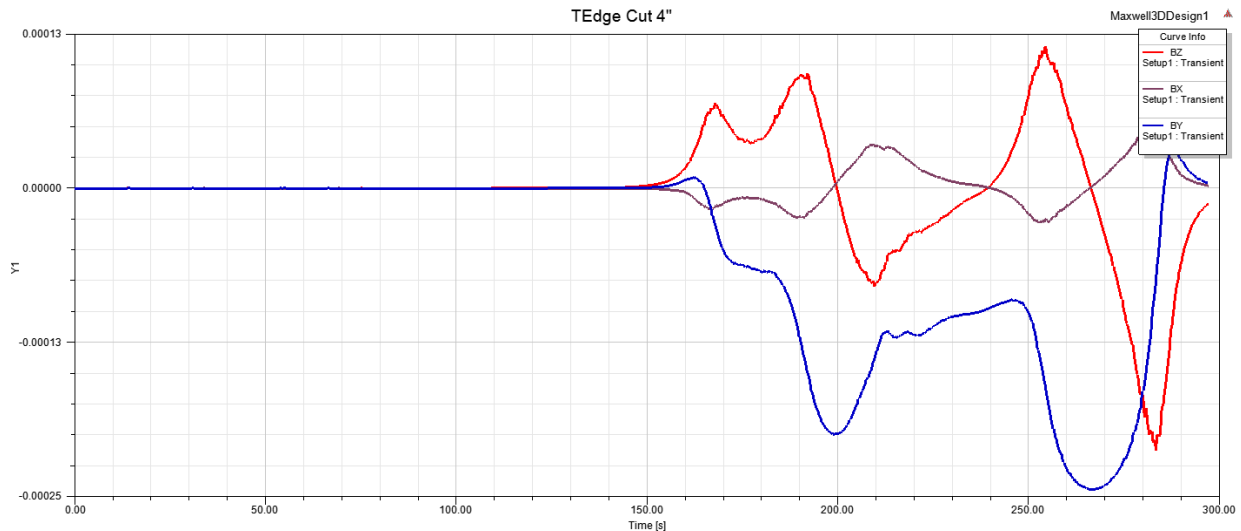


Figure C-44: Results from 4-in. depth, damaged, offset transverse.

C.1.4 Observation and Conclusions

Several different studies were carried out that numerically simulated the MFL method for in-situ flaw detection in concrete reinforcement with primary intent being the inspection of post-tensioning strand or rod. The analyses were intended to determine the feasibility of numerically simulating the MFL method and identify important parameters that have the greatest impact on the observed results. Below is a list of conclusions that were drawn as a result of these studies.

C.1.4.1 Modeling

- The software (ANSYS Maxwell) is capable of simulating passive sensing methods.
- To simulate the passive sensing method a full transient (time-stepping) analysis must be performed. However, this type of analysis can be very intensive and lengthy.
- To have an accurate analysis, the material properties, including B-H curves, for different element should be available.

C.1.4.2 Depth Study

- There is a significant difference in the results when the rod is far from the magnet compared to when it is near the magnet. This was also observed in experiments performed under Section 4.
- At shallow depths (consider 3 in.), the field resembles that of a simple bar magnet with a pole at each end.
- When the rod is deeper (consider 4 in.), there appear to be three poles, one with outward flux in the middle and inward flux at the two ends.
- Results from analyses at depths between these extremes show a complex transition with the change generally occurring at a depth of 3.3 in.

C.1.4.3 Damage Study

- At shallow depths, the damage is not evident in the response, the presence of transverse bars creates a slight ripple in the response, and end effects result in some transverse flux.
- When the strand is deeper, the response gets very complex in the presence of damage and transverse reinforcement.
- It should be noted that in these analyses the material properties of PT rod and mild reinforcement have been assumed to be similar. However, experiments have shown significant differences in the amount of saturation in these materials.

C.2 FIELD SIMULATION

C.2.1 Modeling

An in-service bridge was selected for simulation of field conditions. The bridge consists of precast hollow core slabs which were post-tensioned with PT rods. Bridge inspection has suggested that the PT rods may be subjected to corrosion. The details of the bridge are provided in Appendix A.1. The primary area of interest to be modeled is within span 2 of the northbound bridge. The individual span (span 2) of the northbound bridge is composed of several precast hollow core slabs. The rectangle indicates the portion of interest to be modeled (Figure C-45). The dashed line is the tensioning bar.

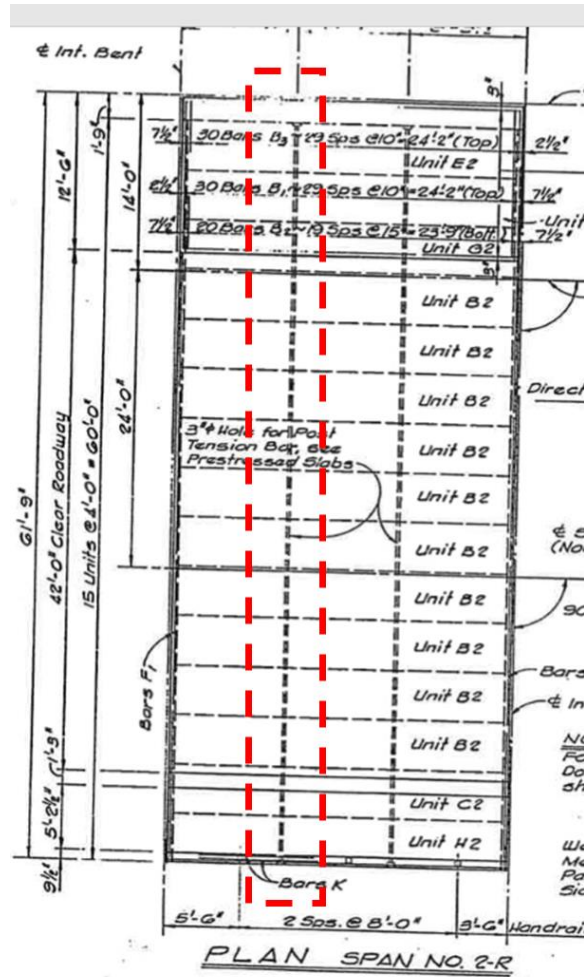


Figure C-45: Plan of span 2 and the highlighted tendon of interest.

Using the methods previously described for the component studies, the entire B2 Unit with all transverse reinforcement and ties has been modeled. The resulting model is shown in Figure C-46. The transverse PT rods are shown extending beyond the first module. In the final model, B2 unit is copied multiple times to encase the PT rod.

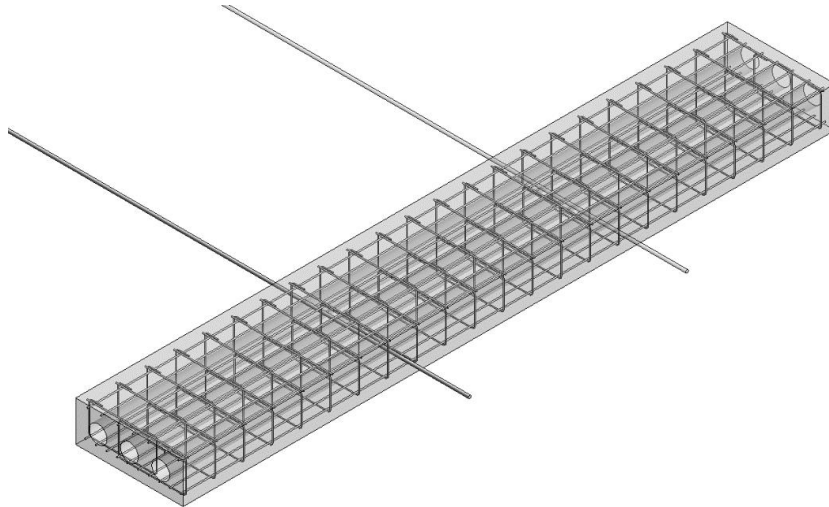


Figure C-46: Model of an individual unit with the PT tendons.

To reduce the size of the model, and subsequent solution time, only a slice of the bridge in the vicinity of the PT bar was retained.

Figure C-47 shows the slice of the bridge with 10 short sections of B2 units and transverse PT.

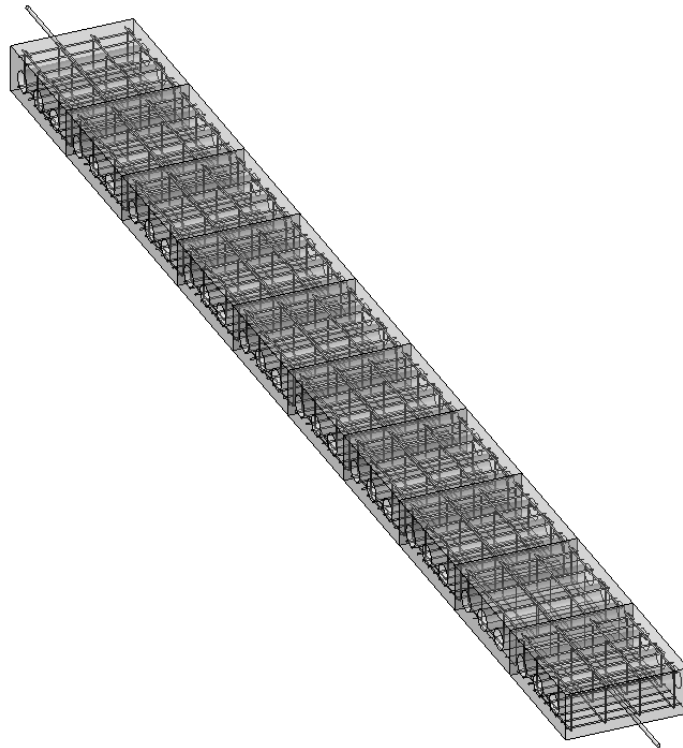


Figure C-47: Model of a slice of bridge showing 10 modules and a PT tendon.

Figure C-48 is a close-up of the model. Note the presence of ties and closure bars in close proximity to the PT bars. An important note is the number of times the bars parallel to the PT bars start and end. Recall that in the component studies, the ends of bars create complexity in the resulting signal.

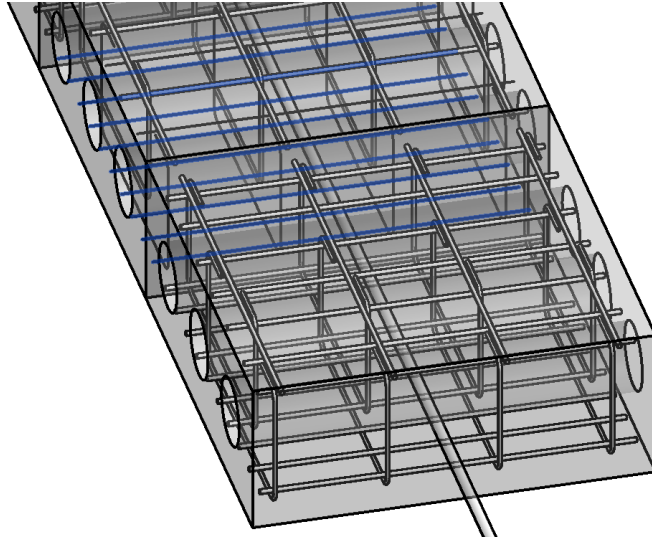


Figure C-48: Close-up of the model.

Damage to the PT Bar was assumed to be a full break with 6 in. of separation between the ends. This matches the borescope findings from the actual structure.

C.2.2 Results

Figure C-49 shows a snapshot of the resulting flux field obtained from the analysis for the models with full details. The flux within the bar is shown in the bottom figure. Due to their complexity, these plots are not useful on their own, but different snapshots can be examined at various points in time to try and explain the flux plots that are shown in the following section.

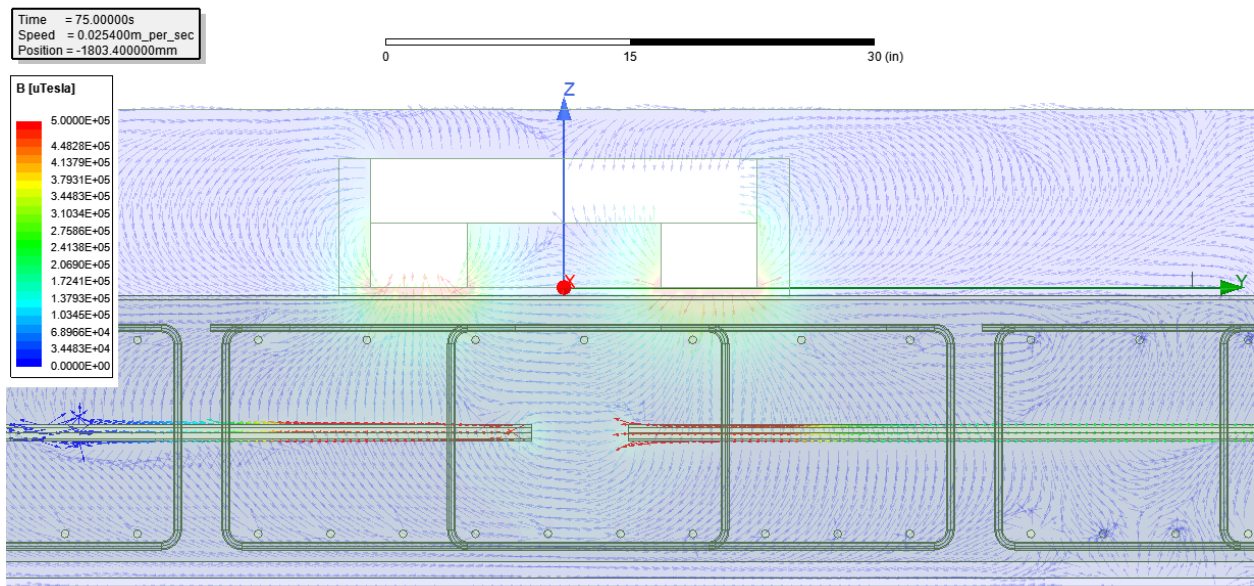
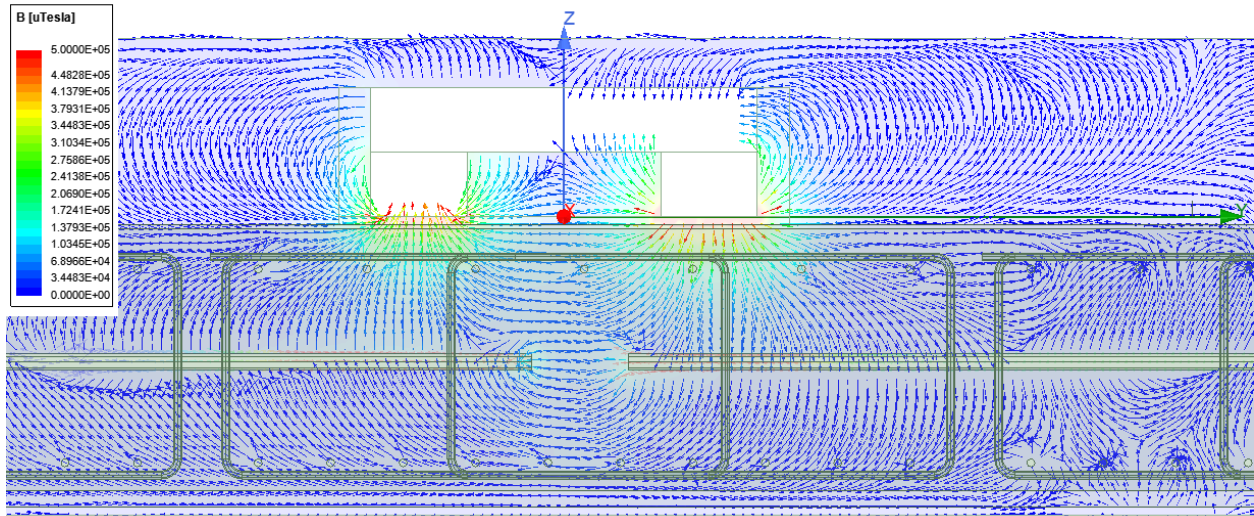


Figure C-49: Magnetic field from the magnet around the bar (top) and in the bar (bottom).

A second model was developed and analyzed in which all the ties and closure bars parallel to the PT bar were removed. The Figure C-50 below shows a flux plot from the analysis.

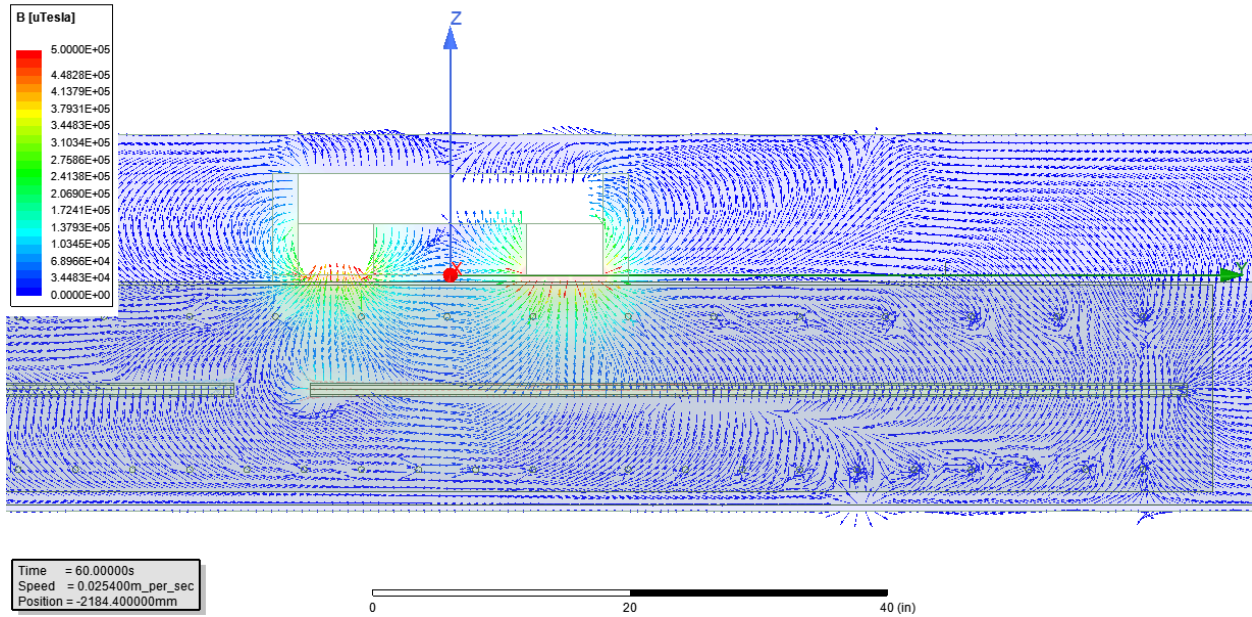


Figure C-50: Magnetic field in models without stirrups.

The following graphs show the flux measured using the passive method where the measurement occurs far from the magnet. In these plots, the break in the strand passes by the sensor at a time of around 218 seconds. Figure C-51 shows the results from the first model (full detail) and Figure C-52 shows the results from the model without the stirrups. In these models, the magnetization and measurement were done on the top of the bridge. The model without stirrups was stopped early but can be resumed if desired. From the results obtained, it is quite evident that the response is complex, and it was determined that useful information was not going to be obtained. The response due to the various elements present is not a summation of individual effects, but there is the interaction between the elements.

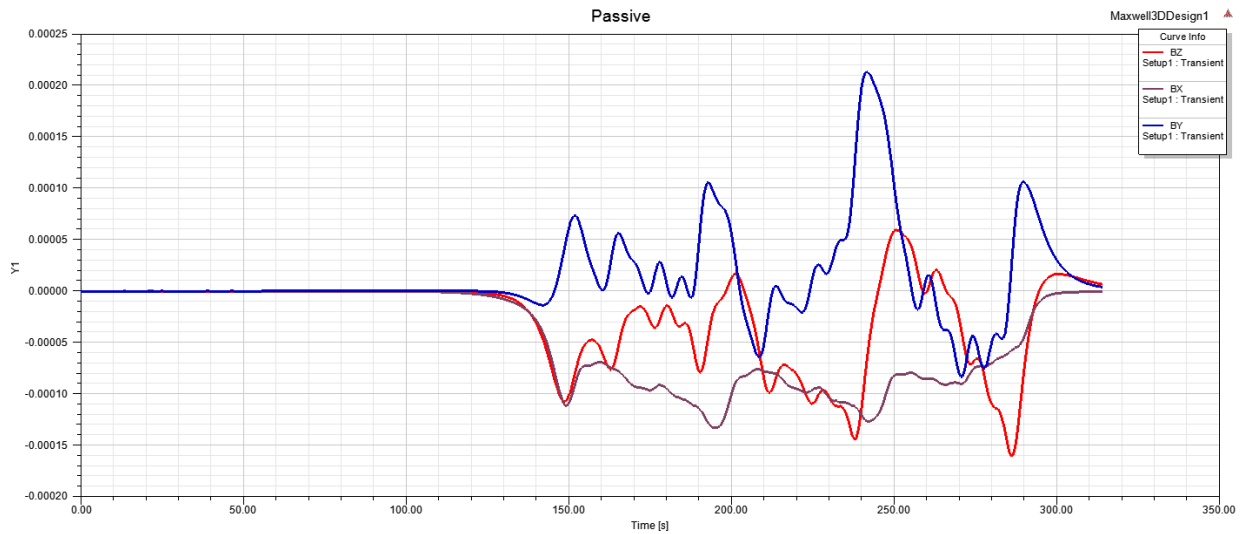


Figure C-51: Results from the full model (magnetized from top measured on top).

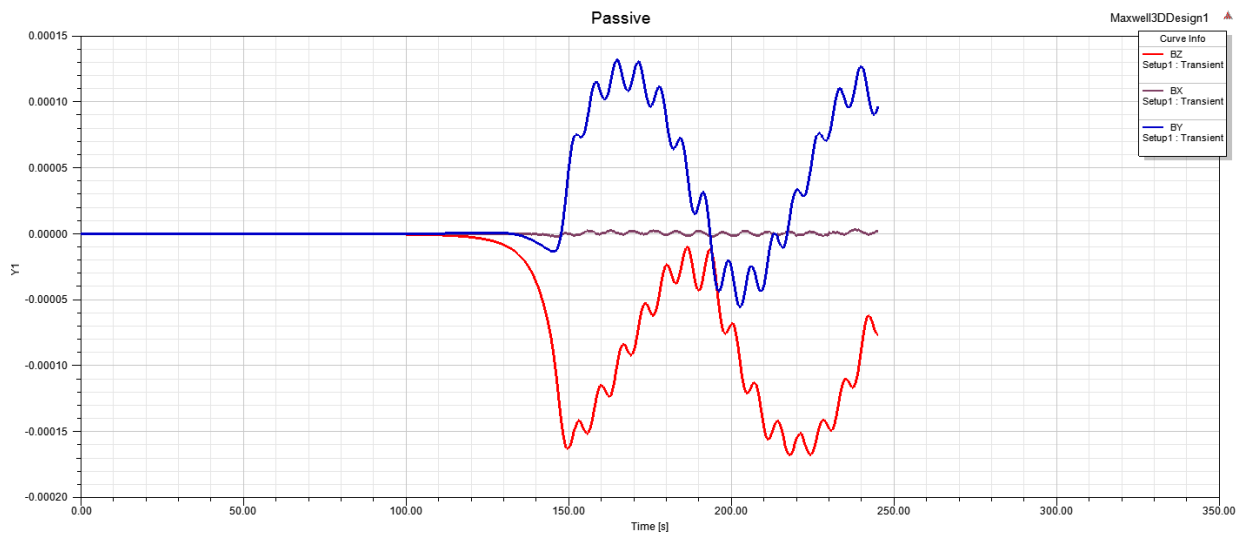


Figure C-52: Results from model without stirrups (magnetized from top measured on top).

The final set of graphs again shows the flux measured using the passive method, but the sensor is now located on the bottom side of the deck directly opposite the magnet. In these plots, the break in the strand passes by the sensor at a time of around 218 seconds. Figure C-53 shows the results from the first model (full detail) and Figure C-54 shows the results from the model without the stirrups. The model without stirrups was stopped early but can be resumed if desired. From the results obtained, it is quite evident that the response is complex.

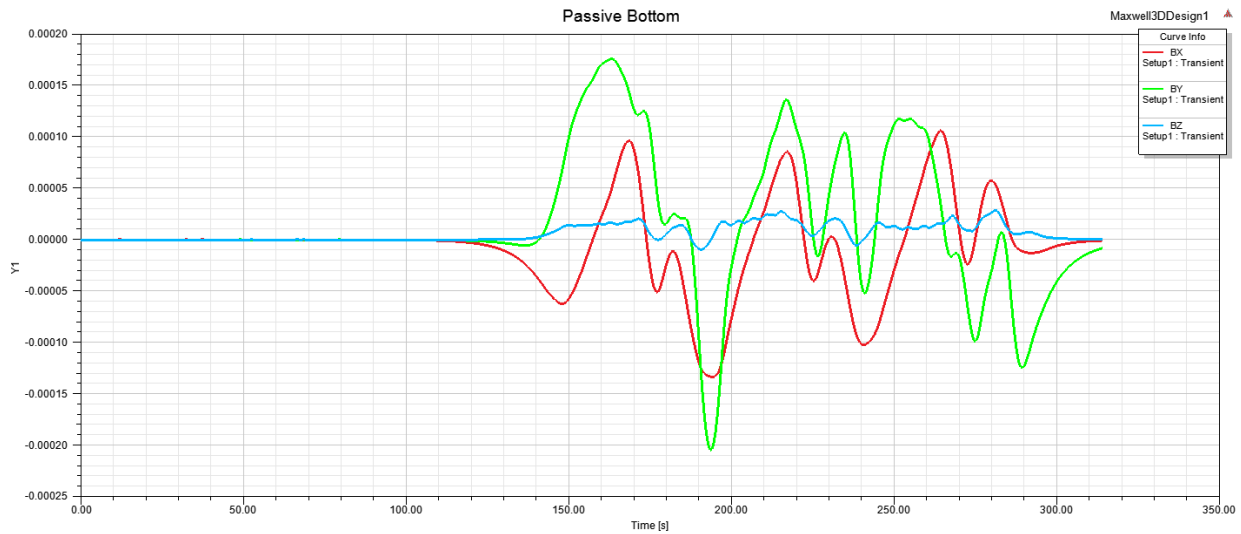


Figure C-53: Results from the full model (magnetized from top measured on bottom).

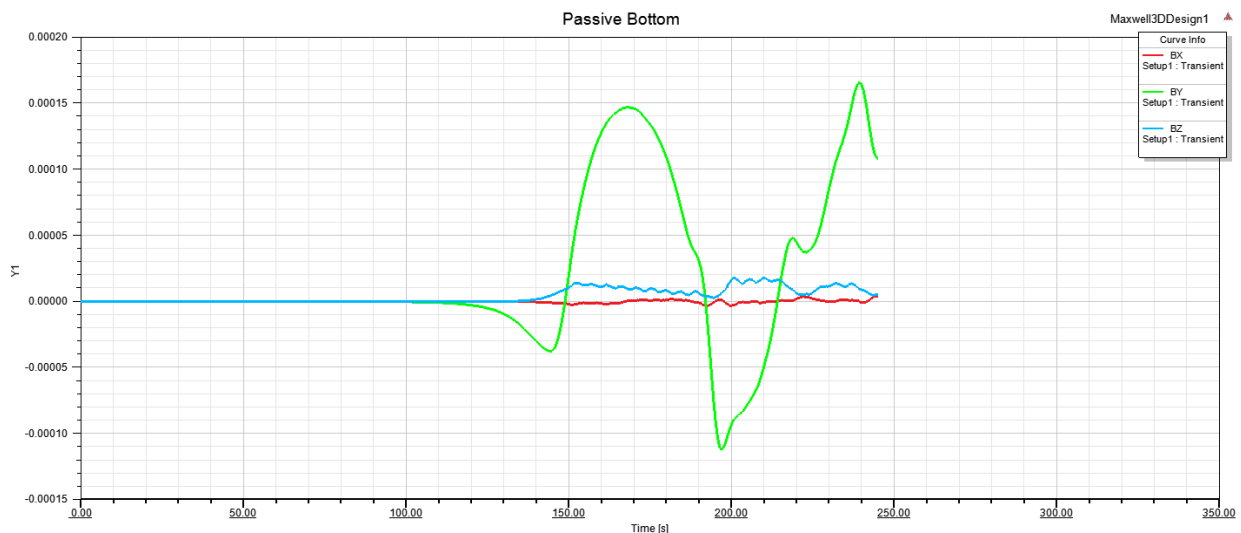


Figure C-54: Results of model without stirrups (magnetized from top measured on bottom).

C.2.3 Magnet Applied to End of Rod

Out of curiosity, magnets were directly attached to the ends of the damaged bar and the sensor was passed over the top. As seen in Figure C-55, despite the presence of a complete break in the PT bar, there was no real effect on the signal as the break, which was located at the midpoint, passed under the sensor.

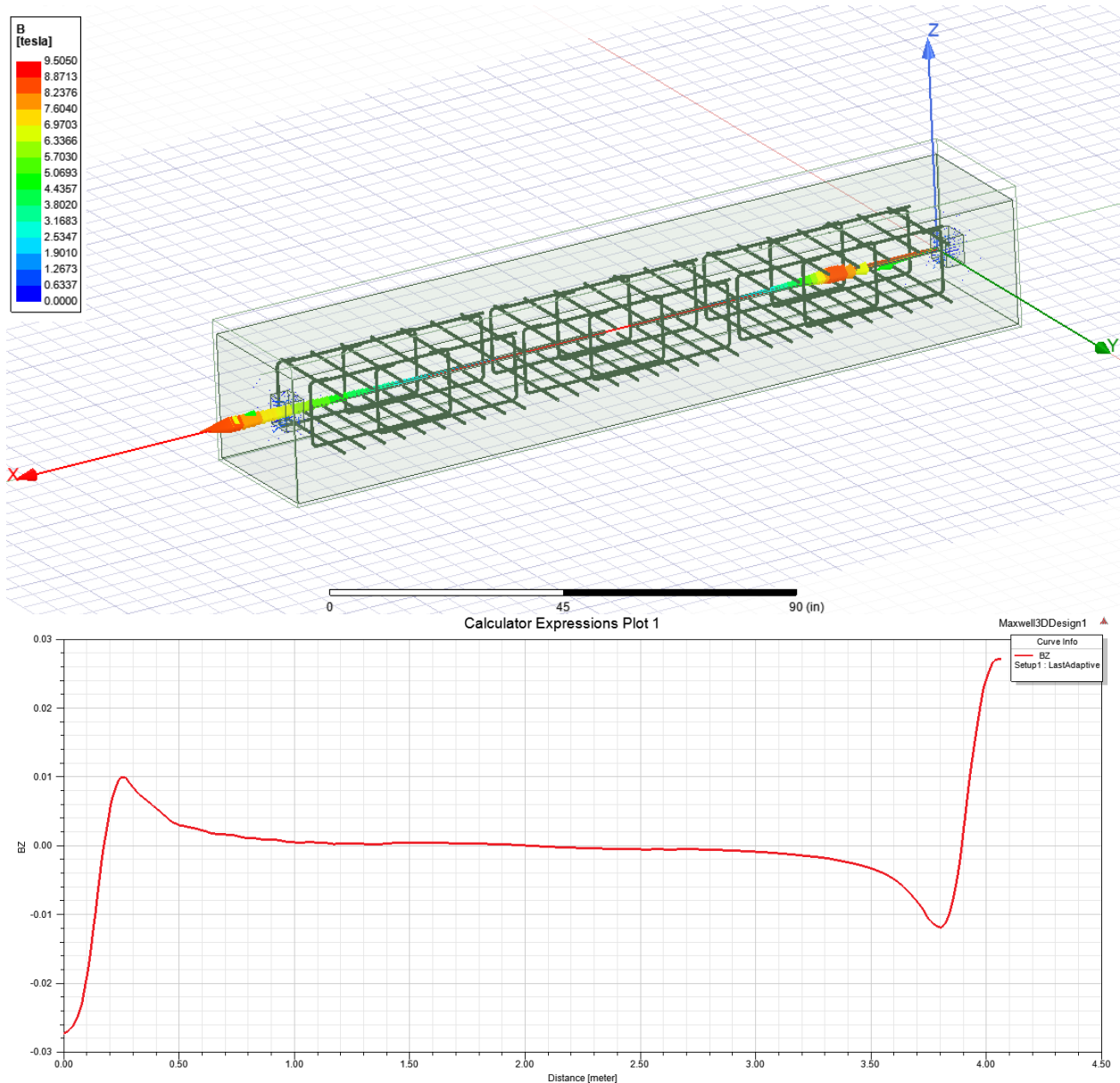


Figure C-55: Results from model with magnet attached to ends of the PT tendon.

C.2.4 Uniform Field

The final simulation applied a uniform field oriented longitudinally with the post-tensioning bar. This field simulates the earth's magnetic field. The relative permeability of the reinforcement results in flux concentrations and the ends of the reinforcement then become poles from which the flux diverges in three dimensions. This flux can then be measured by the sensors passing over the specimen. This analysis was performed on the full model with all reinforcement (Figure C-56), and also the model with only the PT and transverse bars (Figure C-57). The break in the PT is quite evident in the model without ties (Figure C-57).

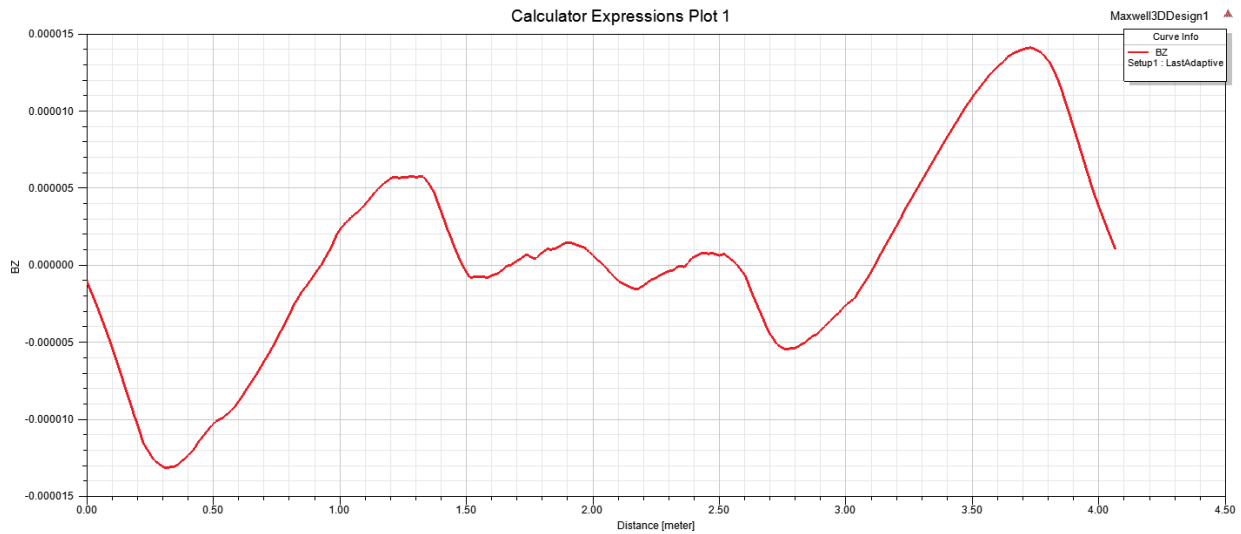


Figure C-56: Results from full model in a uniform magnetic field.

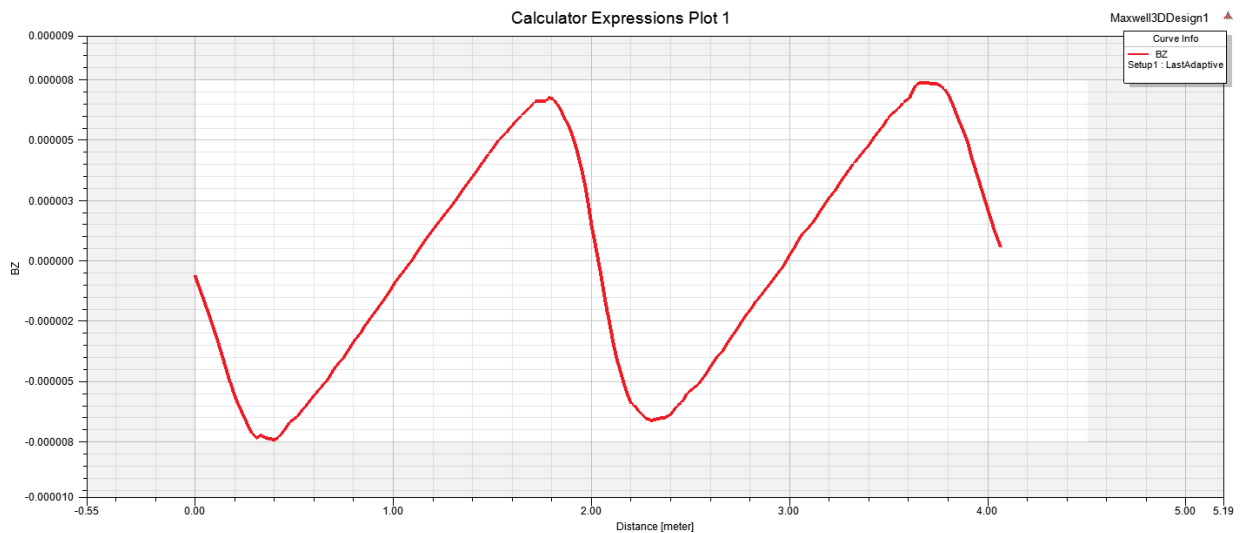


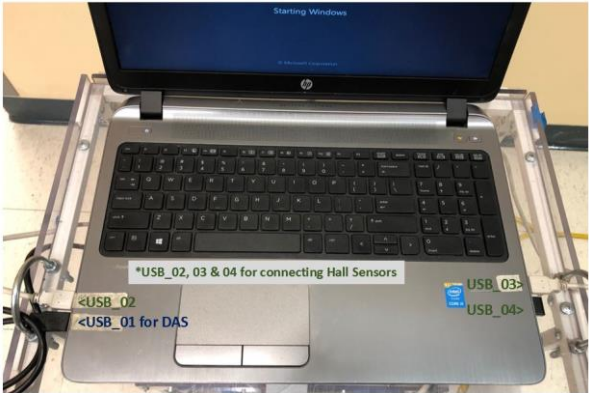

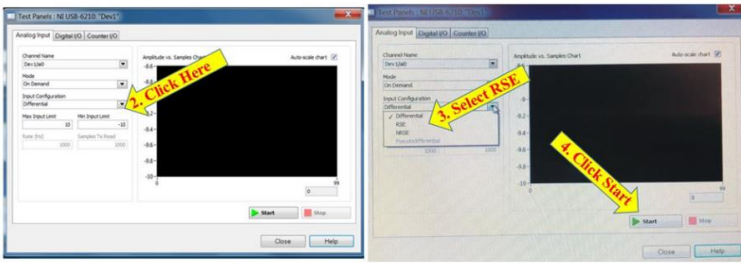
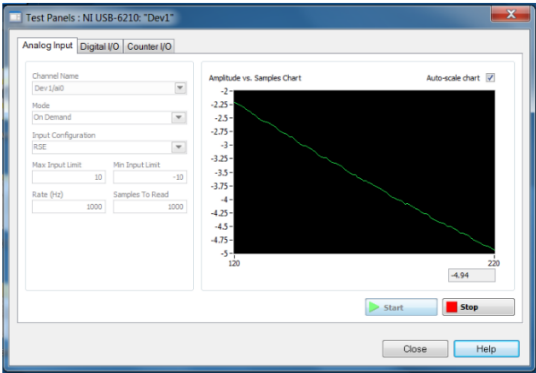
Figure C-57: Results from models without stirrups in a uniform magnetic field.

C.2.5 Observations and Conclusions

From the results obtained, it is evident that the response is complex, and it was determined that at this point relevant conclusions could not be drawn. The one observation was that the response due to the various elements present is not simply a linear summation of individual effects. Rather, there is a complex interaction that occurs between the elements. The next step in the research would be to compare the numerical results with those obtained from laboratory testing on simplistic specimens to validate the results. It seems quite apparent that a wider spacing of magnet poles can reduce the apparent signals from transverse reinforcement.

APPENDIX D Operation Manual

D.1 SETUP FOR DAQ SYSTEM FOR EXPERIMENTAL MEASUREMENT UNITS

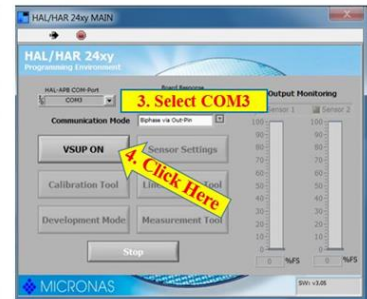
<p>Step-1: The DAQ system is connected to the laptop through the universal serial bus (USB) port.</p>	
<p>Step-2: A pop-up window appears from national instrument on the desktop screen. Click on “Go” next to “Test this device” tab. Another window will appear as shown on the right.</p>	
<p>Step-3: Click to change “Input configuration” from “differential” to “RSE” and then click the start button.</p>	
<p>Step-4: By clicking the start button, the signal will appear in the black region. The signal should appear in parabolic curve tending to be in a straight line. If there is no signal or a straight line, it means the data acquisition system is not working properly.</p>	

D.2 SETUP FOR HAL SENSORS

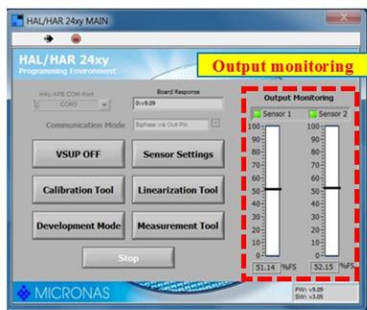
Step-1: Open HAL_HAR_24 application icon on the desktop and a window will appear as shown.



Step-2: Click on the drop-down menu against HAL-APB COM Port. Several options will appear with different COM values. Select “COM3” as shown.



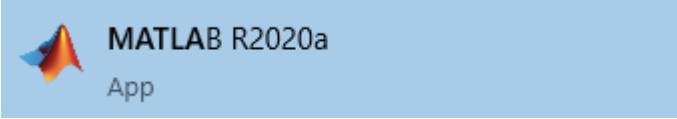
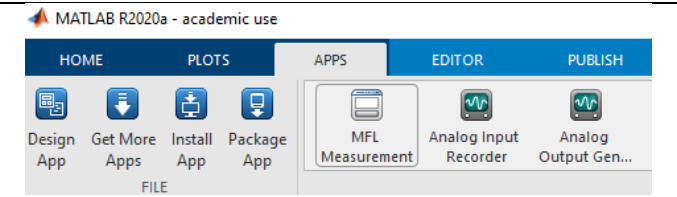
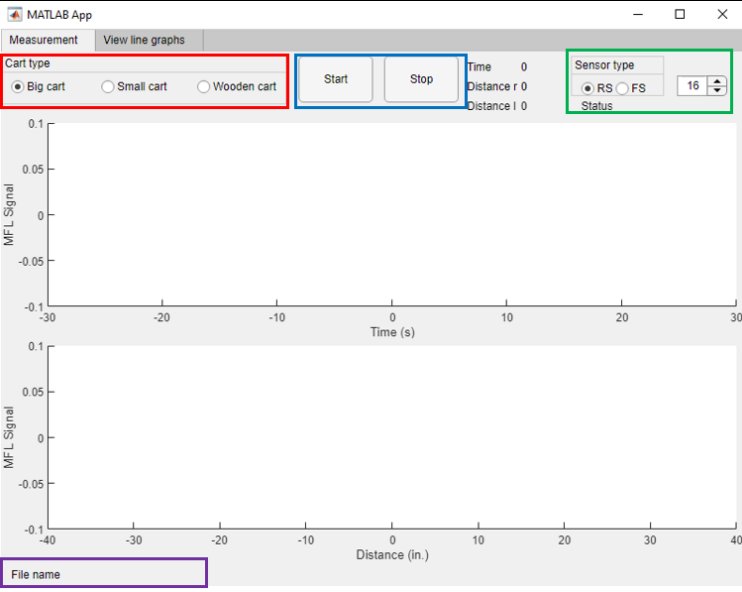

Step-3: Click on “VSUP ON” and a small window will appear for the confirmation of the selection. Select “Yes”. It will show if the sensors are working in “Output Monitoring” window. In case the USB of HAL sensor is not working, following window may appear in this step. Recheck USB connections and try again from Step 1 to 3.



Step-4: Check the “Sensor Settings” as follows. Click on the “Sensor Settings” and a new window will appear. Check all values in “Customer Setup” window.



D.3 FINAL MEASUREMENT UNIT MANUAL

<p>Step-1: Open MATLAB</p>	
<p>Step-2: On “APPS” tab select “MFL Measurement” application.</p>	
<p>Step-3: On “Measurement” tab: Select the cart type (red color box) connected to the computer. Use start and stop (blue color box) buttons to start and stop the measurement. Select the sensor type and number (green color box) for the live plotting during the measurement. The recorded data will be saved in the file (purple color box) shown in the bottom of the screen</p>	
<p>Step-4: On “View Line Graph” tab: Select the data file (red color box) to be plotted from. Select the sensor type and number and plot (blue color box) the graph. Enable (green color box) more data files to plot up to three graphs. Use the filter (orange color box) check box to filter the plotted data. Select a base file (purple color box) to offset the sensor values to Zero. In order to make a base file, measure for at least 15</p>	

seconds in an ambient environment with no or small magnetic field (away from magnets and magnetic materials).

To save the plot and get more options use pop out (yellow color box) button.

Notes:

- For the measurement unit 3b, the middle USB port should be connected to the computer.
- The measurement unit 3a should be connected using the USB port on the cart.
- The measurement unit 3b and the measurement unit 2 should have a stable power supply during measurement.
- The measurement unit 3a can run without a power supply but using a stable power supply is preferred for reliable measurement.
- In case of malfunction Hall sensors in the cart can be changed. The sensors are set to ± 3 mT.

D.4 OPERATION MANUAL

In the remanent MFL method, a tendon or PT rod is magnetized before the HE sensors are used to measure the flux signal. This method allows the magnet assembly to be used independently of the sensing system. The typical operation of the equipment is shown in Figure D-1. Both the sensing system and magnetizing assembly were wheel driven and manually operated. The operational magnetization speed can be varied but typically ranges from 0.5 ~ 1 ft./sec.

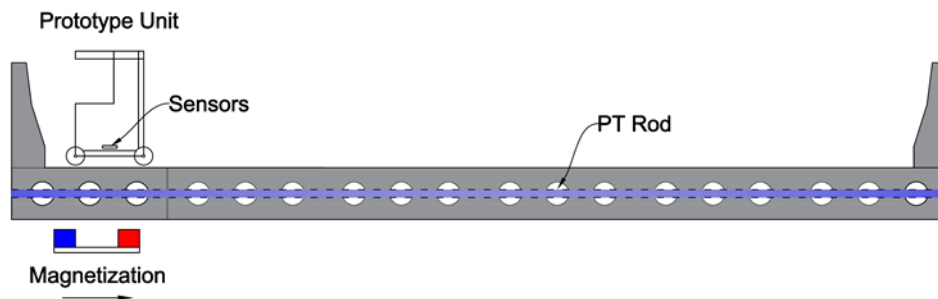
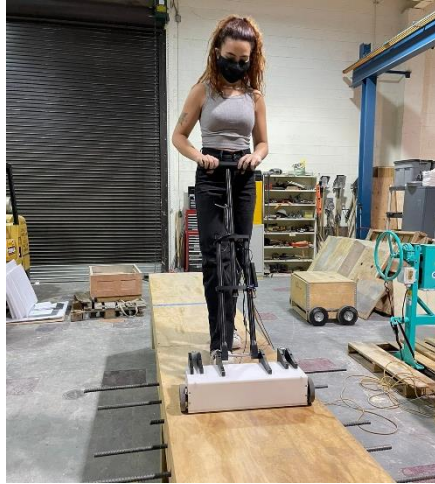


Figure D-1: Typical operation of MFL magnetizing and sensing system.

The magnetization can be carried out from the top or bottom of the bridge along the length of the PT rod or internal tendon. Bottom magnetization scheme may require a support mechanism such as guide rails. To reduce the interference, the support mechanism should also consist of non-ferromagnetic material components. In some cases, the magnetization scheme may consist of moving the magnet over the target area several times. After the magnetization, the measurements are carried out using one of the prototype units. The data is stored in the laptop and a sub-routine was developed in a programming language to visualize the results after each test run.



(a)



(b)

Figure D-2: Operation of MFL testing for (a) lab testing and (b) field testing.

Before the testing is carried out, the orientation and direction of the internal tendons must be determined and marked on the bridge element. For mapping of the tendons and secondary reinforcement, other NDT techniques such as GPR may be used. The prototype unit is then traversed along the marked path. The prototype units developed at FIU are capable of scanning majority of internal tendons located on vertical and horizontal surfaces. The units can also be modified for other applications if railing and additional support mechanisms are provided. To this end, the sensors and the DAQ system can be affixed on these support systems. Few examples where these units can be used are the tendons in deck slabs, cantilever and continuity tendons of box girders, transverse PT rods in bridges, etc.

APPENDIX E TESTING WITH MAGNET 3

A systematic study was carried out to improve the magnetization power of the permanent magnet assembly. Different magnet configurations were developed in this study. Magnet 3 was developed at the later stage of the project. Since, all other prior testing in this report was conducted using magnet 1 and magnet 2; therefore, the efficacy of magnet 3 was tested under laboratory conditions similar to those of other magnets. Table E-1 shows a summary of all the tests that were conducted.

Table E-1. Summary of tests

Test No.	No. of Magnetization	Magnet No.	Polarization	Transverse Reinforcement
1	1	3	S-N	-
2	1	3	N-S	-
3	1	2	S-N	-
4	1	2	N-S	-
5	1	3	S-N	-
6	2	3	S-N	-
7	3	3	S-N	-
8	1	3	N-S	8 rebars (7 in. c/c)
9	1	3	S-N	8 rebars (7 in. c/c)
10	2	3	S-N	8 rebars (7 in. c/c)
11	3	3	S-N	8 rebars (7 in. c/c)

The main goal of these tests was to analyze the difference in the MFL signal results with the effect of different magnets and reinforcement pattern. All tests were carried out in the laboratory on wooden specimens already explained in Section 4.1. Magnetization was carried out from the bottom of wooden specimens and measurement was conducted from the top using measurement unit 3b.

For the first experiment ten steel strands, with 50% section loss in steel strands, was used. The strands were magnetized by using either magnet 2 or 3. For test 1 and 2, tendons were magnetized using the magnet 3. Then, the polarization was changed by flipping the poles of the magnet from north-south to south-north. The purpose of flipping the poles of the magnet was to see the effect of how a single magnetization would affect the signals. As observed in Figure E-1, the signal from test 2 is inverse of test 1 and the signal amplitude is almost similar. This verifies that the magnet 3 can magnetize the steel strands after a single run. The location of the defect is located at 126 inches and shown by a dotted red line. Therefore, it can be concluded that the inflection point caused by the defect is not affected by the direction of poles when magnetizing the strands.

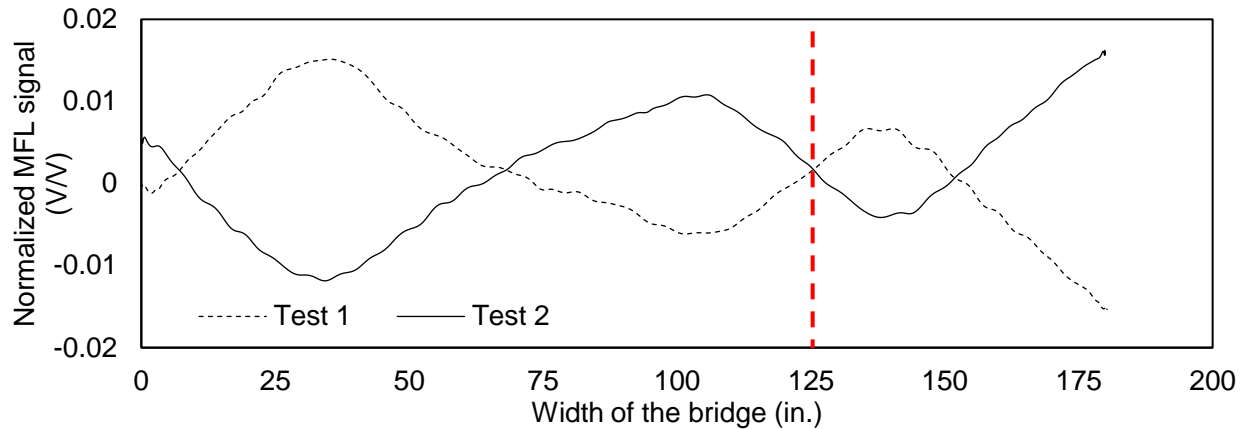


Figure E-1: Effect of changing the magnetization direction for magnet 3.

Test 3 was conducted to analyze the difference in signal when using magnet 2. The polarization direction was kept similar to test 1. A comparison of signals for magnet 2 (test 3) and magnet 3 (test 1) is provided in Figure E-2. It can be observed that the modified magnet 3 has magnetic strength similar to magnet 1 after a single magnetization run.

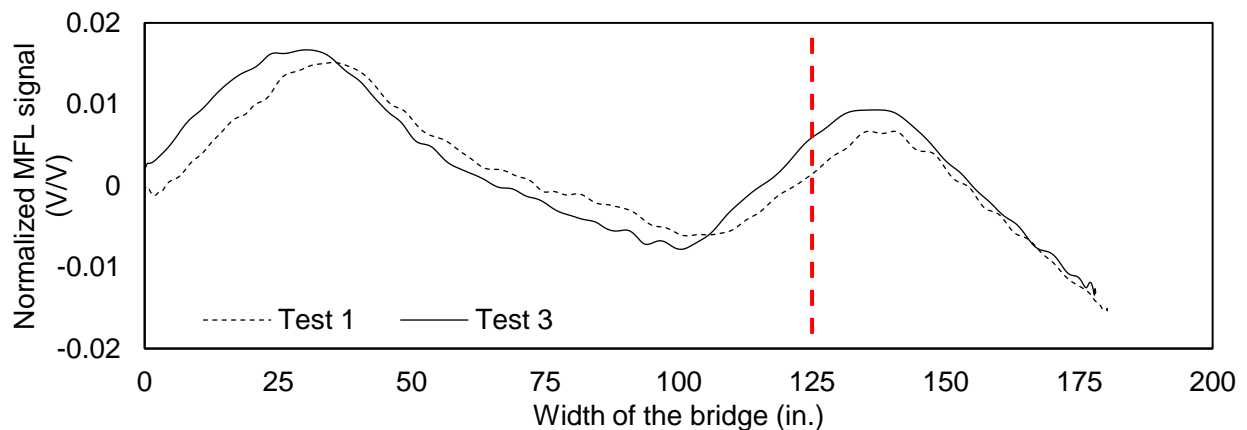


Figure E-2: Difference between using the magnet 2 and 3.

The polarization in this test was changed from test 3 (S-N) to N-S. The aim of test 4 was to see the effect of change in polarization when using magnet 2. The test results are plotted in Figure E-3. As expected, the signal was inverted, and the amplitude of the signal was almost similar to test 3.

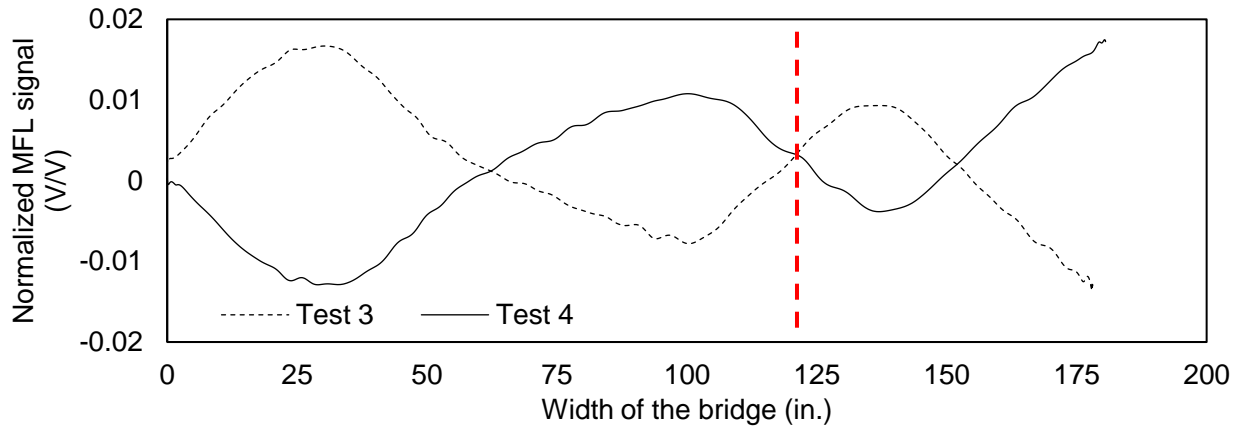


Figure E-3: Change in the polarization of magnet 2.

Test 5 to 7 were conducted to observe the effect of repeated magnetization schemes on signal amplitude. All other test conditions were kept unchanged and the number of magnetizations were changed from 1 to 3. Figure E-4 shows the difference between the results after several times of magnetization. It can be observed that repeated magnetization does not significantly change the amplitude of the signal.

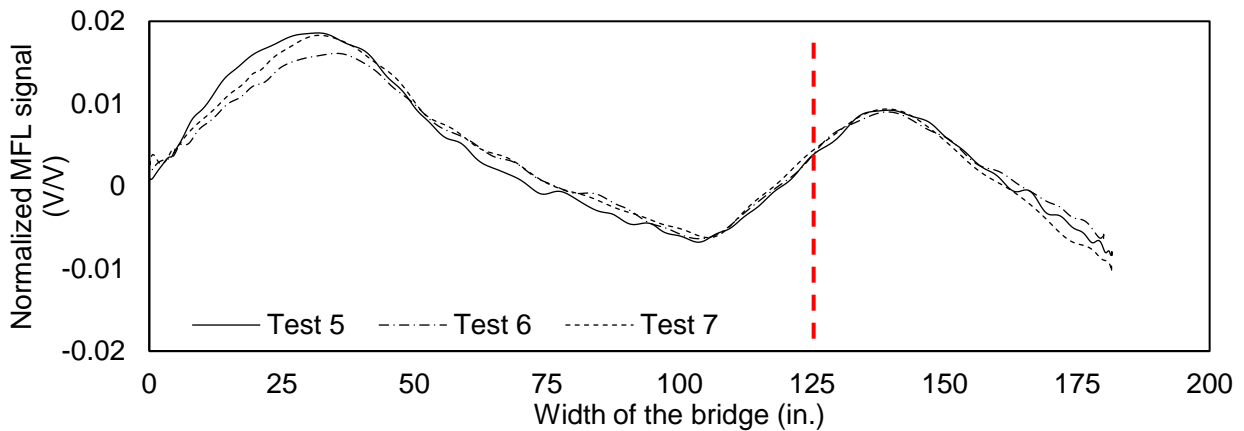


Figure E-4: Results after several times of magnetization.

For the next experiments, eight transverse reinforcement with 7 inches distance were added to the wooden test set up. Magnet 3 was used in all subsequent tests. Figure E-4 shows the difference between the results before and after the addition of transverse reinforcement. Figure E-2 shows the difference between the results when the polarization was changed using the final test set up including the transverse reinforcement. Finally, magnetization was repeated to see the difference between the results after magnetizing the same section three times. Figure E-3 shows the difference between the results after magnetizing the final test set up several times without changing the polarization.

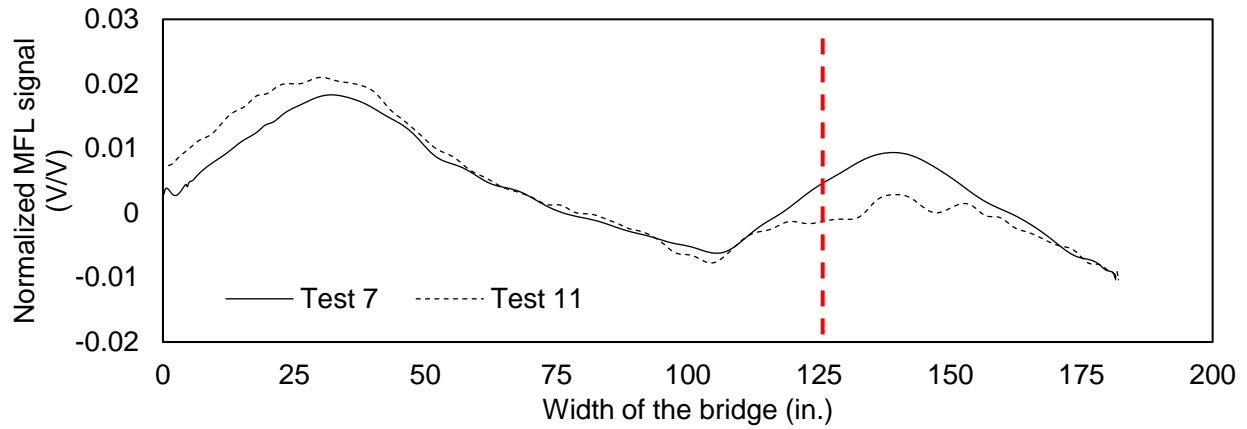


Figure E-5: Effect of transverse reinforcement.

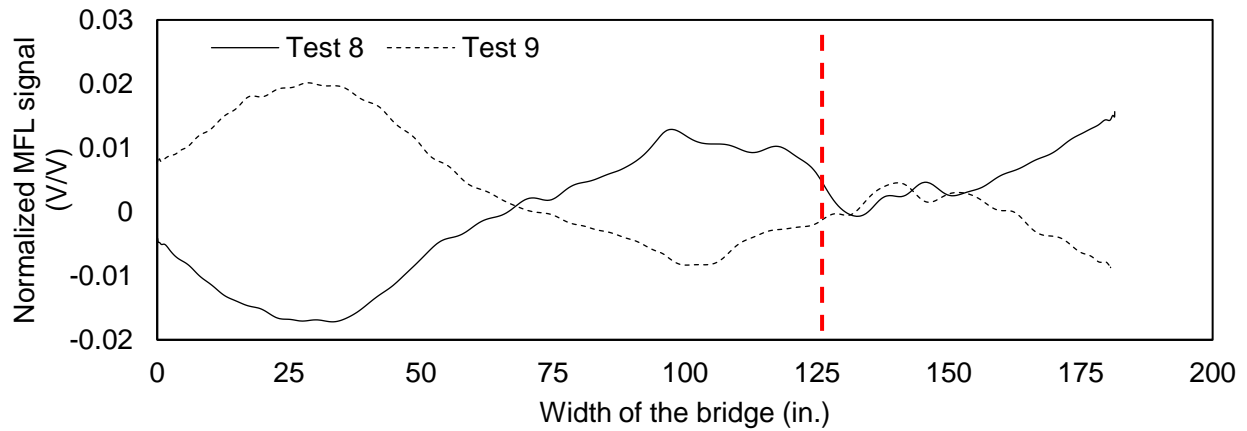


Figure E-6: Difference between the results when the polarization was changed.

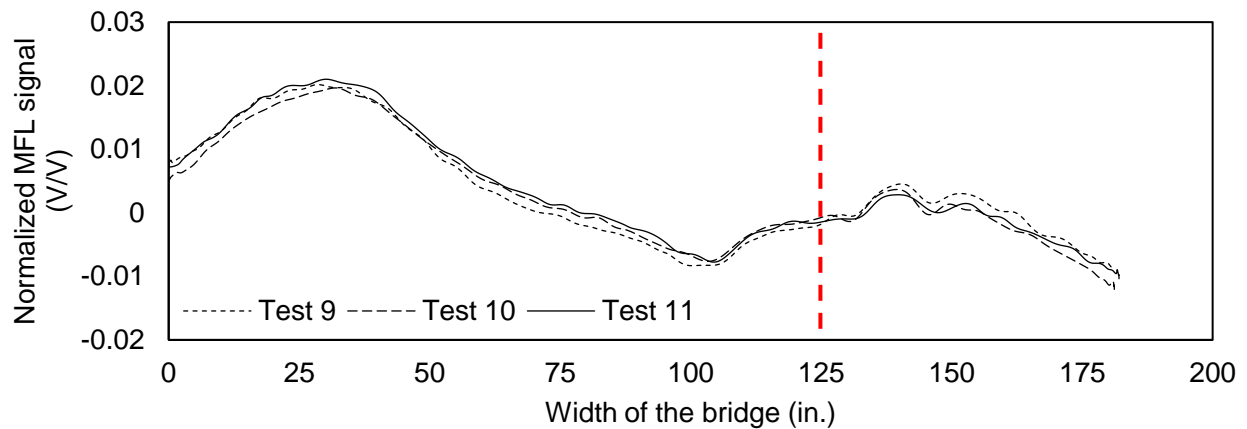


Figure E-7: Results after several times of magnetization.